ANALOGUE MODELLING OF PYROCLASTIC DENSITY CURRENT DEPOSITION

PETER JAMES ROWLEY

ROYAL HOLLOWAY, UNIVERSITY OF LONDON

A THESIS SUBMITTED FOR THE DEGREE OF
DOCTOR OF PHILOSOPHY

JANUARY 2010

I declare that the work presented in this thesis is my own.

Pete Rowley

Abstract

Pyroclastic density currents (PDCs) are one of the greatest hazards to populations living near active volcanic centres, yet the granular physics which dominates their depositional behaviour is poorly understood. A series of flume experiments are used to investigate the initiation, flow and deposition of polymict granular charges as an analogue for the dense granular basal current found in PDCs and other geophysicical flows. A technique is developed to allow interrogation of flume deposits in three dimensions, and therefore to analyse the ability of flume experiments to recreate sorting and deposition geometries typical of geophysical systems beyond runout and crude thickness similarities. Polymict charges provide sorting analogues for typical PDC clast types (i.e. lithic and juvenile pumice), and are able to reproduce classic small-volume PDC (and debris flow) features, including levees, distal and surface concentrations of pumice analogues, and ventral proximal concentrations of lithic analogues.

Sequential charges and stratified substrates permit the investigation of reworking in granular systems, and scaling demonstrates relevance to a wide gamut of geophysical flows. Conduction of granular temperature from a flow to a static substrate encourages remobilisation. Velocity contrast at the flow-substrate interface encourages growth of what appear to be the first recorded Kelvin-Helmholtz (K-H) instabilities observed at the interface between a shearing grainflow and static substrate. Mathematical modelling indicates conditions within PDCs are favourable for K-H instability growth. This has ramifications for temperature proxy data, radiogenic dating by included phenocrysts or charcoals, calculation of eruptive volumes, and sedimentation rates. Partial growth of K-H instabilities appears to be a ubiquitous feature at deposit contacts, and geometry of these is similar to recumbent flame structures in field PDC deposits. K-H growth is implicated as a syn-depositional method of recumbent flame formation, eliminating the need for post-depositional loading and shear deformation required by current explanations.

TABLE OF CONTENTS

DETAILED TABLE OF CONTENTS

LIST OF FIGURES

LIST OF TABLES

ACKNOWLEDGEMENTS

This work would not have been possible without the help, advice and support of a great many people and organisations. First and foremost I would like to thank my supervisors Martin Menzies, Dave Waltham and Peter Kokelaar, who have allowed me to develop this project in directions it otherwise might not have gone, and whose advice and assistance in this I greatly respect and appreciate.

Developing the laboratory techniques used in this work was entirely reliant on the generous donation of laboratory space provided by Ken McClay and the Fault Dynamics Research Group at Royal Holloway. In addition to this, I was afforded invaluable help and support by Jonny Wu and Sohail Wahid, who gave me the grounding in the sandbox modelling techniques necessary to take the work forwards. I am indebted to Mick Slocombe for his expertise, time and skill employed in making, modifying and improving the flumes. Funding provided by the University of London Central Research Fund was invaluable, and without which this project could not have grown the way it has.

The field work would have been impossible without the generous financial support provided by the Kirsty Brown Memorial Fund, and Earth Sciences Department Research Committee at Royal Holloway. In addition, I must express my sincere gratitude to Shane Cronin and Gert Lube at the Volcanic Risk Solutions Group, Massey University (New Zealand). Not only have they been invaluable in gaining a better understanding of the processes active around Ngauruhoe, but the time spent in the field with Gert was fundamental to me getting to grips with so much volcano in so little time.

Developing both the processes and theory during this PhD has entailed a stream of fascinating and useful conversations with very large number of volcanologists, sedimentologists, modellers, physicists, tectonic geologists and others. It would be remiss of me, however, to go without mentioning Mike Branney, Eoghan Holohan, Colin Wilson, Mike Cottam, Ben Clements, Jocelyn McPhee, Gary Nichols, Peter Burgess, Dennis Meyer and Aaron Elligsen for their beneficial and valued input. I am indebted to many of the staff at Royal Holloway for not only their technical assistance and advice, but also the enthusiasm and interest they have always shown in this project, making the dark mornings when everything is going wrong a far more tolerable experience. I would particularly like to thank Kevin D'Souza, who has provided everything from laboratory advice, photographic equipment, and generosity with his time, through to beers and a laugh - all provided with a smile.

Three and a half years on a single project inevitably has its ups and downs, and throughout that process I have been graced with an amazing bunch of friends. The ladies and gentlemen in 202b (past and present, honorary and actual) I will miss you all terribly. Anna - I'll miss my daily dose of sardonic Scots humour, Clare - you kept me pretty much sane next to that door which probably deserves a medal. Christina - the biting, scornful and mocking humour will be very much missed, and I can't thank you enough for your help and advice in the final stages of putting this together. It's been a blast and I couldn't have hoped for a better bunch of people to share it with.

I am sincerely thankful to my family for the support they've provided throughout this, particularly of course mum and James, who have provided me with 30 years of love, support and encouragement, and whom I hold entirely responsible for me turning out the way I have.

Finally, I don't have the words for how grateful I am to Hollie for putting up with me throughout this, right from the slightly startled expression on her face when I said I wanted to start a PhD, through the whole process to this point now. Thank you, I love you.

This work is dedicated to the memory of Allan Rowley, who ignited my curiosity, and without whose influence, support, advice and guidance I could not have walked this path.

DEFINITIONS

architecture - The overall structure of a deposit, including it surface topography, distribution, and internal structure.

ash - fine grained pyroclasts with diameters under 2 mm. Analogous to colloid through medium sand sizes using the Wentworth sedimentary grainsize classification.

block - Large pyroclasts, over 64 mm in diameter. Analagous to cobble and boulder sizes using the Wentworth sedimentary grainsize classification.

block and Ash flow - A pyroclastic flow consisting of poorly vesiculated blocks, lapilli and ash of similar composition, which typically forms as a consequence of a collapsing lava dome. Their deposits are usually small volume.

de-interlace - A processing technique carried out on video footage. Video frames are composed of odd and even lines, with the odd lines containing data from the 'current' tiemstamp, and the even lines containing data from the next time stamp. Deinterlacing separates these two images and recombines the correct data with the correct frame. An interpolation algorithm is used to fill any missing data.

debris flow - a geophysical flow of saturated unconsolidated material

debris avalanche - a geophysical flow of unsaturated dry blocks

fluidisation - in this work, fluidisation is used in the specific sense to describe the conversion of a granular material into a fluid-like state by injection of fluid (e.g. exolution from juvenile clasts), or by vibration (leading to dilation).

granular flow - any flow predominantly composed of non-cohesive particles.

granular temperature - shear-induced random vibrations in a granular medium, and its resultant dilation.

ignimbrite - the deposit of a pyroclastic density current rich in pumice lapilli and pumiceous ash.

Kelvin-Helmholtz instability - An instability which occurs with velocity shear in a continuous fluid, or with sufficient velocity difference across an interface of two fluids.

lapilli - pyroclastic particles between 2 - 64 mm diameter. Analogous to course sand through pebble sizes using the Wentworth sedimentary grainsize classification.

monodisperse - a mixture containing a single particle population.

polydisperse - a mixture containing several discrete particle populations.

pyroclast - juvenile fragment produced by volcanic activity.

pyroclastic density current (PDC) - a "ground hugging current of pyroclasts and gas (including air) that moves because it is denser than the surrounding atmosphere (or water): i.e. an underflow." (Branney

and Kokelaar, 2002).

static stability - the condition under which the denser layer sits below the less dense layer, making the contact gravitationally stable to instability growth.

steady - Time invariant.

underflow - any gravity current, i.e. where the dense regions occupy a position below more buoyant regions.

unsteady - Time variant.

waning - decrease of a flow parameter through time with respect to a single spatial point.

waxing - increase of a flow parameter through time with respect to a single spatial point.

CHAPTER 1: INTRODUCTION

1.1 Aims

The aim of this work is to develop a series of analogue experiments which replicate the granular depositional system found at the base of some pyroclastic density currents (herein abbreviated to PDCs). A variety of flume experiments and techniques will be used and developed in order to investigate the effects of sorting, reworking and deposition on the architecture of deposit and substrate systems.

1.2 Classification of volcanic activity

In order to discuss the formation of PDCs it is important to first understand both what a PDC is, and the nature of the volcanic eruptions which create them.

The term 'pyroclastic density current' is used to describe "a ground hugging current of pyroclasts and gas (including air) that moves because it is denser than the surrounding atmosphere (or water): i.e. an underflow." (Branney and Kokelaar, 2002). As this definition shows, PDCs comprise a wide-ranging gamut of flow types, represented in the field by an equally diverse range of resultant deposit lithologies.

PDCs are produced by a range of volcanic vent processes, (e.g. Williams 1957; Druitt, 1998; Branney and Kokelaar, 2002). The following section introduces the basic terminology, and the volcanological processes involved in the generation of PDCs. There are three classification schemes which are relevant to the basic understanding of PDC-forming magmatic eruptions; one considers the physical characteristics of the eruption style, the second considers magnitude, and the third considers intensity.

1.2.1 Eruption Style

Eruptions may broadly be described by their effusivity; that is, the continuum between effusive activity (dominated by the eruption of fluid products, resulting in the generation of lavas) and explosive activity, where high volatile contents in the source magma cause fracturing (ductile or not) of the magma as it exsolves gas and erupts, causing the formation of pyroclasts, which subsequently fall or flow (forming PDCs) to generate pyroclastic deposits. The style of eruption is classified according to comparison to several type volcanoes, and can be briefly summarised as follows:

Hawaiian – Generally effusive, with lava emission from fissures or vents. Lava fountains may be generated, with ejected lava reaching altitudes of up to several hundred meters.

Strombolian – small pulses of lava bursting in a summit crater, commonly generating incandescent cinder, lapilli and bombs. No sustained eruptive columns are generated, but material may reacha s far as several kilometers in altitude (although more ypically hundreds of meters). Discrete but regular eruptions, recurring in second to minute timescales.

Vulcanian – Short lived explosive activity, with irregular intervals (quiescense may range from days to millenia), often associated with viscous magmas.

Pelean – Often slow effusion of lava domes, interspersed with vulcanian-type eruptive episodes. Cycles between volcanic episodes may be in the order of years to centuries. Small volume PDCs are commonly generated from collapsing lava domes (typified by the classic 'Nuee Ardentes' style of flow).

Plinian – Eruption of viscous magma, ejecting pyroclasts to altitudes of tens of kilometers. Eruptions may last in the order of hours to days, with states of quiescence lasting in the order of hours to centuries (or greater). Eruption volumes range from 0.1 km^3 up to >1000 km^3, with the largest intensity eruptions (see section 1.2.3) often being described as Ultra-Plinian. Widespread (1000's km^2) dispersal of tephra and PDC deposits is typical.

1.2.2 Eruption Magnitude

Rather than considering the eruptive style, it is often more informative to simply deal with the magnitude of an eruption – that is, the mass or volume of the released material. Due to vesiculation of juvenile particles volume can be a problematic value to calculate, making mass preferable in many ways. However, as magmas vary in density this is itself a flawed system. There are, as a result several systems in use. As an example, the system used by Pyle (2000) considers the mass (m, in kg) of material ejected and calculates a magnitude (M) according to

$$M = \log_{10} m - 7 \quad . \qquad [1.1]$$

Using this, to give an example, the Mt St. Helens eruption in 1981 would register as M=4.9. It is informative to investigate magnitude of eruptions plotted against their frequency (Figure 1.1).

1.2.3 Eruption Intensity

Eruption intensity assesses the rate of mass eruption from a volcano (kg s^{-1}). In this way we can compare the behavious of volcanoes with similar total volume, but varying flux. Two volcanic events producing 1,000,000 kg of material will be markedly different if the intensity of these eruptions is different - that volume produced in minutes requires much larger ejection rates than that same volume ejected in days or weeks.

1.2.4 Volcanic Explosivity Index

Eruption magnitude and intensity may usefully be considered alongside each other, as done with the Volcanic Explosivity Index (Newhall and Self, 1982). This classification scheme was drawn up to act as a semi-quanititative method of assessing volcanic activity in the geological record. VEI 0 represents small volume (<1 x10^4 m^3) and/or effusive eruptions, while VEI 8 represents colossal eruptions (>1x1012 m3), such as the Fish Canyon eruption of the La Garita caldera, 27.8Ma.

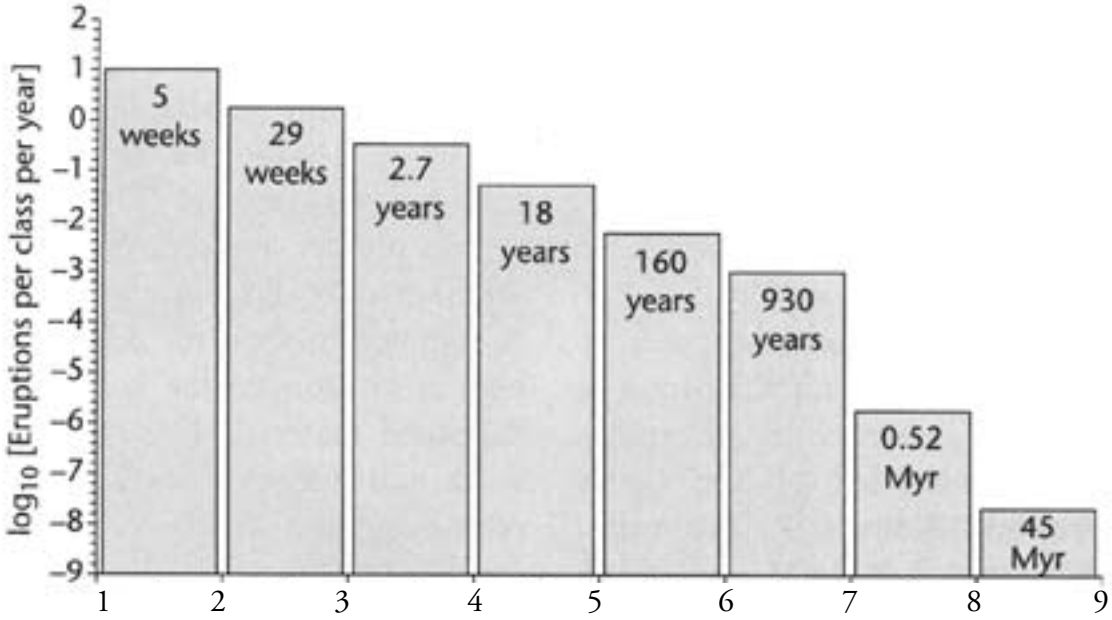

Figure 1.1 Magnitude – frequency plot for volcanic eruption records (last 300 years for $M < 6$, last 2 kyr for $6 \leq M < 8$, and 45 Myr for $M \geq 8$). M9 is represented by a single eruption (Fish Canyon Tuff). Modified from Francis and Oppenheimer, 2004.

1.3 Classification of PDCs

PDCs occur in a wide range of scales and situations, The smallest (in the order of thousands of cubic meters) tend to occur as block and ash (BAF) flows, derived from spalling off or collapse of lava domes, or as small single pulses derived from Strombolian or Vulcanian eruptions, with flow lifetimes in the order of seconds to minutes. Frequently with runouts in the order of hundreds of meters, the deposits are often channelised, demonstrating features such as lateral levees of coarse particles, terminal pumice or scoria dams, and lobes of material forming at the distal extent (e.g. Merapi PDC deposits). PDCs can commonly reach millions of cubic meters, with thicknesses ranging from centimeters to tens of meters. These flows exist for lifetimes of minutes to hours. The very largest PDCs, derived from caldera-forming eruptions (e.g. the Bishop Tuff, California) may be thousands of cubic kilometers in volume, with extents covering thousands of square kilometers, and thicknesses reaching hundreds of meters. The PDC forming event in these cases may last days.

1.3.1 Formation

PDCs form almost exclusively from high intensity magmatic events, or eruption into water or water-laden sediment (phreatomagmatism), with a smaller number generated from low intensity dome growth and subsequent collapse. There are a wide range of PDC deposits (e.g. (Sparks R. S., 1976; Fisher, 1986; Branney and Kokelaar, 1992), and the wide range of explosive eruption mechanisms allows categories of eruptive event to be drawn up. Tables 1.1 and 1.2 summarise two alternative classification schemes which relate PDC formation to eruptive styles.

Comparison of these two classifications is an interesting exercise, and demonstrates why several different classifications are prevalent within the literature. The Branney and Kokelaar (2002) scheme is

TABLE 1.1 PDC CLASSIFICATION AFTER BRANNEY AND KOKELAAR (2002).

Type	Description
A	Short single-surge current, derived by momentary collapse from a Plinian eruption column *
B	Sustained current derived from prolonged pyroclastic fountaining. The height of the jet (gas thrust) that feeds the current may vary and is transitional into C *
C	A sustained current derived from a prolonged low pyroclastic fountain (boil over) during an explosive eruption. This lacks the kinetic energy derived from the potential energy of a high fountain. It may be accompanied by a buoyant eruption column that does not feed the current.*
D	Current with a single (or multiple) surge derived from lateral blasts initiated by catastrophic decompression of a magmatic and/or hydrothermal system. Known examples were sustained for only short durations and did not produce large volume ignimbrites.
E	Single-surge current derived from a collapsing lava dome or flow front. Hot rock avalanches generate turbulent density currents. Block and ash flows tend to develop overriding low-concentration dispersions by rapid generation and segregation of relatively fine pyroclasts from underlying relatively high-concentration debris falls and granular flows. Most pyroclastic density currents produced in this way generate small volume block-and-ash flow deposits, and detached surge deposits
F	Deposit derived pyroclastic density current caused by gravitational collapse and avalanching of unstable loose ignimbrite, sometimes long after the eruption has ended. The current may be a single-surge or more sustained where the collapse is retrogressive. lithofacies and granulometry of the ignimbrites formed by the deposit-derived currents are similar to those of the parent ignimbrite, which suggests similar mechanisms of transport and deposition.

* Resulting deposits are described in detail throughout Branney and Kokelaar (2002).

based entirely on the nature of the eruption leading to the associated PDC. Because this classification is largely based on the continuity of the eruption it is easy to use in the classification of *observed* volcanic activity.

In contrast, the Williams (1957) scheme is based on observations of specific volcanoes and their deposits. The classifications are concerned as much with lithology as with eruptive style. This is particularly useful when looking at older eruptions, as it allows analysis of PDC deposits to provide direct analogues to modern day examples. The problem with this scheme is that it is based on a relatively small number of volcanic examples, when volcanoes are in reality a continuum. It is inevitable that many volcanic eruptions (and hence deposits) do not neatly fit into any single category.

A volcanic succession in the field may comprise units derived from any or all of these processes, depending on the specific volcano in question. Due to the relative simplicity of the analogue modelling performed, the Branney and Kokelaar (2002) scheme will be used throughout this work, with specific examples referring to the Williams (1957) scheme where appropriate.

1.3.2 Recording of flow

Pyroclastic flows are not only a very hostile environment for measuring equipment, but are also unpredictable. An eruption may widen or distort the vent, which in turn may effect the rate of eruption, angle and direction of ejection, or the height of the column (e.g. Ogden and Wohletz, 2009). As a result the likely path of any subsequent fountain-derived PDC will vary (Ross and White, 2006). For this reason, until a reliable method for sampling flows in motion is developed, the research into PDC flow will rely on a great number of assumptions and simplifications largely based on observations of flow, and analysis of subsequent deposits.

The initiation of these phenomena is largely unpredictable, so most of what is known about them is derived from eye witness accounts (e.g. Nairn and Self, 1978) and the study of resulting deposits

TABLE 1.2 PYROCLASTIC FLOW AND ERUPTION CLASSIFICATION AFTER WILLIAMS (1957)

Category	Sub-classification	Description
Flows related to domes or crumbling lava flows	Merapi type	Flow forms by non-explosive disintegration and gravity-collapse of lava domes and spines, or by the break-up of lava flows on steep slopes. Not buoyed up by exsolved gases. Result in chaotic unsorted, unstratified deposits. Very little pumice, generally small runout
	Peléean type	Formed by explosive eruptions immediately before or during dome emplacement (occasionally by low angle blast, e.g. Mt St. Helens). Ejecta vary from almost wholly lithic to almost wholly pumicious. Largest, most gas-rich and most destructive flows occur early in dome emplacement, composed of effervescing magma providing large amounts of ash. Later flows from a more stable dome are generally more blocky. Deposits vary greatly, often confined to topographic depressions. Heterogeneous, unsorted, unstratified. Often contacting sub-angular dome carapace sections, effervescing bombs from the plastic interior, and sand to dust particulate debris. Porosity high (particularly if early in dome emplacement). Accidental lithic fragments are rare. Not welded, but maybe indurated by compaction.
Flows from summit craters	St. Vincent type	Flows produced by gravitational collapse of ejecta at the margins of vertical eruption columns. The column is initially formed by a dense lower part accelerated by decompression. Subsequently, a hotter lighter fraction rises up through the denser atmosphere. Once mixing with the atmosphere and fall-out ejecta no longer reduce the effective density of the column below that of the surrounding atmosphere collapse occurs. The material reaches the ground as a glowing avalanche (nuée ardentes). These are highly mobile flows, leading to unstratified (or poorly stratified), poorly sorted, and unwelded deposits. Bombs and blocks make up 3-5% total volume. Little lapilli, 90% sand size. Crystals make up 45% of most bombs, but up to 73% of ash
	Krakatoan type	Pumiceous flows discharged by large upwelling from vents on composite cones; eruption commonly resulting in caldera formation. Pumiceous flows preceded by pumice falls as the gas pressure falls, and usually involving magmas more fluid than seen in Peléean, St. Vincent or Asama types. Hence, much more pumiceous material and less lithic debris. Pumice flows are poorly sorted, with irregular stratification. Course fragments are located towards the top of the flow. Pumice flows often demonstrate sub-parallel ridges at their edges caused by differential flow rates, and the flows thicken towards their terminus.
	Asama type	Flow formation intermediate between those of Peléean type and those of St. Vincent and Krakatoan types. Initial discharge of gas-rich magma produces a pumice fall followed by pyroclastic flows of diminishing gas content. The flows are issued from the summit crater as the magma foams over the rim and sweeps downslope. Vesicularity decreases during eruption. The earliest flows are plastic enough to anneal, often compact and crudely jointed. No flattening. Later pyroclastic flow is from more viscous magma, and spread less widely than the earlier flows, often confined to narrow channels. The deposits consist of dense or slightly vesicular blocks and bombs with little juvenile ash. Some blocks up to 30m across. No later flows are welded or indurated by compaction.
Flows discharged from fissures	Valley of Ten Thousand Smokes type	Eruptions from one or more short linear fissures. Flows are predominantly sand and dust sized mingled with lapilli. Almost completely unstratified deposits, rare bombs and lithics, completely unsorted. Lenses of fluviatile pumice separate some flows laid down by rivers. Weakly indurated, but some are highly welded and show columnar jointing. Not characterized by distortion of glass shards or flattening of pumice
	Valles type	Eruptions of silicious pumice from accurate fissures formed by regional arching of the roofs of large bodies of rising magma. Ejecta volumes so great that calderas form along the accurate fissures as they collapse. Voluminous flows. Relatively small volumes of air-fall pumice followed by much larger volumes of commonly welded ignimbrite.

TABLE 1.3 NON-GENETIC LITHOFACIES ABBREVIATIONS FROM BRANNEY AND KOKELAAR (2002)

Symbol	Lithofacies
T	tuff/ash
LT	lapilli-tuff/lapilli-ash
L	lapilli
Br	breccia
Ag	agglomerate
Co	cobbles (i.e. rounded blocks)
m	massive
(n)	normal-graded
(nl)	normal-graded lithics
(i)	inverse-graded
(ip)	inverse-graded pumices
(n) (i)	normal-to-inverse graded
s	stratified (e.g. tractional)
xs	cross-stratified (e.g. tractional)
//s	parallel-stratified (laminated)
//b	parallel-bedded (thin beds)
p	pumice-rich
l	lithic-rich
sc	scoria-rich
o	obsidian-rich
cr	crystal-rich
fpoor	fines-poor
frich	fines-rich
f	directional grain fabric
i	isotropic; no directional grain fabric - may have a compaction fabric.
acc	accretionary lapilli-bearing
ves	vesicular
lens	lens(es)
e	eutaxitic
vap	vapour-phase altered (e.g. sillar)
lava-like	lava-like
v	vitrophyre (welded and glassy)
rheo	rheomorphic (e.g. with elongation lineations and folds)
Examples	
mLT	massive lapilli-tuff (or lapilli-ash)
mLT(nl, ip)	massive lapilli-tuff/ash with normal-graded lithics and inverse-graded pumices
mLTf	massive lapilli-tuff with directional grain fabric
sLT	stratified lapilli- tuff/lapilli-ash
dsLT	diffuse-stratified lapilli-tuff/lapilli-ash
bLT	thin-bedded lapilli-tuff/ash (beds centimetres-thick)
sT	stratified tuff/ash
//sT	parallel-stratified tuff/ash
xsT	cross-stratified tuff/ash

(e.g. Nakada et al., 1999; Saucedo et al., 2004; Sparks *et al.* 2002, Wilson and Walker, 1982). The eyewitness accounts are descriptive only of the outer regions of these flows because the lower regions are hidden by over-riding turbulent ash clouds. Whilst attempts have been made to record temperature of flows as they pass instruments (Cole, *et al.*, 2002), getting any real idea of what is going on inside a flow is a challenge, both due to the unpredictability of flow intiation (and therefore sensor placement), but also the highly destructive nature of PDC being impractical for the placement of delicate instrumentation.

1.3.3 Lithological descriptions

The preferred method in this work for describing PDC deposits is to use the non-genetic lithofacies descriptions presented by Branney and Kokelaar (2002) – summarised in Table 1.3. This ensures deposit descriptions are based on stratigraphy rather than any implied process, and allows more direct comparisons to be made between laboratory deposits and field lithologies.

1.3.4 Depositional models

The interpretation of PDC deposits has not been straightforward and several models have evolved over time to explain the deposit architectures seen in the field. The majority of work has been focused on the formation of ignimbrites – defined by Branney and Kokelaar (2002, p 125) as "the deposit of a PDC rich in pumice and pumiceous ash shards". Two key models for their formation have developed over the last 40 years; en masse deposition and progressive aggradation.

1.3.4.1 En masse plug flow

The *standard ignimbrite flow unit* is a concept which describes ignimbrite formation as an en masse deposit (e.g. Sparks *et al.* 1973; Sparks 1976; Sheridan 1979; Wright and Walker 1981; Freundt and Schminke 1986). The massive lithologies commonly associated with ignimbrites are envisaged as the 'frozen' deflated body of a flow which is only semi-fluidised during motion, and with inflation unlikely to exceed 25% (Faqih *et al.*, 2006). Any vertical stratigraphy in a deposit is interpreted as representative of structure within the flow at the time of deflation and sedimentation. Several other authors developed the complexity of the standard ignimbrite flow unit to take into account features such as fines depletion (Walker *et al.* 1980), veneers and 'jetted' pumice deposits (e.g. Wilson and Walker 1982), low aspect-ratio deposits (Walker 1983) and stratified basal layers below massive ignimbrites (Valentine and Fisher, 1986). The problems associated with the plug flow model are that it requires internal sorting mechanisms to generate a wide range of complex stratigraphies which are observed in PDC deposits, and which vary longitudinally and laterally across deposits.

1.3.4.2 Progressive aggradation

Early work on ignimbrite deposits interpreted the poor sorting and occasional evidence for uphill flow as being indicative of a low concentration flow of suspended material (e.g. Murai, 1961), with the thicknesses of ignimbrite being veneer deposits which are representative of very much thicker, sustained, and mostly over-passed source flows. The later work of Fisher (1966) interpreted poor sorting as a result of density stratification within the flow, with the deposit progressively aggraded by an overpassing flow.

Branney and Kokelaar (1992) revisited progressive aggradation as a mechanism for ignimbrite emplacement and further developed the scheme to account for welding and facies variations (Branney and Kokelaar 1992, 1994, 1997, Kokelaar and Branney 1996). The classification of pyroclastic 'surge' and 'flow' is replaced by a continuum classification instead based on the dominant particle support mechanism at the lower flow boundary zone, namely between:

- Fully dilute PDC – particle interactions are insignificant, while fluid turbulence dominates flow. Laminar bedding is a common product. Encompasses successions previously termed 'surge', whilst also accounting for transport in the upper region, head, and buoyant plumes associated with larger density stratified currents.

- Granular fluid-based PDC – high clast concentration at the lower flow boundary with particle support dominated by grain collisions. Turbulence and traction at the lower flow boundary zone are suppressed, leading to massive, diffuse bedded or bedded lithofacies, with grading patterns recording the evolution of the flow through time.

Progressive aggradation of an ignimbrite at the denser basal flow boundary zone of a 'typical' PDC is dominated by high concentration laminar flow (e.g. Branney and Kokelaar 1992; Bursik and Woods, 1996; Dade and Huppert 1996; Freundt, 1999), while the bulk of the flow volume is commonly passing as a dilute turbulent over-riding flow. As a result of this scheme the sedimentary processes

are virtually independent of the over-riding parts of the current; deposit stratigraphy is a product of the basal flow boundary zone conditions and their variation, unrelated to the vertical structure of the PDC as a whole. The exception to this is particle supply, which is provided to the basal zone through settling from the over-riding current.

The precise structure of the flow may exist within a wide continuum, from fully turbulent, density stratified systems with or without saltation (from which the deposit simply aggrades from direct fallout), through a range of density stratified systems in which dense granular fluids and/or fluid escape dominate the basal (aggrading) zone of the flow (See Figure 1.2). A full assessment of these schemes

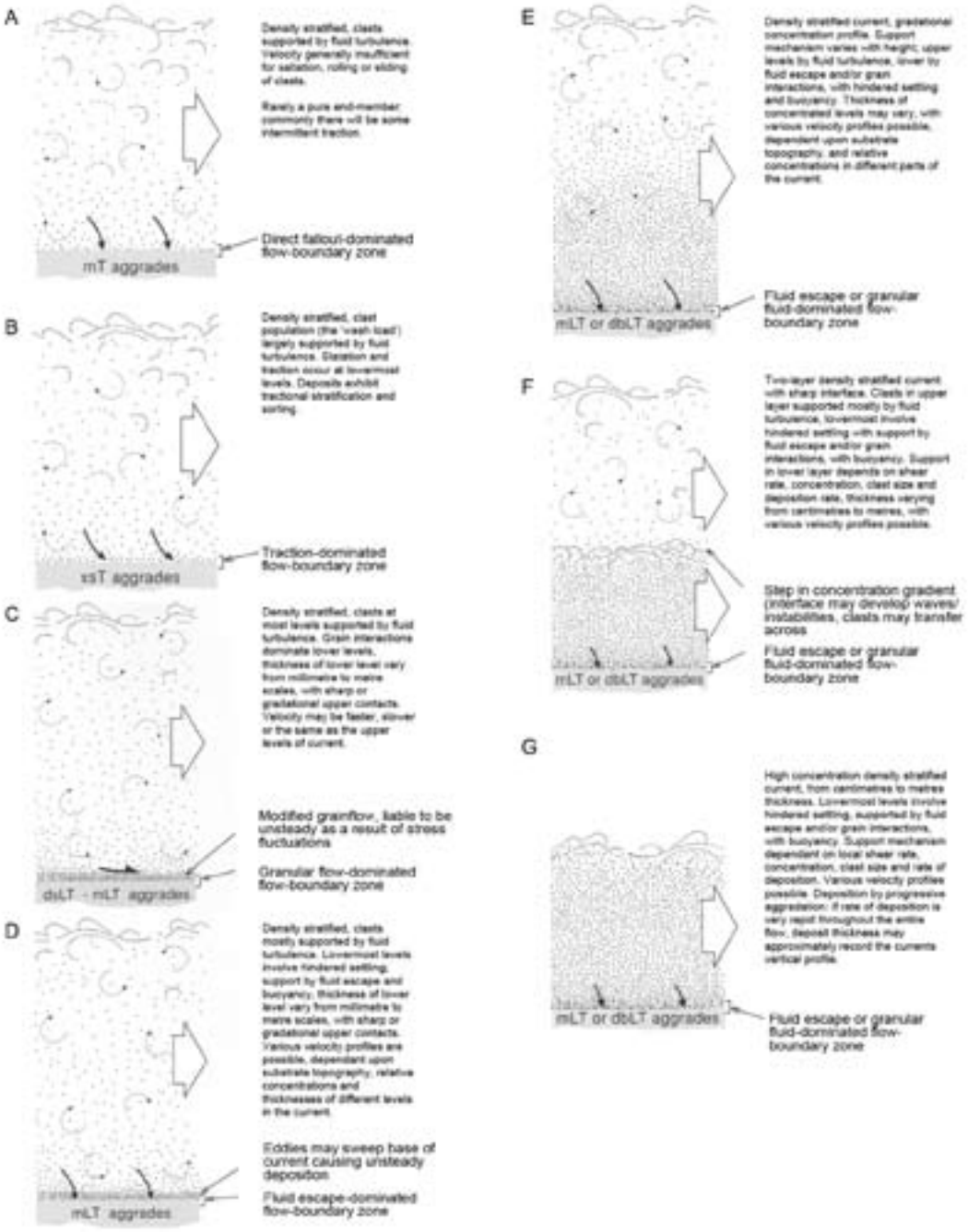

Figure 1.2 A spectrum of PDC profiles, representing members of an intergradational continuum, from fully dilute (A and B) to granular fluid based (C - G). Modified from Branney and Kokelaar 2002.

can be found in Branney and Kokelaar (2002, Figure 2.9). Note that the type G flow described in Figure 1.2 permits a plug-flow like sedimentation within a progressively aggraded scheme.

1.4 Objectives

Pyroclastic density currents are a very complex flow to attempt to model. They are polydisperse and move over complex 3D terrains. Attrition, erosion and deposition evolve the charge as it moves away from the vent, and the internal dynamics of these flows are liable to be highly variable both laterally and longitudinally. In order to better understand these flows, and how they deposit analogue and numerical modelling is forced to make a wide range of simplifications.

Ideally, numerical models should be able to accurately reproduce the deposits formed by PDCs flowing over complex terrains. However, to date the modelling is restricted by a lack of understanding of the physics of granular flows which dominate these systems, and the complex interactions between the particles within a flow, and the flow itself as it traverses different substrates. Ideally a numerical model should be able to:

1. Consider supply flux during current initiation and flow

2. Allow for particle settling from upper turbulent zones to the lower dense regions of flow

3. Correctly model erosive and depositional areas of flow

The key product of any model should be accurate deposit thickness calculations for a given flow throughout its depositional area. In order to truly interrogate whether a model is correctly dealing with flow mechanisms, however, it would be highly informative to generate a model which is able to deal with particle sorting mechanisms, and hence generate internal deposit geometries. In turn, comparison for field deposits would allow verification of not only deposit thickness data, but that the processes at work are being correctly modelled. To date a lack of tightly constrained physical parameters in experiments which assess the internal geometries of flume deposits makes such a model impossible to validate.

In order to provide data to further develop the numerical modelling and understanding of PDC dynamics, this work develops a laboratory modelling approach. With sedimentation of ignimbrites being dominated by the mechanisms active in the flow boundary zone of density stratified PDCs, and the significance of dense granular flow at this interface, use of polymict charges is developed in order to attempt the generation of typical ignimbrite stratigraphies such as reverse graded pumice, and normal graded lithics. Furthermore, by utilizing multiple charges this work also aims to investigate the role of reworking in dense granular systems. Branney and Kokelaar (2002) emphasize the significance of waxing and waning flow, and the evolution of PDCs as vent dynamics change. Simple modelling of these pulses as individual charges may enable some insight into the degree of reworking thin flows are capable of.

The analogue experiments will help constrain :

1. Initiation characteristics from static granular piles
2. Flow behaviour and particulate sorting downslope
3. 4D depositional behaviour of dense granular flows
4. Interaction between a static granular substrate and an over-riding flow
5. The extent to which 1-4 influence final internal deposit geometry.

CHAPTER 2: REVIEW

2.1 The physics of pyroclastic density currents

The subject of PDCs is one which has been of growing interest in recent decades. Like many geophysical flows, PDCs are not standard fluid flows; they are a multiphase process, comprising solid particles (i.e., clasts) and interstitial fluid (which may be liquid or gaseous). However, because the particles are usually denser than the interstitial fluid it is the particles themselves which have by far the greatest influence on the movement of the flow (Bagnold, 1954). The result of these dominant grain interactions is that standard Newtonian fluid physics do not accurately describe the flow properties of these systems.

Granular flows have been studied in great detail, as the physics of these regimes has increasingly been recognized as important in a great many areas of science and technology. Studies include interstellar dust clouds (Spahn *et al.*, 2000), pharmaceutical production (van der Weele *et al.*, 2001), and civil engineering (Houlsby, 1979). Despite the apparent simplicity of granular materials - exemplified by the work of Bagnold (1954), in which they are considered as interactions between inelastic spheres - there is still no model for granular flow behavior that approaches the stature of the equivalent Navier-Stokes equations for Newtonian fluids. There have been attempts to adjust the Navier-Stokes equations to fit granular gases (e.g. Brey *et al.*, 1998), but these have proved to be unsuccessful in fully predicting their behaviour.

2.2 Development of granular physics

The earliest significant development in the study of granular materials was that achieved by Coulomb (1776), whose study of soil mechanics introduced the idea of shear strength, and his calculations form the backbone of the so called Mohr-Coulomb friction regime. The first work which recognised granular flows as being significantly different to Newtonian fluids was carried out by Hagen (1852) and Reynolds (1885). Hagen (1852) in particular was interested in how hourglasses worked, and Reynolds (1885) in the dilatancy of granular materials. Reynolds recognized that as shear stress is applied to a granular mass it begins to dilate and flow. Later Bagnold (1954) looked at large solid spheres as a way of approximating granular flows. Much research in the 1960-70s switched to a focus on fluid dynamics and aerodynamics, so that by the 1970s it was felt by some that "nowadays only a few experts are concerned with the flow of powders and bulk solids" (Wieghardt, 1975).

By the 1980's computing power was reaching a stage where numerical simulation of flows was becoming a possibility, and hence a large inter-disciplinary network of scientists found themselves working on granular physics research from many different directions, and using a variety of scientific approaches, including both mathematical and analogue modelling. Volcanologists specifically started taking a greater interest following the 1980 eruption of Mount St Helens (Wilson and Head, 1981; Kuntz, *et al.*, 1981), when understanding the behaviour of PDCs was recognized as a priority.

Granular materials behave very differently to the standard states of matter, and for this reason it has been argued (Mehta and Barker, 1994) that they should be considered a state of matter in their own

right. To understand how the unique properties of granular materials arise, it is first important to consider a typical granular material.

2.3 Inertia, collision and friction

Most granular systems are made up of macroscopic particles, and these particles transfer forces between each other. The interstitial fluid in systems with low fluidisation is generally considered to be irrelevant due to it minimal viscosity and comparatively insignificant density. The importance of interstitial fluids in granular systems can be expressed through calculation of the flows Bagnold number:

$$N_B = \frac{\phi \rho_s \delta^2 \gamma}{(1-\phi)\mu} \qquad [2.1]$$

By relating the solid volume fraction ϕ , the solid particle density ρ_s, strain rate γ, average particle diameter δ, and viscosity of the interstitial fluid μ , the equation will characterize the importance of the interstitial fluid to momentum transfer (Bagnold, 1954). For $N_B \leq 40$ the material is described as macroviscous, where the interstitial fluid is important in momentum transfer. For $N_B \geq 450$ the flow is described as inertial and momentum transport is by particle interaction (Iverson and Denlinger, 2001).

The Savage number is useful to demonstrate the relative importance of momentum transfer between particles to that by inter-particle friction:

$$N_S = \frac{\rho_s \gamma^2 \delta^2}{(\rho_s - \rho_f) g d \tan\varphi} \qquad [2.2]$$

Here, ρ_f is the density of the interstitial fluid, g the gravitational acceleration, d the flow thickness and φ the internal angle of friction (Savage, 1984). Where $N_S \geq 0.1$, momentum transfer will have an important grain collision component and is said to be in the collisional regime, while below this value, the flow is frictional.

The balance between frictional and viscous forces in a granular system may be described by the dimensionless friction number (N_f) , with $N_f \geq 2000$ indicating the collisional regime is dominant. N_f may be defined by

$$N_f = \frac{N_B}{N_S} \qquad [2.3]$$

Finally, the Darcy number (N_D)may be calculated to assess the extent to which a flow is governed by viscous or pore pressure effects - i.e. the tendancy for pore fluid pressure between moving grains to buffer their interations. The Darcy number may be defined by

$$N_D = \frac{\mu}{\phi \rho_s \gamma \kappa} \qquad [2.4]$$

where κ is permeability, and transition betwen inertial and collisonal flow occurring at N_D between 1000 - 6000.

TABLE 1.1: BAGNOLD AND SAVAGE NUMBERS FOR GEOPHYSICAL FLOWS (FROM IVERSON AND DENLINGER, 2001)

	Elm Rock Avalanche	Mount St. Helens PDCs
Bagnold number	4×10^8	9×10^5
Savage number	0.1	0.001
fluidisation number	4×10^9	9×10^8
Darcy number	2×10^{-8}	3×10^{-7}

To give examples of how these non-dimensional values are represented in typical geophysical flows, two examples are given below (Iverson and Denlinger, 2001).

The figures presented in Table 1.1 must be taken with some caution due to the sensitivity of these parameters to particle diameter, which is itself a parameter with a great range of variability in these flows, and likely to vary considerably spatially within the deposits. For the Bagnold number, both flows occupy numerical fields within inertial flow categorisation, but the Savage number is far nearer to the boundary between collisional and frictional regimes. Indeed, because the particles fragment through attrition as the flow propagates, transition between the early collisional regime and later frictional regime may play be a significant part of the slowing mechanism of PDCs. It is also worth considering that it is likely these values will vary significantly at different points (both spatially and temporally) in the flow. However, only in very unusual circumstance will the Bagnold number approach a macroviscous regime for the bulk flow (Bursik, *et al.*, 2005).

Importantly, grains do not display elasticity in their collisions, resulting in grain interactions dissipating energy. Granular materials often demonstrate a number of unusual features, whether they are in their solid, liquid or gaseous states (Jaeger *et al.*, 1996). It should be noted that because of the random arrangement of particles in any granular medium, each configuration has its own unique properties that render any kind of reproducibility difficult to achieve.

2.4 Granular Temperature

Another fundamental point of understanding granular media concerns granular temperature. Because the physics determining motion is determined largely by particle interaction, the analogy between the random motion of granular particles and the thermal motion of molecules in kinetic theory is such that granular media can be assigned a 'temperature' (Ogawa, 1978). The value assigned to this is the mean-square of the random velocities around the mean velocity. As the granular temperature

increases, so does dilation of the pile. As dilation of the pile occurs, flow becomes increasingly possible. A granular pile at rest, with a temperature of zero can be described as a granular solid. As the temperature increases, and grains are able to move from their previously stable arrangement, the material can be described as in a granular fluid state.

2.5 Granular solids

The typical granular solid is a pile of grains at rest. For the purposes of simplicity let us consider a homogenous collection of spheres of the same diameter and density. At rest these spheres will sit in a pile with a stable angle of repose (Luck and Mehta, 2004). It would be incorrect, however, to assume that these spheres sit in a perfect geometrical arrangement. The random packing of spheres at rest was first studied by Hales (1727). Much subsequent study has showed that spherical packing under gravity can vary significantly between random close packing (RCP) and random loose packing (RLP) limits (e.g., Bernal and Mason, 1960). These limits were defined respectively as volume fractions of 0.64 (Scott, 1960) and 0.55 (Onoda and Liniger, 1990). Clearly, this is significantly less than the volume fraction of 0.74 which is achieved by face-centre-cubic packing – believed to be the closest arrangement of identical spheres achievable (Rogers, 1958).

The heterogeneous packing of spheres and the three-dimensional transfer of forces through the particles leads to stress chains forming within the pile. These features were demonstrated by Liu *et al.* (1995) using crossed polarized light to reveal stress induced birefringence in a static pile. These stress chains appear to have significant implications for propagation of pressure waves through materials (Liu and Nagel, 1994), which in turn influences how a pile destabilises. External vibrations are able to disturb the packing of the grains within the pile, allowing them to travel slowly through granular phase-space as portions of the 'solid' pile begin to deform in a liquid manner (Mehta, 1994). This suggests that granular piles are particularly sensitive to destabilization in the event of seismic activity, and therefore potentially critical in the destabilization of PDC deposits in active volcanic zones. Granular modelling generally assumes Mohr-Coulomb failure criteria, which describes pile responses to shear and normal stress fields:

$$\tau = \sigma \tan\left(\phi\right) + \Psi \qquad [2.5]$$

Where τ is the shear strength, σ is the normal stress, ψ is cohesion and φ is the angle of internal friction. Cohesion is the tendancy for particles to stick together, and will grant shear strength to a body.

2.6 Granular fluids

Once the stability of a granular pile is overcome, either through modification of the stress regime or removal of a confining wall, the pile (or parts of it) will begin to flow. Until these shear stresses overcome any applied normal stress on the pile it will remain static and stable. One fascinating

feature of granular flows is that when flow is initiated from a static pile the grain pile as a whole is not necessarily involved in achieving a new stable angle of repose (See Figure 2.1). This is in contrast to Newtonian fluid which flow as a single entity.

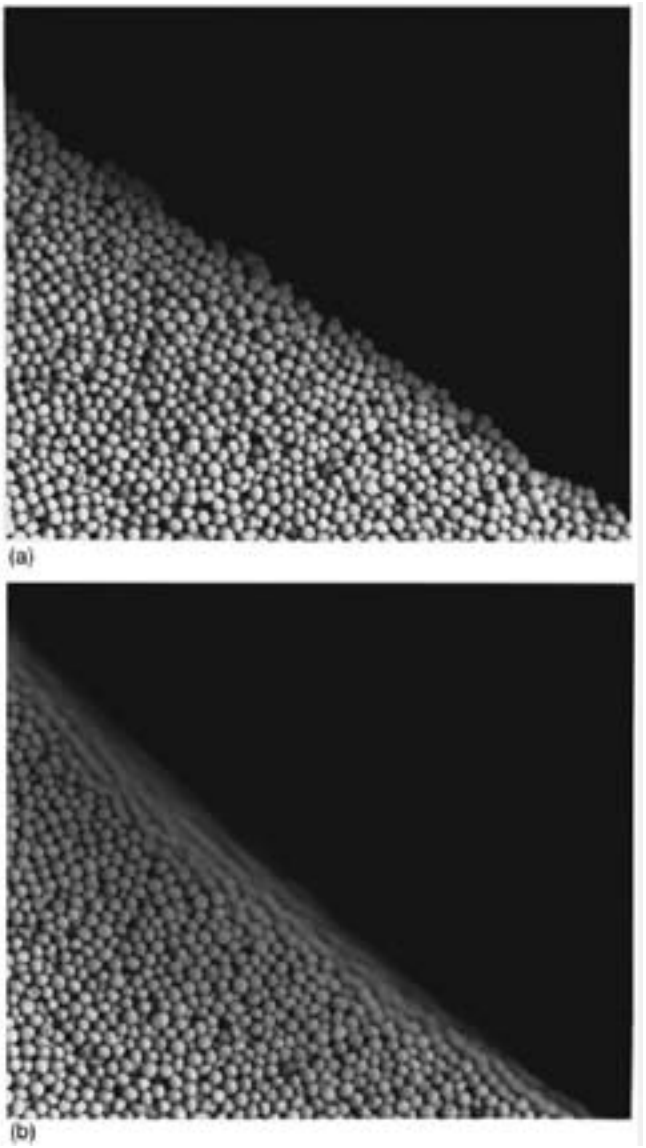

Figure 2.1 Surface flow on a granular pile (a) Pile of grains at rest. (b)The same pile of grains after tilted above the angle of repose. The flow is clearly only taking place in the surface region of the pile. (Jaeger, Nagel, and Behringer, 1996)

It should be noted that flow of a granular pile is accompanied by dilation because the grains must have space to move past each other ("Reynolds dilatancy"). As flows move faster, their dilation increases, and a large continuum of possible flow states becomes apparent. The two extremes of these are considered as dense slow flows and rapid gas-like flows. In volcanological terms the best analogies are (a) the shear-dominated dense basal region of a PDC (i.e., dense slow flows) although this is still a fast moving flow in comparison to the plastic deformation typically regarded in the category of dense slow flows, and (b) the more turbulent pyroclastic surge (i.e. rapid gas-like flows). With greater flow energy, smaller particle sizes and lower density contrasts, granular gas behaviour will be replaced by fully dilute turbulent gas suspensions, with saltation and traction of larger/denser pyroclasts. Having these different flow types in different spatial domains of the same flow is by no means unusual in natural systems, and the transition between these types of flow is a major area of study (Hou *et al.*, 2003). As dilation increases, the bulk density decreases. The bulk density ρ_b of a flow is calculated as:

$$\rho_b = \rho_s (1-\varepsilon) + \rho_f \varepsilon \qquad [2.6]$$

Where ρ_s denotes solid particle density, ρ_f denotes the interstitial fluid density, and ε the interstitial fluid fraction.

2.7 Granular processes

2.7.1 The brazil nut effect

Granular fluids have been known to demonstrate some peculiar features. Perhaps the best known is that of the 'brazil nut effect' (herein abbreviated to BNE). Vibration of a bowl of mixed nuts (i.e., pile of heterogenously sized particles) results in the larger particles working their way to the top (e.g. Shinbrot and Muzzio, 1998). Extremes of density in either direction from the average particle density in the flow can increase the speed at which the larger particles work their way to the top (Mobius *et al.*, 2001). However there appears to be a 'reverse brazil nut effect' (RBNE) if density reaches high enough values (Hong *et al.*, 2001). The BNE is caused by a combination of (a) the development of convective cells within the material, (b) sifting, and (c) the role played by interstital gas. Although the mechanics of the interstitial gas effect are not well understood, it has been closely studied by several groups (Mobius *et al.*, 2001; Yan *et al.*, 2003; Kudrolli, 2004; Druitt *et al.*, 2007).

The importance of the BNE and RBNE effects for PDC flow and deposition is related to the polymict nature of these flows, typically comprising significant differences in the density of particles (e.g. low density juvenile pumice compared higher density lithic material) and size (μm scale ash particles through to cm scale clasts). PDC deposits like ignimbrites commonly contain lenses of pumice clasts, perched lithics, as well as reverse graded pumice clasts and normal graded lithic clasts. For some or all of these features the BNE and RBNE may be the dominant process in their formation.

2.7.2 BNE/RBNE versus inverse and normal grading

It is important to distinguish between the *processes* of BNE and RBNE, and the *lithologies* of inverse and normal grading observed in many sedimentary systems. BNE and RBNE are sorting mechanisms which are able to move large particles vertically through an actively flowing granular system. Normal grading describes a lithofacies where large clasts are concentrated at the bottom of the sequence, grading up to finer particles towards the top, while inverse grading describes the opposite.

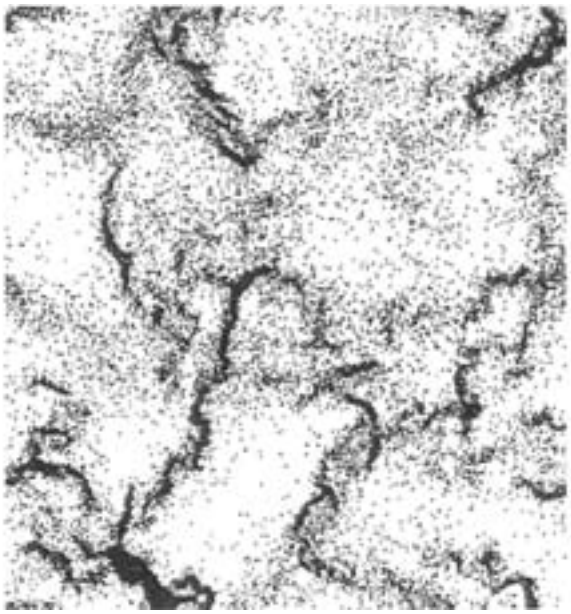

Figure 2.2 Typical clustering in 2D inelastic collisions from Goldhirsche and Zanetti (1993)

If a stratigraphy is lain by a granular current then inverse and normal grading can only be directly related to BNE and RBNE (respectively) if the deposit is known to have sedimented from a plug-like flow (*en-masse* deposition). In these situations the vertical stratigraphy in the deposit directly relates to the vertical architecture of the depositing current. In progressively aggrading systems BNE and RBNE may be considered active processes within the granular fluid layer, but the deposit architecture will be strongly influenced by sediment supply, flow migration, and other factors to produce a grading pattern

which can not directly represent the effects of a purely BNE/RBNE sorting mechanism. However, it should be noted that a sustained granular fluid, being fed a sediment supply will continuously sort material according to BNE/RBNE processes. As a result, the distal deposit would become enriched in the 'floating' particles, so even in aggrading systems BNE and RBNE are likely to have first-order control over particulate sorting.

2.7.3 Density, compressional and rarefaction waves

Visualisation experiments using X-rays to penetrate inside a granular mass of rough materials have demonstrated that density waves can be observed in flows. These same density waves are absent when near spherical smooth particles are used (Baxter *et al.*, 1989). This suggests that grain shape is a significant factor in effecting the flow interior structure and consequently may have important implications for the study of PDCs, as the particles are far more heterogenous than would be found in most industrial applications.

In addition to these phenomenon, vibrated grain piles and flows have also been shown to exhibit both travelling and standing waves on their free surface, with both compressional and rarefactional motions (Ocone and Astarita, 1995). The rarefaction waves were shown to smooth out as they propogated, whilst the compressional waves reinforced each other to a point where they became shocks.

2.7.4 Clustering

When the granular temperature gets high enough the flow dilates to a gaseous state – the solid particles are in suspension within a turbulent gaseous interstital fluid. Because the particles are still interacting inelastically any attempts to use the theory of ideal gases to model these multiphase dynamic phenomenon will not succeed. However, there is an interesting feature that develops from inelastic interactions; cluster formation (See Figure 2.2). Given time an environment of granular particles colliding inelastically and moving chaotically will begin to cluster (Goldhirsch and Zanetti, 1993). Clustering of particles in a confined region encourages further collisions and energy dissipation. It is therefore likely to be a significant process in causing material to sediment back from over-riding turbulent, particle-laden gas to denser granular fluid states. This has implications for the transition of particles into the dense depositional regions of PDCs. The clustering effect can also induce sorting in polydisperse granular gases (Mikkelsen, 2002), and (potentially) deposition from highly fluidised currents.

2.8 Capturing flow features

Because granular flow is dominated by collisions between particles, and these particles collide inelastically, energy is quickly dissipated by the flow. This leads to another interesting feature of granular media. In order to maintain granular temperature, energy must be continually added to balance that which is lost through particle collisions. In PDC, and other mass flows, this energy is usually added through gravitational acceleration as the flow moves down-slope. Once the granular temperature drops the flow will stop moving (Campbell, 1990). Critically, this can happen very rapidly, so can lead to the preservation of flow structures within the deposit. In the case of sustained PDCs which deposit through aggradation, in order to maintain the dense granular current over significant runouts

(kilometre scales) several other mechanisms for increased mobility and momentum transfer can be considered. The dense granular fluid at the base of the current will gain momentum throughout the lifetime of the flow through interaction with the over-riding turbulent suspension (e.g. Dufek *et al.*, 2009), as well as experiencing increased mobility through gas exsolution from juvenile clasts. This in turn will increase the pore pressure, significantly improving mobility and hence runout (e.g. Druitt *et al.*, 2004, 2007). The granular temperature of the flow as a whole is also maintained by constant settling of low-momentum particles, resulting in prolonged mobility through the aggradation of a deposit; the loss of slow moving particles from the flow reduces the chance of other particles colliding, and therefore themselves losing large proportions of their own momentum (Newton's third law of motion).

2.9 Modelling

2.9.1 Challenges in modelling PDCs

Modelling by its very nature requires simplifications in order to be a practical tool. Without these simplifications the number of variables becomes such that any useful model would require a perfect understanding of conditions before, after and during the flow. Simplifications such as assigning all particles uniform grain shapes, sizes and densities are reasonable when dealing with grain silos and *may* provide first-order accuracy modelling geophysical systems - at least where variations in these parameters within a flow are not extreme. However, these assumptions provide no ability to assess the sorting mechanisms in a flow, and hence the validation of modelling through deposit analysis. Pyroclastic flows are a mixture of lapilli and ash size particles (See Figure 2.3) with larger ejected blocks as well as entrained material from the vent or the substrate during transportation and erosion. That gives extremes in particle size ranging from over 5 m to under 1 μm (Clarke *et al.*, 2002). Because of the explosive nature of many eruptions which lead to the PDC, there is also as huge diversity in particle density. The erupted felsic pumice and ash will often have density values of below 1000 kg m^{-3}, whilst lithics entrained during eruption or flow will have densities of *ca.* 2500 kg m^{-3} (Sparks, Wilson, and Hulme, 1978). Both density and particle size evolve during flow as exsolution of gas from juvenile clasts causes both expansion and fragmentation. Once flowing, these particles are also colliding thus causing attrition. It is a reasonable assumption that many of the larger blocks will be broken up as the flow moves. All of this demonstrates that particle size, density and shape are not only significantly more variable than current modelling efforts suggest, but also evolve during the development of the flow and

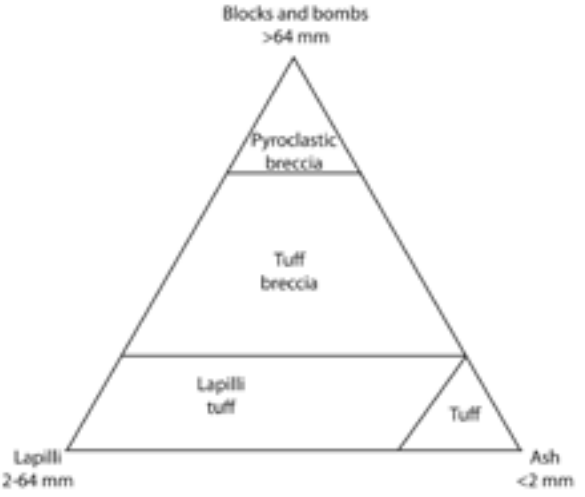

Figure 2.3 Grain-size ternary diagram for naming of volcaniclastic rocks, adapted from Fisher (1961) to follow Schmid (1981) in abandoning "lapillistone"). Divisions at 25% ash vs lapilli, then 25% and 75% ash vs blocks and bombs.

spatially within it. In summary, PDCs are characterized by:

- Heterogeneity in particle density, size and shape
- Variability in particle supply during the flow lifetime
- Transport and deposition over complex topographies
- Potential for reworking of loose substrate of similar material
- Wide range of resultant lithofacies
- Variety of depositional mechanisms
- Variability in volume and area of deposition
- Variability in temperature
- High pore pressure and mobility
- Evolution of parameters spatially and temporally within the flow

All of which together adds layers of complexity to an already complicated area of physics. Consequently numerous assumptions are made in any attempts to model pyroclastic flows. Some of these common assumptions include:

- Uniform particle size
- Uniform particle shape
- Uniform particle density
- Irrelevance of interstitial fluid
- Uniform stresses within the bulk material
- Non-erosive behaviour
- No addition of material during flow
- No evolution of flow properties during flow

These assumptions allow modelling to be carried out, but it must be considered that flow behaviour in systems where so many variables are discounted is likely to miss subtleties in flow and deposition of PDCs. In assessing controls on flow and overall deposit geometry, assumptions of particle density and particle shape are unlikely to effect first order relevance - most PDCs are composed of fairly

similar particles, with lithic clasts and so forth generally a minor constituent. However, these become significantly more important if we are to consider sorting effects within flows, and the internal features which result in the deposits. The remaining assumptions are perhaps more serious. Evolution of material during flow is very difficult to control, so is unlikely to be considered in laboratory experiments. Interstital fluid and pore pressure are also challenging, and require complicated experimental set-ups. Collapse from granular piles is subject to variations in the random packing within the intial pile, and as such is impossible to control - however, it is highly unlikely to have any first order significance in deposit formation. The particle size, erosion and entrainment variables are more viable for testing, and likely to have significant impacts on the geneartion and structure of deposits.

PDCs have the added complexity that they show the full range of flow dilation as the granular temperature increases, from static grains at rest in a stable pile (the deposit) through to inflated granular liquid, to a granular gas, with high particle excitation and flow dilation. Due to this dynamic change within the system the complex transitional behavior between these states is also significant (Kadanoff, 1999).

Both numerical and analogue models are useful tools for the volcanologist. Analogue models are valuable when the physics is poorly understood, as they provide a baseline for numerical models to match. Analogue modelling also allows the introduction and assessment of awkward variables such as mixed grain types and complex basal features relatively simply. Being able to observe an actual flow in progress is also informative, especially when using particle or flow-region tracking features such as colour-coded bands in the flow.

Numerical modelling on the other hand requires an understanding of the physics behind the flow in order to be able to start developing the accuracy of the model. Assumptions such as shape of grains and slope geometries are simplified to avoid very complex calculations. A vital feature of a numerical model is the simplicity of scaling up to natural dimensions, and the ability to interrogate the flow (or resulting deposit) at any desired point temporally or spatially. It is also much faster to change values for variables in a numerical model, allowing genetic algorithms to assist in rapidly narrowing down flow specifics (e.g. Goldberg, 1989). One of the disadvantages of a numerical model, particularly when dealing with poorly understood physics of a flow, is that inaccuracies in the models results are difficult to identify; just because a surface topography appears to be correct at a point, it is not necessarily a product of a realistic flow mechanism.

Numerical modelling of flows can be carried out using one of two general schemes: the Eulerian and the Lagrangian. The essential difference is the Eulerian method tracks overall fluid properties at a given point or segment, whereas the Lagrangian approach deals with individual particle trajectories.

2.9.2 Numerical models and theory

It is important to note that throughout the majority of the 20th Century the vast majority of granular flow modelling was carried out in relation to industrial fields (e.g., flow of grain in silos and other containers), and the relevance to PDCs iwas largely unappreciated. However, this changed following

the eruption of Mt St. Helens in 1981, and a spate of explosive volcanic activity throughout the 1990's most notably Unzen, Japan (1990-95); Pinatubo, Philippines (1991); Fuego de Colima, Mexico (1991-present) and Soufrière Hills, Montserrat (1995-present). These eruptions were well studied (e.g., McEwan and Malin, 1989; Levine and Kieffer, 1991; Nakada *et al.*, 1999; Voight *et al.*, 2002; Sparks *et al.* 2002) leading to a wealth of information upon which subsequent modelling could be based.

Early theories of pyroclastic flows, (Anderson and Flett, 1903) struggled to explain fluidization and tended to rely on particles within the basal part of the PDC being surrounded by gas, which provided buoyancy as it expanded. By the 1960s and 70s this theory had developed to suggest that entrapment of cold air and its subsequent heating might be the main cause of reduced friction within the flow (McTaggart, 1960). More recent work has confirmed that high pore pressure is vital in achieving long runout flows (e.g. Druitt *et al.*, 2004), with exsolution of gas from juvenile particles, and the expansion of entrained gas under high temperatures likely to be major contributors.

Observation of the 1974 Fuego (Guatemala), 1975 Ngauruhoe (New Zealand) and 1981 Mount St. Helens (US) eruptions lead to a study of depositional features such as reverse grading, lobate fronts and levées. These eruptions lead various authors to conclude that the fluidization resembled more closely that of a high yield-stress density current with non-Newtonian physics (Nairn and Self, 1978; Wilson and Head, 1981). This development, along with the wealth of observational data now available lead to a number of models being developed (Battaglia, 1993; Wilson and Head, 1981). The key feature was a frictional term proportional to some power of velocity. It should be noted that these models were all developed while en-masse deposition was the most probable inferred mechanism for ignimbrite formation.

These early models had particular problems achieving a reasonable value for flow speed without inferring that the flow was turbulent (e.g. McEwan and Malin, 1989; Levine and Kieffer, 1991). This contradicted current understanding, as it ignored the levees and other obvious depositional features that were consistent with non-Newtonian behaviour. Since then it has been demonstrated that these features are not restricted to non-Newtonian flows (Major and Iverson, 1999; Pouliquen, Delour, and Savage, 1997).

2.9.3 Alternative friction models

Savage and Hutter (1989) argued that inter-granular interaction rather than interstitial gas was the important dispersive pressure. This led to the conclusion that once within the frictional regime (as determined by the Savage number expressed in equation [2.2]) the initiation of flow movement (or shear stress at failure) was proportional to the normal stress acting on the pile. This is known more commonly as Mohr-Coulomb friction, and various studies were made using Mohr-Coulomb friction to describe granular flows – most comprehensively achieved by Savage and Hutter (1989), who developed a series of motion equations able to describe a deforming granular mass moving down a slope, based entirely on a Mohr Coulomb friction term. Savage and Hutter (1989) demonstrated that shear stress is proportional to normal stress even in inertial regimes, so therefore the following

equation can be derived to give the conservation of energy for a friction coefficient of tan$\emptyset_{bed}$:

$$mgH = \tan\phi_{bed} mgL_1 \cos\theta + \tan\phi_{bed} mgL_2 \quad [2.7]$$

Where the mass m of a block placed on a slope of angle θ, at height H, and length L_1 above a horizontal runout of length L_2. This leads to:

$$\frac{H}{L} = \tan\phi_{bed} \quad [2.8]$$

The validity of using a Mohr-Coulomb friction term in PDCs was tested by Hayashi and Self (1992). They studied the ratio of height descended H and the runout length L in pyroclastic flows in comparison to the H/L ratio in volcanic and non-volcanic landslides. Their study argued that although there was an amount of scatter in all the data, regression lines of H/L versus deposit volume for the three plots were indistinguishable, and concluded that it is unlikely that pyroclastic flows have a significantly different emplacement mechanism to other geophysical flows. The scatter is attributed to differences in material properties. This view is not, however, universally held; PDCs and some large debris flows demonstrate a runout length above that which might be expected from the standard Mohr-Coulomb friction terms. Dade and Huppert (1998) proposed that rather than assuming shear stress as proportional to the normal stress, it is constant. For a flow of mean width w:

$$mgH = \tau w L^2 \quad [2.9]$$

Because volume $V \propto m$, then for constant shear stress τ, and shape factor $\lambda = wL$

$$A \propto V^{2/3} \quad [2.10]$$

Using this scheme Calder *et al.*(1999) and Legros (2002) produced convincing results demonstrating that when separated into distinct environmental categories (such as water content) this latter method produces better collapse reproduction than the Mohr-Coulomb models. This would suggest that runout is indeed controlled by a constant stress condition rather than the Coulomb model which assumes it is a constant slope condition, at least in certain situations.

2.9.4 Modelling approaches

Numerical approaches to granular flow modelling have generally pursued two paths; Eularian depth averaged integration (e.g., Gray, Wieland, and Hutter, 1999) and Lagrangian discrete particle simulation (e.g., Hanes and Walton, 2000). In terms of understanding physical principles, the discrete particle method is a useful approach and has a great deal of value. However, in PDC modelling, due to the large number of particles, and variables of the flow, depth averaged modelling has been used almost exclusively. Depth-averaging is used extensively within fluid dynamics, and has been imported to granular flow mechanics. It operates through the integration of flow properties throughout the range of the vertical dimension of the flow. In terms of geophysical flows this is its depth (where runout

is very much greater than flow width, and width is in turn greater than depth). Key assumptions with this method are that variations in the properties of the flow within that dimension are either non-existent or have no effect on flow behavior. As has been demonstrated in this Chapter, those assumptions are not necessarily valid when discussing PDCs. The flow mechanics and structure from the upper surface through to the basal interface would appear to be significantly more complicated than assumed when using a simple depth averaged model. Furthermore, in small channelised flows it is possible that channel with is very close to the dimensions for flow thickness, rendering the assumptions made for depth averaging invalid.

Modelling thus far has succeeded in providing a reasonable match of deposit thickness in respect to simple 2D analogue models of granular flows (e.g. Denlinger and Iverson, 2001), and there have been a number of partially successful attempts at 3D modelling of these same situations (e.g. Gray, Wieland, and Hutter, 1999). Denlinger and Iverson (2001) focused on a depth averaged model and attempted to match a small analogue flume experiment, using a 0.5 m slope and subsequent horizontal runout. This model used a Coulomb friction law, which was shown to be effective at matching speed and runout lengths in laboratory scale flows (Savage and Hutter, 1991). The results from this experiment are shown in Figure 2.4. At first glance the results appear to be a good match from the analogue experiment to the numerical model. However, closer analysis shows several key issues. Whilst the flow-front has a good match to that observed in the experiment, by 0.32 seconds the numerical model has not initiated as quickly. At 0.53 seconds the flow is demonstrating a geometry significantly different to that in the experiment; the flow depth in the model at 80cm along the flume is ahead of the bulk of the flow in the experiment by some 10cm, and also is not demonstrating the pile developing at the break in slope (shown as a slight topographic high 100cm downslope in the flume experiment). The tail-end of the flow shown in the 0.93 second time-slice shows significant differences between the two, with substantial thicknesses still being evident at the sidewalls in the numerical model upslope of the break in slope. The final deposit at 1.50 seconds has similar extent, but the geometry of the topographic highs is inconsistent with the laboratory model. The numerical model would appear to respond to sidewall interaction significantly differently than the charge within the laboratory flume does.

The 3D work of Gray *et al.*(1999) was also compared to a laboratory analogue model, and again used a Coulomb friction law. Similar criticisms to the Denlinger and Iverson experiments (Figure 2.4) remain; although the flow front is broadly similar to the experimental front, the pile shape and height are significantly different, particularly later in the simulation.

Many of the inaccuracies occurring in these models may be simply due to assumptions being made by using the depth averaged model, as outlined earlier. Several workers have recently started developing two-layer depth averaged analyses, notably Doyle *et al.* (2006). The advantage of these systems is that although they still rely on depth averaging, it is possible to depth average separate layers in the flow, one above the other. This fits well with a model of a density stratified flow. Crucially, it opens the possibility for modelling sedimentation from one of these layers to the other as the flow regimes change. Multi-layer modelling of PDC appears to be a convincing step in the right direction; the

simplifications made in the older single layer models are demonstrably not valid when compared to flow observations in the field.

Perhaps the one factor most noticeably lacking in work to date is the erosive aspect of the flows. There is very little work dealing with the erosive action of granular fluids or PDCs, and indeed there has been little work in identifying reworked material within PDC deposits in order to constrain erosive models. However, it is clear from many examples of cross-cutting relationships in the field that PDCs are a powerful erosive force, and this is likely a significant aspect in the impact of a PDC on a volcanic environment.

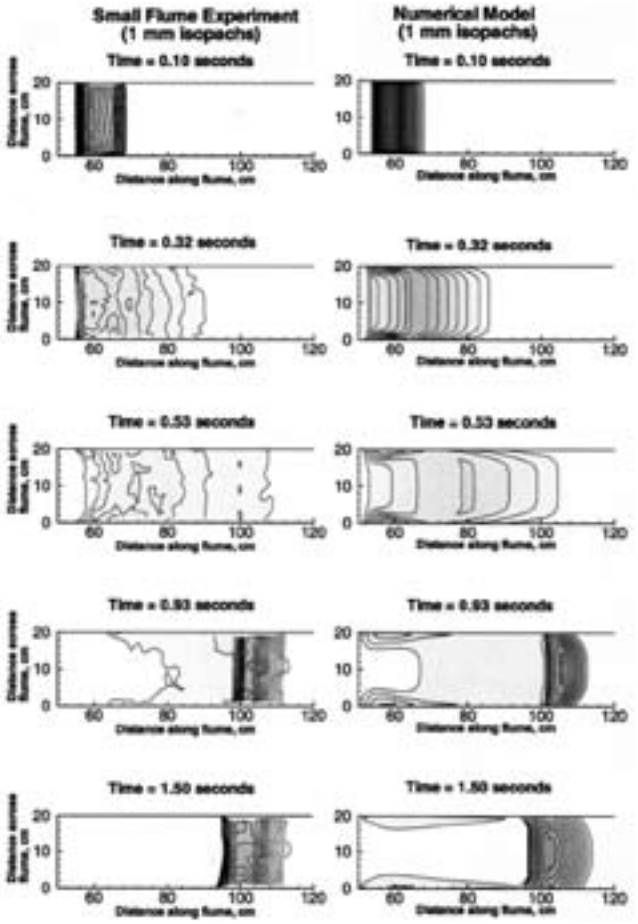

Figure 2.4 Denlinger and Iverson (2001) flume results

2.10 Objectives

In order to further develop the numerical modelling and understanding of PDC dynamics, this work develops a laboratory modelling approach. With sedimentation of ignimbrites being dominated by the mechanisms active in the flow boundary zone of density stratified PDCs, and the significance of dense granular flow at this interface, use of polymict charges is developed in order to attempt the generation of typical ignimbrite stratigraphies such as reverse graded pumice, and normal graded lithics. Furthermore, by utilizing multiple charges this work also aims to investigate the role of reworking in dense granular systems. Branney and Kokelaar (2002) emphasize the significance of waxing and waning flow, and the evolution of PDCs as vent dynamics change. Simple modelling of these pulses as individual charges may enable some insight into the degree of reworking thin flows are capable of.

The first stage of analogue experiments will help constrain:

1. Initiation characteristics from a static granular pile

2. Flow behaviour and sorting downslope

3. Depositional behaviour of dense granular flows.

CHAPTER 3: PROCEDURE AND VALIDATION

3.1 Field Validation

The laboratory experiments have been designed to provide analogues for PDC flows and deposits. A wide variety of granular density currents exist in nature, and the dense granular flows found at the base of PDCs are notable for their particle heterogeneity, in terms of not only size, but also density and proportional variation. In order to validate the results of the experiments against a field analogue, the 1975 PDC deposits of Ngauruhoe, New Zealand are used to a) provide direct structural comparison and b) inform the selection of flow materials. These are small volume (5000 m^3) andesitic composition deposits formed by small, discrete Vulcanian eruption pulses (Lube *et al.*, 2007). Furthermore, the design of the flume experiments was influenced by more broad measurement and analysis of volcanic slopes. In later chapters experimental results are compared with ignimbrites from the Bandas del Sur formation in Tenerife, Spain.

3.1.1 Slope Analysis

In order to generate a typical volcanic geometry for the final flume design used in the internal geometry experiments a series of volcanic cone profiles were analysed. A range of PDC generating edifices were studied, with profile photographs of their cones traced, and measured. Comparisons of these slope traces against reference slopes may be seen in (Figure 3.1). Not included are edifices produced by caldera-forming eruptions. These eruptions are capable of producing sustained PDCs, and are inferred to be the mechanism for formation of the very largest ignimbrites such as the Bishop Tuff. Calderas formed by these eruptions are commonly several to tens of kilometres across, making relation to the local topography largely meaningless in terms of runout slope geometries.

The indication that 30-35 degree upper slopes are typical of explosive volcanic cones was used to inform the design of the third-stage flume. The runout slopes of these volcanoes are not always captured, and in the cases of island volcanoes are missing entirely.

3.1.2 Ngauruhoe Samples

Fieldwork on the 1975 PDC deposits on Ngauruhoe provided an excellent opportunity to gather sample material from unusually dense and small volume deposits. With a maximum runout of approximately 1km, and individual flow volumes in the region of <5000 m^3 (Lube *et al.*, 2007) they are quite different from 'typical' ignimbrite style PDC deposits, but are useful as an end-member study of purely granular deposition as represented by small scale laboratory flume experiments. As a classic stratovolcano Ngauruhoe displays a near constant 29° slope on its North-West flank from its summit (2291 m) down to the Mangetepopo Valley at approximately 1300 m (far left edge of Figure 3.2). The cone is composed of unconsolidated scoria and ash deposited from density currents and fallout, along with numerous largely brecciated lava flows. The source of these flows is not necessarily Ngauruhoe itself, as it is only one of 12 vents in the Tongariro complex. High altitude and low rainfall have enabled excellent preservation of these dry deposits. Located within a World Heritage Site, sample collection was very strictly limited to a 5 kg total. As such a small number were collected for various points in a single flow to give an idea of material properties at various points across and

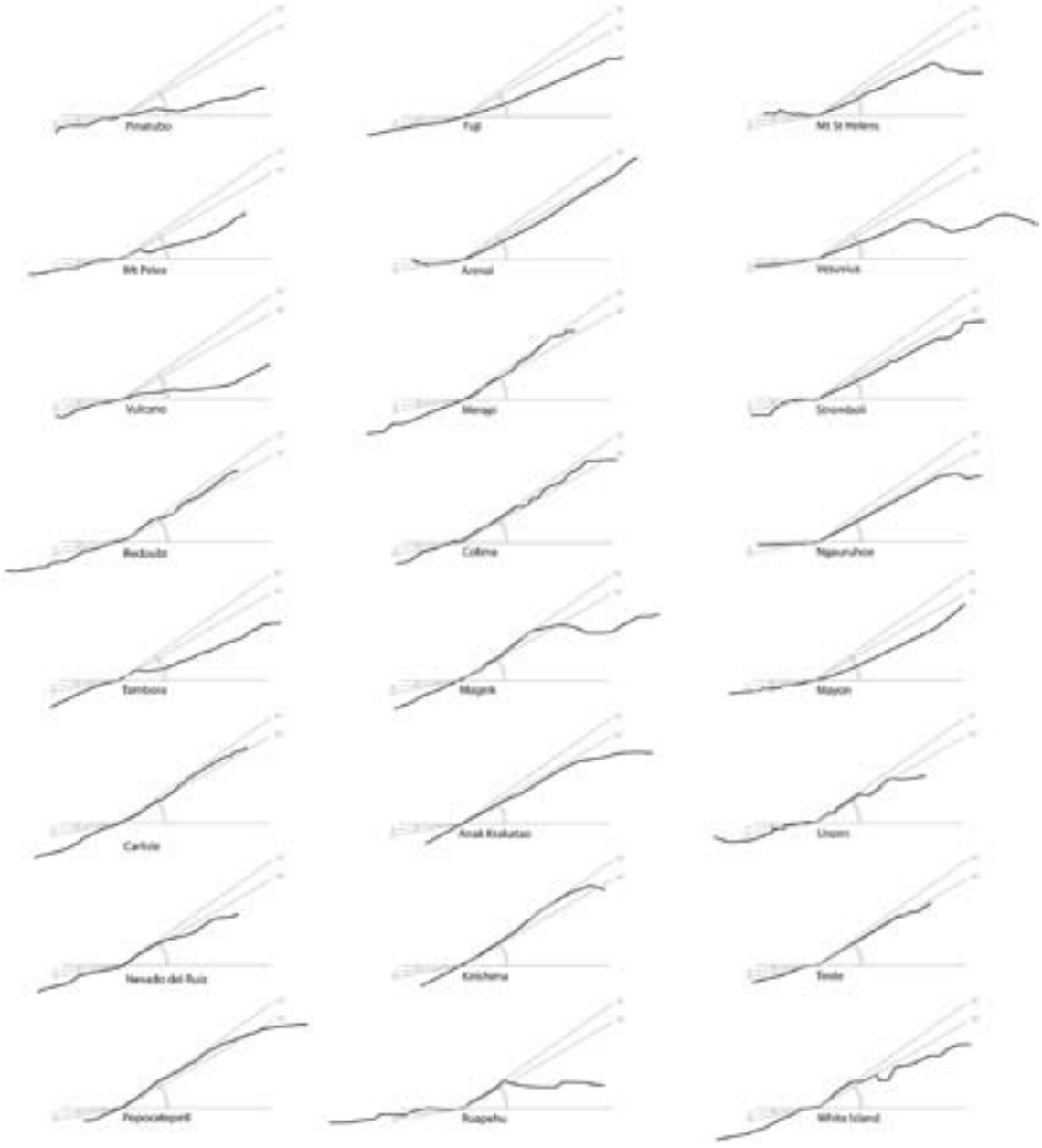

Figure 3.1 Traced profiles of a selection of stratovolcanoes placed against a reference chart comparing 30 and 35 degree upper slopes alongside 5 and 10 degree lower slopes. Many of the profiles are traced from aerial photographs which will slightly underestimate slope angles. Lower slopes are not always captured, particularly in the case of island volcanoes which frequently demonstrate steepened shorelines due to erosion.

down the flow. Studies conducted by Lube *et al.*, (2007) provide detailed cross sections of these flows, demonstrating typical levee-and-channel morphologies (Figure 3.3).

Samples collected comprised large scoriaceous blocks (up to 400 mm diameter in the field) allowing displacement experiments to calculate density, as well as fine grained (lapilli to ash grade) internal material which has been subjected to sieving to generate grain size charts at different positions in the flow (see section 3.2.4).

Specifically the fieldwork was focused on a series of pyroclastic flows deposited during the most

recent eruption in 1975. In the afternoon of February 19th 1975, after 7 days of intermittent volcanic tremors, Ngauruhoe commenced a 5 hour burst of activity which ejected 3.9 x 10^6 m^3 of material from the main vent. Approximately two thirds of this material was ejected as airborne ash, with the remaining third forming a number of small volume scoriaceous pyroclastic flows ejected in two distinct phases flowing down the north western side of the volcano. These resulted in sequences of often inter-digitated deposits no more than approximately 1200 m in runout. Due to the elevation and the relatively dry climate of this part of the North Island the deposits have seen comparatively low erosion rates, and as such are an excellent example of small volume flows.

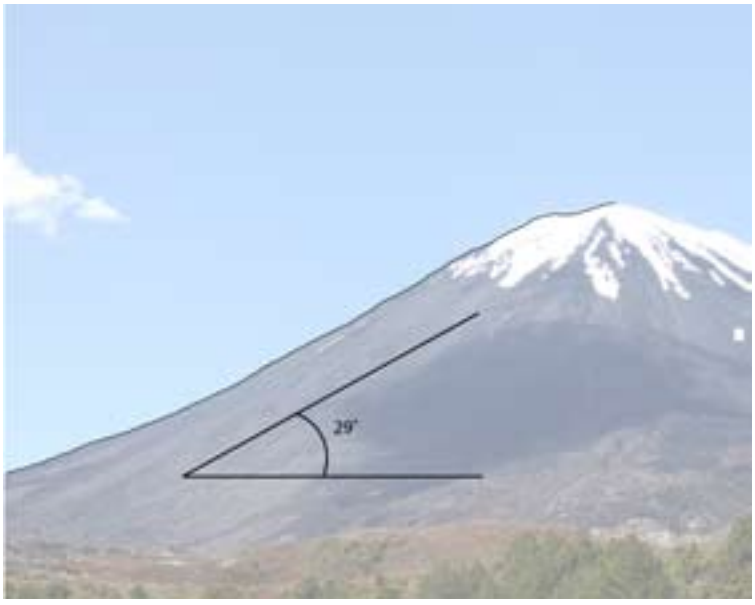

Figure 3.2 29 degree slope set against a photographic image of the north west flank of Ngauruhoe, taken from 39° 8' S 175°36'E looking east.

The field-based aspect of the trip had four distinct aims;

1. to identify overall variation within the deposit
2. to establish the finer scale structure of the deposit (e.g. grading, presence of flow-features, lateral, longitudinal and vertical sorting effects)
3. to collect representative samples for laboratory analysis

The samples were collected in order to provide data to inform later experimental material selection. Due to the sample collection restrictions it was important to concentrate collection to a single deposit. For this reason each flow unit was carefully assessed, and the most appropriate for the research needs was selected prior to any collection taking place. A number of desirable deposit features were identified prior to entering the field. These included good preservation throughout, a clear proximal source, a relatively straightforward run out system with distinct features that would allow more detailed model testing and manageable size within sample constraints and time.

Of the 1975 deposits, Lube *et al.* (2007) identified 6 distinct flows;

I. Flow from eruption Phase 1 overlain by lobate Phase 2 flow. Smooth facies grading.

II. Phase 1 flow overlain by eruption Phase 2 flow. 80m cliff creates break in flow.

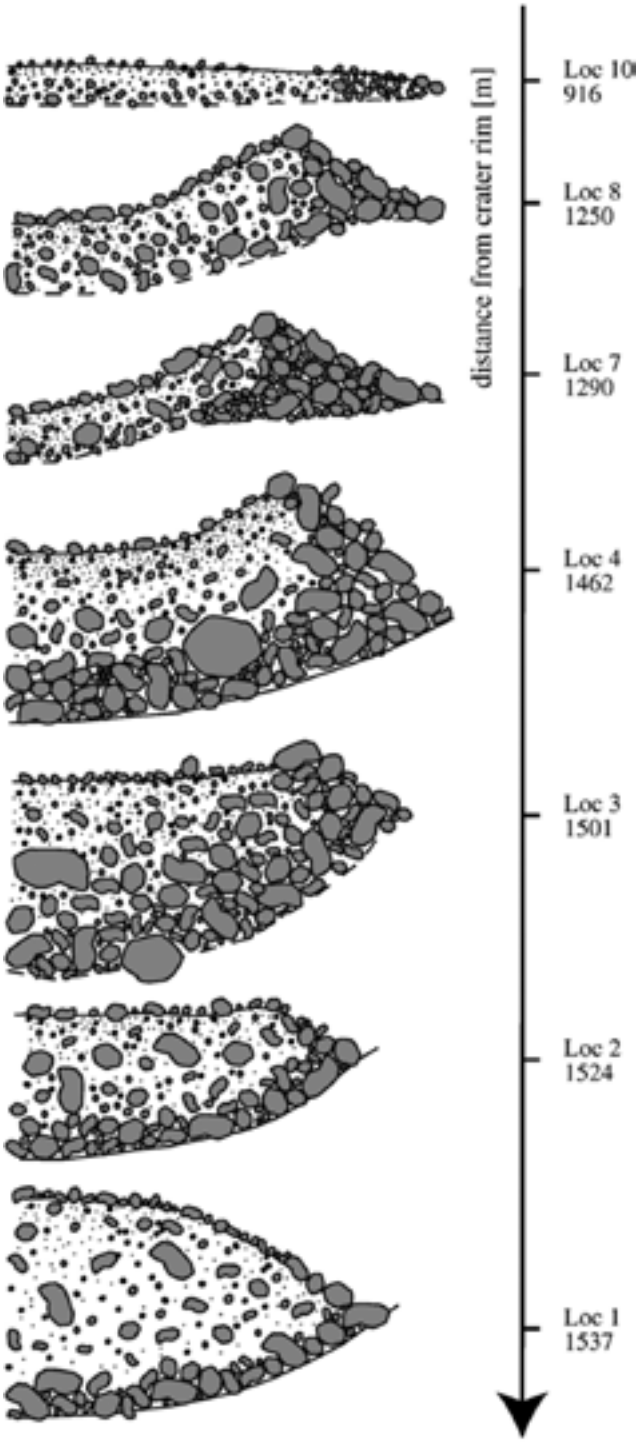

Figure 3.3 Scaled drawings demonstrating cross sections through channels at increasing distance from vent of Ngauruhoe 1975 PDC deposits. Adapted from Lube *et al.* (2007).

III. Phase 1 flow, some forking of the flow at its distal end. Facies grading not distinct.

IV. Very small volume Phase 1 flow. Poorly defined upper flow path.

V. Relatively small volume flow. Clear facies grading.

VI. Large Phase 1 flow. Some forking. Clear facies grading

Flow VI was selected as it had a relatively good proximal preservation (~300 m absent from the proximal scree slope), clearly identifiable edges, a small amount of forking and demonstrated a number of facies systems along its length. One very distinct feature of flow VI was its interaction with a pre-existing lava flow at approximately 1400 m altitude, where the current became confined within a steep-walled channel, then broke out to deposit into the Mangetepopo valley.

3.1.3 Deposit Description

The North Western flank of Ngauruhoe is layered with numerous pyroclastic deposits and lava flows composed of andesitic to phonolitic material (Christenson, 2000), leading to a confusion of channel interaction which can at first instance be difficult to differentiate. From a distance the blocky levees of the lava flows can easily be mistaken for pyroclastic levee deposits.

Flow VI has a run out of approximately 1.8 km from the vent of the volcano, The first 800 m from the vent are in a northerly direction, before veering to the north west, dropping down to 1375 m in altitude as it reaches the head of the Mangetepopo valley. The upper 300 m are entirely obscured by scree collapse from the vent (Figure 3.4).

Figure 3.4 A view from the upper scree slopes on the vent (taken from ***ca.*** 2050m altitude) showing the upper reaches of flow VI and the domination of scree on the very upper slope. The scree material is largely composed of the same material as that found within the flow. A forking melt water channel can be seen bifurcating around the upper edge of the deposit.

The uppermost visible part of the flow has a veneer-like morphology rapidly transforming into a levee and channel system with broad levees (Figure 3.5), composed largely of scoriaceous blocks and lapilli ranging from 10 to 150 mm in diameter with occasional large blocks up to and over 1000 mm. Mixed within this scoriaceous material there was <10% highly reddened material which appears to represent entrained agglutinate from the proximal vent area. The channel itself appeared to be largely empty of contemporaneous deposits. This could be either due to lack of deposition or removal due to wind action and snow melt runoff. Clear evidence for run off activity can be seen in the small erosion channels cutting through parts of flow VI caused by annual melt water (pale ribbon-like channels visable in the centre of Figure 3.3).

At around 1700 m altitude the depositional style changes as the slope steepens. There are no clearly identifiable deposits from the flow, although the channel is visible as an erosive feature. The levees are masked by scree from the summit area. As the slope comes to a shallower angle again the levees re-appear. They are composed of material which is indistinguishable from those higher on the slope (scoriaceous blocks and lapilli ranging from 10 to 150 mm in diameter with occasional large blocks up to and over 1000 mm). The central channel at this point has no visible deposition occurring within it.

Figure 3.5 The uppermost recognisable deposition of flow 6. Clear levee and channel facies with occasional large blocks. In the middle distance can be seen one flank of Tongariro itself, defining the opposite side of the Mangetepopo valley.

Figure 3.6 The upper-mid section of Flow 6 demonstrating a wide levee and channel facies at the point of bifurcation. A central ridge develops and evolves into the dividing levees. The channel within the levees at this point has little to no deposition.

By 1500 m elevation the slope profile has evolved in such a way that the levees contain deposited channel material (Figure 3.6). Below 1470 m altitude flow VI is confined within the levees of an old lava flow. This channeling has been linked to the comparatively long run out of flow VI for its volume (Lube *et al.*, 2007). The only significant deposition in this section is where the flow overtopped the outside bends in the occasional gentle curves developed by the channel.

At the distal end the flow follows a breach in the lava channel (Figure 3.7) and spills out into the head of the Mangetepopo valley. This breach drops the flow by approximately 10 m over a horizontal distance of approximately 20m. There is no deposition in this phase, leaving only the scoured channel.

On escaping this narrow channel into the wide plain of the valley the flow rapidly dissipated energy and started depositing classic levee and channel morphologies (Figure 3.8 and Figure 3.9). Several large (2 m high) teardrop-shaped, steep sided lobes of material terminate within 30 m of the breach (Figure 3.10). These are characterized by clast-supported scoriaceous material, often bread-crusted, with occasional red agglutinate clasts.

Stacking of one lobe on top of another suggests several pulses of flow in this particular channel, and run out of multiple small volume charges, forming anastomosing levee and channel morphology as far as 100 m further on (Figure 3.11) supports the idea of several discrete currents coming down this same axis of flow. Importantly the levees in the distal run out phase reduce to as little as 0.1 m in height as measured from the surface of the channel deposit.

Figure 3.7 Steeply eroded channel breach through a pre-existing lava flow. No deposition occurred in this phase of flow.

Figure 3.8 On escaping the confined lava channel the associated energy reduction resulted in a rapid transition to levee and channel morphology, with 1 m or more levee height.

Figure 3.9 The tallest levee within flow VI, demonstrating the fine grained material contrasting against the larger overlying and infilling blocks of material. These blocks are comprised of scoria demonstrating a large range of vesiculation, as well as <5% reddened agglutinate presumably entrained in the flows upper transition.

Figure 3.10 Larger channels terminate in lobate deposits which are characteristically steep sided, with moderately well sorted blocky scoriaceous material making up the bulk of the surface.

Figure 3.11 The distal phase of run out and deposition consists largely of anastomosing shallow levee and channels.

Figure 3.12 Large blocks of pumiceous material survived run out in the flow. These blocks are surprisingly fragile and can shatter easily. Distal toe of flow. Shovel is 1m long.

3.1.4 Field samples

Sample collection was conducted in order to define physical parameters for the various flow materials, and as a record of evolution of the flow material with distance from vent. Sample locations are presented in (Table 3.1). It is worth noting that the terminology used here is sedimentological rather than volcanilogical due to the greater sensitivity to the relevant grain sizes, most particles simply sitting within the lapilli classification (2-64mm diamter) of volcaniclastic material classification. The samples fall into two general categories; clast supported gravel-boulder grade material from levees and distal lobes, and matrix supported channel fill material. The field descriptions which follow include detail on the locality as well as the specific sample due to the inability to sample many of the large blocks present at any given locality.

TABLE 3.1 DESCRIPTION OF SAMPLE LOCALITIES

Sample number	Altitude	Latitude	Longitude	Situation
PRNg6-01	1389 m	39° 8' 28.32"S	175° 37' 36.95"E	Distal lobe front
PRNg6-02	1403 m	39° 8' 29.72"S	175° 37' 37.78"E	Distal internal flow material, at base of breech
PRNg6-03	1393 m	39° 8' 28.90"S	175° 37' 36.41"E	Internal flow material, distal runout
PRNg6-04	1496 m	39° 8' 35.12"S	175° 37' 42.96"E	Internal flow material, midslope
PRNg6-05	1704 m	39° 8' 50.14"S	175° 37' 58.22"E	Levee material, upper slope
PRNg6-06	1394 m	39° 8' 28.90"S	175° 37' 36.41"E	Distal runout levee material

3.1.5 Sample descriptions.

PRNg6-01

Poorly sorted medium to very coarse gravel, with occasional boulders. Unconsolidated, clast supported, and composed largely of dark scoriaceous material (>90%) with occasional reddened agglutinate material. Vesicularity of material appears to grade substantially from no obvious vesicles to extremely vesicular. Large fragile blocks of highly vesicular material have survived transport in the flow intact to this point (Figure 3.11).

PRNg6-02

Dark grey, unconsolidated matrix supported, poorly sorted sand containing ~20% fine-coarse gravel. Gravel is comprised largely of vesiculated material, largely equant, sub rounded to very angular in shape.

PRNg6-03

Medium grey, unconsolidated matrix supported, poorly sorted sand containing ~25% fine-coarse gravel. Gravel is comprised largely of vesiculated material, largely equant, sub rounded to very angular shape.

PRNg6-04

Medium grey, unconsolidated matrix supported, poorly sorted sand containing ~20% fine-coarse gravel. Gravel is comprised largely of vesiculated material, largely equant, sub angular to very angular shape.

PRNg6-05

Medium –coarse gravel, including frequent small cobbles and occasional boulders. Material is generally well vesiculated with very unvesiculated material.

PRNg6-06

Very poorly sorted clast supported fine gravel-cobble grade material demonstrating variation between highly vesiculated to unvesiculated pieces. Vesiculated make up by far the majority, with <10% made up of unvesiculated clasts. Shape varies from angular to sub-rounded, with the unvesiculated pieces tending to angular, and frequently tabular in shape.

3.1.6 Sample analysis

The samples were divided into two groups for the analysis stage; samples PRNg6-02, PRNg6-03 and PRNg6-04 were dry sieved to give an insight into the fines component of the flow, while the remaining samples were subjected to density analysis in order to define the limits of particle density and Vesicularity within the flow materials. Ngauruhoe field samples were size graded in the RHUL Earth Sciences Department laboratories using standard sieve trays.

3.1.6.1 Fines samples

For the fines component, a 9-sieve stack was used, and each sample subjected to 30 minutes on the shaker table. The largest sieve used was 2.8 mm, (-1.5Ø), and any sample retained at this level was excluded from further analysis. This was so an upper limit on the sample could be defined, and to

reduce any statistical errors derived from the relatively small sample volumes getting distorted by individual large clasts. The sample mass was measured before sieving, with the mass of the 2.8mm sub-sample removed from this total in order to define the sieving error. The GRADISTAT analysis package was used to perform statistical analyses on the samples, with summary results presented in Table 3.2. A plot of cumulative grain size for the three samples is displayed in Figure 3.13. Detailed GRADISTAT results are shown in Appendix D.

Sample PRNg6-02 is noticeably finer grained than samples PRNg6-03 and PRNg6-04, with approximately 5 times the silt/clay grade fines than the other two samples. PRNg6-02 has a lower mean (266.5 μm versus 465.6 μm and 434.9 μm respectively according to the Folk and Ward (1957) method), and has a leptokurtic distribution (tails of distribution more poorly sorted than central portion). This contrasts with the identical platykurtic distribution (0.780) demonstrated by PRNg6-03 and PRNg6-04, indicating a wider distribution of particle size. PRNg6-03 and PRNg6-04 are both remarkably similar in all respects and show almost identical sorting (2.731 and 2.738 respectively), slightly better sorted than PRNg6-02 (3.702). This places all samples within the poorly sorted classification (Folk and Ward, 1957). The similarity between PRNg6-03 and PRNg6-04 is interesting because they are from very different locations in the flow with approximately 300 m of run out separating them, a large distance of that being a non-depositional channelised system. PRNg6-02 on the other hand is only 40m from PRNg6-03. The 02 sample, however, is taken from the point at which the flow exits the steep-walled lava channel. The implication of this is that the sudden reduction in flow energy caused excessive deposition of the clay-grade fines.

3.1.6.2 Coarse Samples

The levee samples have been analysed so as to extract useful data imposed by density variation within the flow material. Due to the limitations on collection volumes imposed by the New Zealand Department of Conservation, these cannot be considered a statistically significant sampling of density distribution within the flow, rather a demonstration of some of the variation in densities found at different points in the flow and deposit. Each sample comprised numerous individual subsample clasts, each of which was weighed and submerged in a displacement tank to determine volume.

Figure 3.14 presents the results of Archimedes Principal density analyses (Appendix D) of the various sub-samples (volumes measured using a displacement apparatus). Note that error bars are almost universally confined within the size of the data point. This error is derived largely from the instrument error in the displacement tank (1ml). Balance error was 0.01 g, except for samples over 200 g for which a larger scale was necessary, invoking an error of 0.1 g. There is an additional error on vesiculated samples, as in order to avoid permeability and porosity issues samples were film-wrapped prior to submertion, giving a slight over-estimation in volume (in the order of $\ll 1$ cm^3).

The vesiculation fields in Figure 3.14 are derived assuming the clasts were derived from the same andesitic magma with a density of 2.56 kg m^{-3} (Christenson, 2000; Johnson and Olhoeft, 1984). Vesiculation fields are defined by percent volume, assuming a vesicle mass of 0.00 kg m^{-3}.

TABLE 3.2 SUMMARY OF GRADISTAT ANALYSES

	PRNg6-02	PRNg6-03	PRNg6-04
Sieving error	0.10%	0.20%	0.10%
Sample type	Unimodal, Poorly Sorted	Unimodal, Poorly Sorted	Unimodal, Poorly Sorted
Textural group	Sand	Sand	Sand
Sediment name	Poorly Sorted Fine Sand	Poorly Sorted Very Coarse Sand	Poorly Sorted Very Coarse Sand

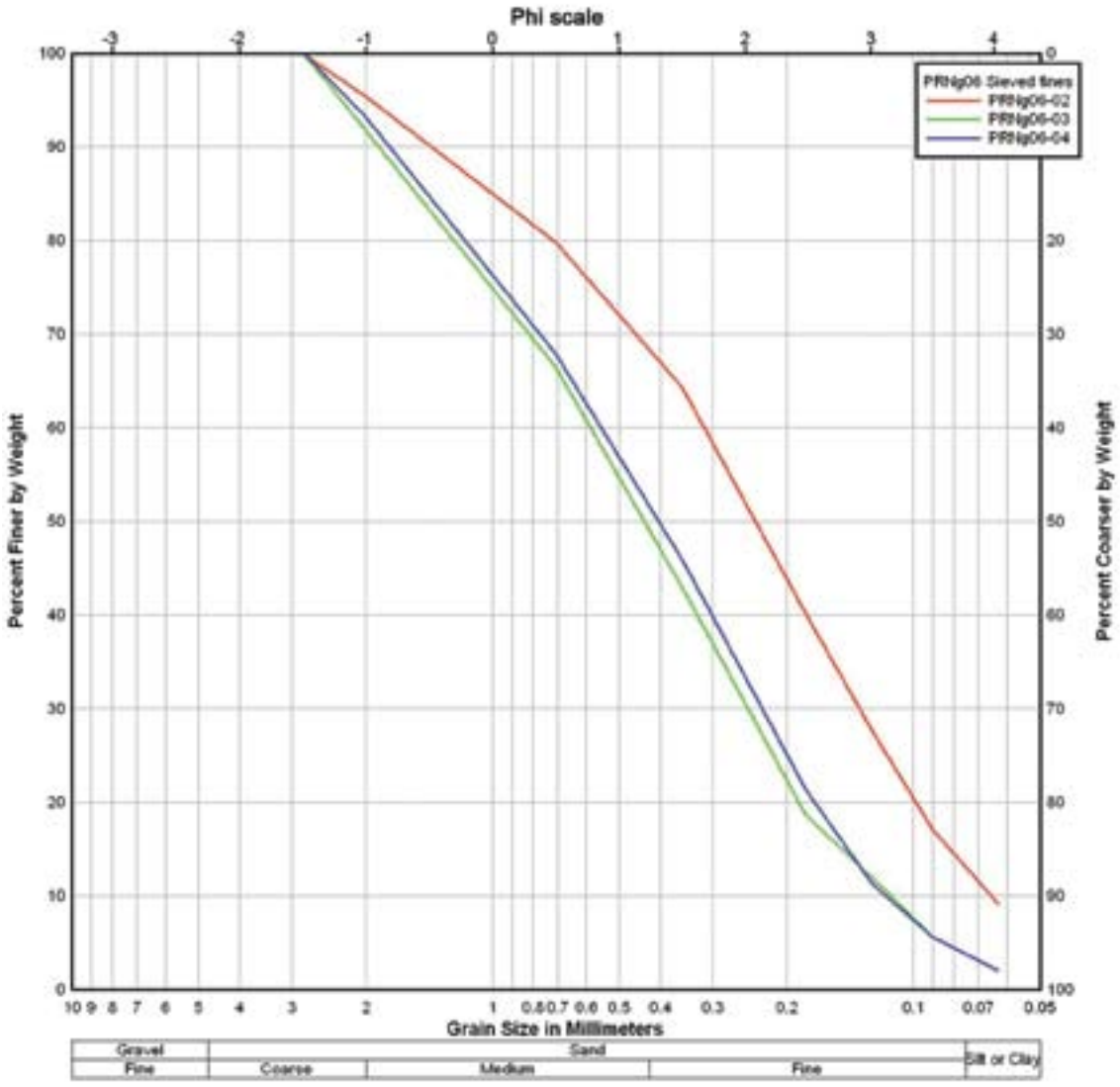

Figure 3.13 Results from dry sieving

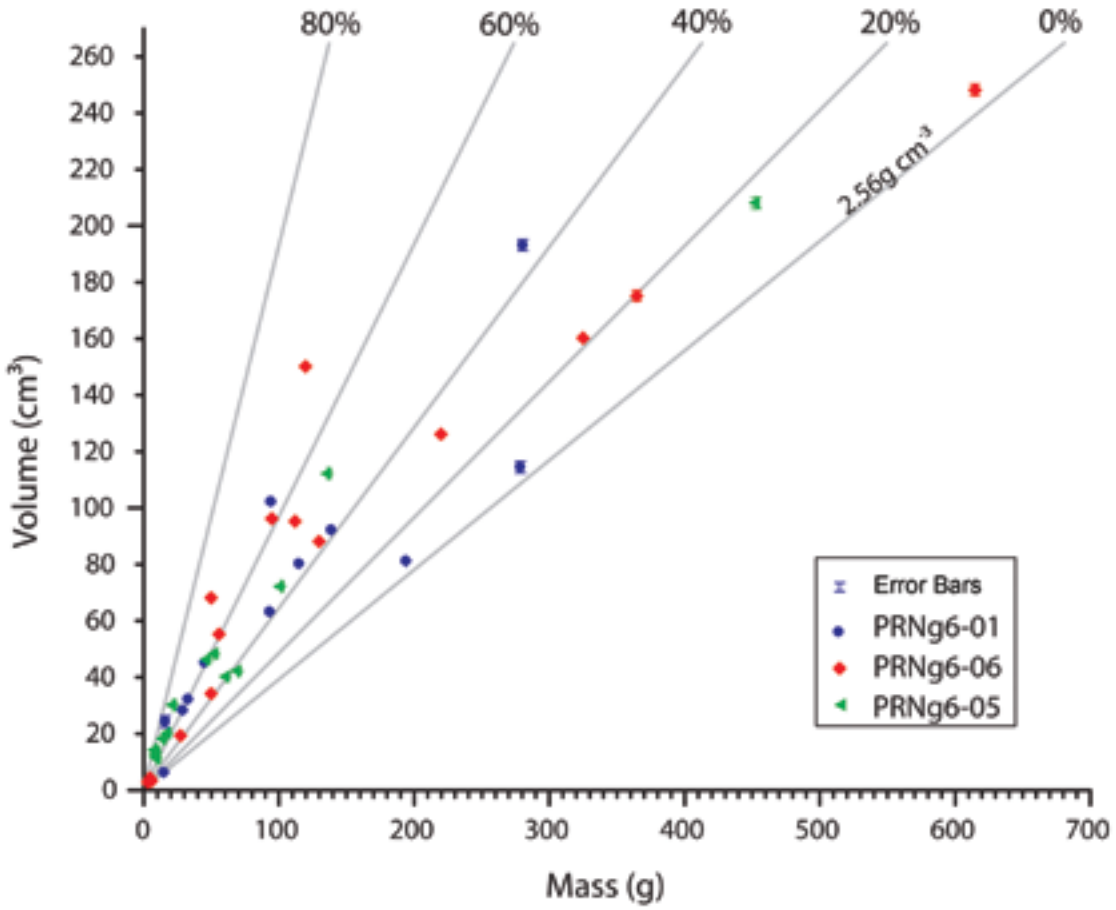

Figure 3.14 Mass plotted versus volume for each sub-sample within PRNg6-01, PRNg6-05 and PRNg6-06. Trend lines are added for calculated vesiculation percentages from a uniform source magma, assuming a vesicle mass of 0.

Clearly there is a large range in particle density throughout the deposit, ranging from juvenile material with very low vesiculation through to pumiceous blocks with 80% vesiculation. Reddened agglutinate was present throughout the flow, concentrated in the surface deposits of proximal to distal parts of the flow. Figure 3.13 indicates that greater vesiculation is found in smaller particle sizes, or rather that vesiculated material was more likely to break into smaller pieces during flow. However, without a greater sample size this cannot be statistically proven.

3.1.7 Internal Flow Features

While very few internal sedimentological flow features were observed within the flow the park restrictions did not allow detailed study. The most obvious feature was the distinct difference between the fill material represented by Sample PRNg-03 and the overlying clast-supported gravel to boulder grade material represented by PRNg6-06. These two samples were taken from the same locality, separated by 1m of vertical distance from the base of the channel to the top of the levee. The boundary between the fines-rich matrix supported sand and the overlying levee material was distinct, with the grading transition occurring in less than 100mm of vertical distance. The general profile of the flow was broadly in agreement with the analyses conducted by Lube *et al.*(2007) on the other nearby 1975 PDCs.

3.1.8 Summary of field analogue potential

Firstly, the depositional mechanism represented by the Ngauruhoe deposits is not that of a 'typical' density stratified current relevant to ignimbrite forming PDCs. The Ngauruhoe deposits are very small volume, short run-out and (in places) highly channelised, with relatively low fines content and relatively high particle density. They are inferred to have very rapidly deposited with the vertical deposit structure more accurately recording the current stratigraphy than may be assumed in other, more sustained or large-scale PDCs. These conditions make the 1975 Ngauruhoe deposits ideal for comparison to laboratory flume experiments as part of a more general study of dense granular flow.

The data collected in this fieldwork give a basic set of parameters which may be used as baselines in more generalised numerical and analogue modelling attempts for small volume flows. The data gathered on density and particle size variations have been used (although not exclusively) to inform the materials chosen for use in the laboratory experiments later in this work.

The channelisation of flow VI provides several distinct features to reproduce, and may assist in constructing more generic PDC models; as noted by numerous authors (Druitt, 1998; Sohn *et al.*, 2005). Many PDCs exhibit greater run out than may be predicted by accepted frictional systems; channelisation is believed to be a significant factor in many cases. As such, Ngauruhoe flow VI is an interesting example, exhibiting both channelised and non-channelised behaviour.

Flow VI has a geometry which lends itself to modelling, and the samples collected allow for a broad approximation of the flow material to be reconstructed should the opportunity arise in the future. Furthermore, a high resolution DEM has been generated by the Volcanic Risk Solutions group at Massey University, New Zealand, offering considerable potential for future numerical modelling.

3.2 Experimental Materials

A variety of materials have been used in the various analogue experiments. The first phase of experiments utilised 90 μm diameter silica sand. In order to use a material with more uniform characteristics (i.e. density, diameter, roundness, sphericity) the subsequent experimental phases moved to using silica and ceramic beads of various diameters in order to assess the impacts of varying size, shape and density within a charge. A full breakdown of experimental material properties is provided in Appendix C. Bead grain size analyses were provided by the Quality Control laboratory of Sigmund Lindner GmbH using Camsizer apparatus, while the LA60 sand analyses were carried out by Klinkmuller *et al.* (2008).

3.2.1 Sand

The sand used in these experiments is a 200 μm diameter coloured silica sand used widely in sandbox modelling. These sands were analysed by Klinkmüller *et al.*, (2008) and shown to have the properties outlined in Table 3.3

The variability in grain shape suggested in Table 3.3 can be more clearly visualised using electron microscopy to image individual grains (Figure 3.15).

TABLE 3.3 PROPERTIES OF LA60 SAND (after Klinkmüller *et al.*, 2008)

Grain Shape		
	Aspect Ratio	1.492
	Angular % by mass	47.95
	Subangular % by mass	42.85
	Rounded % by mass	9.19
Mean grain size (μm)		205

The large range of grain shape is a significant feature of this sand as a modelling material, as angular materials have significantly higher friction coefficients than rounded materials (Mair *et al.*, 2002). Figure 3.15 shows that the LA60 sand has relatively good level of size-sorting but the mean particle aspect ratio of 1.492 (Klinkmüller *et al.*, 2008) means that the irregularities in roundness are significant. This makes numerical modelling of the sand behaviour in a granular flow environment potentially challenging, due to the size and shape sorting demonstrated in granular systems (see Chapter 2).

3.2.2 Silica glass beads

Various diameters of silica beads have been used throughout the analogue series of experiments. Small beads have acted as bulk-flow material with larger beads being included to investigate BNE and RBNE sorting effects. Large silica beads are used in these experiments to act as a crude pumice clast analogue (material properties summarised in Table 3.4). Assessment of the effects of size segregation

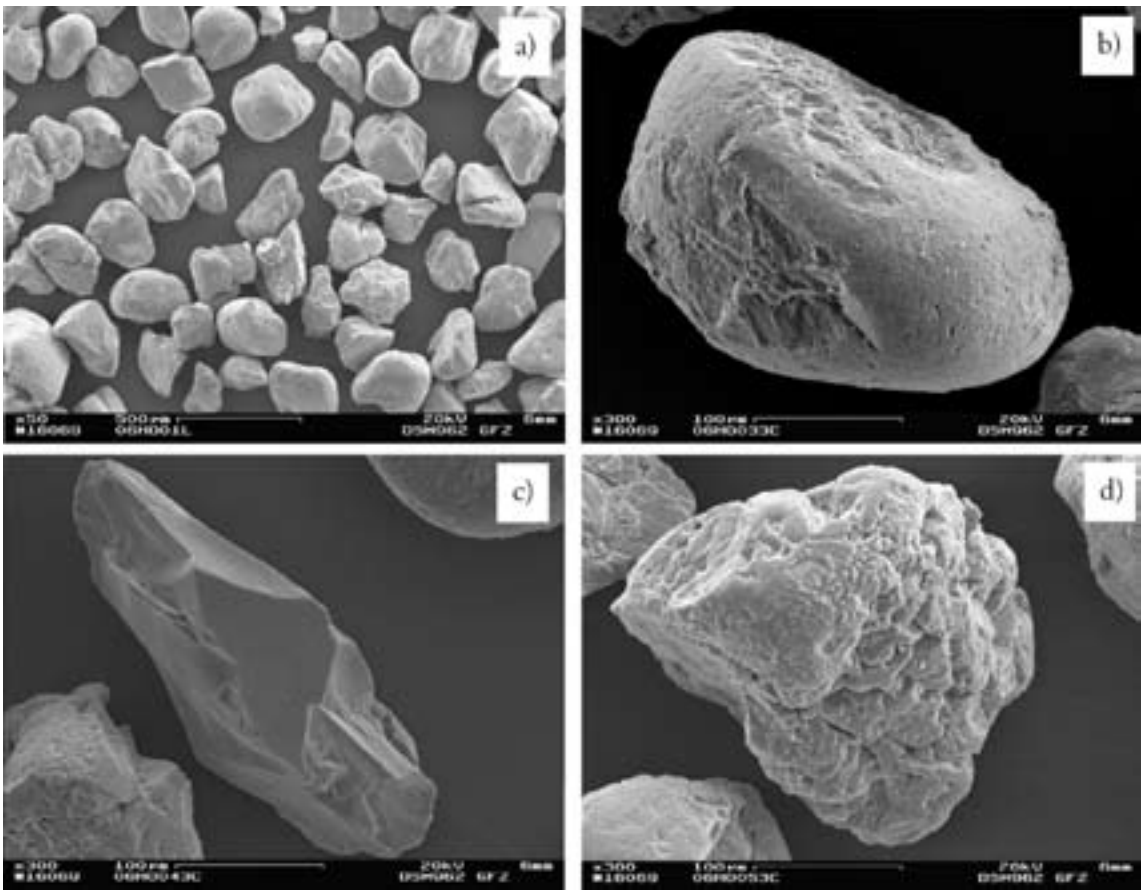

Figure 3.15 Electronmicrographs of a range of LA60 sand. The relatively good sorting is in contrast to the high variability in grain roundness seen in a), with rounded (b), angular (c) and subangular (d) examples of grains. From Klinkmüller *et al.*, (2008)

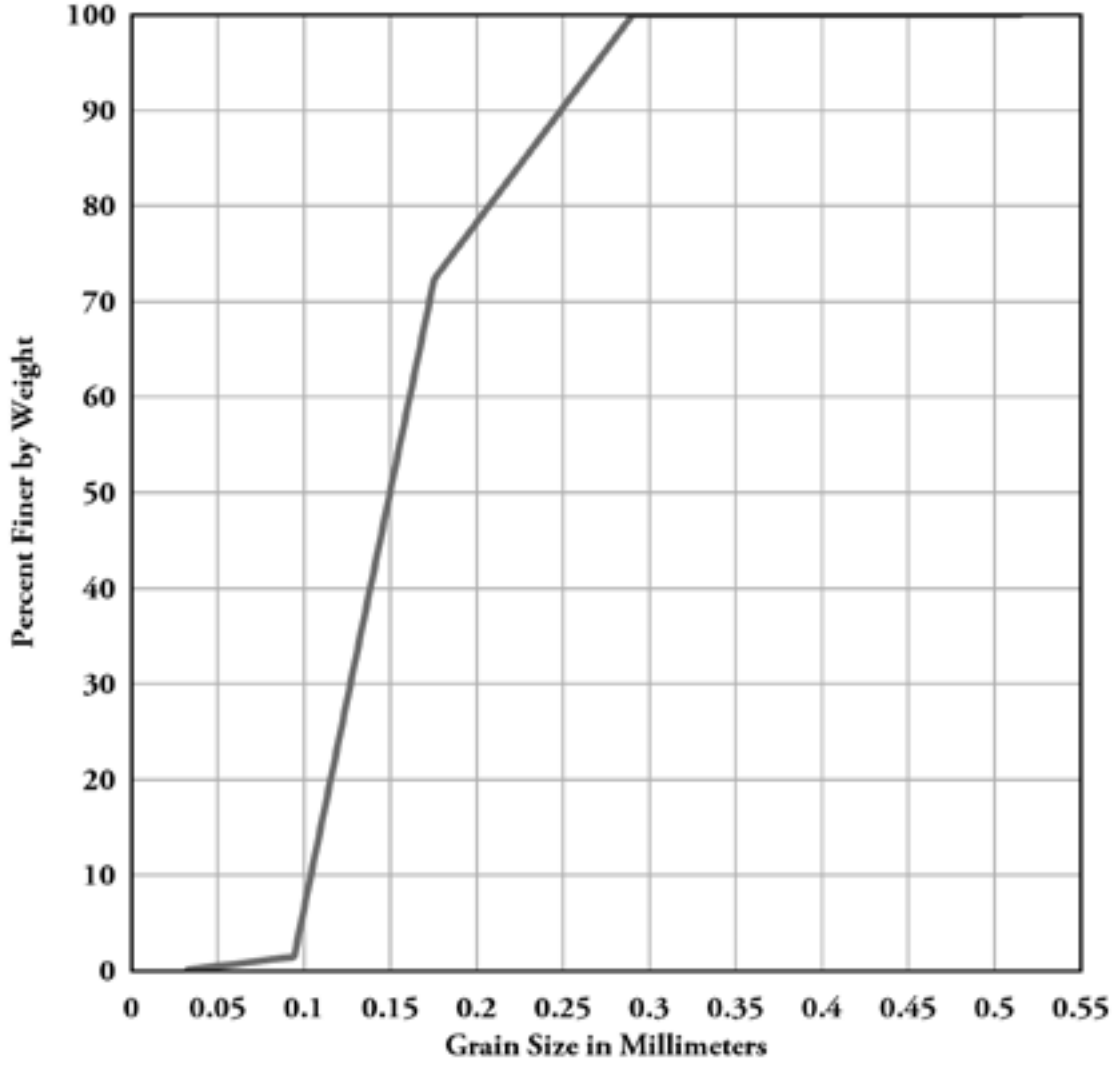

Figure 3.16 Grainsize analysis of LA60 sand, generated from data in Klinkmüller *et al.*, (2008)

in these flows is permitted due to the identical particle density (2500 kg m^{-3}) and similar bulk density (1470 kg m^{-3} in the 1.00-1.20 mm diameter range beads, 1510 kg m^{-3} in the 0.20-0.30 mm diameter range).

In the early experiments metallic coloured beads were used so that point lighting would enable easy identification of individual beads. However matt-finish beads were used in internal geometry experiments in order to ensure even colour in section photographs.

These beads are specified as having a roundness >95% (short a, (see Figure 3.17), and grainsize distribution analyses (Figure 3.18, Figure 3.19) demonstrate the very tightly controlled size range in a typical sample.

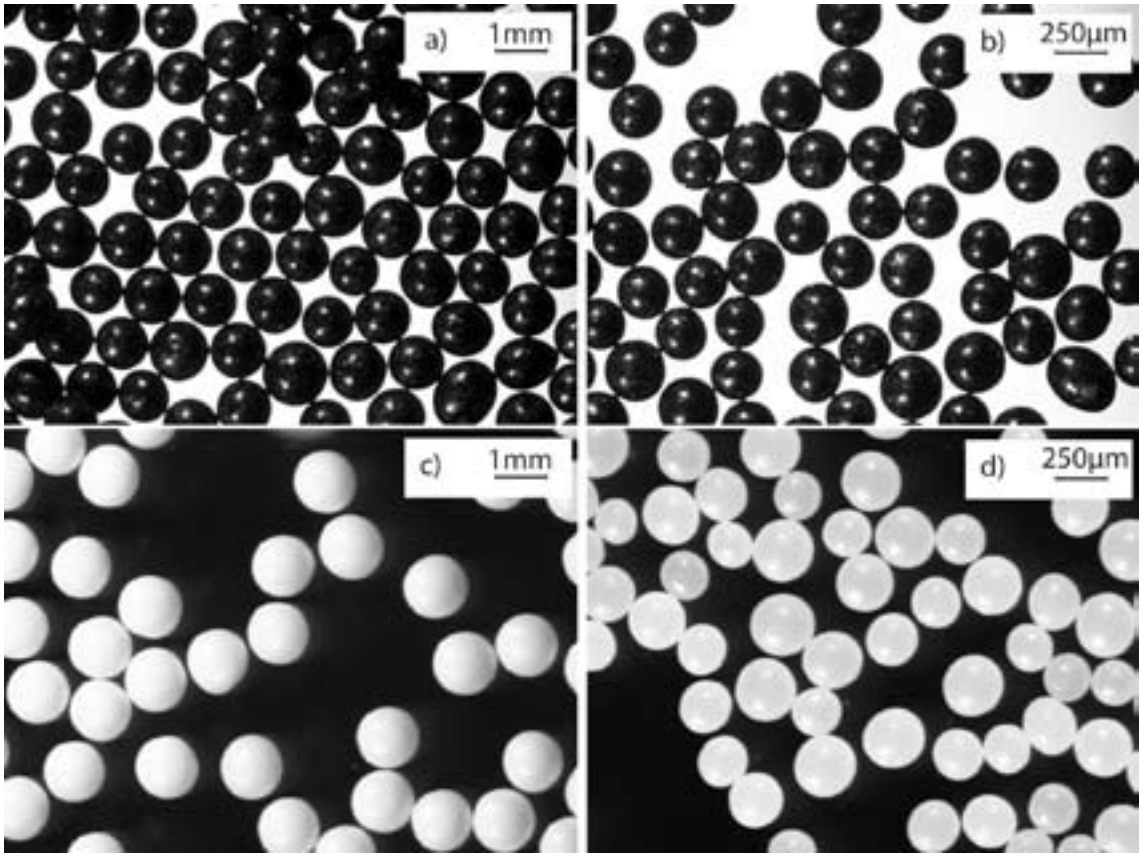

Figure 3.17 Micrographs of the four principle bead types used in the experiments. a) 1 mm diameter silica, b) 250 micron diameter silica, c) 1 mm diameter ceramic, d) 250 micron diameter ceramic

TABLE 3.4 PROPERTIES OF EXPERIMENTAL BEADS

Type	Diameter (mm)	Specific density (kg/m^3)	Bulk density (kg/m^3)	Sphericity	PDC analogue
Glass	1.00-1.20	2500	1470	>0.95	Pumice
Glass	0.20-0.30	2500	1510	>0.95	Pumice
Ceramic	1.00-1.20	6000	3720	>0.99	Lithic
Ceramic	0.20-0.30	8000	3852	>0.99	Lithic

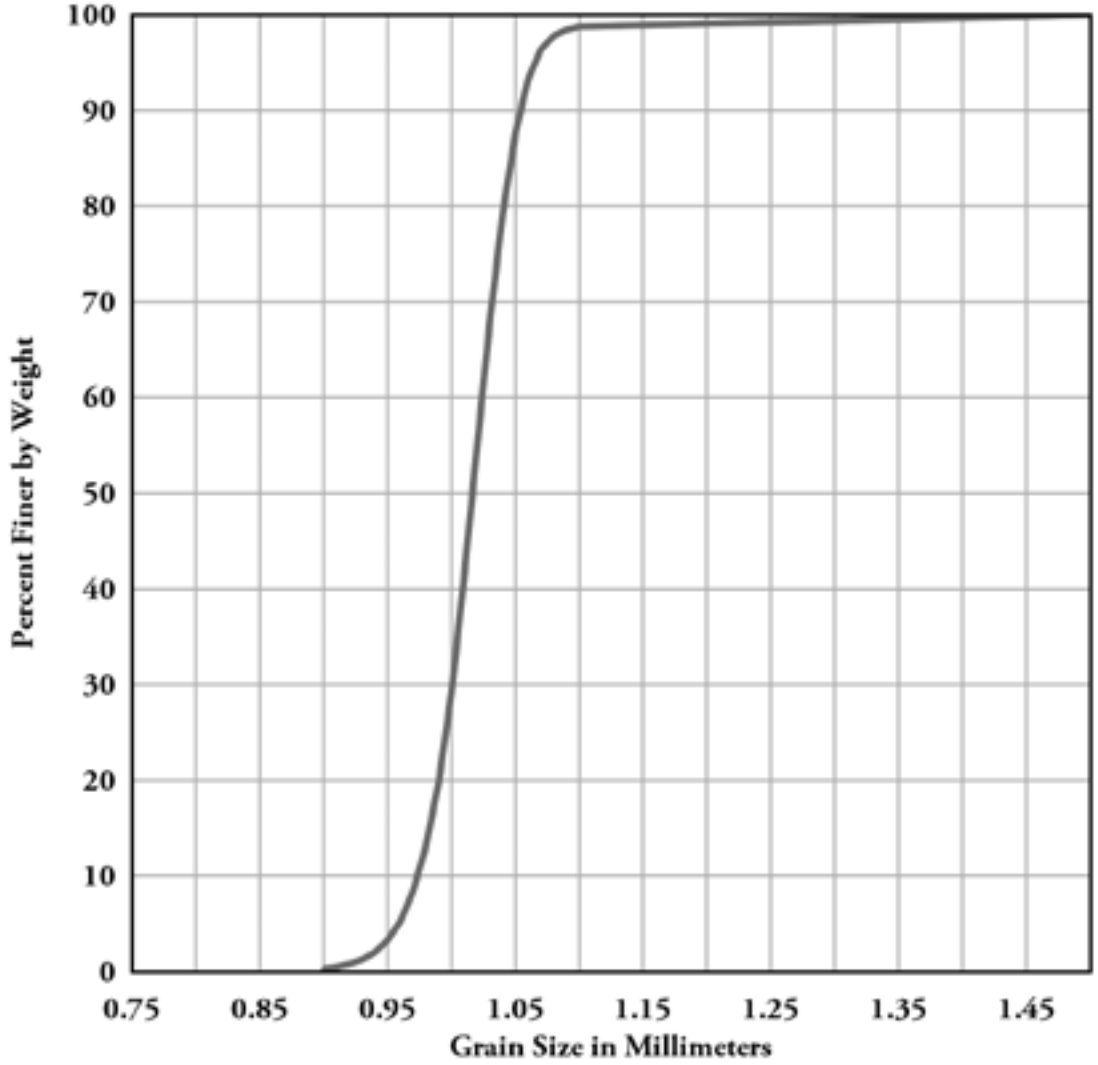

Figure 3.18 Grainsize analysis of 1.0 mm diameter glass beads. Data provided by Camsizer analysis carried out at Sigmund Lindner GmbH

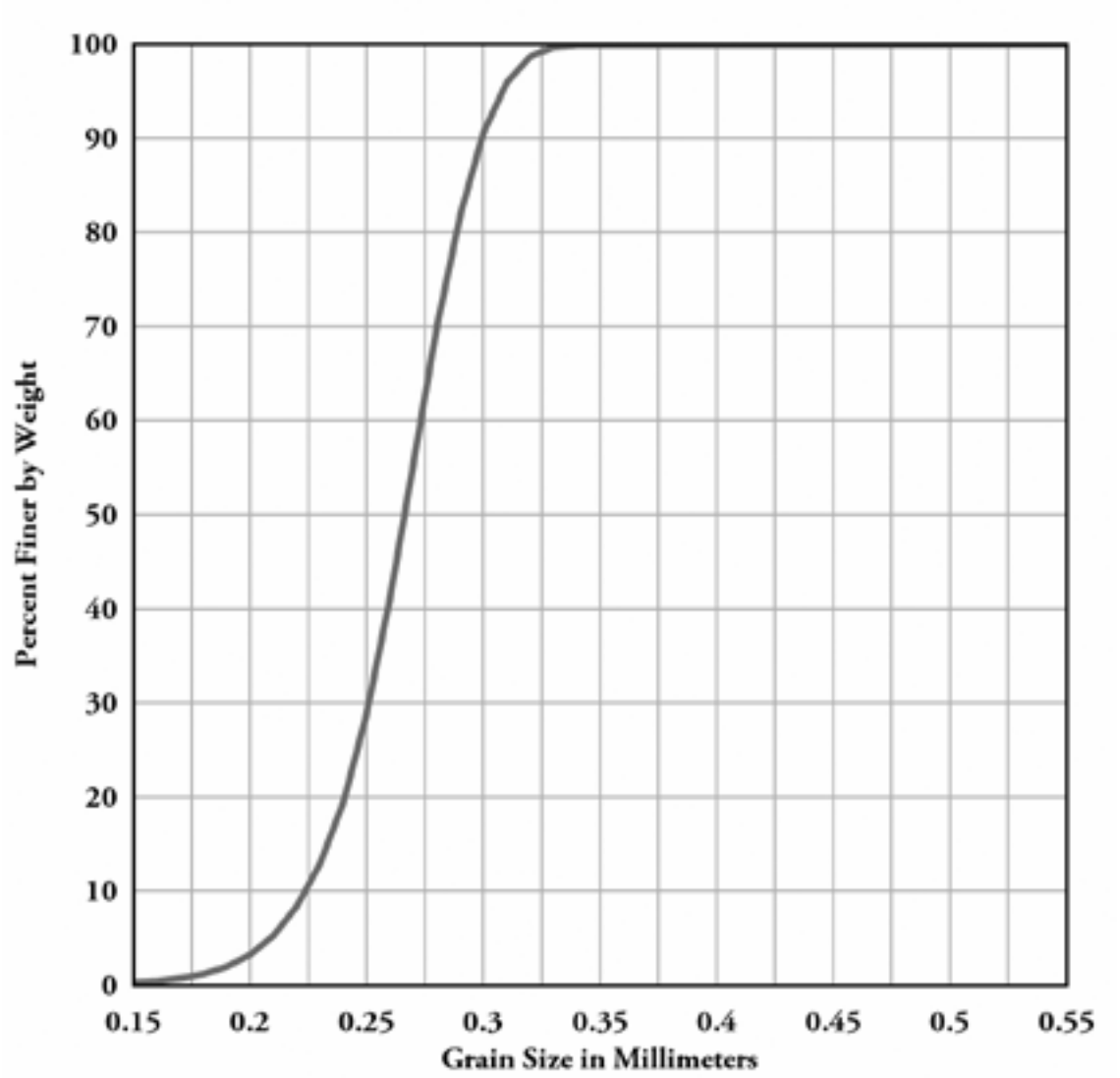

Figure 3.19 Grainsize analysis of 250 micron diameter glass beads. Data provided by Camsizer analysis carried out at Sigmund Lindner GmbH

3.2.3 Ceramic beads

Ceramic beads have been used in various experiments to act as analogues for lithic particles, and to more generally assess the effects of density settling in these flows (6000 kg m^{-3} specific density, 3720 kg m^{-3} bulk density), The exceptionally high cost of these beads precluded their use in all experiments. These beads are specified as having >98% roundness (Figure 3.17). Typical grain size distributions are shown in Figure 3.20, Figure 3.21.

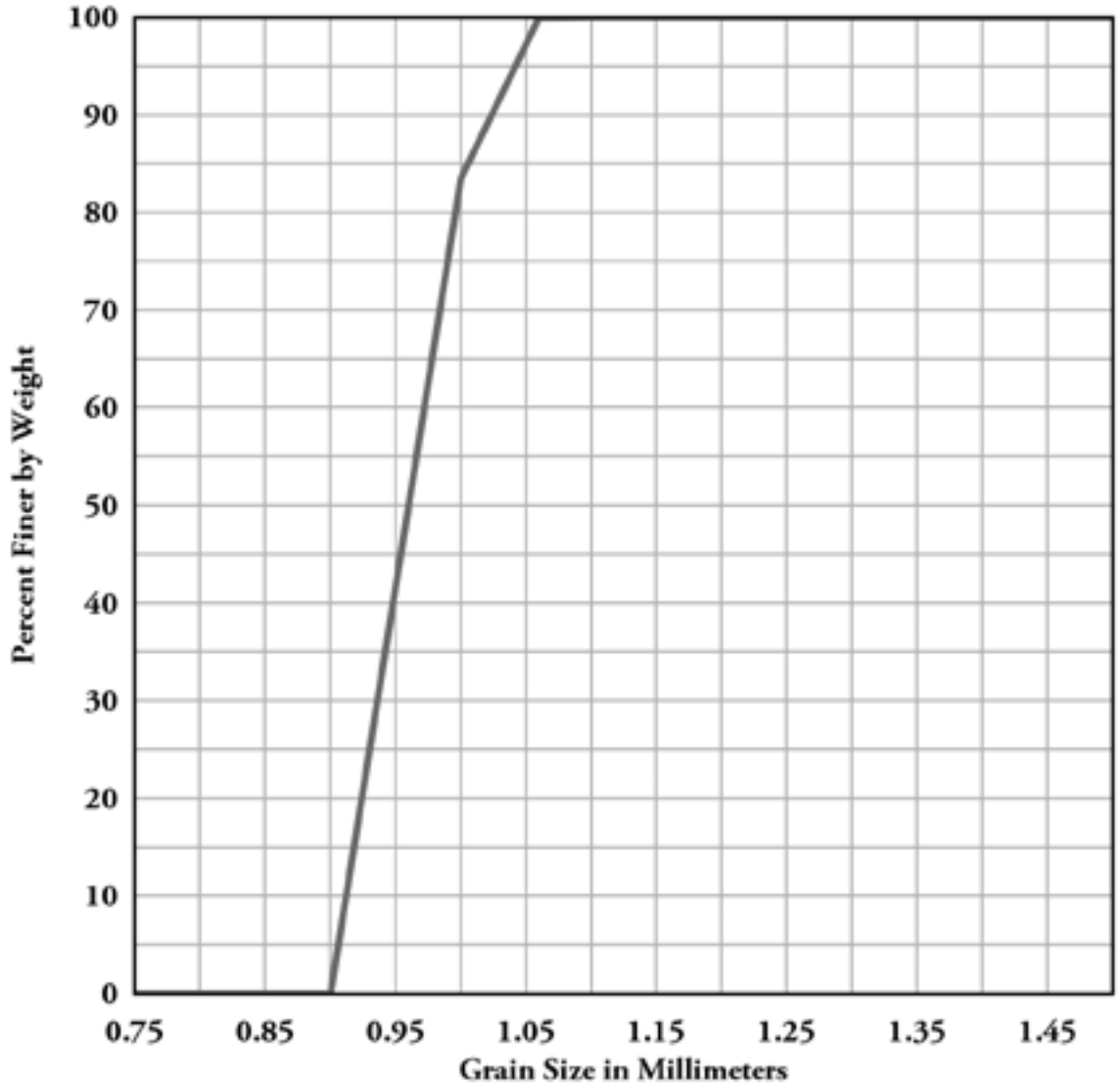

Figure 3.12 Grainsize analysis of 1.0 mm diameter ceramic beads. Data provided by Camsizer analysis carried out at Sigmund Lindner GmbH

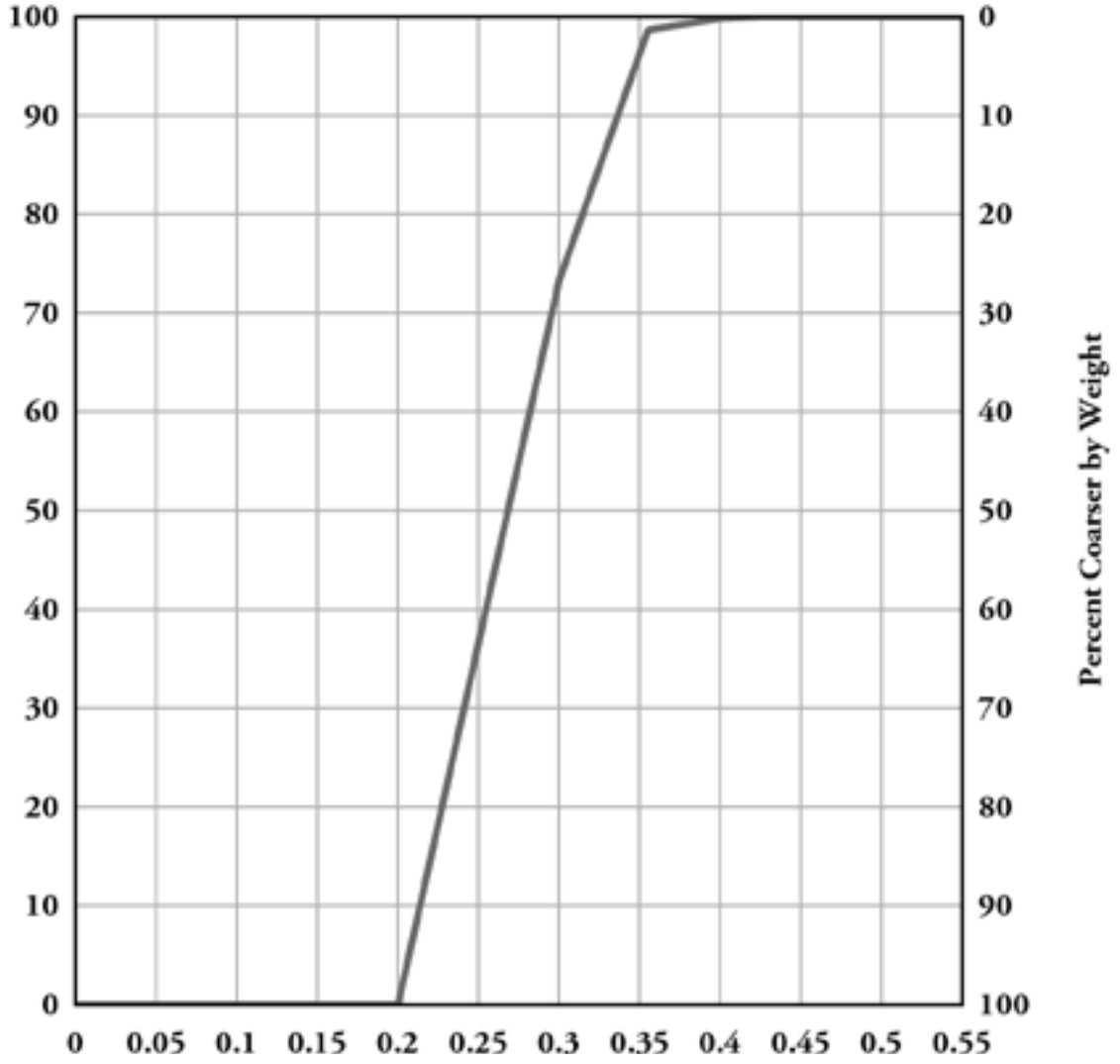

Figure 3.21 Grainsize analysis of 250 micron diameter ceramic beads. Data provided by Camsizer analysis carried out at Sigmund Lindner GmbH

3.3 Phase 1: 2D Analogue Flume

3.3.1 Objectives

Attempts at generating a detailed numerical model of granular flow are dependant on having detailed data on flume and flow material properties. In addition, it is difficult to truly assess the validity of a flow model purely on the basis of the depositional surface geometry; Initiation mechanism, flow velocities, flow geometry, and sedimentation rates are all significant contributors to the flow motion. Early investigation with a very simple numerical model demonstrated that it was possible to generate very similar topographies with quite varied flow dynamics.

In order to investigate these effects, and permit the generation of a sophisticated numerical model a simple analogue flume experiment was designed (herein referred to as flume A). The design of the flume was to serve several requirements:

1. Allow direct comparison with the work of Denlinger and Iverson (2001)

2. Allow the investigation of particle motion in cross section

3. Permit the study of varied flow parameters such as flow material, release mechanism and flume basal friction

A Perspex-walled flume was constructed, 450 mm long 45 degree slope, transitioning to a horizontal runout at a point break in slope, measuring 100 mm wide. The transparent Perspex was used in order to permit visual observation of the flow and deposit edge. The flume was fitted with an interchangeable release hopper – both vertical lock-gate and raised drop-chute designs were constructed. The charge is placed in the hopper and released by removal of a restraining gate. The flow is recorded using high speed video capture., and the deposit recorded by much higher resolution digital stills photography. Various coated baseplates can be added to the flume to vary the basal friction behaviour.

Due to the small frame size of PAL-I specification video (625 lines) separate cameras were focussed on different parts of the flow to gain a reasonable image quality, or separate runs were carried out with the camera focussed on a specific region of flow. Digital still photographs were taken before and after each run to give a detailed record of initial charge and final deposit geometry. In editing sound queues were used to ensure frame synchronisation with experiment run time in video sequences where the release gate was out of frame.

3.3.2 Procedure

The charge for each experiment is defined by volume accurate to 0.1 cm^3. Charge volumes vary from 100 – 500 cm^3. This charge is added to the hopper either as a single unit, or carefully sifted in as coloured layers according to the experimental requirements. Experiments were carried out in a room with constant 35% humidity, with materials stroed in open containers at room conditions for at least 72 hours before use.

The charge is photographed, and the video camera checked for position and focus. The gate is manually released and the camera activated. The resulting deposit is photographed, and the flume can then be cleaned and reset for the next run. If friction pad bases are used these can be fixed to the flume base using tape.

3.4 Phase 2: 3D Surface Topography

3.4.1 Objectives

Following the results of the analogue experiments carried out in flume A it became necessary to redesign the flume and experiments to look at how particle parameters effect the surface topography of the final deposit. Polymict charges appeared to produce significant sorting features, and the assumption that the flume could act as a 2D analogue was challenged by apparent lateral sorting.

The flume for the second phase (herein referred to as flume B) was designed to be wider in order to better evaluate the sidewall friction effects seen in the first flume, and with a smoother transition from slope to runout to reduce the apparent hydraulic jump effects observed in flume A. It measures 150 mm wide, with a longer shallower slope, longer runout and a 150 mm radius curved transition to the

runout surface in order to reduce the hydraulic jump effects. By focussing on the deposit topography the necessity of using Perspex was removed, enabling a move to wood construction and the associated reduction in electrostatic effects on the flow materials.

3.4.2 Procedure

Each charge is measured by volume accurate to 0.1 cm^3. Charge volumes vary from 100 – 1000 cm^3. The hopper is then filled with either a monomict charge or well mixed polymict charge. By mixing polymict charges in the hopper any sorting demonstrated in the deposit can be inferred to have occurred during flow or deposition.

The charge is photographed, then the lock gate is released, and the subsequent deposit is photographed. A steel wire probe is used to measure deposit thickness. A network of sample points spaced at regular intervals give a basic topography, with extra sample points added as necessary to account for unusual features, or feature details which sit between sample points.

3.5 Phase 3: 3D internal geometry

3.5.1 Objectives

Probing and dissecting the earlier polymict experiments clearly demonstrated that complex internal geometry had developed. In order to investigate these features, a process modified from structural sand-box modelling was adopted. By setting the deposit in gelatine then slicing the block a series of stacked profiles through the deposit allow for a 3D reconstruction.

Early experiments in this phase used the same flume as in the 3D topography experiments in phase 2 (flume B). Later experiments were carried out in a new flume (herein referred to as flume C) designed to make the experiments more closely analogous to PDC. The slope angle was lowered to 35 degrees, and a more gentle 600 mm radius curve to the runout was fitted. The runout angle of 5 degrees was a compromise; designed to encourage overpassing of subsequent pulses and charges, whilst keeping runout distance within the flume length limit of 2 m. This angle also acts as an analogue for the runout angles demonstrated on volcanic slopes (Figure 3.1). In addition to this a low friction coating (Tigerbase®) is applied to the flume walls and base to ensure easy removal of set packs.

3.5.2 Procedure

The charges for these experiments are defined by mass using balances accurate to 0.1 g. Charge volumes vary from 300-1500 g, with individual component materials making up predetermined fractions of that total. The flume is assembled using petroleum jelly as a water-tight sealant between sections, and the charge is placed into the hopper and levelled. An alcohol based antistatic hydrophobic solution is wiped on all flume surfaces one minute prior to the lock gate being released. This ensures the solvent has evaporated before the charge is run, while the antistatic properties ensure electrostatic effects on particles are minimised. Sequential charges can be released into the flume by removing and cleaning the hopper, replacing and refilling it. Following release of the charge(s) they are photographed, and the deposit is set the deposit prior to slicing. Once set, removable flume sides allow the resulting block to be extracted and moved to the slicing apparatus.

3.6 Setting procedure

The pouring of gelatine solution into the flume has clear potential to disrupt the deposit. For this reason each run was packed with extra material to behave as a protective layer onto which tissue paper is layered to maintain a coherent upper surface onto which the solution can be carefully poured. The addition of the protective packing layer is a delicate process as some surface structures are at or near the angle of repose of the materials, leading to low stability. In addition, even very small drop heights (~30 mm) are sufficient to give packing material enough momentum to penetrate the loose deposit surface. Various packing materials were experimented with:-

a) Initially 60 μm diameter silica sand was used, but proved to have a significantly faster setting time than the larger beads. This led to difficulties in removing the pack from the flume, and then in slicing the deposit. Subsequent slices also suffer from delamination problems at the contact between the material types.

b) 250 μm beads were used in several cases. These are the same as those used in the deposit so it eliminates differences in setting time or delamination of the resulting pack. The cost of beads is a significant consideration.

c) 200 μm sand has a similar drying rate to the 250 μm beads. The low cost and ability to use large quantities provides a very stable pack for slicing. This enables slicing intervals to be reliably achieved at 10 mm thicknesses even in packs with high concentrations of 1mm diameter beads.

Using spherical beads leads to packing and porosity issues which can impact upon the effectiveness of penetration of the setting agent; the approach used was adapted from modelling techniques used in sand based materials which do not suffer from the same problem. This unavoidable issue leads to an unpredictable setting which, in some cases, results in large regions of the deposit remaining unbonded. This leads to loss of the pack as it is removed from the flume. This resulted in an average 30% failure rate on run setting. Evolution of the gelatine solution recipe and packing technique reduced this from an initial 50% to near 15% in the later stages, with the final version comprising a ratio of 1.5 litres of boiling water to 350 ml of dry gelatine powder. Within the first two hours of the solution being added it is necessary to top up the pack with more solution as it impregnates. After approximately 20 hours the side walls of the flume are removed, and the tissue paper carefully lifted to remove any overlying remaining gelatine. A blade is carefully run under the pack before transfer to the slicing apparatus.

3.7 Slicing

The slicing apparatus evolved somewhat during the experimental run. The initial model comprised a running wire slice. This caused vertical stress on the pack which tended to increase delamination, and smeared material down the slice faces. The final incarnation of the slicer utilised a vertical stainless steel blade which significantly reduced these issues. Early runs using 90 μm packing sand were able to achieve slice thicknesses down to 15 mm (10 slices from each pack). Use of 200 μm beads as packing materials brought potential slice thickness down to 10 mm (15 slices per pack).

3.8 Scaling

3.8.1 Dimensional analysis

Comparison of analogue models to real-scale phenomenon is a non-trivial concern. If you wish to shrink the physical dimensions of a system but maintain its geometrical similarity to the full scale system, then conditions and measurements must be scaled in kind. Dimensional analysis allows these calculations to be carried out, by assessing complex systems in their most simple form and then permitting quantitative calculations to be based upon them. The Buckingham ∏ theorem used in this paper to perform dimensional analysis relies on defining the parameters which control the behaviour of the modelled system. Vitally, dimensional analysis is able to deal with problems in which the equations and boundary conditions are not fully accepted or understood. This is particularly important as we are dealing with (1) poorly constrained granular physics (see Chapter 2.2) and (2) PDCs and debris flows which have wide ranging and in some cases poorly constrained flow parameters.

The basis and methods of Buckingham ∏ theory are well described in Sonin (2001). In order to perform dimensional analysis we must first isolate the important parameters. All physical properties can be defined in terms of the 7 base quantities (i.e. dimensions) of length, time, mass, temperature, current, number of elementary particles and luminous intensity. For the purposes of describing the properties of geophysical and laboratory flows the only ones we need consider are length (l), time (t) and mass (m). Using square brackets to define 'the dimension of', we can eliminate discussion of units and deal purely with magnitude of these dimensions, and hence state that:

$$\begin{aligned} [l] &= L \\ [t] &= T \\ [m] &= M \end{aligned} \qquad [3.1]$$

Where L, T and M represent the dimensions of length, temperature and mass without any arbitrary unit system. We can now use these base quantities to form derived quantities. For example, density is defined as $\rho = m/v$ and has the dimension of $[ML^{-3}]$. It follows that if we transform from these dimensionless parameters to a system using *Système International* (SI) units then density is defined by units of kg m^{-3}.

The principal of the ∏ theorem is that for a given system with n variables and k dimensions, the system can be described by n-k dimensionless numbers. Different systems which share the same dimensionless magnitudes can be considered equivalent.

The experiments are designed to replicate the conditions in a grainflow at the base of a density stratified PDC. Cohesionless flows occur as true grainflows where interstitial fluids are unimportant, and modified grainflows (Lowe, 1982) where the flow is modified by either a pore fluid or over-riding current. Two important simplifications apply in our parameterisation of this scaling:

1. We ignore evolution, addition to or removal of flow material during transport (effects of

processes such as particle collisional interaction, exsolution and vesiculation, deposition, erosion and entrainment of underlying substrates, and addition of material from over-riding turbulent currents)

2. We assume perfect inelastic particle collisions

This complete set of parameters can be simplified prior to commencing with dimensional analysis. We narrow this down to an independent set by eliminating variables which are dependant on those we already have. For example, if we know flow runout and velocity, we are able to calculate emplacement time and can exclude it from further analysis. Equally, we are able to calculate the fluid volume fraction (ϕ_f) from the solid volume fraction (ϕ) by ϕ_f=1-ϕ .

The shortened list of physical parameters is summarised in Table 3.5, along with a number of dimensionless parameters known to usefully describe and scale geophysical flow systems (Iverson and Denlinger, 2001). The definitions of these numbers are discussed later in section 3.8.2.

Of these variables we select runout length (l), particle density (ρ_s) and flow velocity (v) as repetitive; that is, we can use their dimensions to define the dimensions of any other variable. In order to use these parameters we must define their dimensions in terms of M, L and T.

We now combine these to define our dimensionless Π parameters.

Vertical distance travelled

We now consider the dimensions of these parameters. H is given an exponent of 1, and in order to get this into a dimensionless form the exponents must sum to 0.

$$\begin{aligned} [l] &= L \\ [\rho_s] &= ML^{-3} \\ [v] &= T^{-1} \end{aligned} \qquad [3.2]$$

.

$$f(H) = H, l, \rho_s, v \qquad [3.3]$$

.

$1+a-3b+c=0$ for L

$b=0$ for M

$-c=0$ for T so $c=0$

Substitute values for b and c in to the Equation 3 term for L

TABLE 3.5 LIST OF PHYSICAL AND DIMENSIONLESS ANALYSIS FOR SCALING OF GRANULAR FLUME EXPERIMENTS

Physical parameters	Symbol	SI Units	Dimension	Experiments	Debris flow††	PDC††
gravity	g	m s^{-2}	LT^{-2}	9.81 m	9.81 m s^{-2}	9.81 m s^{-2}
Runout	l	m	L	0.8 - 1.2 m	3 -10 km	2 – 100 km
particle density	ρ_s	kg m^3	M L^3	2500 - 6000	1000 – 3000	500 – 3000
fluid density	ρ_f	kg m^3	M L^3	2	2	2
particle diameter	Ø	m	L	250 µm – 1 mm	1 µm – 3 m	1 µm – 0.1 m
solid volume fraction	ϕ	-	-	0.55 – 0.64	0.5	0.5-0.95
flow thickness	d	m	L	0 - 2 cm	0 – 5m	0 – 10m
flow velocity	v	m s^{-1}	LT^{-1}	2	0 – 30	0 – 120
internal friction angle	φ	º	-	25-28	28-42	25-50
Vertical distance travelled	H	m	L	0.4 - 0.5 m	200 – 2000m	0.5 – 10km
Depositional slope angle	θ_r	deg	-	5	0 - 30	0 – 30
cohesion	Ψ	Pa	$[ML^{-1}T^{-2}]$	10 – 100	~10** – 100,000	2000 – 100,000
particle roundness	R	-	-	0.95	01 – 0.9	01 – 0.9
fluid viscosity†	µ	Pa s	$ML^{-1}T^{-1}$	1.78×10^{-5}	1.78 × 10–5	1.78×10^{-5}
Dimensionless parameters						
Savage number	N_S	-	-	0.15 - 0.9	0.1	0.001
Bagnold number	N_B	-	-	2 x 10^5	4 x 10^8	9 x 10^5
Friction number	N_f	-	-	5 x 10^5	4 x 10^9	9 x 10^8
Darcy number‡	N_D	-	-	1.3 x 10^{-6}	2 x 10^{-8}	3 x 10^{-7}

* inferred from Schellert 2000 and Soria-Hoyo et al., 2008.
** Fiorelli and Wilson 2004
† PDC values assume air at 15º C. Values are likely to be higher in ash laden flows (Fisher, 1966)
†† Representative values of large and small flows, from Iverson and Valance (2001), using the Elm Rock avalanche and Mt St Helens PDC data, in turn compiled from Hsu¨ , 1975, and Wilson and Head, 1981; Kuntz et al.,1981; Hoblitt, 1986.
‡ Based on estimated permeability values from Bear, 1972

$1+a=0$ so $a=-1$

Therefore

$$\Pi_1 = \frac{H}{l} \quad . \qquad [3.4]$$

This same process can be applied to the other variables

Flow thickness

This follows the same dimensions as height scaling, therefore

$$\left[L\right]^1 \left[L\right]^a \left[ML^{-3}\right]^b \left[LT^{-1}\right]^c \qquad [3.5]$$

$$f\left(d\right) = d, l, \rho_s, v \qquad [3.6]$$

therefore

$$\Pi_2 = \frac{d}{l} \quad . \qquad [3.7]$$

Particle Density

$$f\left(\rho_f\right) = \rho_f, l, \rho_s, v \qquad [3.8]$$

$$\left[ML^{-3}\right]^1 \left[L\right]^a \left[ML^{-3}\right]^b \left[LT^{-1}\right]^c \qquad [3.9]$$

$-3+a-3b+c=0$ for L

$1+b=0$ for M so $b=-1$

$-c=0$ for T so $c=0$

$a=0$

Therefore

$$\Pi_3 = \frac{\rho_f}{\rho_s} \qquad [3.10]$$

Particle diameter

Follows the same dimensions as height scaling, therefore

$$f\left(\delta\right) = \delta, l, \rho_s, v \qquad [3.11]$$

$$\left[L\right]^1 \left[L\right]^a \left[ML^{-3}\right]^b \left[LT^{-1}\right]^c \qquad [3.12]$$

$$\Pi_4 = \frac{\delta}{l} \qquad [3.13]$$

Solid volume fraction

This parameter has dimensions of unity, resulting in

$$\Pi_5 = \phi \qquad [3.14]$$

Internal friction angle

This parameter also has dimensions of unity, therefore

$$\Pi_6 = \varphi \quad [3.15]$$

Runout slope angle

This parameter also has dimensions of unity, therefore

$$\Pi_7 = \theta_r \quad [3.16]$$

Cohesion

$$f\left(\Psi\right) = \Psi, l, \rho_s, v \quad [3.17]$$

$$\left[ML^{-1}T^{-2}\right]^1 \left[L\right]^a \left[ML^{-3}\right]^b \left[LT^{-1}\right]^c \quad [3.18]$$

$-1+a-3b+c=0$ for L

$1+b=0$ for M, so $b=-1$

$-2-c=0$ for T, so $c=-2$

Therefore $a=0$

$$\Pi_8 = \frac{\Psi}{\rho_s v^2} \quad [3.19]$$

Roundness

This parameter has dimensions of unity, resulting in

$$\Pi_9 = R \quad [3.20]$$

Viscosity

$$f\left(\mu\right) = \mu, l, \rho_s, v \quad [3.21]$$

$$\left[ML^{-1}T^{-1}\right]^1 \left[L\right]^a \left[ML^{-3}\right]^b \left[LT^{-1}\right]^c \quad [3.22]$$

$-1+a-3b-c=0$ for L

$1+b=0$ for M so $b=-1$

$-1-c=0$ so $c=-1$

Therefore $a=-3$

$$\Pi_{10} = \frac{\mu}{l^3 \rho_s v} \qquad [3.23]$$

TABLE 3.6 SUMMARY OF DIMENSIONLESS SCALING PARAMETERS

	Scaling parameter
Π_1	Vertical distance travelled
Π_2	flow thickness
Π_3	particle density
Π_4	particle diameter
Π_5	solid volume fraction
Π_6	internal friction angle
Π_7	depositional slope angle
Π_8	cohesion
Π_9	particle roundness
Π_{10}	viscosity

Table 3.2 summarises the dimensionless Pi numbers and the parameters which they analyse (gravity is not assessed as it is constant). Figure 3.22 plots the approximate ranges for the scaling parameters $\prod_1$ to $\prod_{10}$, with debris flows represented by the red range bar, PDC by blue and the flume experiments in green (original data and charts provided in Appendix B). For most parameters the flume experiments represent a smaller extent of variation, but in a region within the extents of the geophysical flow examples. These imply that the experiments are suitably scaled for at least part of the range of geophysical flows. Three parameters bear more careful comparison. $\prod_8$ representing scaled cohesion sees an experimental range in line with that for debris flows, but very far from the PDC range. This is largely due to the high cohesion of ash-grade particles. The flume experiment flows are largely cohesionless. $\prod_9$ assesses particle roundness, and the spheres used in the flume are more round than any particles you would expect to find in geophysical flows. Baxter *et al.* (1999) demonstrated that grain shape has at least some part to play in granular sorting mechanisms, so any granular sorting mechanisms in the flume may be expected to be retarded - albeit to a small degree - in geophysical systems. Finally, $\prod_{10}$ assesses viscosity, and the experimental range can be seen to be somewhat higher than that for PDCs, and only matching the extreme cases of debris flows. This scaling is largely effected by runout, and it may be inferred that the higher $\prod_{10}$ values demonstrated by the flume are as a result of the low cohesion, and greater permeability. Fluidisation, and the associated increases in pore pressure (and reduction in cohesion) lead to long runouts - observed in both landslides and PDCs. The flume experiments are highly collisional, with no significant pore pressure to enable dilation and increased mobility, and hence display a correspondingly low runouts, resulting in high dimensionless viscosity.

3.8.2 Other dimensionless parameters.

Table 3.1 included a range of dimensionless parameters already understood to describe and scale geophysical systems (also outlined in Equations 2.1, 2.2., 2.3 and 2.4). More specifically, the dimensionless parameters quoted are those proposed by Iverson (1997) to quantify the relative importance of the four categories of forces which dominate granular flows; collisional, viscous, frictional and effects due to pore pressure.

The dimensionless Bagnold number (Equation 2.1) is important for distinguishing the various

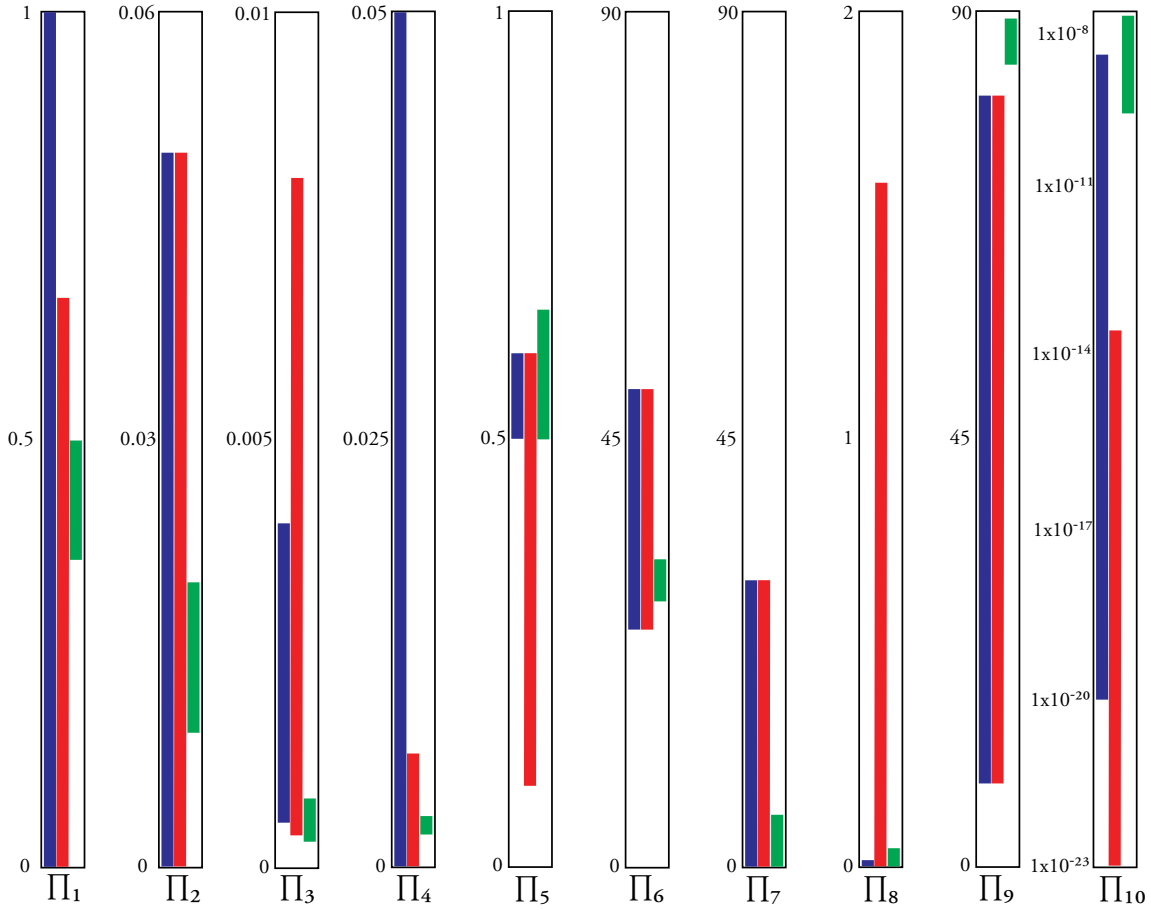

Figure 3.22 dimensionless scaling equivalency of the parameters Π_1 to Π_{10}, with debris flows represented by the red range bar, PDC by blue and the flume experiments in green

contributions of grain collision and viscous stresses in steady, uniform shear flows as assessed in Bagnold's experiments (1954). $N_B \leq 40$ indicate a 'macroviscous' system with normal stress and shear stress in the bulk material being proportional to shear rate. $N_B > 450$ indicate a collisional regime with normal and shear stresses proportional to shear rate. ϕ_* represents the closest possible packing, and therefore maximum extent of solid volume fraction. Grain concentrations in pyroclastic flows are unknown, but values for ϕ in the majority of debris flows appears to be greater than 0.5 (Iverson and Denlinger, 2001). The N_B values for the experiments demonstrated in Table 3.1 indicate similar scaling to PDC for the laboratory experiments, missing the debris flow field by several orders of magnitude. However, comparison to both systems is - in terms of defining the flows as collisional or viscous - valid, as all three are very much greater than the collisional-viscous transition (N_B=450).

The Savage number (Equation 2.2) represents the ratio of inertial shear stress associated with grain collision to shear stress associated with friction and loading of the granular mass (Savage, 1984; Savage and Hutter, 1989; Iverson, 1997), so acts to distinguish between collision and friction effects. At $N_S > 0.1$ collisional behaviour becomes dominant. The values for N_S demonstrated in Table 3.1 indicate that the flume experiments are more collisional than either the PDC or avalanche examples, but it should be noted that small variations in the internal friction angle of the material are able to bring the

values for the experiments very close to those for the debris flow. The lab experiments, however, are unable to approach the values typical for PDC.

Fluidisation number (N_f) (Equation 2.3) describes the balance between frictional and viscous forces, and can very simply be defined by N_B/N_S, with transition between these systems occurring at N_f =2000. The values shown in Table 3.1 indicate that all three flows occupy the frictional regime, and are several orders of magnitude beyond this transition value (although the geophysical systems are several orders of magnitude beyond the flume experiments).

Finally, the Darcy number (N_D) (Equation 2.4) distinguishes between the effects of viscous flow and pore pressure, with a transition value in the range of N_D=1000 - 6000. The calculation of this value is problematic, as it requires an understanding of the hydraulic diffusivity of the unit during flow. Major (2000) demonstrated that sandy-gravel debris flows with fines contents of <2 wt% typically have hydraulic diffusivity values in the order of 10^{-4} m^2 s^{-1}, while those with increased fines content (5 to 50 wt%) have diffusivities in the (remarkably similar) range of 10^{-6} - 10^{-7} m^2 s^{-1}. Using values in these orders for the geophysical flows and experiments suggests Darcy number values for the debris flow and laboratory experiments very far below the transition to a pore-pressure dominated system. The Darcy numbers for PDC are much closer to the transition, and are likely to be higher than calculated, due to the fluid viscosity values assumed in these calculations, which are probably much lower than might be seen in a highly ash-charged PDC (Fisher 1966). Significant pore pressure effects will buffer grain interactions, and this is believed to be a significant factor in the otherwise anomalously long runout observed in some debris flows and PDCs (e.g. Sparks, 1976, 1978; Wilson, 1980; Lube *et al.*, 2009).

3.8.3 Summary of scaling

In summary, it is apparent that the scaling of these experiments is highly suitable for comparison to geophysical systems where we find shorter runouts and low fines contents. The flows are particularly suitable for debris flow-type deposition, and are closely analogous to the activity typified by the Ngauruhoe 1975 deposits described in this chapter.

It is worth mention that adapting the flume experiments to scale to bigger PDCs would have required moving to a much finer particle size. Unfortunately, there are a number of powder effects such as high cohesion which would make intiation from a static pile problematic, and working with powders also brings a suite of health and safety concerns which the laboratory facilities available were not equipped to adequately deal with. Furthermore, powders are unable to provide the particle uniformity required by these experiments for them to meet their original requirement of narrowing parameters for numerical modelling (i.e. particle roundness).

The fact the scaling is closer to the small volume PDCs and debris flows does not preclude comparison with larger sustained currents. The dense basal granular current of PDCs is an end-member within a stratified current, and the conditions in this region are in the extremes closest to matching scaling with the experiments. While the experiments are unable to reproduce the longevity and overpassing

of these systems, the interactions between the granular lower flow boundary zone and substrate are very similar to the system represented by the flume experiments. We can therefore infer that the flume experiments reproduce similar interaction at flow contacts to sustained PDCs.

CHAPTER 4: INITIATION, FLOW AND DEPOSITION

4.1 Introduction

The depositional region of PDCs is dominated by granular flow interactions (see Chapter 3). In order to generate baseline data for further work a series of flume experiments are carried out to

1. assess the effects of sidewall friction, and whether narrow flume experiments are effective 2D analogues for numerical modelling of deposition
2. investigate how simple flume geometries impact flow and deposition
3. constrain the nature of flow initiation from static grain piles
4. discover whether initiation has a direct influence on the depositional characteristics of a flow
5. investigate the effects of varying basal friction and its impacts on deposition.
6. test different release mechanisms and their ability to effect deposition.
7. evaluate whether these small flume experiments reproduce plug-like or aggradational depositional mechanisms.

In order to investigate the behaviour of monomict charges at key points in an experimental flume, this Chapter will present the results from a series of experiments conducted and recorded using high speed video capture. The procedure is outlined in detail within Chapter 2.4. Both Perspex and rough bases are used to investigate the effects of basal friction, and the release from a static pile is compared alongside release from a vertical drop chute. Coloured layers are used to investigate the deformation of the charge as it moves down the flume and deposits. It is important to note that this flume design only allows side-wall observation of the flow, but experiments were lit to cast a shadow of the flow plan-view onto the backdrop. This enables at least some basic observation of the 3D development of the flows in cases where no frictional base-plate is installed in the flume. All experiments are conducted using 200 μm LA60 sand described in Chapter 2.3.1.

4.2 Initiation

4.2.1 Lock gate release

Initiation from a 250 cm^{-3} static confined pile (Figure 4.1) demonstrates a number of interesting features. The gate is clear of the pile after 0.12 seconds, and at this point the pile maintains its vertical unconfined face. Over the succeeding stills it is apparent that flow from the base of the pile leads to a destabilisation of the material riding above. 0.24 seconds after release the flow front has a flat steeply dipping surface. Over the next 0.20 seconds the flow elongates; the rear part made up of a seemingly coherent pile whose flow is restricted by the flow in front. The frontal part of the flow develops an

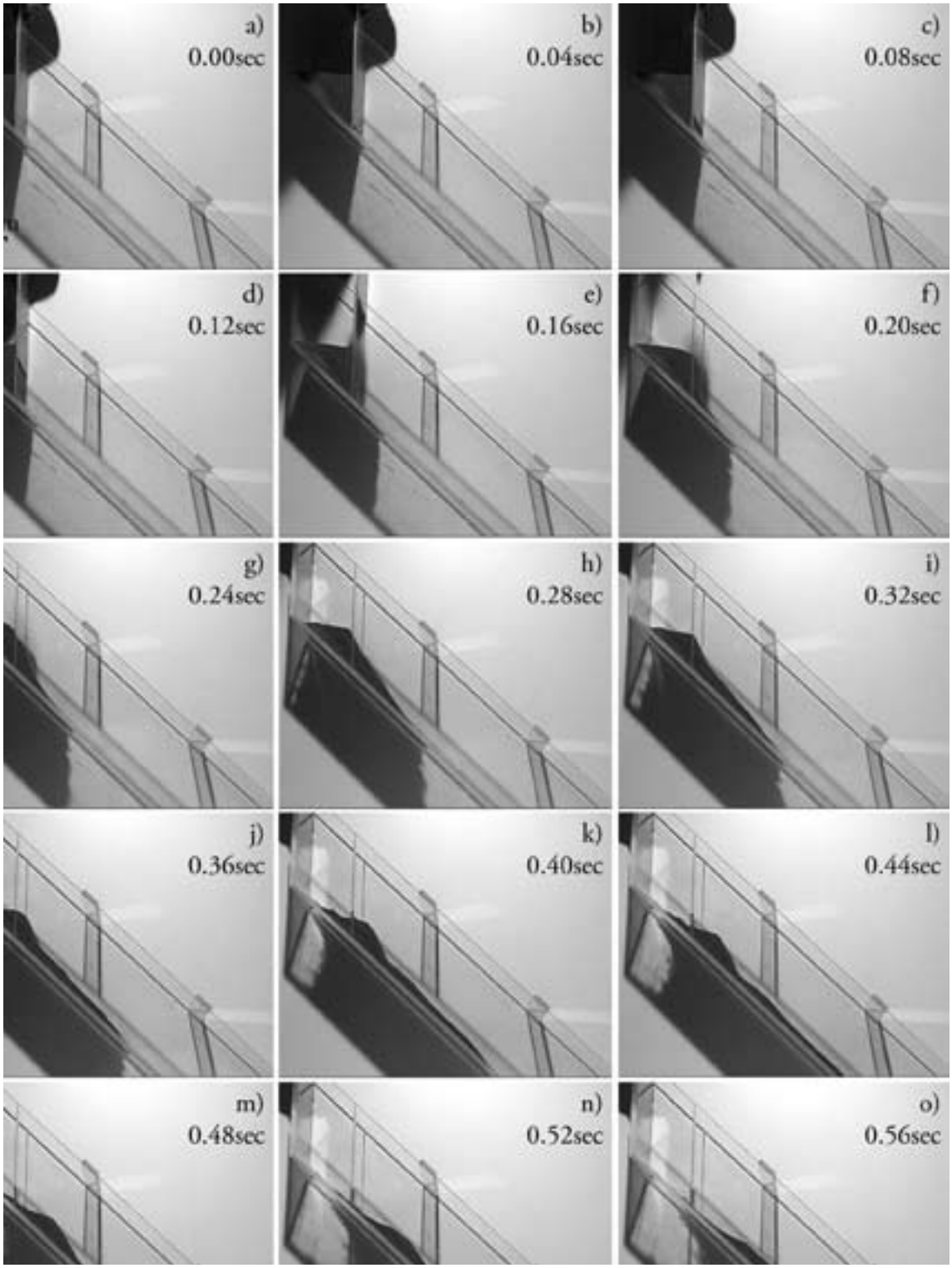

Figure 4.1 De-interlaced images from 25 frames-per-second footage showing initiation of flow following release of a static pile from behind a vertical lock gate.

undulating surface, and demonstrates thicknesses ranging between ~2 mm to ~15 mm at a peak-to-trough wavelength of approximately 75 mm.

It is important to highlight the shadow of the flow cast on the backdrop. Whilst the flow appears to initiate relatively evenly across the flume, side wall effects soon become apparent. Figure 4.1k (0.40 seconds after release) clearly demonstrates a curved rear to flow, indicating flow retardation at the side walls. This feature is maintained even when the most proximal material has begun to flow downslope (Figure 4.1o)

An identical experiment using a larger (500 cm^3) charge demonstrates similar behaviour, and grants a better insight into the behaviour of the front of the pile when the retaining wall is removed (Figure 4.2). As the front basal region of the pile begins to move, the upper part collapses downwards onto it. By 0.24 seconds into the flow distinct ridges are appearing along the upper surface of the flow. These ridges imply that some regions of the flow are moving faster than others, and are possibly indicative of active shear planes with extensional movement within the body of material.

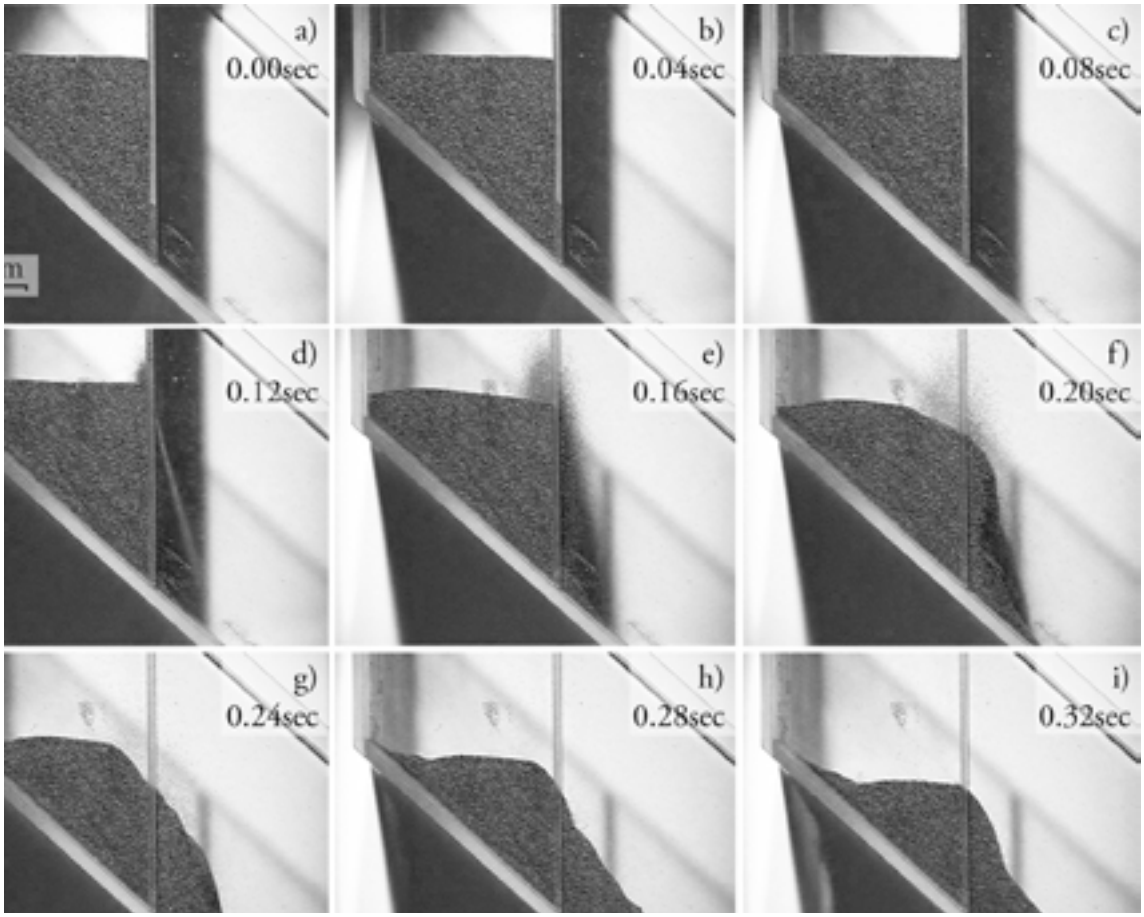

Figure 4.2 De-interlaced images from 25 frames-per-second footage showing the initiation of a 500ml flow following release of a static pile from behind a vertical lock gate.

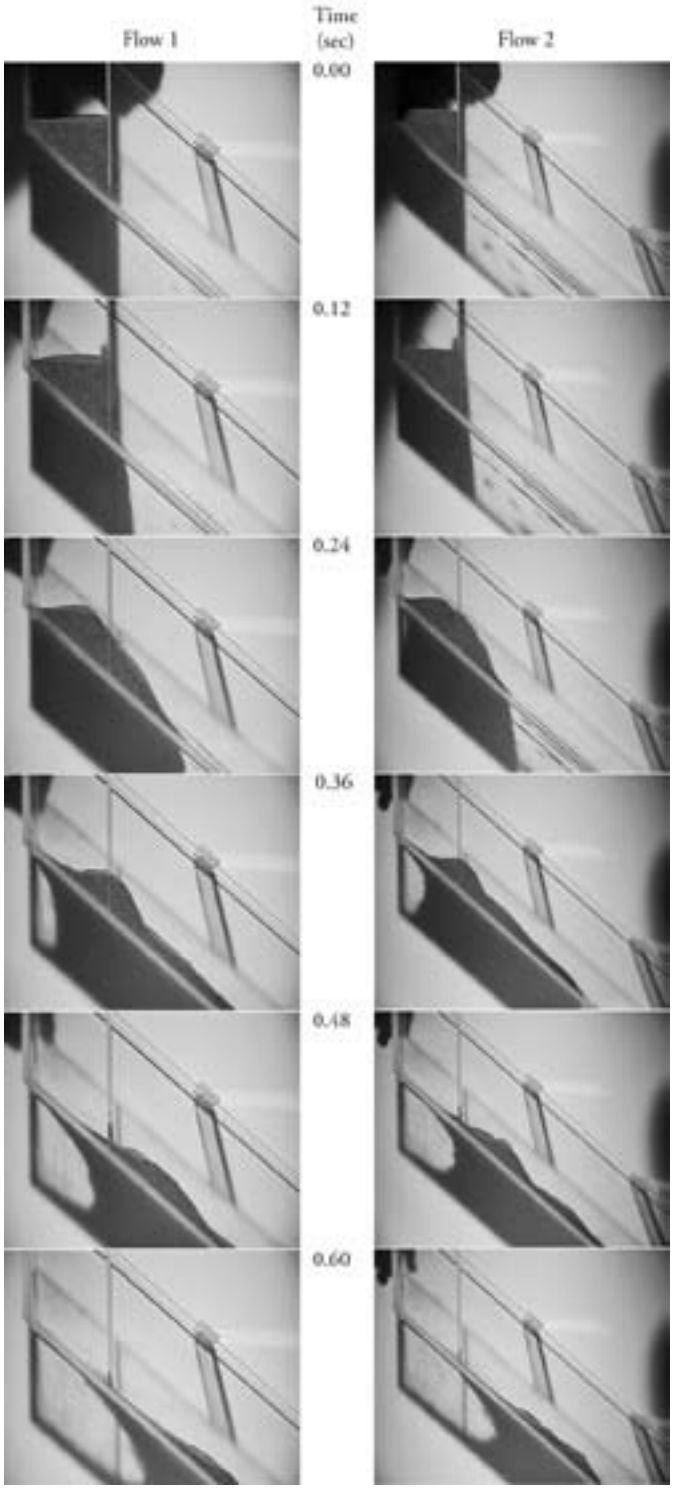

Figure 4.3 Comparison between two identical charges and their development from intiation. Differences are interpreted as a result of both stress chain and random packing features outlined in Chapter 1.4, and difference in frame synchronisation between the two experiments.

The most striking feature of these initiation events is that they appear to maintain relatively coherent units within the flow for some time. There is very little particle movement evident in the upper regions of the flow, where the grains appear to remain stationary relative to others around them. There is very little apparent inflation of the flow which would be necessary to generate true collisional grain flow throughout the media. This tallies with the findings of Faqih *et al.* (2006) who suggest inflation of these dense flows will lie between 10-30%.

As indicated in Chapter 1.4 stress chains and random packing within a static granular pile can have a significant impact on the initiation of a pile. For this reason each experiment behaves somewhat differently. Figure 4.3 demonstrates the differences between initiation of two identical charges. It is clear that the geometry of initiation, and the resulting flow are significantly different. By 0.24 seconds there is a clear second-order difference in the surface topography of the charge as it begins to collapse, with flow 2 showing more complex ridge structures. By 0.60 seconds they appear to have translated into a more uneven flowing surface than demonstrated in Flow 1. It must be considered that some of the variance in Figure 4.3 (and between any time-equivalent frames in other figures) is due to slight differences in the frame timing between the two experiments. Recorded at 25 frames per second, the images may be out of synchronisation

by as much as 0.02 seconds. While this is not significant in the timescales of feature development, it does introduce some error with direct comparison between frames. The degree of variation due to this in comparison to that due to differences in the random packing and subsequent failure of the granular pile is not assessed in this work.

The apparent en-masse behaviour of regions of the sediment pile are difficult to see in any detail using homogenous charge material. In order to better study the behaviour a crude stratigraphy is introduced. Dyed sand, identical to that used in previous experiments, is layered into the hopper. Any deformation of these strata will highlight motion within the charge (Figure 4.4).

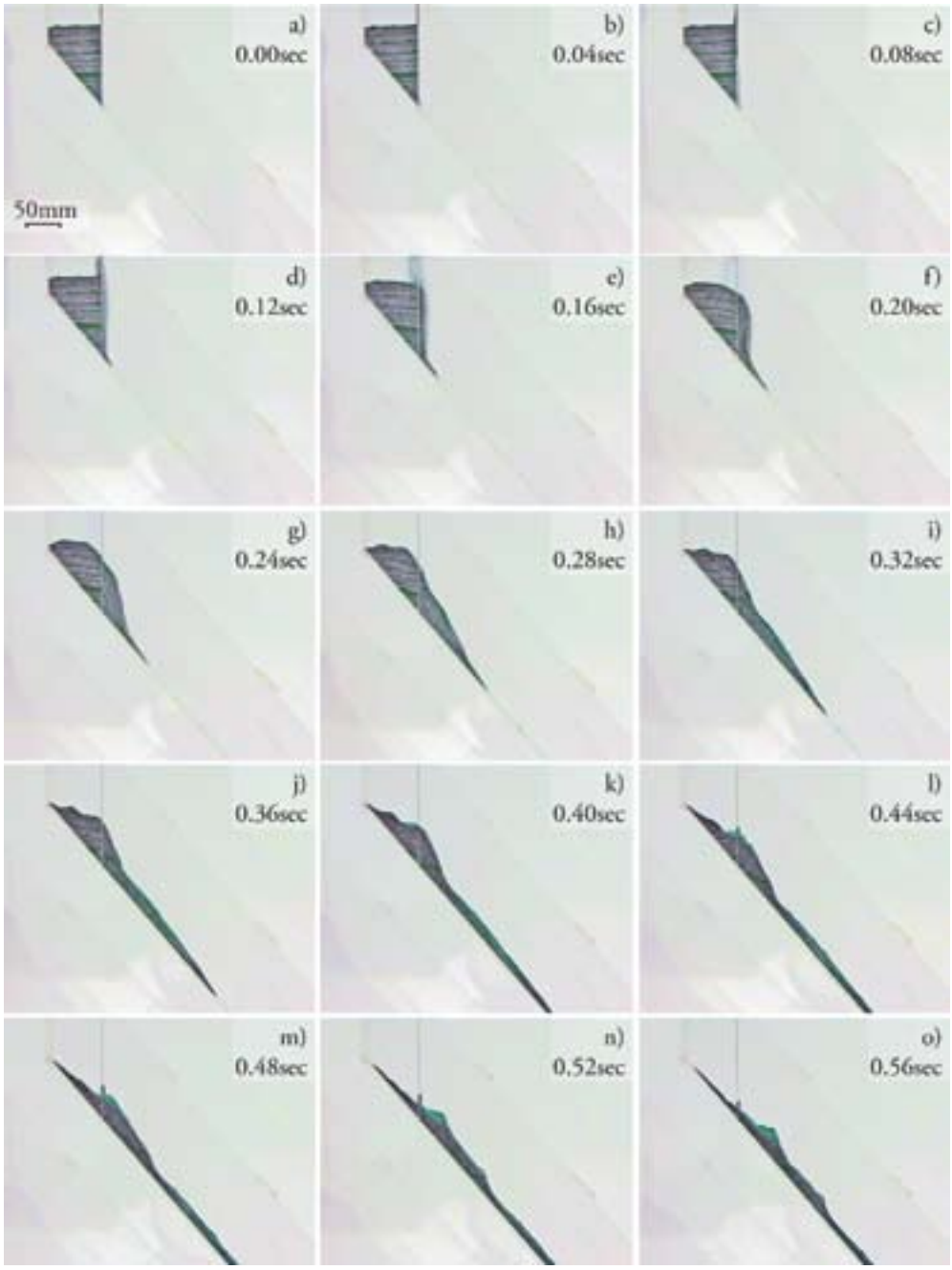

Figure 4.4 Selected de-interlaced images from 200 frames per second footage showing the initiation of a 500ml flow from a static colour-stratified pile from behind a vertical lock gate

The stratified pile grants some insight into the initiation of the sand pile. The downward deflection of the strata in the upper front of the pile (becoming evident at 0.16 seconds after release) shows the gravitational collapse of the unsupported free vertical surface. The lower front has at this point already begun to flow downslope. At 0.24 seconds it is apparent that the front of the pile has uniformly thinned and spilled onto the flume slope. By 0.28 seconds the reduction in overburden pressure has enabled shear planes to develop in the remaining pile. These normal-fault-like planes are first visible as breaks-in-slope on the upper pile surface, then as deflections in the stratigraphy in the pile. By 0.32 seconds these deflections are strongly sheared (Figure 4.5). After 0.36 seconds the resolution of the video images makes it difficult to discern accurately how the flow interior develops, but the topographic development indicates further small shear planes are generated toward the rear of the pile as it continues to move.

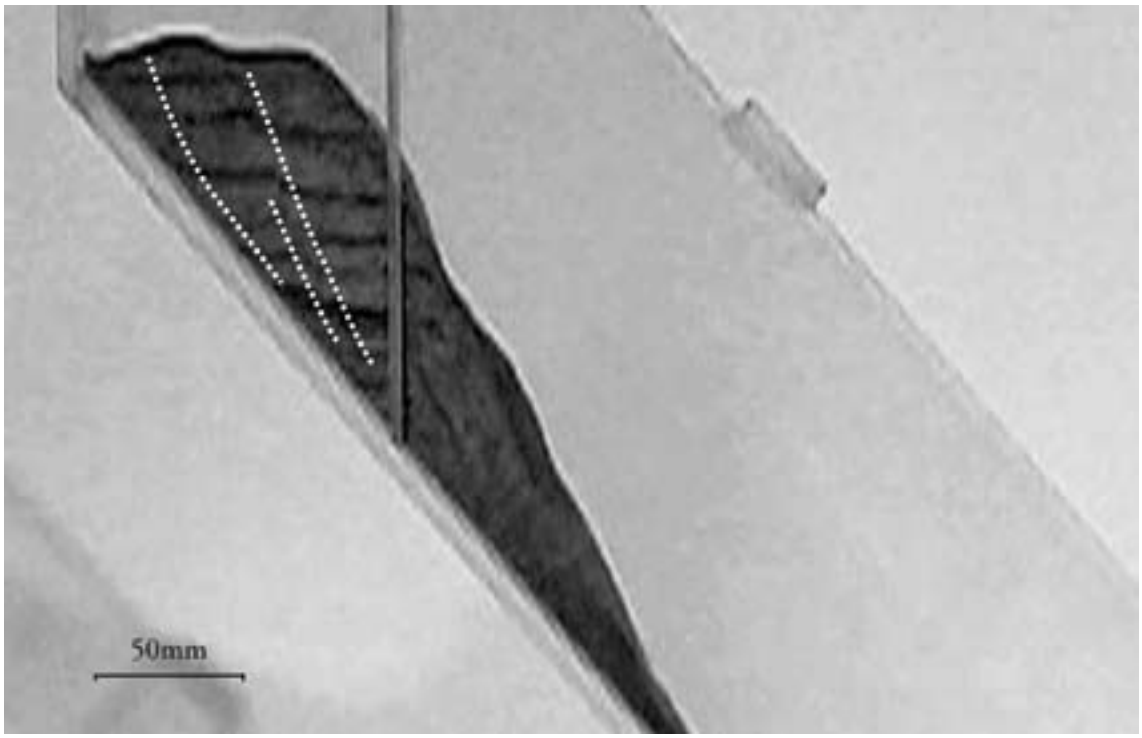

Figure 4.5 Interpretation of shearing regions generated during intiation of flow from a static pile

4.2.2 Increasing basal friction

To attempt to trigger more mixing in the flow the basal friction in the system can be increased by adding a baseplate coated in course sand paper (Figure 4.6). A large stratified charge is used in order to gain information on the internal behaviour of the flow, and any differences which may be apparent in comparison to the lower basal friction model.

The initial stages of the flow are very similar to those of earlier flows. The front pile top collapses down onto the flow initiating from the base of the pile, with a progressive slump forming the front region of the flow. However, it is apparent by 0.28 seconds that the majority of pile failure has occurred. The high basal friction has prevented the rear of the pile from collapsing, and the shear

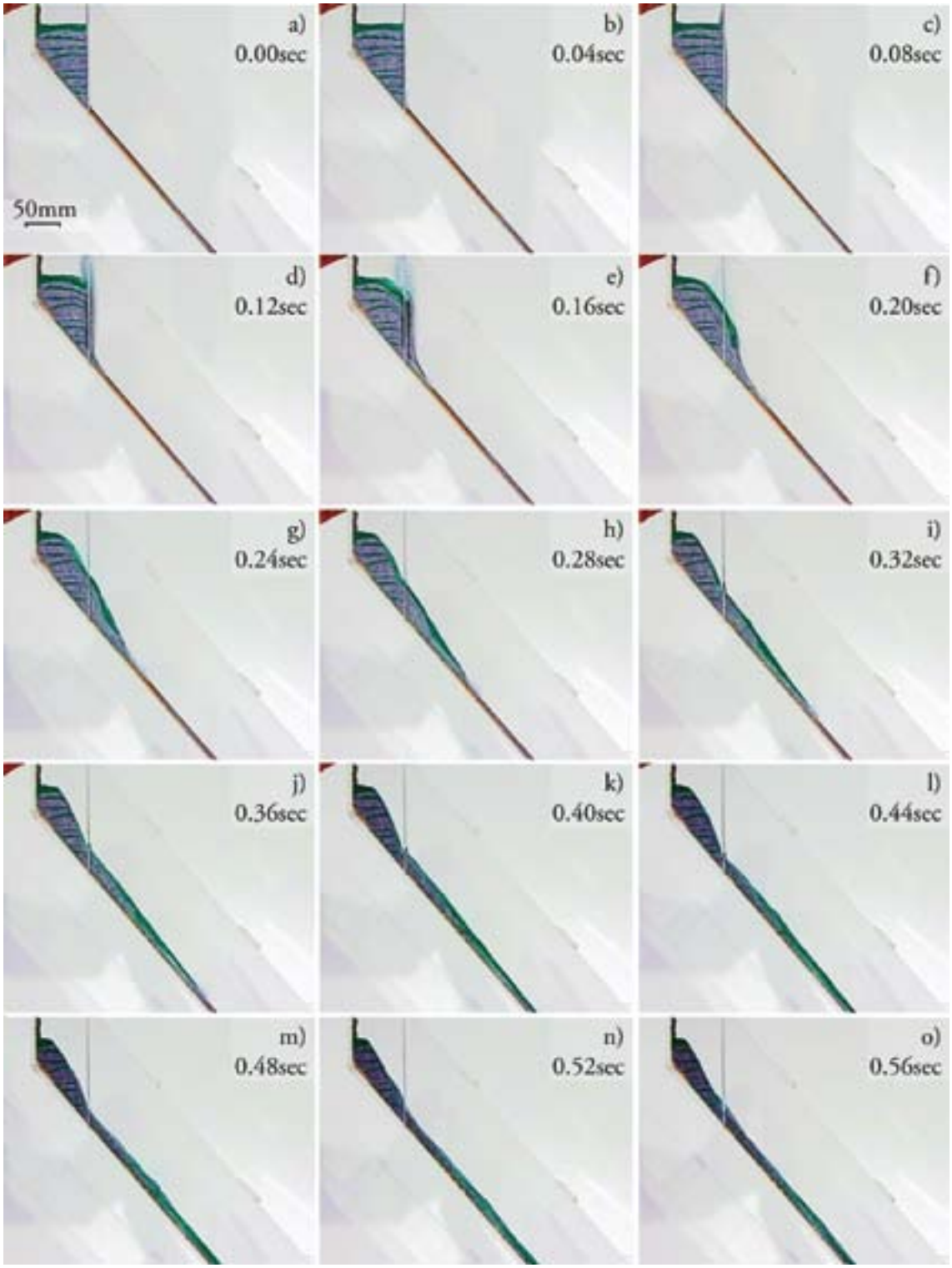

Figure 4.6 Selected de-interlaced images from 200 frames per second footage showing the initiation of a 500cm^3 flow from a static colour-stratified pile from behind a vertical lock gate, running onto a course sandpaper base.

planes which appeared to be instrumental in the collapse of the previous piles are not able to initiate. For the following 0.28 seconds there is a small scale saltating flow from the front of the remaining pile as the surface normalises down to the angle of repose of the material (Figure 4.7).

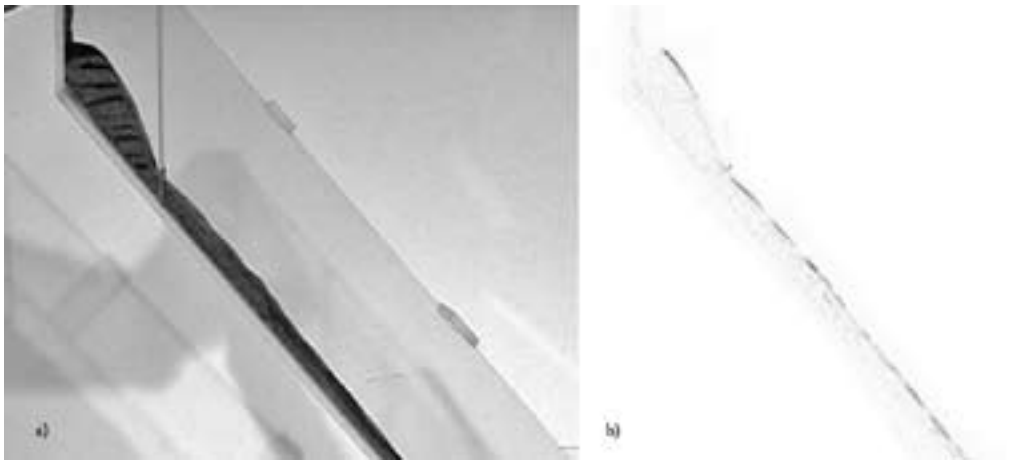

Figure 4.7 a) apparently static pile after collapse of the main flow. b) a difference-comparison image of a) and a frame taken 0.2 seconds later. Dark areas indicate regions which have moved between these two frames, demonstrating the areas of the pile still actively flowing. This method will accurately represent flow from the static pile, but will underestimate flow in the uniformly grey flow on the slope.

Although the precise detail in the flow section is difficult to ascertain from the video stills, it appears that the flow in motion is at least partially mixed. There is an additional feature visible in this experiment which was not apparent in earlier ones; a diffuse saltating 'bow-wave' riding at the very front of the flow (e.g. near centre frame in Figure 4.6g, not apparent in figures 4.1g or 4.4g). This implies that the rough basal surface is disturbing particles in the flow, causing increased mixing.

4.2.3 Drop chute release

Lock gate experiments were able to generate flow when there was very low basal friction. The significant increase in basal friction introduced in later runs had a strong retarding effect on flow initiation from a static pile. In order to assess the mixing within a flow which initiates from a system with pre-existing momentum a simple drop-chute was devised. Charges are identical to those in earlier lock-gate release experiments. To allow for the low visual resolution achievable with the video equipment, coarse layering is used. Whilst this potentially obscures the resolution of internal deformation, it ensures that layers are clearly discernable in these drop-chute experiments where there is rapid vertical movement (Figure 4.8).

Unlike the vertical release gate, the drop chute generates significant charge activation throughout the release action of the gate. As a result, by the time the gate is released fully, the rear part of the charge has reached the slope and begun to flow. At 0.44 seconds it is apparent that the front of the falling pile lands directly onto the flow-front generated by the already flowing rear-charge material. At 0.52 seconds (Figure 4.8n) interpreted and enlarged in Figure 4.9) deflection in the strata indicates that shear planes are again forming to enable the extension of the flow, although the shearing region appears broader than those seen in the previous experiments. In contrast to the shears formed in a

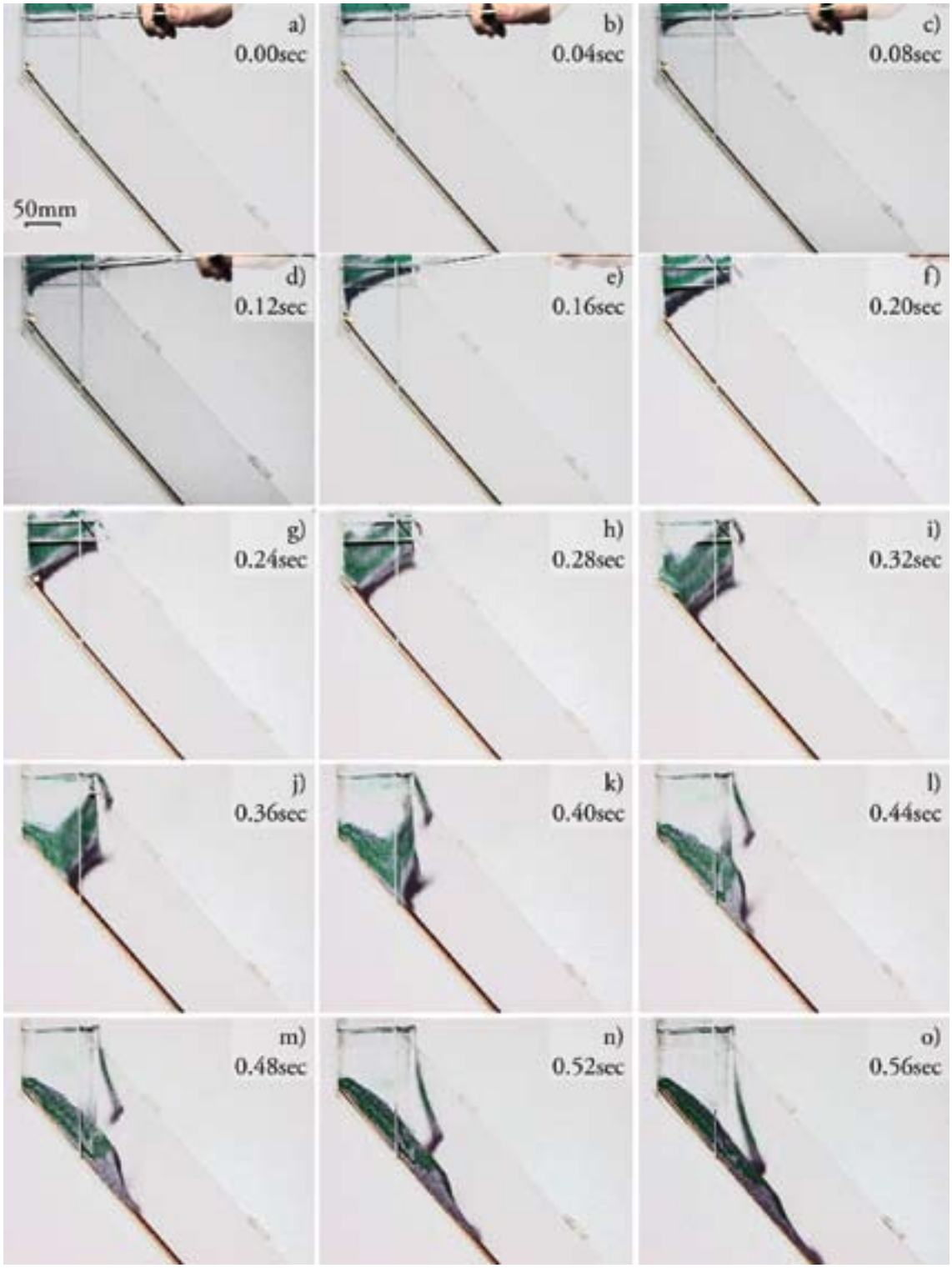

Figure 4.8 Selected de-interlaced images from 200 frames per second footage showing the flow initiation of a stratified 500 cm^3 charge released from a vertical drop chute, running onto a course sandpaper base.

lock-gate release (Figure 4.5) the shear zones are at much steeper angles, with the angles sitting in the range of 60-90 degrees from horizontal. A highly convoluted surface has been generated between the initial sediment to make contact with the slope and the subsequent material, with the shearing zones appearing not to directly interact with this early material.

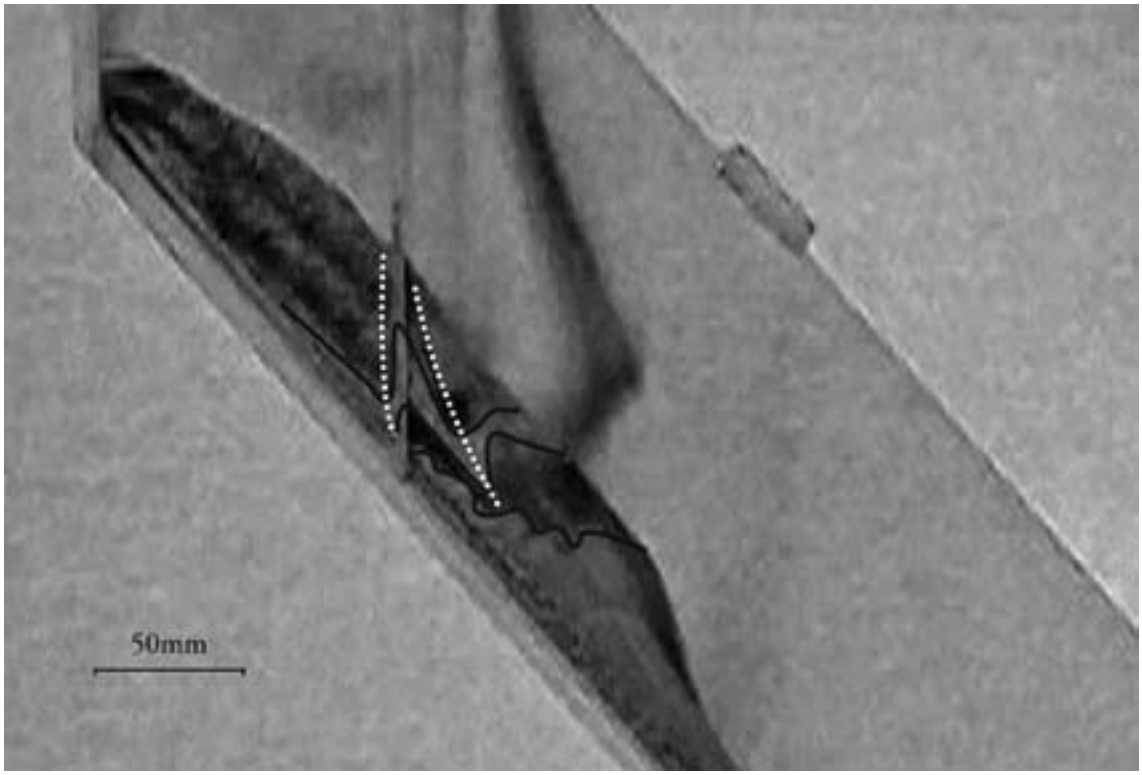

Figure 4.9 Interpretation of flow structure 0.52 seconds after release from a drop chute. The white dashed lines indicate inferred shear regions.

The shear surfaces generated in these experiments can be directly related to those seen in field scale structures seen in granular sedimentary piles. Perhaps one of the best examples of this is in the failure slopes seen in scoria cones (Figure 4.10). While these do not typically collapse into PDC, the lapilli pile is closely analogous to the experimental pile; relatively monomict, with generally good particle sorting. PDC deposits are more poorly sorted, but similar slope failures might be expected. This would provide an excellent mechanism for retrogressive collapse of PDC deposits, remobilising to form secondary PDC - for example the remobilisation at Mount St Helens, 1980 (Rowley *et al.* 1981) and deposit derived PDC from Pinatubo after the 1991 eruption (Torres *et al.* 1996).

Figure 4.10 Section through a scoria cone (El Palmar, Tenerife) demonstrating steeply dipping failure surfaces within the pile.

4.3 Flow

Following initiation it is informative to analyse the development of the charge as it progresses towards the break in slope and subsequent runout. Figure 4.11 demonstrates two time/thickness profiles measured at fixed points down the flume as the charge passes.

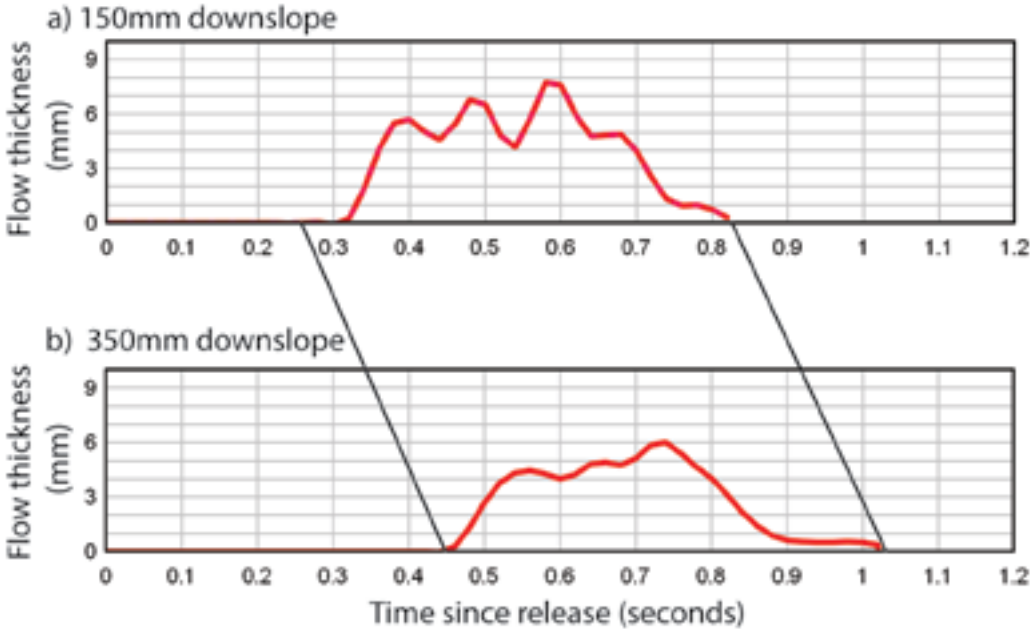

Figure 4.11 Flow thickness at a) 150 mm down-flume of the release gate and b) 350 mm down-flume of the release gate (immediately before the break in slope). Correlation lines between the charts relate the passage of the flow front and the rear of the flow, demonstrating that little or no lengthening of the flow occurred between these points. Irregularities in the flow thickness produced early in the flow are greatly smoothed out by the time the flow reaches the runout surface.

The variations in the flow thickness persist through to the runout surface. The most significant impact on flow behaviour occurs at the break in slope. This sharp boundary between a slope supporting gravitational acceleration, and one triggering deceleration leads to significant thickening of the flow (discussed in the next section). Figure 4.12 demonstrates the behaviour of a 500 cm^3 flow as it encounters the break in slope, as now described.

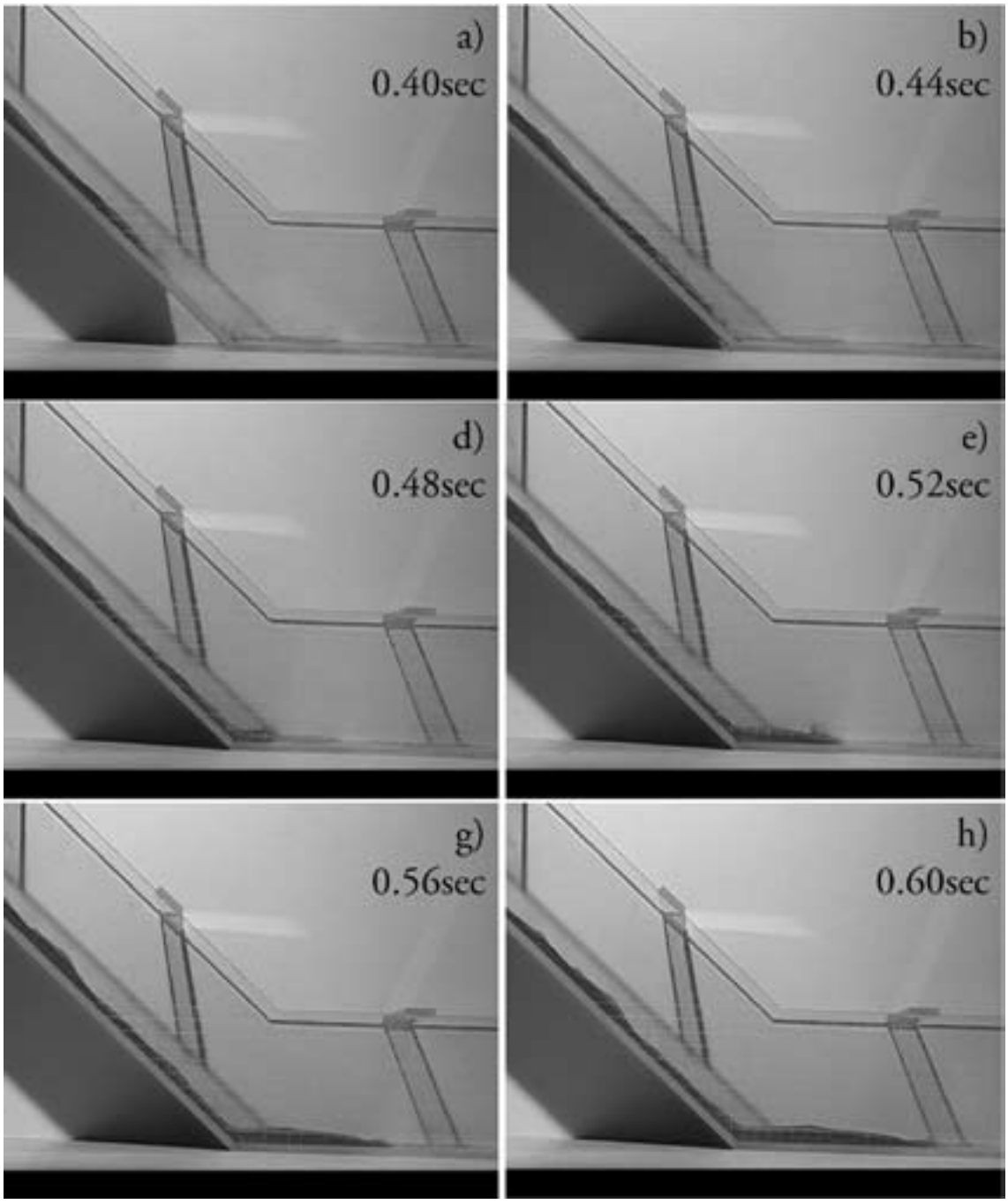

Figure 4.12 500 cm^3 flow propagating across the break in slope

4.4 Deposition

4.4.1 Low basal friction

Figure 4.13 considers deposition of a flow derived from a released static pile such as observed previously in Figure 4.1. Firstly it can be noted that the variations in flow thickness evident during initiation, have apparently become insignificant by the time they reach the break in slope (Figure 4.12 and 4.13). Looking at the region upslope of the break in slope throughout Figures 4.13a-o the only clear change in flow thickness is the initial thickening as the flow head passes, then a continuous flow thickness of approximately 5mm, finally thinning again to 0mm as the tail of the flow passes.

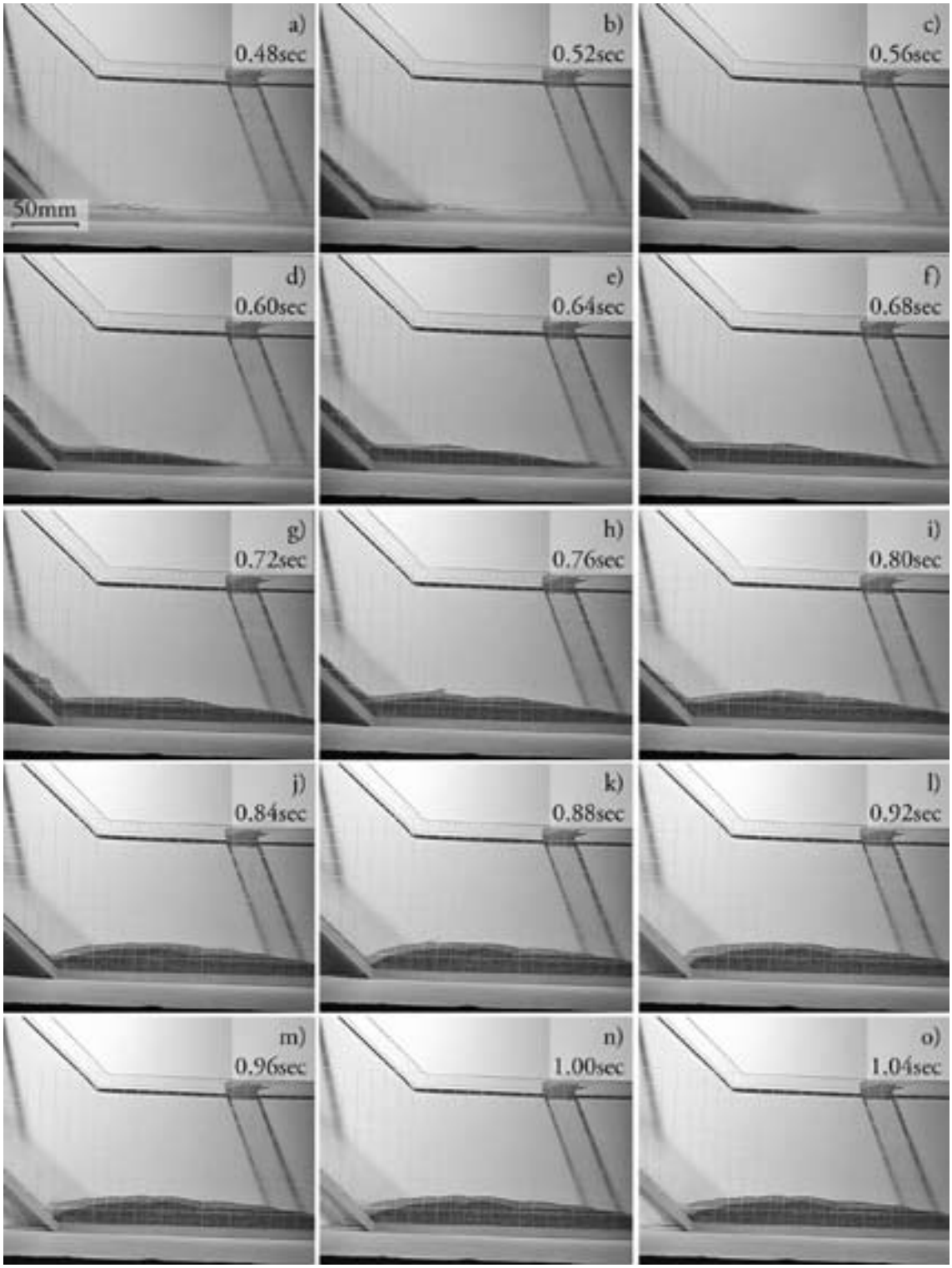

Figure 4.13 De-interlaced images from 25 frames-per-second footage showing deposition of a flow following release of a static pile from behind a vertical lock gate.

It is notable that the transition from flow to deposition in this flume is very rapid, owing to the sudden break in slope. This leads to a granular jump - a system very similar to a hydraulic jump typical of Newtonian fluids (Boudet *et al.* 2007). As flow passes on to the runout surface it thickens to a 7-8mm layer which decelerates as it moves across the runout surface. The flow front velocities (Figure 4.14) show a more complicated trend than might be expected; there is rapid deceleration as the front of the flow crosses the break in slope (a), followed by a period of constant velocity (b). This is probably a result of the thickening of the flow layer, with the momentum of succeeding material preventing the further deceleration of the flow head. By 0.62 seconds the material reaching the break in slope begins contributing more and more to deposit thickening rather than lengthening, and the flow front begins further deceleration (c). After a rapid slowing the flow front extends slowly for another 0.15 seconds (d), before finally coming to a halt (e). The material continuing to flow across the break in slope is now actively thickening deposit. Figures 4.13h and 4.13i appear to reveal an aggrading layer as a forward saltating wave passes across the upper surface of the existing deposit.

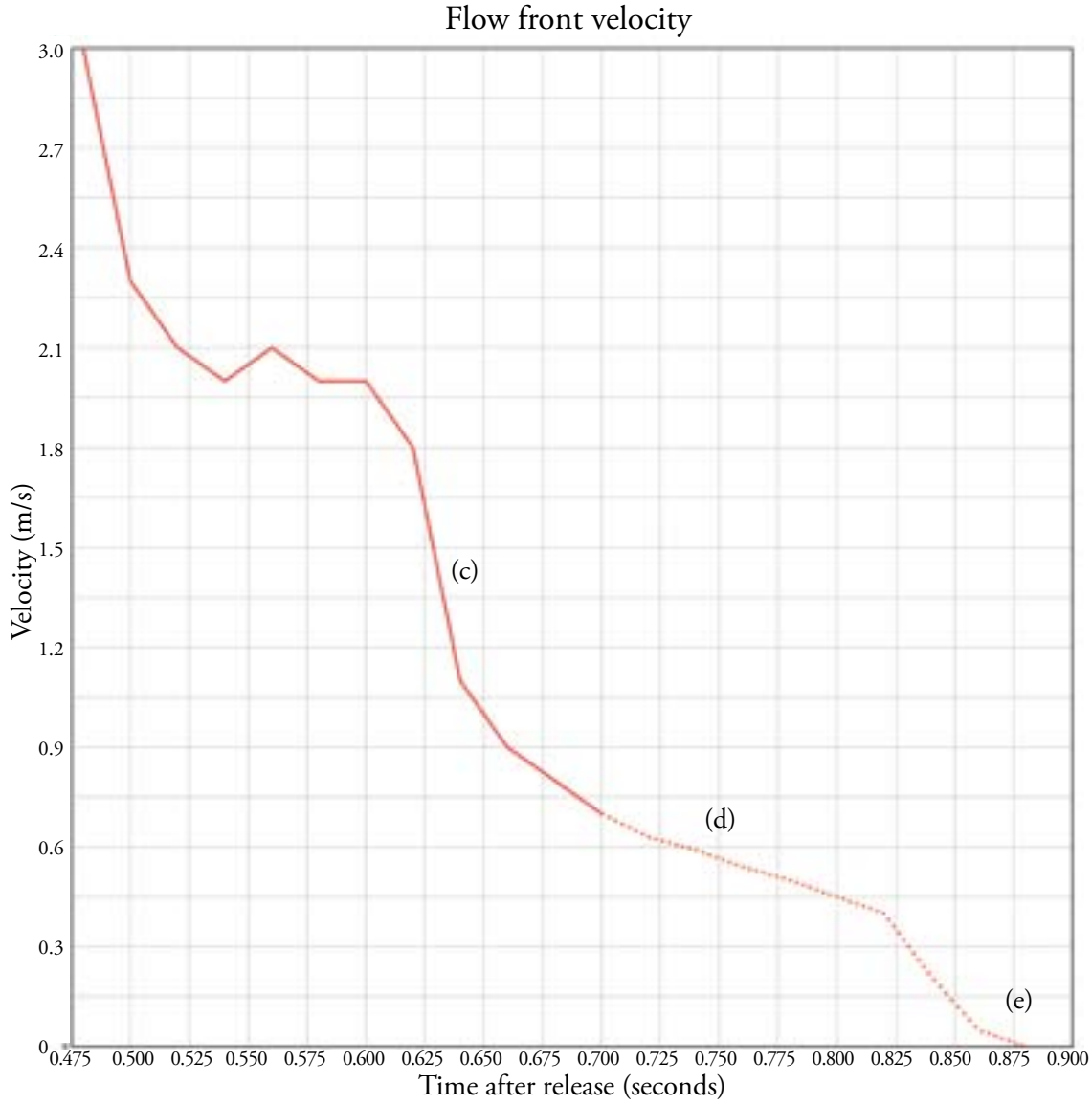

Figure 4.14 Graph plotting calculated flow front velocities between de-interlaced frames shot at 50 FPS of deposition onto a flat horizontal runout surface. Dotted line indicates inferred velocities from in-shot deposit motion when the flow front moves out of frame.

The geometry of a flow is affected by the initiation pile, and activation along stress chains as discussed in Chapter 4.2.1. Individual failure slumps propagating backward through the pile result in pulses of flow being generated. As a result the precise internal geometry of the final deposit is likely to vary in parallel to the variations in thickness and spacing of these pulses within the flow.

The final deposit topography has notable breaks in slope, in contrast to the relatively thin and flat flow "topography" while in motion. Figure 4.13f demonstrates a relatively flat and smooth upper surface as the first flow material begins to come to rest, whereas the deposit topography evident in Figure 4.13o is composed of at least 3 major undulations. These, as well as the apparent velocity differences at various points in the flume during deposition suggest information can be usefully gained from using stratified and coloured charges .

Figure 4.15 shows the deposition of an otherwise identical charge to that used in the experiments shown in Figure 4.13. For the experiment shown in 4.15 the initial charge was stratified. The pulses of colour within the flow, although mixed somewhat during motion down the slope, provide information on how bulk regions of the flow are behaving.

It is possible to trace the movement of individual colour pulses as the deposit forms – for example the pale flow head contacting the runout plane in Figure 4.15b can be seen to remain at the flow head throughout the rest of the experiment. Correspondingly, the dark region which flows directly behind this pale region maintains its relative position and outline throughout deposition. This suggests the flow is moving onto the run out surface as a coherent plug-like flow, with very little mixing between regions, or deformation of the internal flow structure. The thickness of the flow head does not significantly change between Figure 4.15b and 4.15o; i.e. between active flow and deposition. The implication is that flow inflation (granular temperature) is not significant during these experiments. This explains the lack of mixing, as the space between the grains is small and therefore any turbulent/ chaotic particle motions will be minimal.

As the flow head begins to come to a halt (around 0.64 seconds, Figure 4.15e), new flow behaviour becomes apparent. The head of the flow demonstrates nothing other than plug-like behaviour through the sequence. However once this begins to slow, the material still passing from the slope to runout develops a series of stacked over-riding shears. This is most clearly seen in the light-coloured pulse which is starting onto the runout in Figure 4.15g and is subsequently buried by a darker unit which first arrives on the runout surface in Figure 4.15i. This thrust-like stack is clearly evident from the leftward-dipping interfaces between coloured regions in the deposit in the final frame (Figure 4.15o, enlarged and interpreted in Figure 4.16).

The deposit suggests a series of inclined thrust features, associated with ridges on the surface of the deposit, and continuous across the width of the flume. There are indications that the angle of these shear planes steepens as you move towards the proximal end of the deposit.

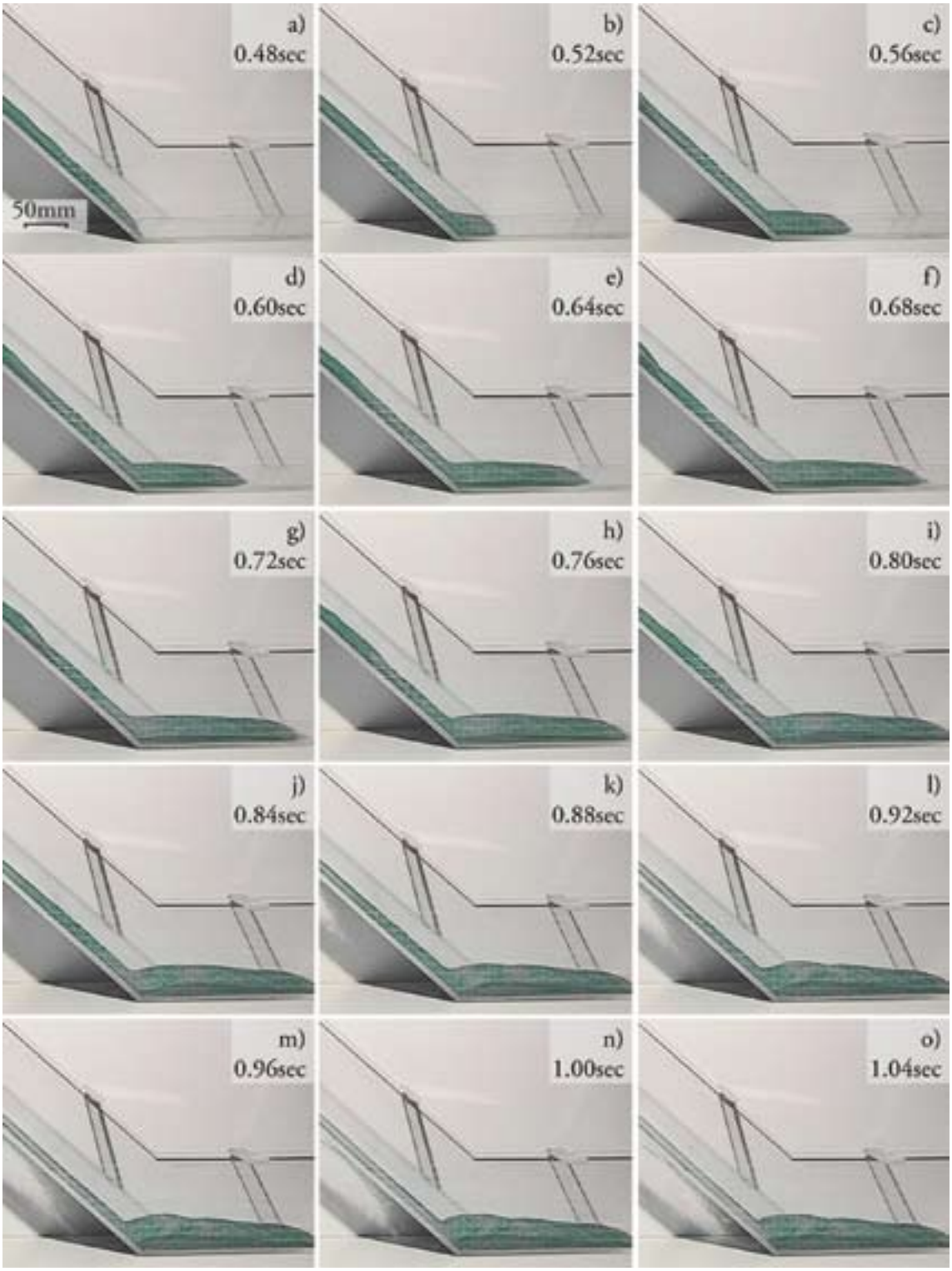

4.15 Image sequence from 25 frames-per-second footage showing deposit of a colour stratified charge onto a horizontal surface. Charge is released from a static pile behind a vertical lock gate.

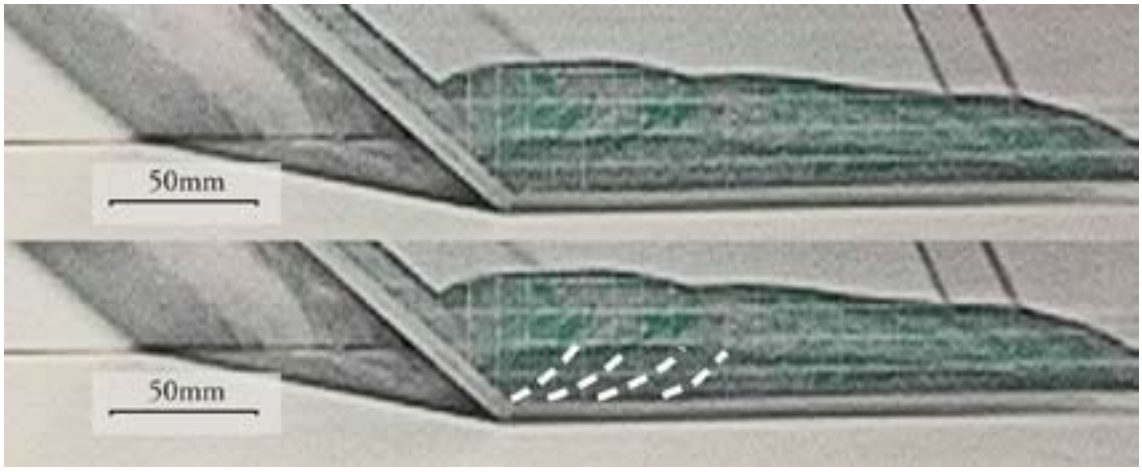

Figure 4.16 Deposit of a colour stratified charge onto a horizontal runout after release from a static pile behind a vertical lock gate. Dashed lines mark inferred shear zones active at various stages during deposition after the flow front decelerated.

4.4.2 Increasing basal friction

Flow deposition with higher basal friction is significantly different. As demonstrated previously (Figure 4.6), lock-gate release only initiated flow in approximately half of the charge, the other half remaining at rest. The resulting deposit is correspondingly reduced in volume (Figure 4.17).

The sequence demonstrates not only the reduced flow volume reaching the runout plane, but also the effects of increased basal friction on this plane; the flow front comes to a halt far more rapidly and closer to the break in slope, leading to the following charge material to build up in a sequence of sub-horizontal wedges, each dipping towards the slope (left of frame).

4.5 Interpretation

Initiation from a static pile appears to be highly reliant on shear-failures (possibly along stress chains) within the resting pile. Following spalling of material from the front of the unconfined, unstable pile, ridges form which appear on the free surface as it begins to flow. These appear to be related to underlying shears forming in the pile, and furthermore are preserved as undulations in the thinning flow, isolating individual micro-pulses within the charge. This implies that internal deposit geometry (and surface features such as ridges) are at least partially (second order) dependant on initiation events. If these shears are related to stress chains (which are products of random packing in granular piles), then there is a significant randomisation in the spacing and scale of features generated by such processes.

A course base restricts the ability of large semi-coherent regions to fail from the static pile, leading to a more continuous flow of grains from the free-surface of the deposit. Shear-failure of the pile is only evident in the early stages of initiation. During flow a rough base retards grain motion in dense flows, resulting in significant proportions of the charge remaining on the slope and not reaching the runout plane. However, the generation of a significant frontal 'bow wave' (e.g. Fig 4.6h) suggests that the irregular surface causes more turbulent mixing when flow dilation is higher.

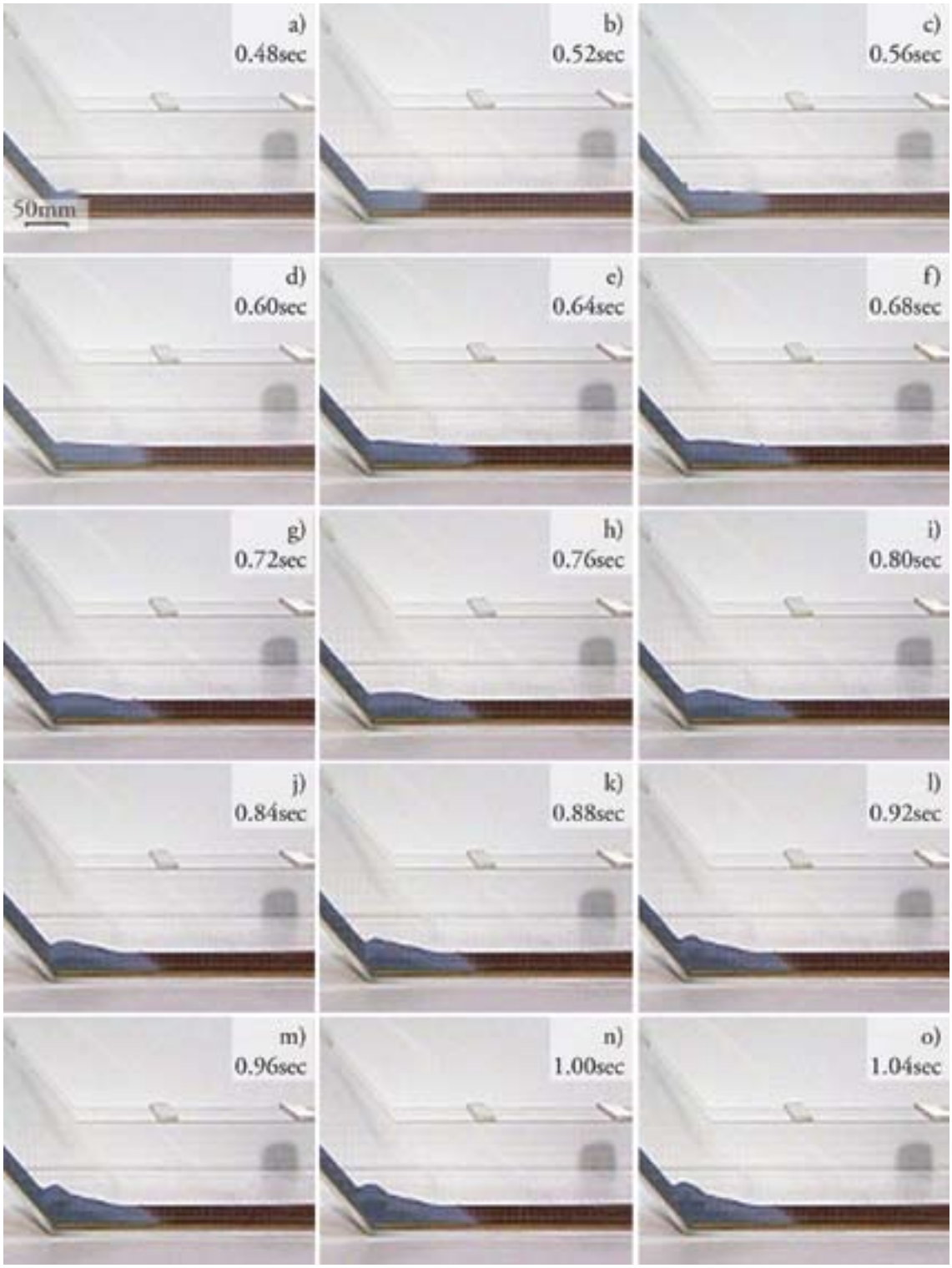

Figure 4.17 Image sequence from 25FPS footage showing deposit of a 500 ml charge onto a course sandpaper horizontal runout. Charge is released from a static pile behind a vertical lock gate.

Small-charge drop flume experiments behave in a similar manner to static pile release experiments in this flume. The charge impacts the flume slope, then proceeds to fail as a coherent static pile. The extra vertical travel above the flume makes direct comparison of initiation speed difficult, but the pile appearance of the drop-chute experiments at 0.40 seconds appears similar to the static pile release

at 0.20 seconds. Unsurprisingly, the flow generated from a drop chute is similarly developed at 0.56 seconds to that from a static pile at 0.36 seconds. This follows from the increased gravitational acceleration inherent within the drop-chute system.

As the flow accelerates downslope it thins, and variations in thickness become less evident. On encountering the break in slope the flow undergoes rapid deceleration and thickening. As the flow front passes along the runout it decelerates to a halt. The material in the middle and rear of the flow continues to transition onto the runout plane, and rides over the deposited material as a series of stacked inclined sequences, separated by distinct shear zones. The base and front of the flow are the first parts to come to a halt, with the proximal upper region the last. This, interestingly appears to have some conflict with the PDC depositional models described in Chapter 1 of progressive aggradation (Branney and Kokelaar 1992) and plug flow (Sparks, 1976). Progressive aggradational deposition would simply aggrade from the bottom upwards, while plug flow would expect to freeze from the front backwards. Both of these mechanisms appear to be at play simultaneously. This appears to correlate to a depositional model proposed by Schwarzkopf *et al.* (2005) to explain the deposits of block-and-ash flows at Merapi, Indonesia. Merapi stratovolcano is the most active volcanic edifice in Indonesia, and is generally characterised by lava-dome activity. Small volume PDCs (e.g. between 0.1 – 0.5 $_{x}$ 10^{6} m^{3} during the 1988 Merapi erupton episode (Schwarzkopf *et al.* 2005)) are often created by gravitational collapse of these domes and spines, leading to it being the basis of the 'Merapi-Type' classification proposed by Williams (1957) - See Chapter 1, Table 1.3. The model proposed by Schwarzkopf *et al.* to explain block-and-ash deposition describes a single flow made up of pulses which rapidly freeze from its front rearward (producing deposits which preserve the flow structure, similar to plug flow), and also from their base upward (similar to progressive aggradation) as a result of energy loss and a reduction in dispersive pressure. The model proposes that subsequent pulses accrete progressively upslope, ramping against or overtopping earlier pulses. Considered as a whole the flow freezes from the distal end first, with each progressive pulse in the flow freezing from the base upward. This description appears to match almost precisely the mechanism observed and described in Figures 4.13, 4.15, 4.16 and 4.17. It seems likely that this apparently anomalous depositional behaviour is a product of small dense flow behaviour. The flume experiments are notably denser, and do not have the fluidisation present in exsolving primary PDC. Merapi-style block-and-ash flows are comprised of dome-derived fragments which do not tend to reach the same levels of vesiculation observed in explosive volcanic events, or exsolve the same amount of gas, leading to lower fluidisation.

4.6 Conclusions

This phase of flume experiments demonstrate that complex behaviour can be observed within relatively simple flume conditions. This preliminary sequence of experiments allows us to assess the validity of the flume and provide a basis for further numerical simulation. Several key observations help address some of the questions posed at the outset:

1. The sidewall friction is significant and even narrow flumes demonstrate significant 3D structure during flow, and hence presumably the deposit

2. The flume design triggers transition from non-depositional flow to rapid deposition due to the sharp break in slope.

3. Failure of the static pile appears to propagate through shear-collapse associated with stress chains in the randomly packed pile, and is therefore not repeatable. The impact of this on overall geometry is, however, second order.

4. Shears formed during intiation appear to be related to pulses within the flow and therefore influence deposition

5. Increased basal friction amplifies the separation effects on the runout, and therefore amplifies the variations resulting from random packing in the original pile.

6. Drop chute release generates structurally similar deposits to pile collapse, and introduces an extra level of complexity in evaluating the development of stratification in charges.

7. Charge deposition resembles aspects of both plug-like (Sparks, 1976) and aggradational (Branney and Kokelaar, 1992) behaviour, strongly analogous to the transport model proposed by Schwarzkopf *et al.* (2005) for Merapi block-and-ash flows.

These observations are vital in informing the design and implementation of future experimental work. Some of the important issues are:

1. Any further flume experiments should be considered 3D models, and hence the deposit must be considered in 3D.

2. The sharp break in slope triggers an artificial deposition, therefore any attempt to consider more continuous PDC-analogue behaviour must use a smoother transition from slope to runout

3. Reproducability of the initiation and flow during these flume experiments can not be considered ideal, and therefore a further sequence of experiments must be carried out to consider the effects on deposit formation

4. Complex 3D depositional structure must be considered, and subsequent flumes should be designed to allow assessment of this structure

5. High friction bases will not be used in subsequent experiments in order to minimise the effects of irregular pile collapse, and focus on sorting during flow.

6. Drop chute releases will be a secondary priority for future modelling, and work will focus on simple collapse from static piles.

7. Depositional behaviour in these experiments is unlikely to reproduce behaviour typical of

sustained currents as a whole, although progressive aggradation appears to be a significant depositional process in the proximal region of the deposits. The depositional mechanism of the flume may be closely analogous to behaviour in smaller volume Merapi-type PDCs ('Type E' PDC in the Branney and Kokelaar 2002 scheme, Table 1.1).

CHAPTER 5: DEPOSIT STRUCTURE AND SORTING EFFECTS

5.1 Introduction

Flume deposition experiments, and numerical models of geophysical systems, are often only considered in terms of the runout and thickness of the deposit produced (e.g. Iverson and Denlinger, 2001). If a greater understanding of granular flows is to be achieved through use of polymict charge deposition, then it is important to gather a dataset of 3D depositional behaviour and sorting of polymict granular systems. This, in conjunction with field-based observations of geophysical flow deposits will offer a level of ground-truthing which is yet to be realised in granular flow modelling (although well developed in other sedimentological systems, e.g. Waltham *et al.*, 2008).

5.2 Sorting and deposition

In order to further investigate the 3D behaviour of the flume experiments developed in Chapter 4, a polymict charge was run. This charge comprised large black (1mm diameter, 100 ml) and small green (0.25 mm diameter, 300 ml) silica glass beads (2500 kg m^{-3})to investigate the effects of size sorting, as well as large white ceramic beads (1mm diameter, 100ml, 6000 kg m^{-3}) to observe the impact of size sorting - i.e. brazil nut effect (BNE) and reverse brazil nut effect (RBNE) detailed in Chapter 2. These materials were selected to act as broad analogues for the three particle populations observed in many PDCs (and the samples gathered at Ngauruhoe, see Chapter 3) - dense lithic clasts (ceramic beads), and large and small less dense clasts to represent pumice clasts, and the ash/lapilli bulk-flow material respectively. The charge was mixed by pouring the beds simultaneously into the hopper, followed by a gentle and very brief stirring. Any greater agitation of the charge led to increased sorting through BNE and RBNE effects.

Figure 5.1 shows an oblique view of the deposit formed by this charge and demonstrates several key features:

1. Distal lobate accumulation of large black silica beads (BNE)

2. Lateral/marginal accumulation of large black silica beads

3. Proximal and basal accumulation of large white ceramic beads (RBNE)

The characteristics observed in these analogue experiments can be extrapolated to features observed in natural PDC deposits

1. Distal accumulation of large black silica beads similar to inverse grading of pumice clasts, terminal pumice dams, and pumice swarms in PDCs

2. Lateral/marginal accumulation of large black silica beads analogous to levee formation in small volume PDC deposits (e.g. Ngauruhoe, Lube *et al.* 2006)

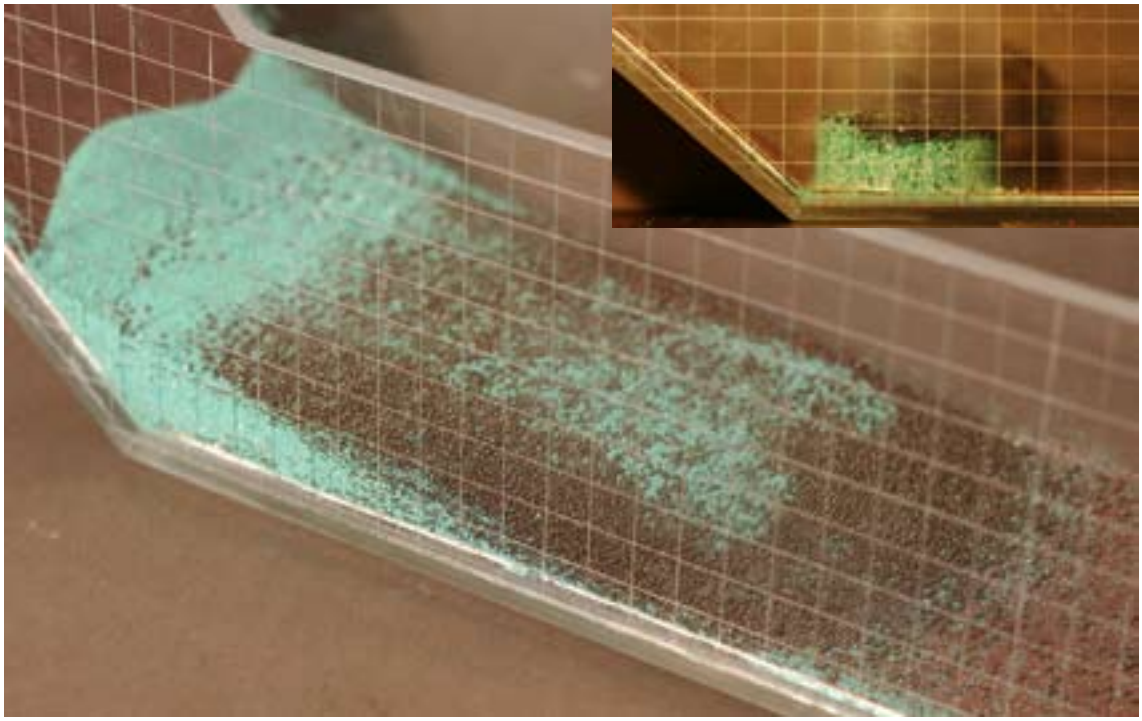

Figure 5.1 Experimental deposit formed by a three-phase granular mixture released from a static pile. The charge was well mixed in the hopper, so all particle sorting is a result of interaction during flow and deposition. inset, detail of crude sectioning showing the centreline internal composition

3. Accumulation of white ceramic beads at the proximal base similar to normal grading of lithic clasts, and their concentration in the proximal extents of PDC deposits.

A setting procedure (detailed in Chapter 3.6) enables investigation of the 3D structure of deposits formed within the flume experiments. This chapter will examine the range of deposits formed by two separate series of flume experiments (outlined in Chapters 3.4 and 3.5). The objectives of these experiments are :

1. to assess the viability of setting and sectioning to give useful 3D information on deposit structure in flume experiments

2. to assess reproducibility of experimental results

3. to investigate particle sorting in polymict charges

Results in this chapter are collated from experiments carried out in Flumes A, B and C (detailed in Chapters , 3.4.1, 3.5.1 and 3.6.1 respectively).

5.3 Surface Topography

Due to the curved transition from slope to runout, different flume material, and lowered slope angle the deposit morphology is different to that seen in the previous flume experiments (see Chapter 4). In order to quantify the flume behaviour, a large series of repeat experiments were conducted in order to understand the reproducibility of these experiments and the scale of perturbations caused by flow

irregularities etc.

Figure 5.2 demonstrates the outline of a typical monomict charge into flume B. There is clear evidence of sidewall friction retarding the flow in both the flow front and rear. By depth-probing at regular intervals along and across the deposit, then recording precise limits of the flow front and rear a good definition of the deposit shape in 3D can be rendered. Repeats of single experiment types demonstrate that the experiments are highly reproducible (Figure 5.2, Table 5.1). The 25-75 percentiles almost all reside within two grain diameters of the median value, although there are fairly wide ranging extreme values demonstrated towards the edge of the flume. The outliers and anomalous data evident in Figure

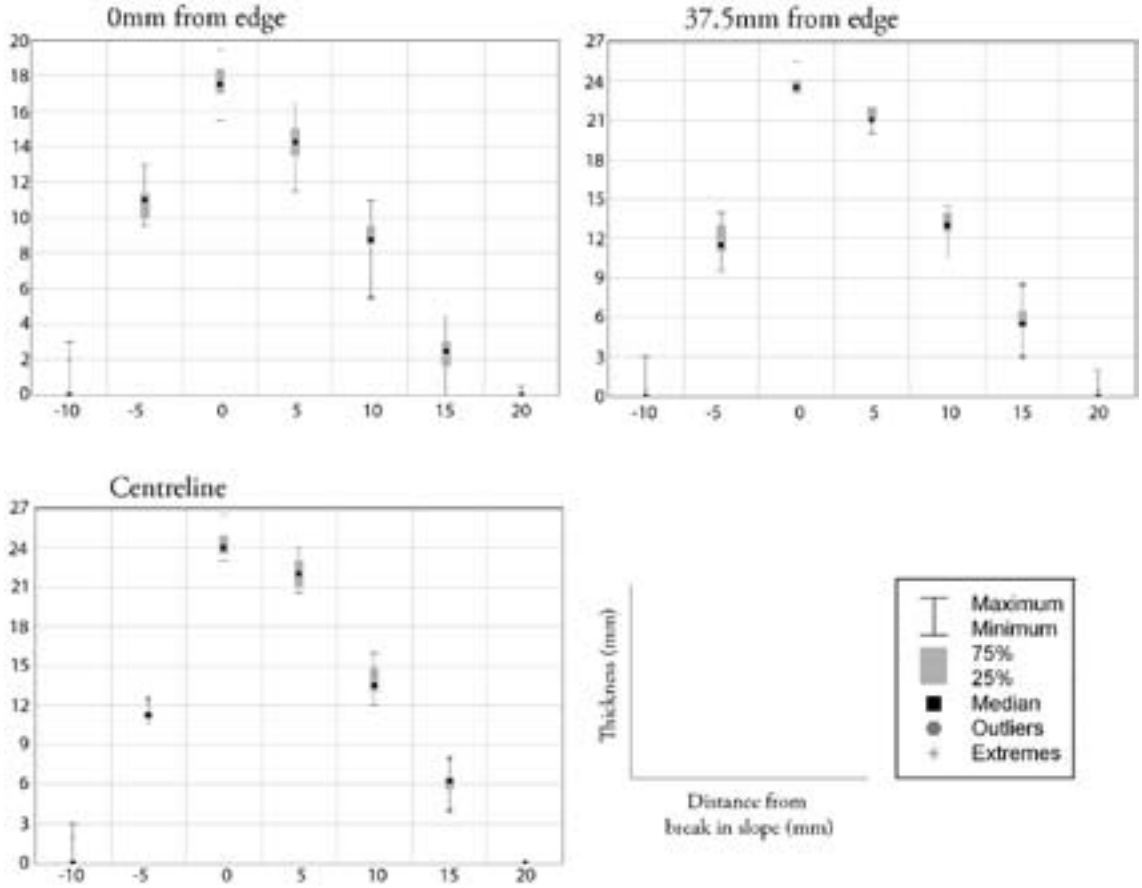

Figure 5.2 Statistical plots demonstrating range of deposit thicknesses in 15 repeats of a single experiment (500 cm^3 monomict charge of 250 micron diameter beads from vertical release lock-gate) in flume B.

5.2 are interpreted as being due to very fine sensitivity of the flume to horizontal levelling between runs. Wedges were used to level the flume as accurately as possible but vibration during charge release is likely to have disturbed this in some situations. The reproduceability of these experiments is inline with the conclusion in Chapter 4 that the affects of initiation from random piles has only second-order effects on the deposit topography. The variation due to charge intiation, while second-order in controlling deposit topography is, however, responsible for at least some degree of the variation seen in the error bars.

TABLE 5.1 STANDARD DEVIATION VALUES FOR REPEAT EXPERIMENTS SHOWN IN FIGURE 5.2

Distance from break in slope (mm)	-10	-5	0	5	10	15	20
St. Dev (mm)							
Centreline	0.929	0.608	0.953	1.100	1.361	1.100	0.000
35.5mm from edge	0.582	1.227	0.725	0.626	0.977	1.150	0.400
Edge	0.884	1.052	1.129	1.294	1.122	1.257	0.136
St. Dev (particle diameters)							
Centreline	3.096	2.026	3.176	3.667	4.538	3.667	0.000
35.5mm from edge	1.939	4.089	2.417	2.086	3.255	3.835	1.334
Edge	2.947	3.506	3.764	4.313	3.742	4.190	0.453
Mean St Dev (particle diameters)	2.661	3.207	3.119	3.355	3.845	3.897	0.596

The data for these experiments shows that even when including the outliers, the majority of standard deviations lie within 2 - 4 particle diameters.

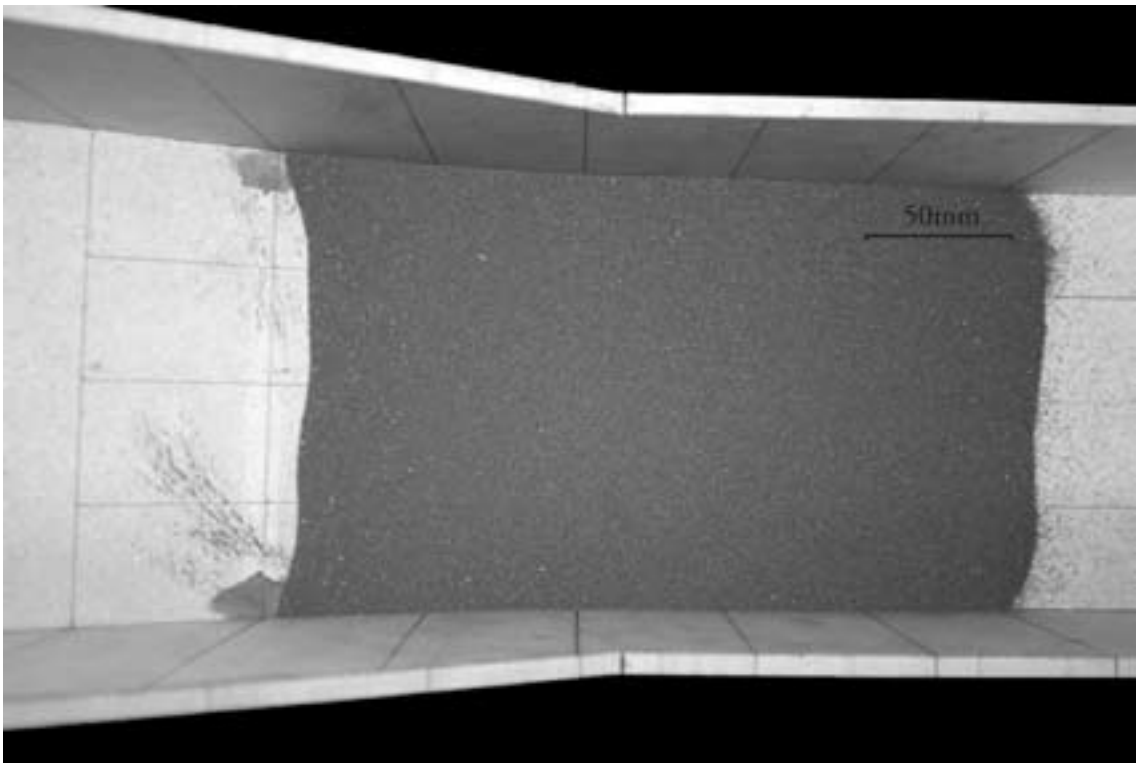

Figure 5.3 Top-down view of a deposit formed by a 500 cm^3 monomict charge in flume B. Grid lines are drawn at 35 mm intervals across the flume width and 50 mm intervals along its length. Break in slope is centre-frame.

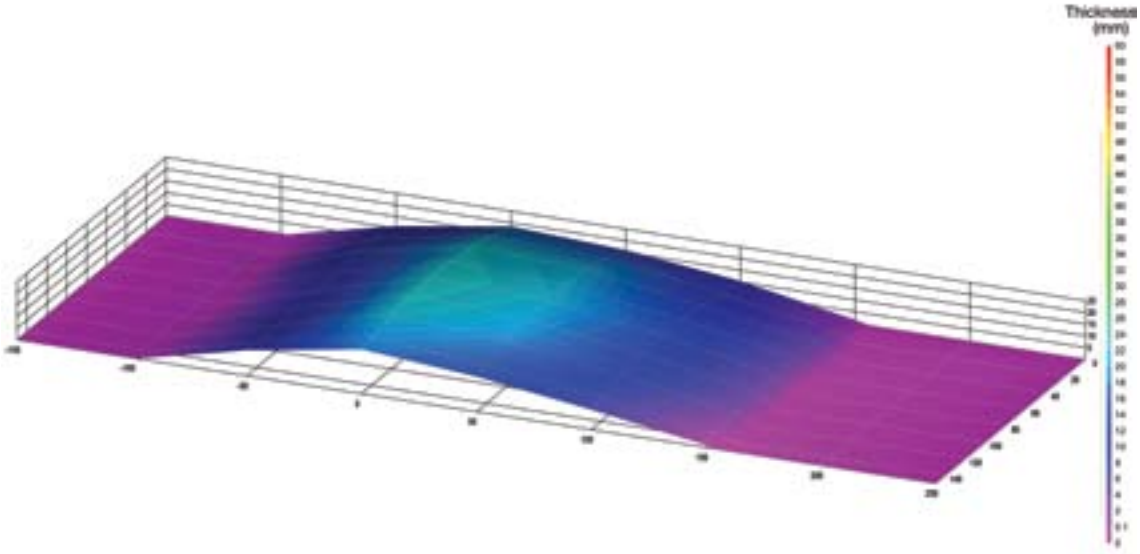

Figure 5.4 3D surface plot of a single experimental charge (500 cm^3, lock gate release, monomict 250 micron beads) in flume B.

A depth profile in 3 dimensions of a single run within this dataset (shown in Figure 5.3) demonstrates the symmetry of a typical deposit (Figure 5.4). The spacing of data points in these particular runs precludes definition of fine-detail surface features, but is a fair representation of the overall structure.

The deposits from these flume experiments are notable for their similarity regardless of variations in charge volume. Each deposit had a steep rear surface at the angle of repose of the beads (28°), concave to the centre. This rises to a high ridge which is marked by local highs approximately 20mm from the flume sides, with lows at the flume edge. The deposit then gently slopes at approximately 5 degrees to the distal toe. The surface on the distal face is marked by very slight ridges created by local flattening and steepening of the slope in ranges between 1 and 10 degrees. These are inferred as being related to front features described in Chapter 3. The centreline deposit profiles of 100, 200, 300, 400 and 500mm volume deposits are shown in Figure 5.5. Precise points of deposit edges and maximum thickness are not plotted, so the extreme proximal and distal deposit slopes will tend to underestimate the true angle of the surface.

The Figure 5.5 profiles support the depositional process observed in previous experiments (Chapter 4). The smaller charges have similar runout, and are not depositing immediately at the break in slope. This implies that deposition was triggered by the fact that the flow-front came to a halt. The front and rear slopes of the deposit are very similar regardless of charge size. Increasing charge volumes simply resulted in deposits with marginally longer distal reach, with the bulk of material depositing proximally, and producing taller piles.

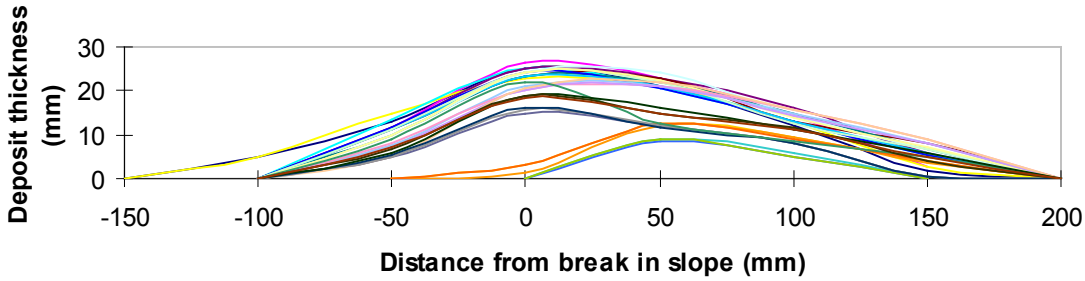

Figure 5.5 Deposit profiles of 30 flume experiments in flume B, using bead charges of volumes 100, 200, 300, 400 and 500 cm^3. Sections are measured down the deposit centreline at 25mm intervals.

5.4 Particle Sorting

The sorting which occurs in granular flows is well studied, and discussed in Chapter 1.5. However, this work is specifically looking at the sorting in flume experiments and the ability of sorting during flow to recreate ignimbrite stratigraphies in deposits. To ensure that sorting features are captured in the deposit, initial polymict charges are mixed to ensure the starting charge is unsorted. All experiments investigating sorting are carried out using beads described in Chapter 2.3 - silica glass beads (250 µm and 1mm diameters, 2500 kg m^{-3}) and ceramic beads (250 µm and 1mm diameter, 6000 kg m^{-3}). Both size and density sorting effects are assessed.

In these sorting experiments the polymict charges are released as homogenised mixed charges. Mixing is carried out in the release hopper. This is done by simultaneous pouring to the bead populations into the hopper, followed by a brief stirring using a spoon. Any further agitation leads to sorting occurring within the charge before release. Once mixed it can be surmised that sorting effects seen in the final deposit occur as a result of real sorting within flow and deposition.

5.4.1 Size

The 'brazil nut effect' (Chapter 2.7.1) suggests that large particles should become reverse graded in a deposit from a polymict granular fluid. A range of experiments were carried out using 250 µm and 1mm diameter silica beads in order to investigate the ability of these short flume experiments to sort the particles, and how that sorting is preserved in the final deposit.

Figure 5.6 shows a top-down view of two of these experiments, (250 µm beads in blue, 1 mm beads in black). The difference between the two is likely due to a combination of;

1. differences in original charge mixing
2. differences in flow characteristics, as outlined in Chapter 3
3. electrostatic effects due to being run in rapid succession (see the 'chains' of particles in Figure 5.6B)

The 'chains' formed at the distal extremeties of Figure 5.6B demonstrate that there is probably at

A

B

Figure 5.6 Plan view comparison of two identical 500 cm^3 polymict charges in flume B

least some elctrostatic effect at work in the flume. This was minimised as far as possible by using wooden flume materials, and ensuring a controlled 35% humidty in the laboratory, however it is clear that even in these conditions at least some electrostatic effect was in action on the glass beads. These effects are minimised by using fresh charges in each experiment, and the minimising of contact and movement of beads before their use in the flume. The fact that these electrostatic features are not present in Figure 5.6A, and only in some particles of Figure 5.6B demonstrates that it is an intermittent problem, and with only second order influence on particle behaviour.

While in some places the large beads are entirely absent, the large particles are clearly concentrated on the upper surface of the flow, but notably have gathered in several specific locations;

1. the flow edges
2. the central rear region
3. the distal toe

The concentration of the large particles in certain regions of the upper surface is surmised to be a

product of the flow motion as it comes to rest. For example, the concentration in Figure 5.6b running across the deposit at the distal end would appear to be related to the geometry of a flow front, as discussed in Chapter 3, the shape deliniating the surface expression of individual thrust fronts as shears develop in the deposit.

Setting and sectioning of this deposit in 5b reveals the extent of BNE sorting. Figure 5.7 shows cross sections through the deposit; Figure 5.7a at the edge of the deposit, and Figure 5.7b at the deposit centre. While there are some large beads in the centre of the deposit, the vast majority have migrated to the upper surface. The internal deposit does not demonstrate any further structure. The edge deposit has a more gradational transition in sorting more typical of normal grading in ignimbrite deposits. The absence of this gradational change in the internal sections implies sidewall effects have been significant in the development of this feature.

Figure 5.7 Sections of the deposit edge from Figure 5b, a) at the deposit edge, b) at the deposit centre.

The appearance of large particle sorting is somewhat different when Flume C is used despite an identical charge. As Figure 5.8 demonstrates, the distal toe has only a small proportion of large beads on its upper surface. In fact, this appears to be a result of saltation on the flume base; approximately 50 g of large beads in this run were recovered from the end of the flume. The sloped smooth runout seems to have encouraged the frontal flow region to pass unhindered, with only the following collisional flow region losing energy sufficiently to come to rest on the runout channel. The large particles quickly sorted to the upper front of the flow, and were not restricted by a break in slope as seen in flumes A and B. As a result, the majority of large particles preserved in the surface of the deposit are towards the central region, analogous to the proximal surface rafts seen in Figure 5.6.

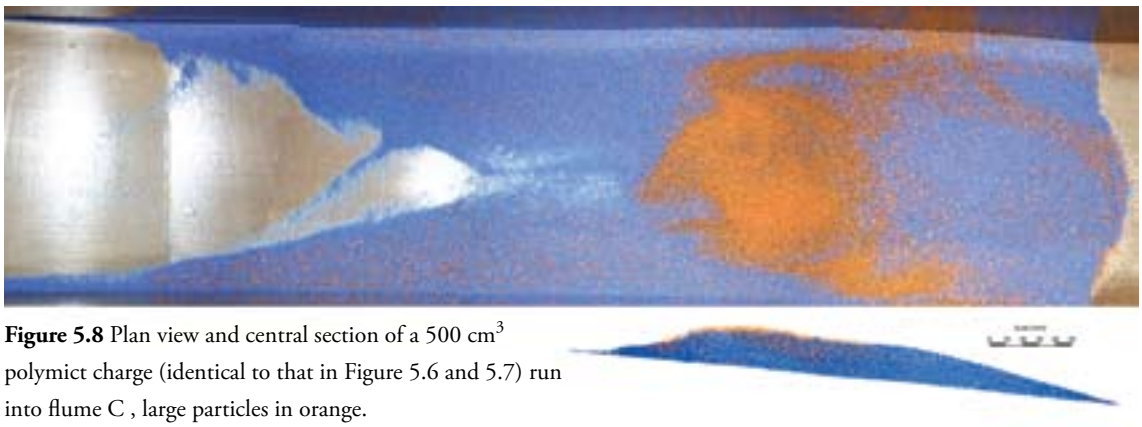

Figure 5.8 Plan view and central section of a 500 cm^3 polymict charge (identical to that in Figure 5.6 and 5.7) run into flume C , large particles in orange.

5.4.2 Density

To investigate density sorting in the flume a series of ceramic beads were used alongside the silica beads from earlier experiments. The ceramic beads are of the same diameter as the silica beads to ensure that density sorting within the flow is considered separately from RBNE effects. Due to the high cost of the ceramic beads these experiments were only conducted in flume C.

The deposit represented by Figure 5.9 (100 cm^3 of white ceramic beads, and 400 cm^3 of blue silica beads) has a similar morphology to that seen in monomict charges, indicating that particle homogeneity has, in this case at least, had no noticeable effect on deposit surface topography. In contrast to this, there is significant internal geometry highlighted by the polymict nature of the charge. Previous high speed footage has indicated that dense particles rapidly settle to the base of the

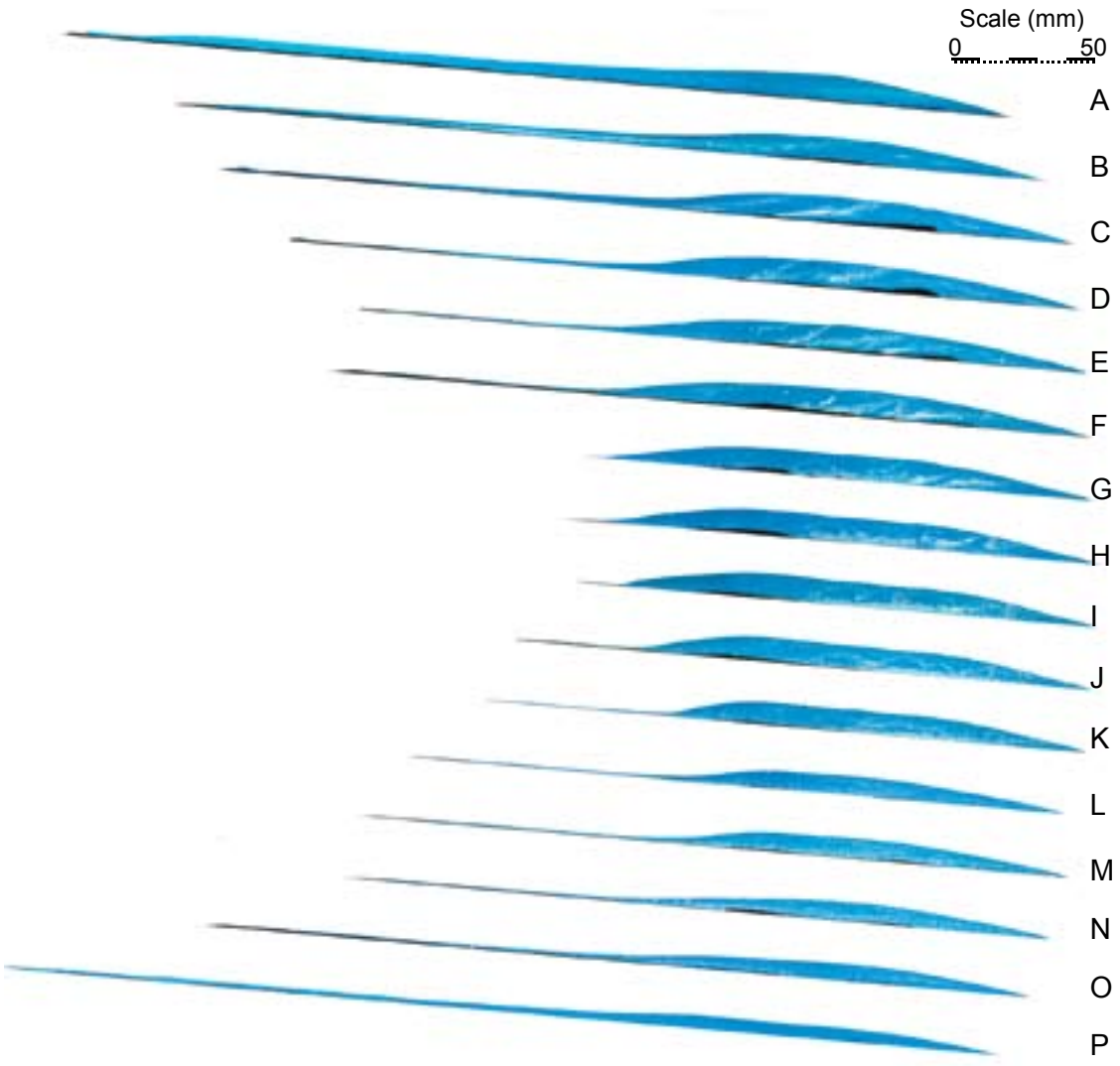

Figure 5.9 Edge to edge sequence of serial slices through a 500 cm^3 charge containing 100 cm^3 of white ceramic beads, and 400 cm^3 of bue silica beads run into flume C. Flow left to right. High concentrations of ceramic particles (white) are concentrated at the base of flow units, with the rear-dipping concentrations inferred to be related to individual 'thrust' fronts as the deposit built up (see Chapter 4.4).

flow (Figure 5.10), so ceramic particle concentrations would be expected at the base of the deposit. While this is indeed the case in some regions (e.g. the central/distal region of slice h), there are striking internal concentrations of ceramic beads, frequently with dips back towards the slope. These appear in some places to be slightly 'smeared' (e.g. slice c), and in other places across the flume develop undulose deformations (e.g. slice j). These concentrations are frequently stacked upon each other in what appear to be dipped successions (e.g. slice e), and are inferred to be the internal representation of thrust-like stacks observed during the aggradation of these flume deposits (see Chapter 4.4), in line with the Schwarzkopf *et al.* (2005) model proposed as dominant in these experiments (Chapter 4.5). This allows us to interpret individual pulse thicknesses in the deposit (5-10 mm) and the angle at which they sit on the underlying substrate (0-30 degrees). Pulse stacks as demonstrated in slice e of Figure 5.8 indicate that the early pulses come in at low angles (0-5 degrees), with later thrusts forming at increasingly steep angles.

One of the striking features of the density separation evident in all of the experiments is the increased concentration of dense particles in the centre of the flume, with relative depletion at the sidewalls. This is clearly demonstrated in Figure 5.9, where there are few white dense particles in slices a and p,

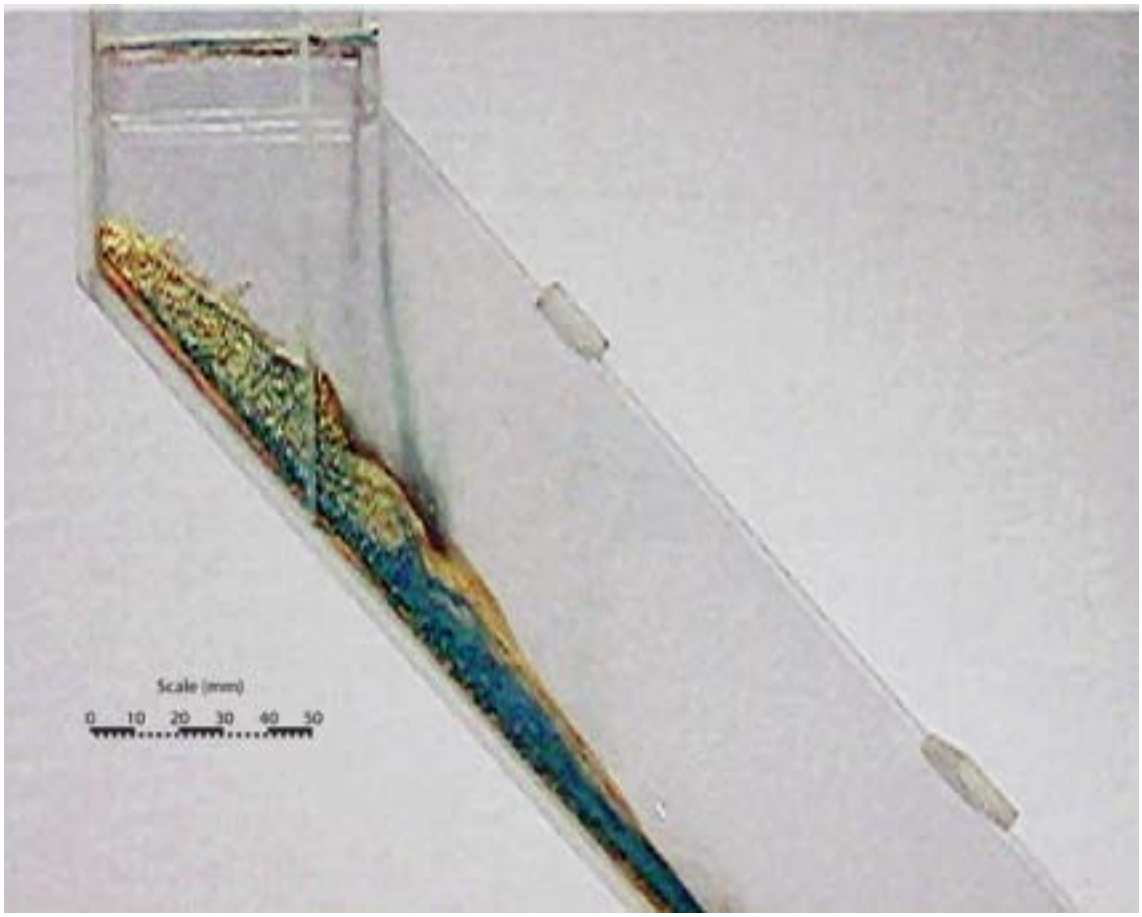

Figure 5.10 Single frame from 50FPS video footage of a 500 cm^3 mixed polymict charge (200 cm^3 yellow vermiculite, 300 cm^3 green sand) 0.72 seconds after initiation from a drop-chute onto a rough basal surface (See Figure 4.8). Rapid particle sorting is observed as the pile initiates to flow on the slope. Once the material has traversed 30 mm beyond the initial collapse pile front (e.g. Figure 4.8l) it is fully segregated and behaving as a two layer flow.

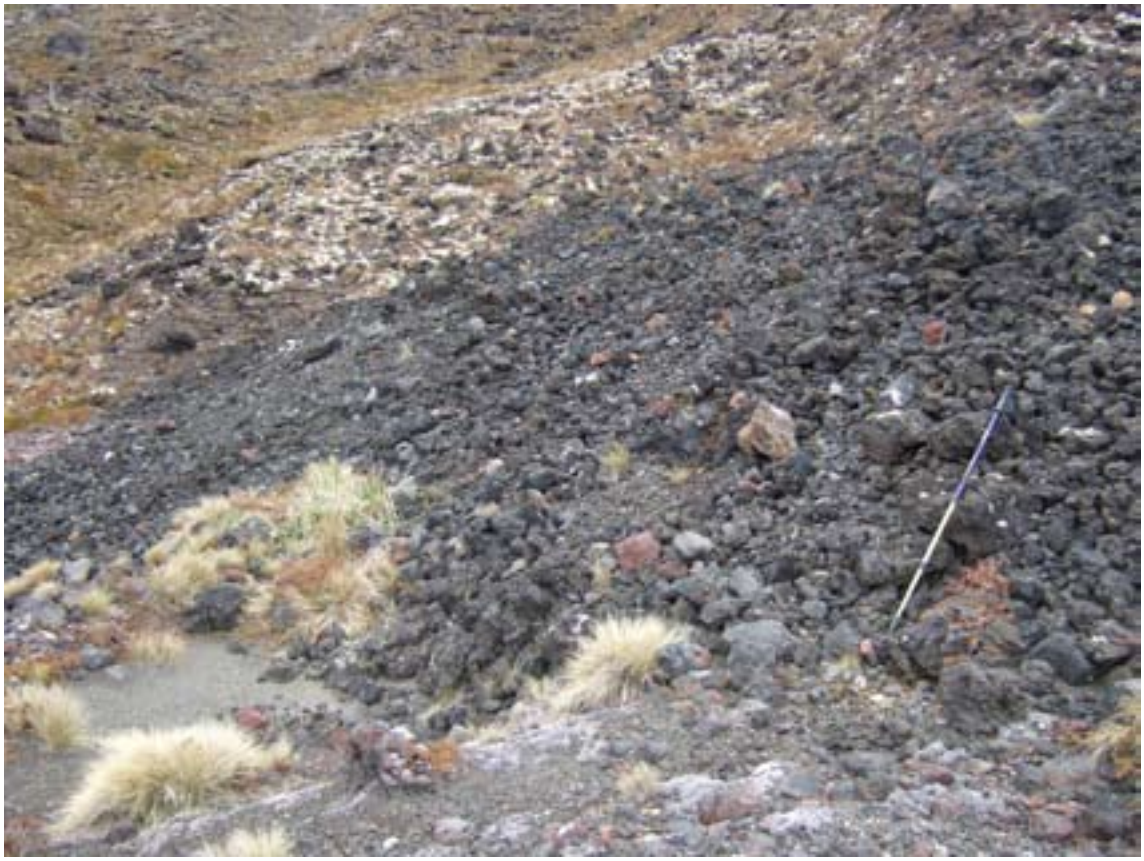

Figure 5.11 Distal lobe front of a Ngauruhoe 1975 flow. Highly clastogenic surface, represented by Sample PRNg6-01, while underlying material is typical of PRNg6-02 (see Chapter 3.2.2).

with increasing concentrations towards the centre of the deposit.

5.5 Interpretation

Particulate sorting in these flume experiments is extensive, demonstrating BNE of large particles, with RBNE sorting of large dense particles. These patterns are similar to normal grading of lithic clasts, and inverse grading of pumice clasts in many massive ignimbrite units. In addition, the lateral concentration of large buoyant particles may be analogous to the levees formed in small volume PDC - for example the 1975 deposits of Ngauruhoe, New Zealand (Lube *et al.* 2006). Levees of large particles in small volume PDCs can be seen to form in both confined and unconfined runout areas (see for example Figures 3.4, 3.5 and 3.7). Additionally these particles concentrate on the upper distal surface of deposits, often highlighting apparent flow pulses. These may be related to rafts in ignimbrite units, or the terminal pumice dams at the distal toes of smaller volume PDCs (e.g. Figure 5.11). In contrast, the lithic particle charges tend to concentrate in the central proximal region of the deposit.

Vertical dense particulate sorting follows that expected by granular segregation, with dense particles settling to the basal region of flows and subsequent deposits. These dense basal zones also appear to highlight individual thrusting/aggrading pulses in the deposit. These further support the supposition that deposits within these flume experiments are accumulating in line with the model proposed by

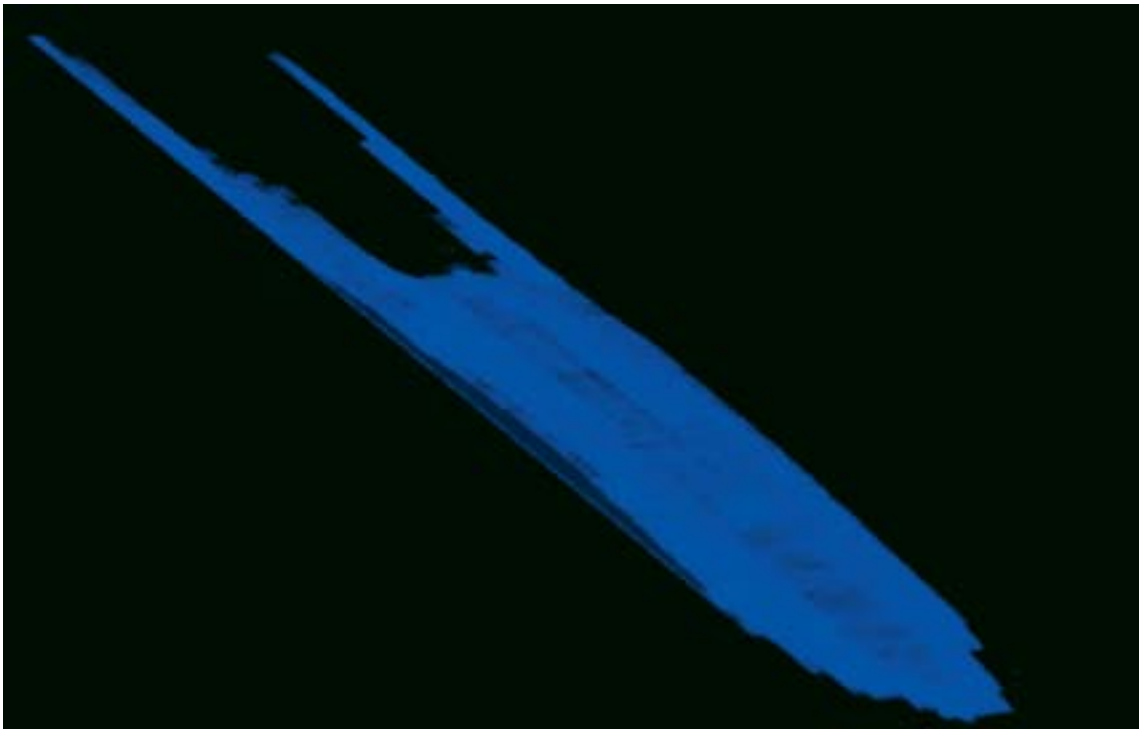

Figure 5.12 3D volume visualisation constructed from 2D slice thicknesses of a 500 cm^3 charge. Long 'tails' of deposit are left in the corners of the flume, with a short deposit length in the centre.

Schwarzkopf *et al.* (2005)(Chapter 4.5).

The patterns of density sorting laterally across the flume and deposit are inferred to be a product of the loss of flow energy at the edges of the flow as it traverses the slope. As the flow front (which is depleted in dense particles) moves, it leaves a slow-moving trail of material in the corners of the flume. These slow moving regions channel the following flow into the centre of the channel, leading to a concentration of dense particles in this region when polymict charges are run. This would also account for the subsequent morphology of the deposit, with long 'tails' at the flume edges, and a relatively short deposit length in the centre line (Figure 5.12). This central region of the flow, rich in dense particles must also develop greater momentum than the bulk flow closer to the edges, perpetuating this pattern throughout the length of the flume.

5.6 Conclusions

Setting and sectioning of flume deposits appears to be a very useful method to assess the 3D internal structure. Revision of the technique (described in Chapter 3.6) allowed the section thicknesses to reliably be brought down to 10 mm when the largest particle sizes were used (i.e. 10 particle diameters). The detail captured in these small scale experiments is quite striking in its resolution and detail, and certainly validates the use of this technique in the future.

In terms of experiment repeatability, the flumes are capable of producing self similar results when carefully managed. They are strongly sensitive to slope, resulting in strongly asymmetrical deposits

when this is not accounted for. Simple levelling of the apparatus before use using suitable wedges eliminates the issue, resulting in repeatable geometries. The reproducibility tests returned standard deviations in deposit thickness of between 2 and 4 particle diameters, even with some extreme outliers due to poor levelling early on.

The particle segregation demonstrated in this flume occurs in all three dimensions. The vertical segregation of large and dense particles is in line with that seen in the literature for granular flows, demonstrating BNE sorting of large particles and normal grading of dense particles. The rate at which this sorting occurs is very rapid, appearing to sort to a significant degree within a few tens of centimetres travel, and within half a second of flow initiation.

The lateral and longitudinal sorting are products of the vertical granular segregation, in conjunction with the flow and depositional patterns within the flume. Lateral depletion of dense particles and concentration of large particles is inferred to be a product of sidewall friction channelising the dense particles. This rapid moving central region then concentrates the large particles to the edges and flow front. As the flow reaches the runout surface these sorting effects are preserved, with distal toe and lateral concentrations of large particles, and basal ventral concentrations of dense particles. Internal concentrations of the dense particles are created by sequential pulses of flow running over each other, each of these pulses comprising a dense base and less dense upper region. This observation is in line with the flow trajectories witnessed by Felix and Thomas (2004) in unconfined granular flows, where tracer particles were seen to travel fromt he flow surface to the flow edges, to subsequently be overtaken by the axial flow.

Several stacked pulses observed in these experiments appear to have quite complicated shear deformation preserved in them; for example the undulose morphology of the dense regions in Figure 5.9j, and the apparently splayed layers in Figure 5.9c.

In summary and to answer the stated aims at the start of this chapter:

1. The setting and sectioning method is practical, and highly capable of producing meaningful and valuable data on the internal geometry of flume deposits.

2. The repeatability of the flume experiments is excellent, subject to careful set up.

3. Granular sorting mechanisms within the flume are in line with those represented in the literature. however, the patterns and behaviour of flow within the flumes has significant impact on the emergence and expression of these sorting phenomenon within the final deposit.

There are several questions raised by this series of experiments:

1. Is the deposit partially aggrading as indicated by the dense layer stratification?

2. How does the deformation of the dense layer stratification develop?

3. Can these flumes be used to model more PDC-typical sustained or pulsed flow events?

4. How do these deposits respond to subsequent pulses of flow?

In order to answer these the experiments will be extended to investigate the contacts and interaction between a flow and a granular substrate.

CHAPTER 6: REWORKING BY SHEARING GRANULAR FLOW

6.1 Introduction

In previous chapters it has been shown that the flumes generate complex 3D internal geometry, and that the setting procedure has proven reliable in preserving small single-charge packs. In this chapter the method is developed to investigate:

1. The interaction between sequential granular charges using these flumes
2. The nature of contacts between sequential charges
3. The nature of contacts between charges and stratified substrate
4. The occurrence and extent of reworking of substrate material by sequential and overpassing flows
5. The behaviour of granular sorting mechanisms (see Chapter 5) in reworked systems
6. The ability of the setting procedure to preserve thick multi-charge packs.

PDC deposits observed in the field frequently show erosion of the underlying substrate (e.g. Brown, 2003). Furthermore, a study by Dufek, Wexler and Manga (2009) has shown that momentum transfer from one layer in collisional grainflows allows for pick up and transport of particles from loose substrates. The procedure developed in this work is ideal for interrogating the deposits formed by these interactions, using multi-component and variously coloured charges to identify contacts and geometries in simple and more complex systems.

6.2 Initial experiments in multi-charge deposits

The first experiment assessing the extent and detail of interaction between multiple charges was carried out in flume B, using polymict charges of beads

6.2.1 Nature of Contacts

Figure 6.1 demonstrates that sequential charges run into flume B generate significant levels of reworking evident at their contacts. *One important observation is that all contacts are sharp, with little or no mixing between charges*. At these contacts are large scale features indicative of reworking, the most notable of which appears to be over-turned or 'smeared' material of charge 1 (blue). This is remobilised from the proximal part of the deposit (blue) to the topographic high of the original lowermost deposit, investigated later in Figures 6.3 and 6.4. The BNE sorting of large particles in the lowermost charge 1 (blue) has been deformed by these reworked structures to form lenses enclosed by charge 2 (red) material. The degree of enclosure varies across the flume, with the centreline showing the least and edges showing the most. The detail of the reworking feature appears in the centre of the flume to have a wave-like geometry, shown in detail in Figure 6.2. Intriguingly, there is clearly material from

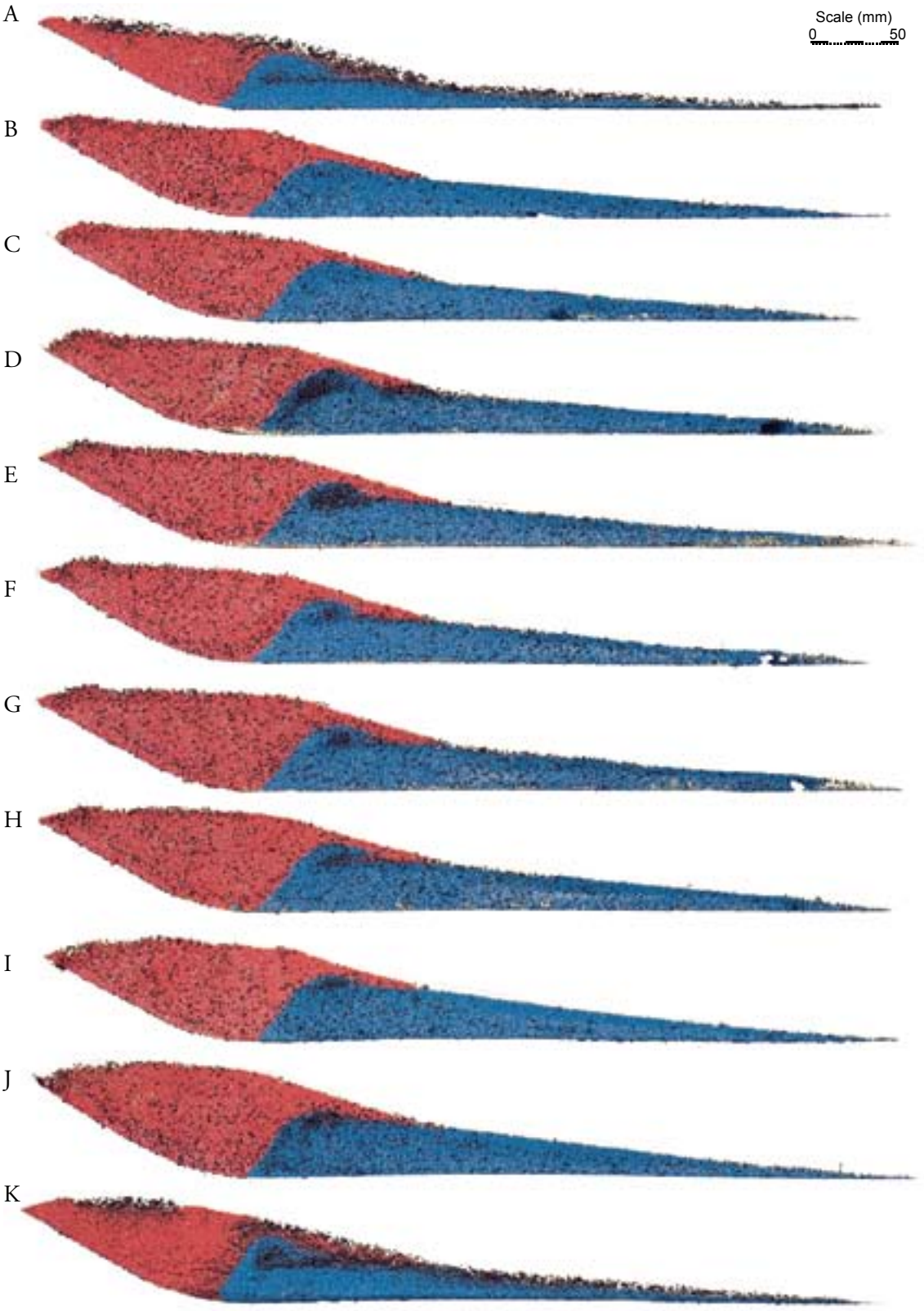

Figure 6.1 Edge to edge sequence of serial slices taken at 15 mm intervals across a deposit from flume B showing the deposit formed by two identical polymict charges each comprising 300 cm^3 small (blue = first charge, red = second charge) and 100 cm^3 large (black) silica beads, and 100 cm^3 small (white) ceramic beads. Flow from left to right.

charge 2 (red) trapped under reworked charge 1 (blue) material; i.e. inverted "stratigraphy" within the deposit. There are two possible mechanisms for this;

Figure 6.2 Detail of reworking in a slice from the centre of the deposit in Figure 6.1

A. inertial loading and shearing of the substrate (charge 1) material over the already deposited material of charge 2, (Figure 6.3a)

B. Rotational turnover (i.e. vortex-like) of the material being reworked. (Figure 6.3b)

Figure 6.3 Illustration of possible mechanisms for the formation of the reworked structures (A) Loading and shearing of the underlying substrate, and (B) Rotational turnover (i.e. vortex-like).

The precise detail of the turnover is not definitive in that regard. However, the edge geometries do not display this entrapment of younger material under older, and the original deposit surface is visually preserved as a concentration of large (black) particles.

Figures 6.4 and 6.5 are 3D surface plots of thickness data from the deposits. In all thickness plots, flume geometry is subtracted to give a flat datum to the chart, resulting in these being true records of thickness but not surface topography. These plots are unable to display multiple depth data for individual XY points. As a result points where there is inverted stratigraphy cannot be represented. In these cases the plotted surface represents the top stratigraphic occurrence of the unit. Despite these drawbacks, the surface plots are very useful in gaining 3D visualisation of the charge geometry. By comparing identical charges from different runs we are able to compare 'normal' deposit surfaces with those generated by reworking.

Figure 6.4 demonstrates the typical geometry of a 500 cm^3 deposit in flume B. A steep proximal slope (approximate angle of repose for the materials) rises to a double peak of ~22 mm approximately 50 mm beyond the break in slope. This then slopes gently down to the distal front of the deposit around

250 mm beyond the break in slope.

Figure 6.5 is a surface plot taken from the deposit seen in Figure 6.1, representing the thickness of the initial charge (blue) after reworking by the second charge (red). This was initially deposited in the flume with a geometry matching that in Figure 6.4. The differences between the thicknesses in Figures 6.4 and 6.5 are due to reworking as a result of a second 500 cm^3 charge passing over and remobilising the initial charge. It is clear that most, if not all, of the reworking has occurred in the proximal 60mm of the initial deposit, and has had a net effect of shortening the rear of the deposit, while thickening the deposit from around 22 mm to approximately 30 mm. The proximal slope of this charge has been significantly over steepened to an angle well above the angle of repose for the materials. This is possible due to the support provided by the bulk of material deposited as charge 2.

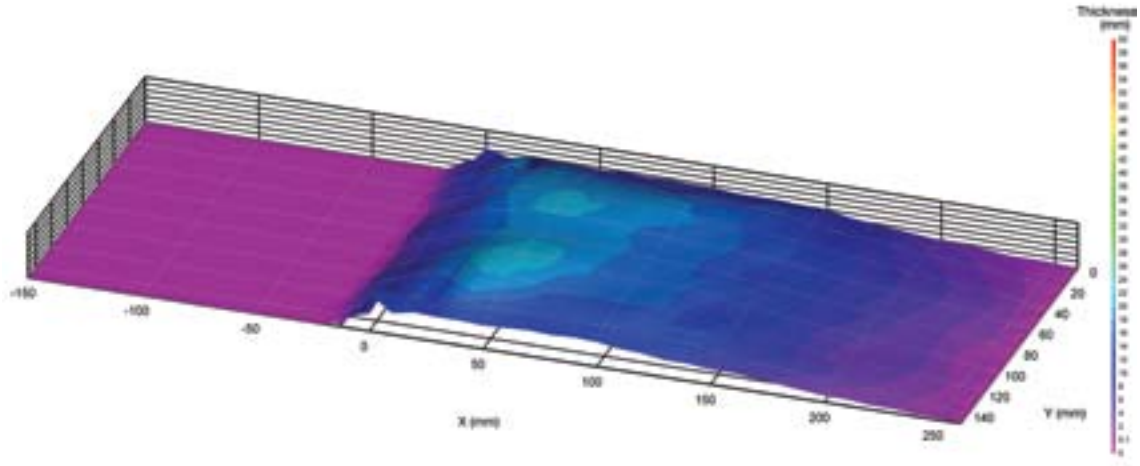

Figure 6.4 Surface plot of deposit thickness from a single polymict charge (300ml small silica, 200ml large silica beads).

A three charge experiment was run into flume B (Figure 6.6) in order to assess the interaction between successively loaded runs. These three charges comprised:

(1) 300 cm^3 small silica (blue), 100 cm^3 large silica, 100 cm^3 large ceramic. This would act as a similar volume charge to that used before, but introducing all three particle types.

(2) 200 cm^3 small silica (red) 50 cm^3 large silica; a small charge with no ceramic beads.

(3) 600 cm^3 small silica (green), 200 cm^3 large silica, 200 cm^3 large ceramic; a very large polymict charge with all three particle types.

The deposit shown in Figure 6.6 exhibits several notable features.

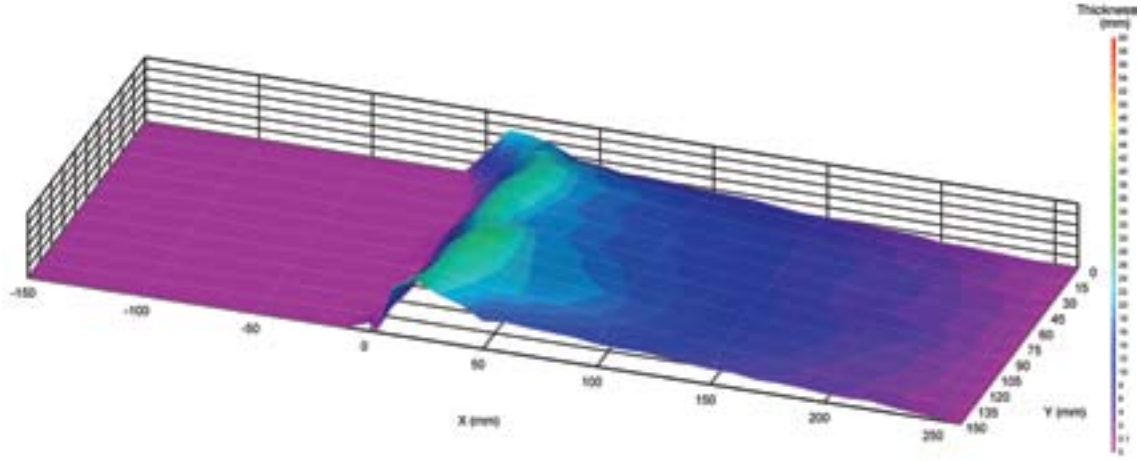

Figure 6.5 Deposit thickness of a single polymict charge (300 cm^3 small silica, 200 cm^3 large silica beads) after reworking by an identical charge (not shown); i.e. representing the thickness of the blue charge in Figure 6.1.

a) The reworking structures formed between charges 1 (blue) and 2 (red) are much smaller scale than those seen in Figure 6.1, despite the overpassing of a third much larger charge. This suggests that a) the reworking layer is relatively thin and b) the amount of reworking is directly related to the volume or mass of the overpassing material.

b) The reworking contact between charges 2 (red) and 3 (green) is strikingly different to that seen between the smaller charges. There is no sign of the roll-over/shear structures at the substrate peak.

c) Indications of similar features developing at the proximal toe of the substrate and at the distal end (see Figure 6.7). Most notably there has been a bulk removal of substrate (charge 2) material from the central axis of the flume, relocated to the flume edges. The first very faint evidence of blurred contacts (mixing) is evident at these side-wall contacts, on the lee side of the reworking - e.g. the lee-side contact between the second (red) and third (green) charges in Figure 6.6K.

As far as granular sorting mechanisms are concerned there is relatively little of note. Individual charges show the BNE / RBNE of the silica and ceramic beads respectively, as described in Chapter 5. There are some trains of large silica beads evident, particularly in the edge sections within the second charge, possibly indicative of traction during remobilisation. The dense portion of charge 3 (green) has reached the distal extent of the charge deposit. This may be a result of these larger beads having greater momentum. The proximal edge of the charge 2 (red) deposit sits on the inclined chute, making an angle with the flume base of approximately 50°. This sudden change of direction required by the flowing charge 3 (green) may have generated considerable disturbance in particle

Figure 6.7 Detail of various inverted stratigraphic structures at the distal end of the deposit shown in Figure 6.6B. The left inversion shows green charge 3 material underneath red charge 2 material. The right inversion shows red charge 2 (and a hint of some green charge 3) material underneath blue charge 1 material.

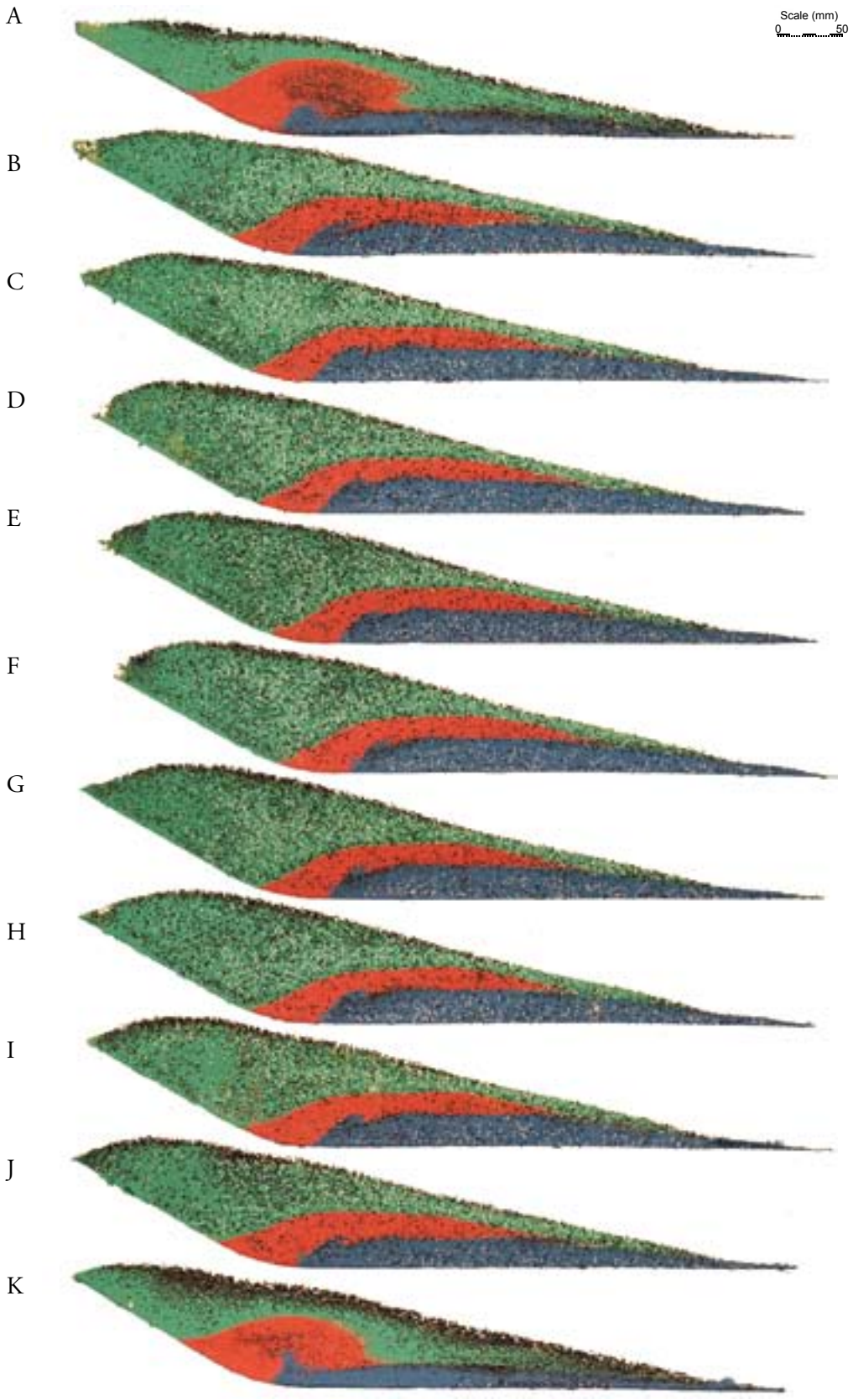

Figure 6.6 Edge to edge sequence of serial slices through a composite deposit formed by three sequential polymict charges (blue, then red, then green). Flow from left to right. Note the sharpness of contacts between successive charges and the overturning of charge deposits at the margins and at proximal locations.

movement vectors. The dense particles, retaining greater momentum will have preferentially moved through this disturbed zone.

Studying the 3D contact geometries between the charges is achieved by plotting deposit thicknesses as in Figures 6.4 and 6.5. These surfaces are displayed in Figures 6.8, 6.9 and 6.10. Again, these are deposit thicknesses, and ignore the underlying flume geometry. Angles at positions $x<0$ are therefore exaggerated by 30 degrees (the flume slope angle upon which these proximal deposit sections are resting). True deposit angular geometry can be seen in Figure 6.6.

Figure 6.8 can be compared with Figures 6.4 and 6.5, which represent identical charges in both pristine and reworked systems respectively. The difference between Figure 6.4 and 6.8 represents the degree of reworking in this experiment, and the difference between Figure 6.5 and 6.8 represent the variation in reworking due to the effects of (1) a smaller subsequent charge, and, (2) a second phase of reworking by a third charge run into the flume. As noted above, the reworked region is much lower amplitude than that seen in Figure 6.4, presumably due to the decrease in the volume of the second charge. This 3D visualisation also suggests that material appears to have been more strongly removed from the central axis of the flume than the edges. This effect is not so strongly observed in Figure 6.4, which shows similar amplitude reworking across the flume (although the nature of the contact/ overturn varied significantly from edge to centreline.)

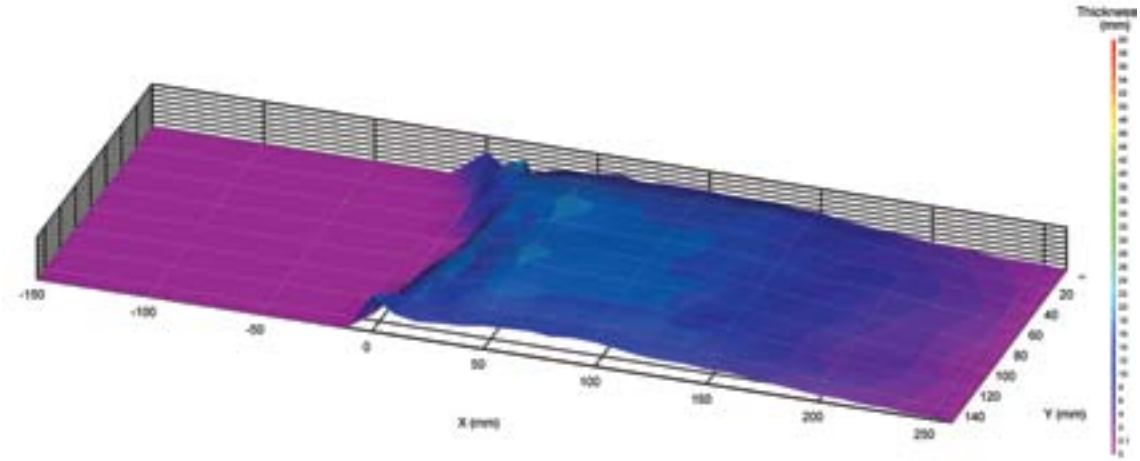

Figure 6.8 Deposit thickness of charge 1 (blue) seen in Figure 6.6.

The contact represented by Figure 6.9 is particularly striking, and represents the contact formed by the passing of the very large third charge over the deposit formed by charges one and two. Figure 6.11 shows the flume after deposition of the second charge and prior to the third and final charge. It is clear the entire upper surface of this charge has been significantly impacted by the passing of charge 3 (green). What is very obvious is that large amounts of material have been relocated from the central axis of the flume to the outer edges. There is no evidence whatsoever of the turnover structures seen in previous contacts. This is an interesting observation, as the reworking features seen up until this point to have been generated by an undefined mechanism.

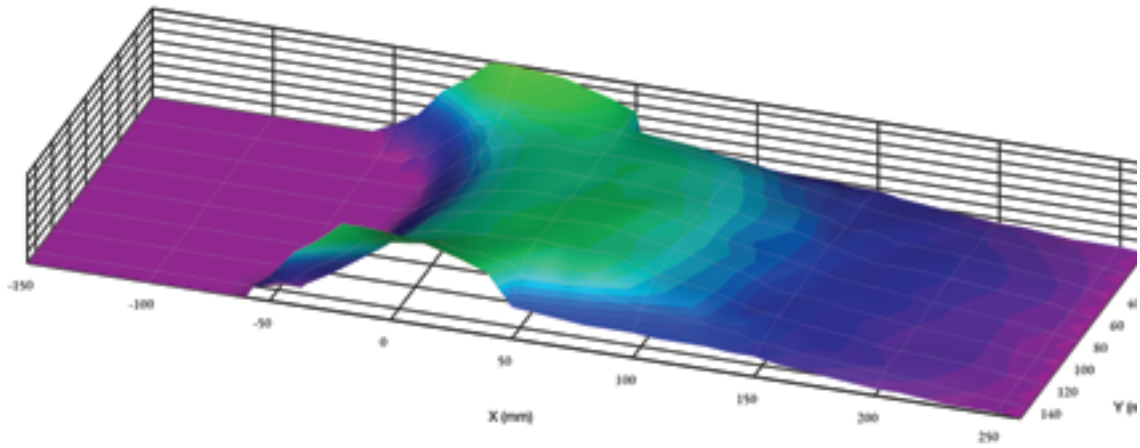

Figure 6.9 Cumulative thickness of charges 1(blue) and 2(red) seen in Figure 6.6

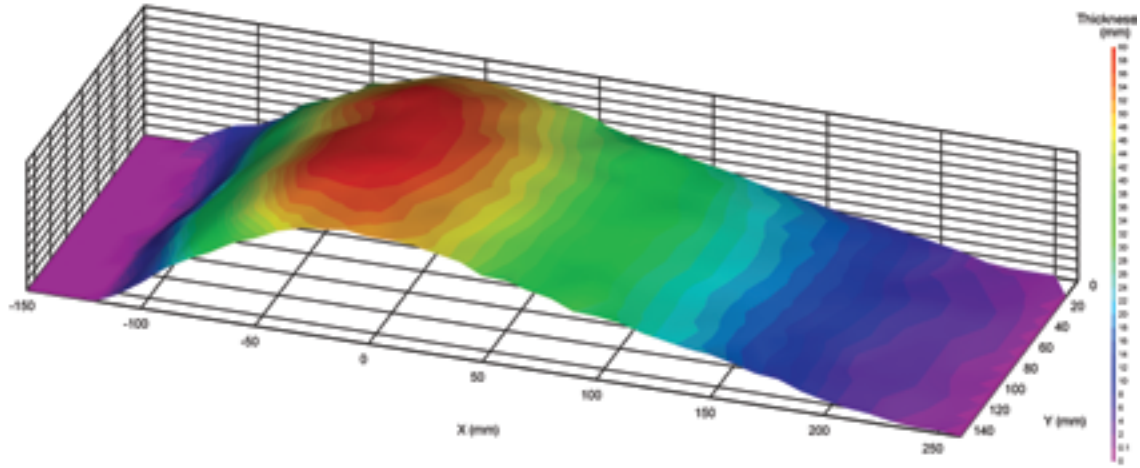

Figure 6.10 Cumulative thicknesses of charges 1(blue), 2 (red) and 3 (green) seen in Figure 6.6.

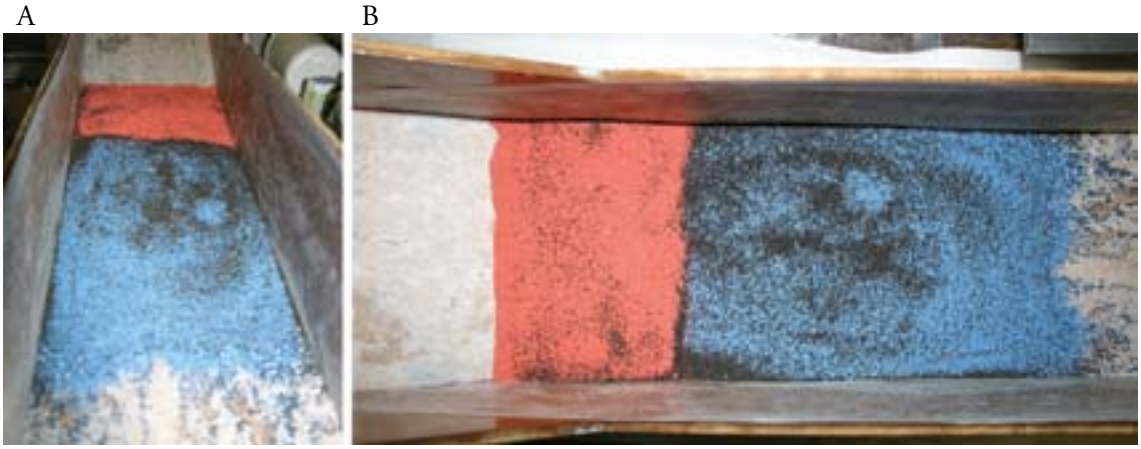

Figure 6.11 Deposit before the final charge is run into the flume. First charge in blue, second in red. (A) looking up-flume, (B) is a plan view.

The two possibilities for the overturn structures were outlined previously (i.e., inertial pushing/shear, and rotational turnover). Firstly, it makes sense that a larger over-riding charge might be expected to amplify the generation of the turnover structures. The observation that the large third charge pushes material to the side of the flume, rather than generating turnover features may be seen as evidence for the inertial pushing/shearing model. The small inversion structures generated on the distal surface (Figure 6.7) would also tend to support formation by this mechanism, being strongly indicative of shear remobilisation of the loose substrate.

Clearly the flume experiments and methodology are able to generate interesting reworking features. However, it is apparent that these are not necessarily meaningful analogues to PDC. The sharp break in slope of Flume B triggers deposition from the current too rapidly to generate any meaningful over-passing of material. Furthermore, the steep proximal slopes of deposits encourage subsequent flows to impact rather than over-pass. As a result, at least some of the reworking features seen so far are derived from inertial impact of a flow into a steep substrate surface, simply pushing material forward. This is in contrast to interaction at the sub-horizontal lower flow boundary zone of a granular flow and substrate which might take place in an aggrading natural system.

The appearance of small, low angle features as demonstrated by Figure 6.7 are perhaps the strongest evidence of shear remobilisation in these reworked contacts beyond simply pushing material out of the way of the encroaching flow - the substrate material being reworked is moving in a direction sub-parallel to the flow direction, and the angle on the distal slope precludes any 'pushing' effect. It should also be noted that reworking which is definitely generated by pushing of material (e.g. the surface represented by charge 2 in Figure 6.6) lacks much of the internal structure we have seen in previous features. This suggests that smaller charges have been able to overpass more gently, and perhaps interact in a system with less loading, whereas the larger charges represented by, for example, charge 3 (Figure 6.6) increase loading to such a degree that it obscures any shear-derived features.

6.3 Flume C experiments

Flume C was designed and built to overcome the experimental difficulties illustrated by earlier runs. A gentle curvature to the break in slope was introduced to encourage a smoother transition from slope to runout, and further reducing the granular jump effect. In addition a five degree sloped runout surface was specified in order to encourage overpassing of subsequent flows. Figure 6.12 shows the results of a run using two identical monomict 500 cm^3 charges, comprising 250 μm diameter silica beads (blue, then red) run into flume C. The first thing to note is that the deposit length and charge runouts are greatly improved. Notably, the second charge is able to overpass a large proportion of the first charge deposit. The contact surface between the charges is marked by a very complex reworking structure.

The edges of the flume demonstrate no obvious reworking (contrary, for example, to that seen in charge 2 of Figure 6.5). In the centre of the flume, however, the reworking is expressed as a vortex-like rollover structure. Between 10-20 mm from the flume edge the structure of these reworkings are considerably more complex. This is interpreted as a result of material being moved from the central

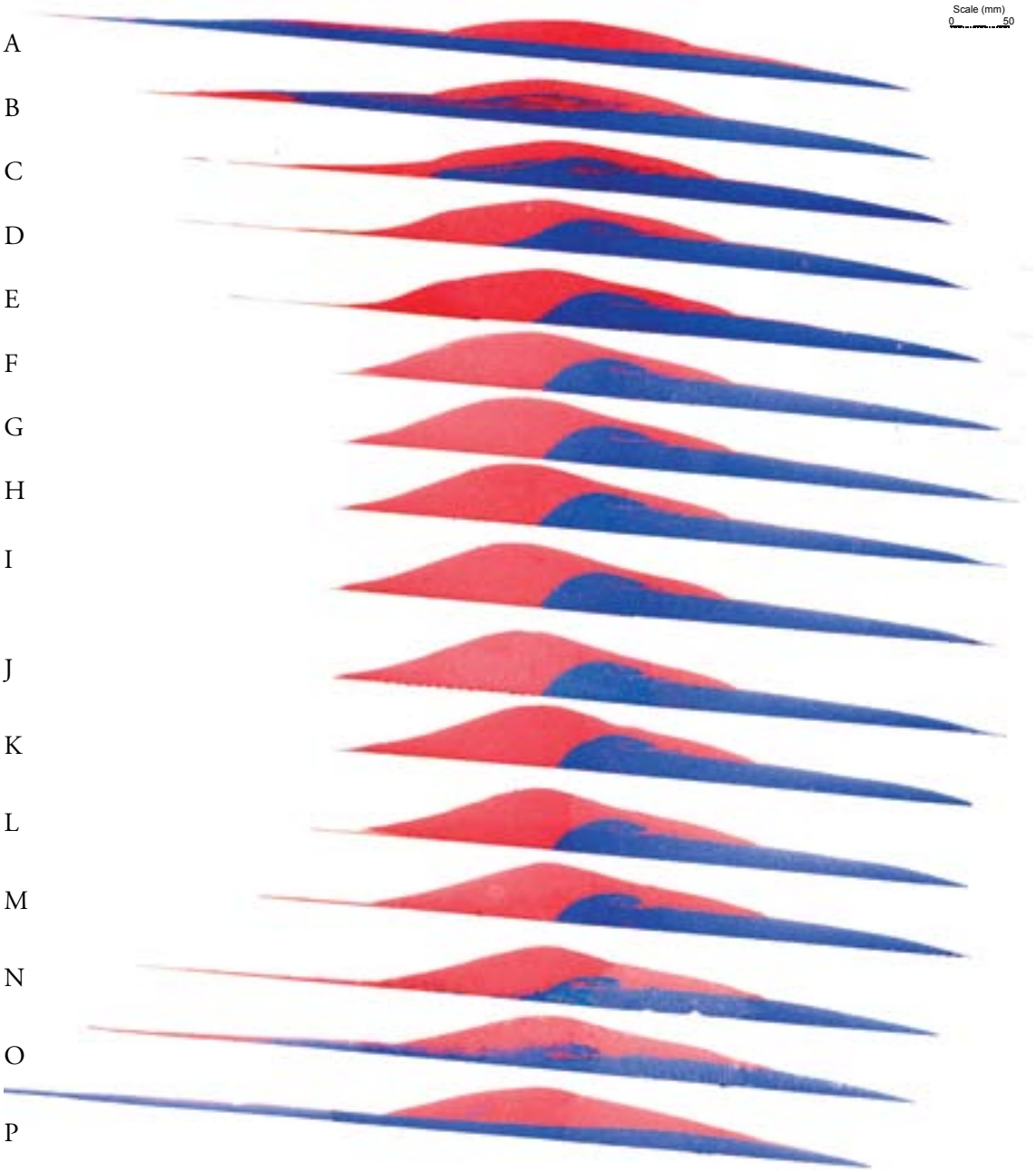

Figure 6.12 Sequence of 10 mm slices through a deposit formed by two monomict 500 cm^3 charges of 250 micron diameter beads (blue, then red) into flume C. Note the occurrence of reworking in a similar location to that observed in flume B, but with an apparently rotational component. Detail of reworking is strongly heterogeneous across the flume.

region of the flume towards the edges. As well as the most obvious rollover structures, there are a number of smaller scale features resembling sheared flame structures often found in sedimentary sequences.

Comparison of two identical experiments demonstrates the reproducibility of these runs as being very good, especially with regard to reworking structures of similar amplitudes, wavelengths and morphologies (Figure 6.13).

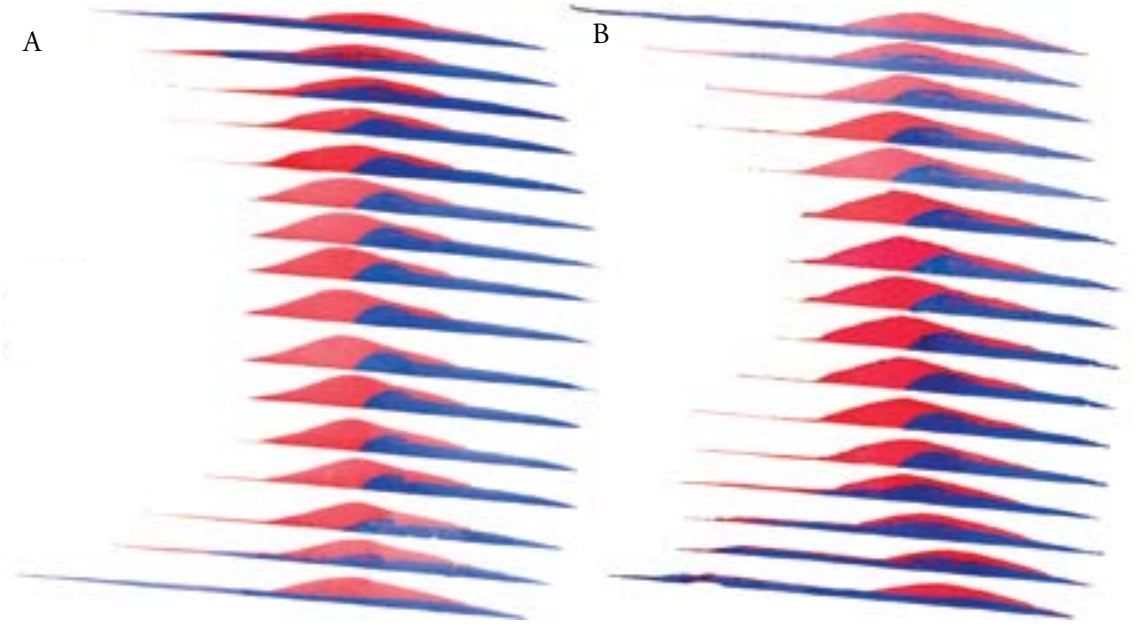

Figure 6.13 Reproducibility of flow features from figure 6.10 and an identical experiment using the same colouration and charge compositions. 10 mm between sequential slices. Note the broad similarities in the architecture of the two flows (i.e., proximal slope, run-out) and the same edge to centre variation across the composite flows. The greatest heterogeneity in reworking is observable within 20 mm of each flume edge in both cases.

The largest reworking structures observed in Figure 6.11 demonstrate a spectrum of morphologies, with five primary groups identified. These are shown in Figure 6.12.

The contacts shown in Figure 6.14 may be seen as type morphologies, and may give some insight into the processes dominant at different points across the flume:

a) no reworking evident, generally found only at the sidewall.

b) strongly sheared series of stacks demonstrating an anomalous 'tongue' behind the main overturn. Several series of inverted stratigraphies may be identified. The reworked structure may show full, partial or no rotation and often exhibits secondary shearing. Generally found within 30mm of the flume sidewall.

c) relatively open vortex structure. Proximal slope of the first charge (blue) is at or near the angle of repose.

d) Oversteepened proximal contact, with a closed overturn revealing little internal structure. Usually located next to a smaller 'sheared flame' structure.

e) Strongly oversteepened proximal contact with clear rotational reworking structure. Usually located next to a smaller 'sheared flame' structure.

Certain morphologies (i.e., open vortex (c) and oversteepened and rotational reworking (e)) are generally identified in the central axis of the flume, 30 mm or more from the sidewalls. These can be considered as a continuum, produced by subtle variations in the loading, velocity and vector of

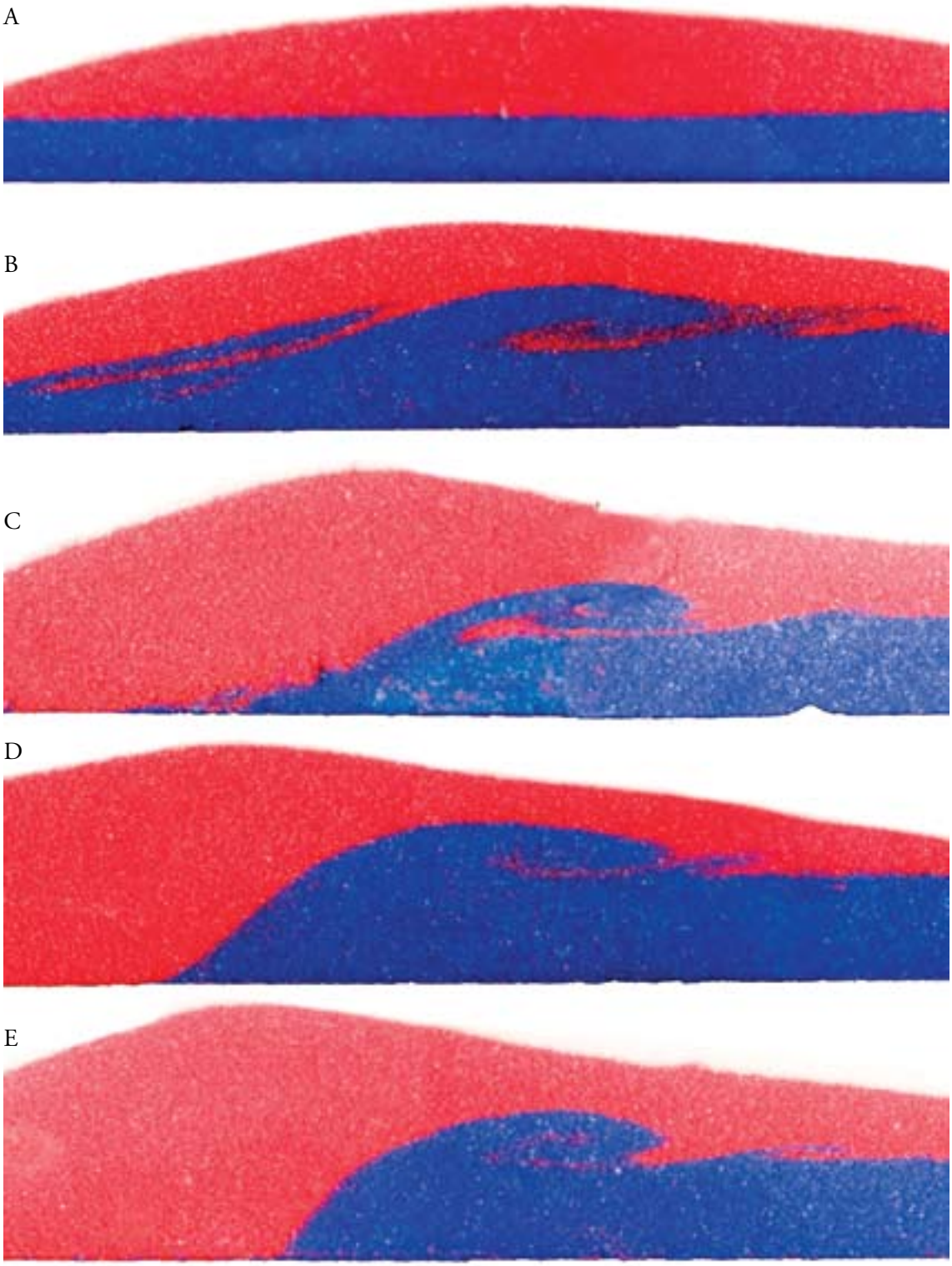

Figure 6.14 Five key morphologies developed at charge contacts. (a) no reworking, (b) sheared stacks, (c) open vortex, (d) oversteepened and overturned, and (e) oversteepened and rotational reworking

flow within the central region of the flume. The differing degrees of oversteepening are probably due to the rate and volume of material removal as the eroding charge passes through, with deposition of the active charge occurring at a rapid enough rate to prevent the substrate material collapsing back to its angle of repose. Similarly, the openness of the overturn structures is likely a product of rate and volume of overpassing material, although it is possible that parameters such as flow dilation (granular temperature) and local substrate slope have a part to play in the explanation. Sheared stack (b) morphology is more difficult to explain, as it shows significantly more complexity than any of the other morphologies. This is interpreted as a product of flow vectors being affected by interaction with the complex proximal geometry of the substrate material. Charge material in the approaching flow is funnelled by the complex geometry of the proximal deposit (Figure 6.15), forcing material from the central axis to the flume edges. This in turn moves material eroded from the centre to the edges of the flume. As flow pulses migrate down the flume they are able to build a sequence of inversion structures toward the flow edges as typified by morphology b). No-reworking (a) morphology demonstrates the lack of reworking evident at the edges of many experiments. It is inferred that the high sidewall

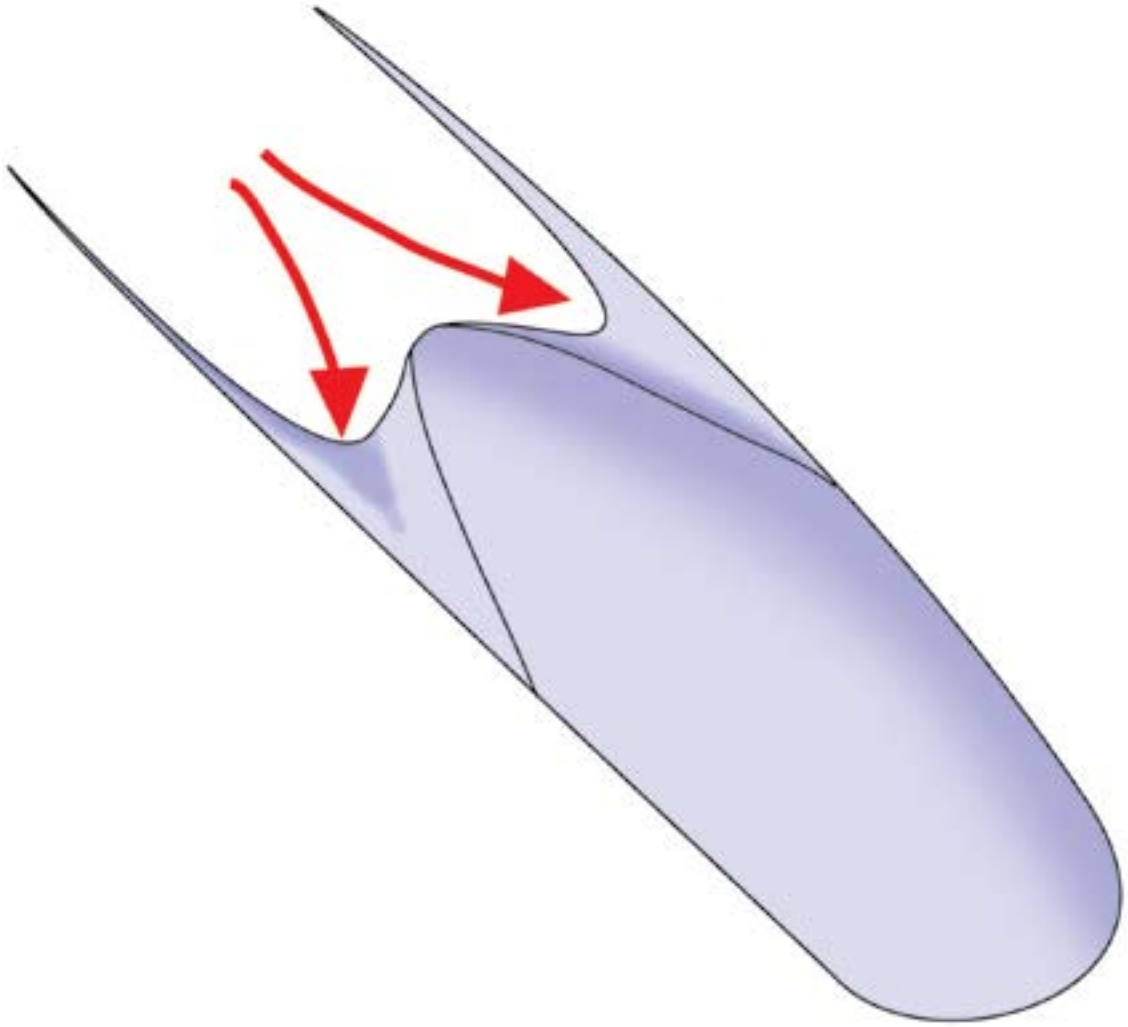

Figure 6.15 Shaded illustration of typical geometry formed by the first charge into flume C, and the diversion paths (in red) likely to be followed by any subsequent charge.

friction causes these zones to be entirely depositional, unable to remobilise underlying substrate.

The vortex-like nature of the large overturn structures is intriguing, and by using a stratified substrate we are able to more closely investigate the form of these reworkings. Additionally, by laying a horizontal substrate into the flume we are able to remove any effects created by the active charge

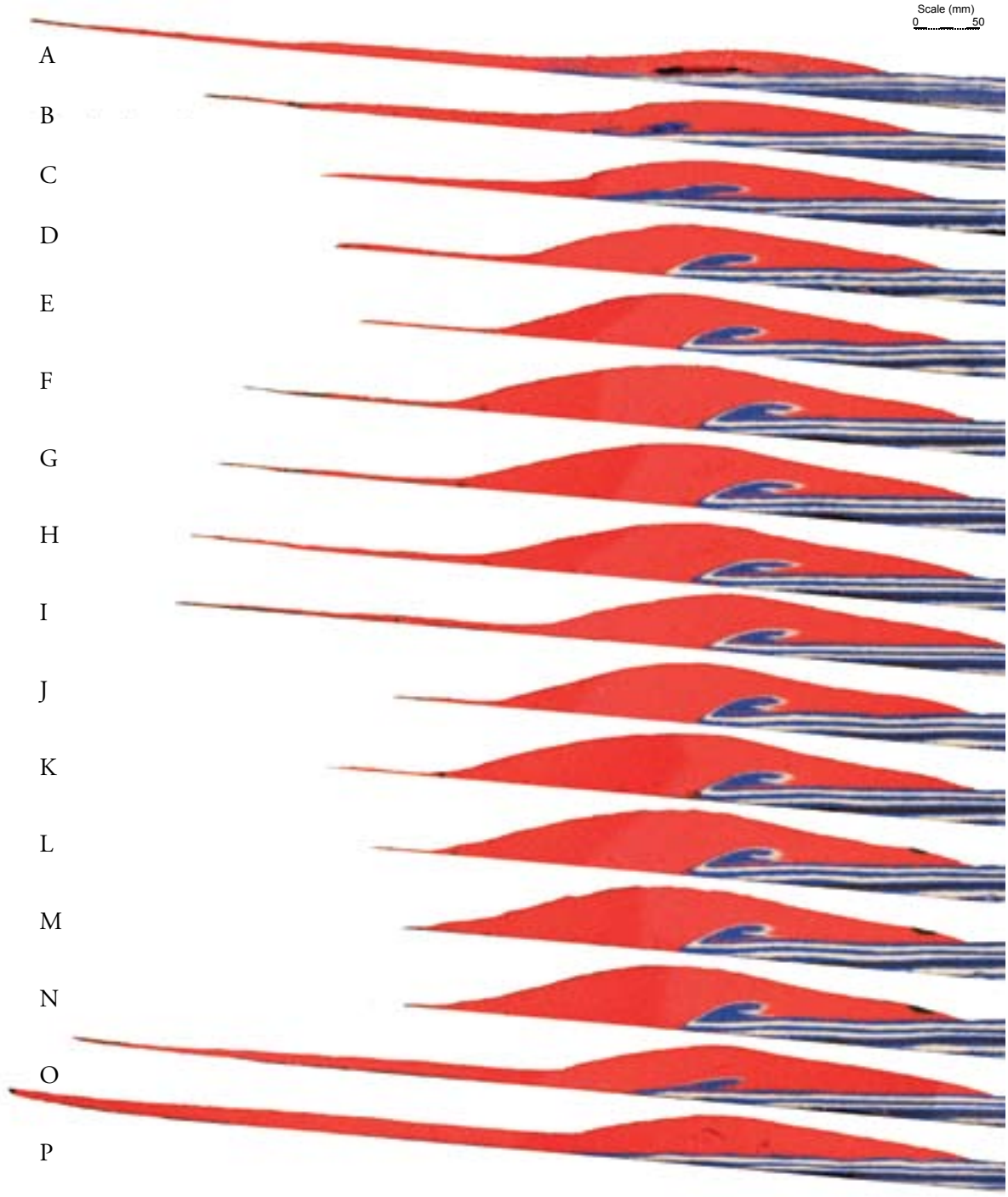

Figure 6.16 Sequence of slices made at 10 mm intervals through monomict deposit of 250 μm glass beads (red) layed onto a stratigraphy of layered 250 μm glass beads (white, blue, black) to reveal the internal detail of the overturn structures. Stratigraphy demonstrates the rotational nature of the features, which appear to have propagated forwards during growth, entraining material from the charge within the vortex.

coming into contact with a substrate dipping back towards the slope. A sequence of coloured layers are placed horizontally in the flume until they reach 100 mm from the break in slope. As a result, the active charge transitions as normal from the slope to the runout surface, propogates for 100 mm along the 5° runout surface, then contacts a 0° granular substrate composed of 250 μm glass beads (Figure 6.16).

Runout onto a pre-existing horizontal topography generates similar overturn structures to those seen in Figure 6.12. Furthermore, the stratigraphy of the substrate is fine enough to allow resolution of the internal details of the reworking. Figure 6.17 is an interpretation of a single overturn section, with correct way up indicated by green arrows at various points on the structure. The red dotted line marks an approximate division between the upper and lower sections of the overturn, the point below which apparently correct way-up is produced locally by full 360° rotation of a coherent stratigraphy. The yellow dotted line marks an inferred shear region below which a second inverted through to normal stratigraphy sequence can be observed. This lower structure is interpreted as the leading edge of the vortex rotation which has subsequently been buried by a vertically migrating shear zone. It has then been overpassed by the further propogation of the vortex feature.

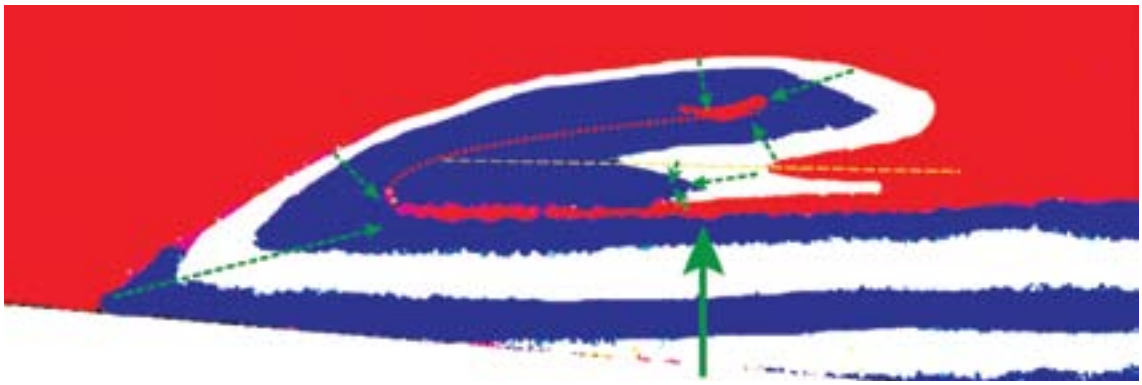

Figure 6.17 Interpretation of a single overturn structure in a stratified substrate. Green arrows mark the 'correct' way up for local sections (i.e. arrows pointing down indicate inverted stratigraphy), red dashed line marks the approximate central zone of the turnover, and the yellow dashed line marks an inferred shear zone.

The importance of Figure 6.17 is that it clearly demonstrates the nature of the reworking structures. They are developed by full rotational stuctures, grown by a roll-up of substrate occurring at the contact between it and the over-riding flow. The mechanism inferred from Figure 6.3 (inertial loading and shear) may in fact produce a vortex . The vortices generated in this system are interpreted to be Kelvin Helmholtz (K-H) instabilities. K-H instabilities grow spontaneously in systems with velocity and density contrast between layers. K-H-like instabilities have only recently been identified in granular fluids (Goldfarb *et al*. 2000, 2002).

K-H instabilities are generated at the contact between parallel streams of fluid with velocity shear, where there is either an infinitesimal or finite thickness interface. Rotational growth is encouraged by the velocity gradient across the interface as shown in Figure 6.18, in which the rotational arrows indicate the self-induced (clockwise) movement of the vorticity sheet.

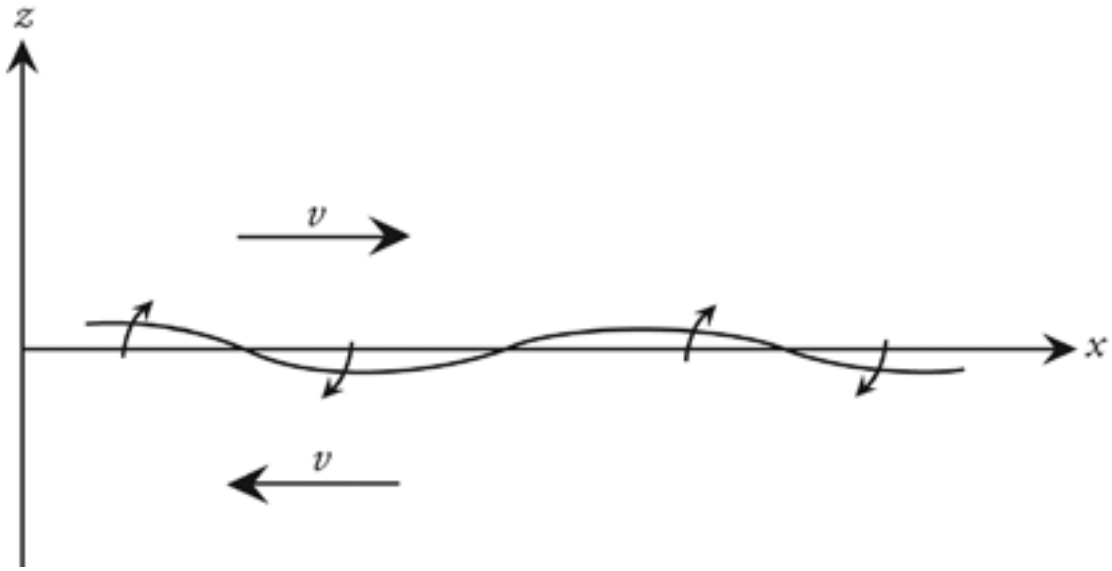

Figure 6.18 Growth of a sinusoidal vortex sheet, after Batchelor 1967. At any point where $z \neq 0$ then the local velocity has an x component of $x \neq 0$. The clockwise velocities develop and amplify the sinusoidal displacement.

In order to develop a better understanding of the growth of these instabilities a modified topography using stratified ridges will be used. We already know that the largest turnovers occur where the flow interacts with a substrate contact dipping back towards the flume slope. The intention is to attempt to accelerate the growth of instabilities. If these are K-H-like instabilities a pre-existing topographic feature will act as a seed for initiation of the instability. Because these flume experiments are very short lived, the deposits are freezing rapidly. In a sustained current the shearing interface might be expected to have lifetimes in the order of seconds to minutes. The rapid freezing of the interface in the flume may be seen as capturing the early formation of these features, which in a sustained flow would propagate and develop into fully mixed zones. By accelerating the initiation of the instabilities in the flume we can investigate what they will look like in a more developed phase of growth. Furthermore, it is an opportunity to investigate the growth of the lee-side sheared flame-like features observed

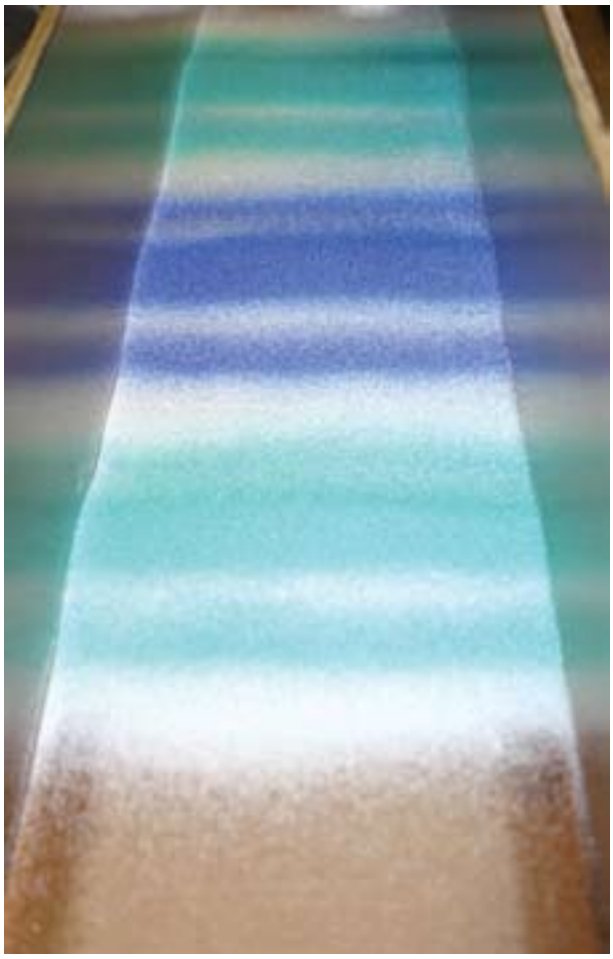

Figure 6.19 View from the flume slope onto the runout surface prior to the charge being run. Three stratified ridges are built upon a continuous white base layer.

in previous experiments. By placing a sequence of ridges at the approximate wavelengths seen for previous instability growth, we may see whether secondary flame structures are potentially related to secondary instability growth.

The ridge features are laid in a similar manner to the topography in Figure 6.16. The topography has a 1mm base of white coloured beads beginning 100 mm from the start of the flat runout surface (as before). This white layer is lying at between 4-5°, and the stratigraphy of the ridges is lain parallel to this. At 200 mm intervals 100 mm long ridges are constructed using stratified layers of coloured beads. These extend from edge to edge within the flume (See Figure 6.19). A single 500 cm^3 monomict charge of 250 μm glass beads is run onto this surface (Figure 6.20).

The structure evident in Figure 6.20 is striking. The turnovers seen in the previous stratified experiment are reproduced, but the pre-existing geometric deformation due to the ridges accelerates the growth of the instability, allowing it to grow to a greater degree. The shear zone inferred in Figure 6.17 is again present, and shows greater displacement. Intriguingly, the features formed from the first green ridge appear to show some upward deflection at the distal end. This may be the result of the shear zone being deflected by the shear instability growing in front of the second (blue) ridge.

The instabilities generated at the second ridge are notable for appearing towards the sidewalls similar to the secondary flame structures observed in the previous multi charge experiments in morphologies

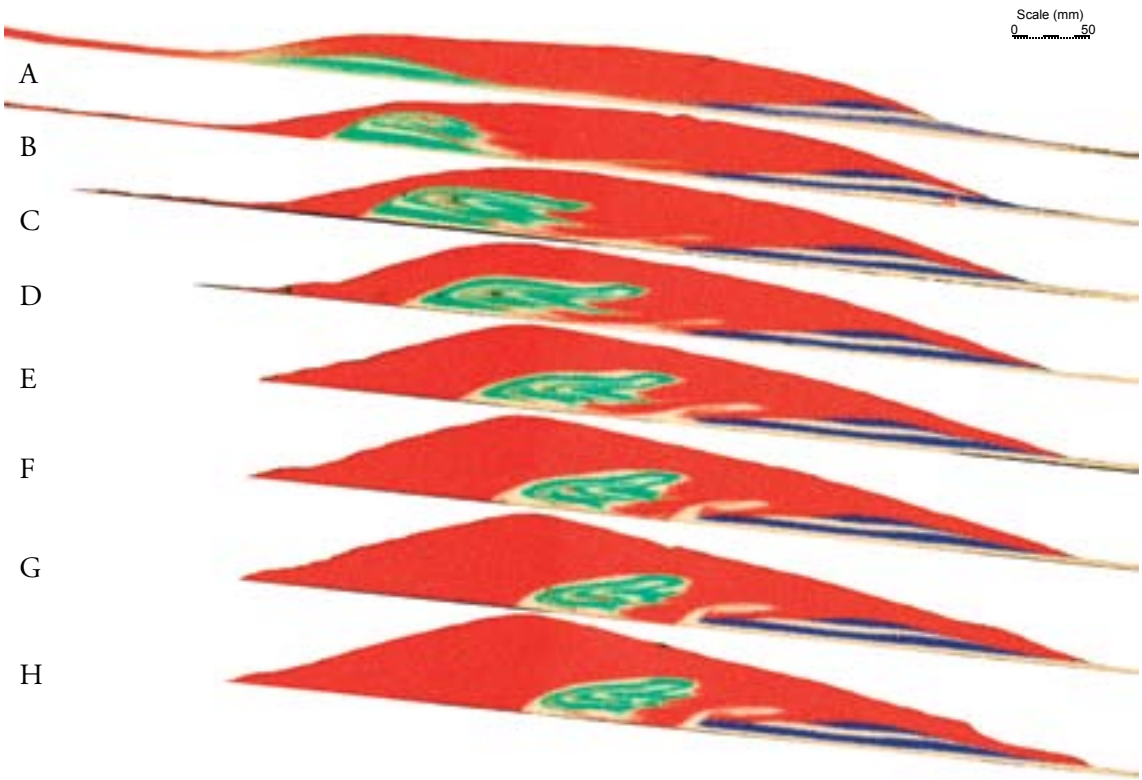

Figure 6.20 Edge to centreline sections taken at 10 mm intervals, showing the results of a 500 cm^3 charge (red) of 250 μm glass beads run onto a stratified sequence of ridges built of identical glass beads.

d) and e). However, the accelerated instability growth produced by this ridgey terrain has enabled these features to develop more fully. Furthermore in the centreline of the flume a full rollover is evident in the stratigraphy. The progression from edge to centreline in fact appears to preserve the full development process of instability growth. It would appear to indicate that the sheared flame-like structures observed in earlier experiments are due to the same process as the fully developed rollover features.

An interpretation of a single slice (Figure 6.21) highlights the inferred shears developing within the primary instability, and allows closer inspection of the detail of the rollover. The inflection at the distal end of the primary instability does indeed appear to be at a similar angle to the growth of the secondary instability, separated by a constant thickness of material (indicated by dashed black lines). These thicknesses are possibly related to the thicknesses of shearing pulses within the aggrading deposit (as seen in Chapter 4).

Figure 6.21 Interpretation of a single slice, showing a 500 cm^3 monomict bead charge (red) running over a series of stratified ridges (green / blue / white). Yellow dashed lines indicate inferred secondary shear zones through the reworking instability feature. Black dashed lines indicate geometric similarity between instability morphologies possibly related to flow pulse thicknesses.

The shear zones forming within these instabilities are symptomatic of a unsteady granular shears. The depositing flow is composed of thin dense shearing material which rapidly sediments as a sequence of pulses which ride over each other. The ability of these pulses to remobilise substrate material is clearly evident in the growth of these turnover features, and the internal shears within them are inferred to be caused by secondary shear created by an over-riding pulse. There is therefore the pulse which initially generates the K-H-like instability being disrupted by pulses of further material adding momentum and loading to the growing system. These pulsed variations would create an environment for unsteady instability growth, leading to the multiple internal shear deformations. Further down-flume where fewer pulses reach, the secondary instabilities are unaffected. In a pervasive system these instabilities would form, grow, and migrate downstream with the shearing material. The implications for this in geophysical systems are explored in Chapter 7.

In order to gain some insight into how several sequential pulses may interact, an experiment is carried

out using three identical monomict charges. It is notable that difficulties were encountered in the setting and sectioning of these thicker charge piles. The gelatine solution had difficulty penetrating the pack, resulting in some pack failure when removed from the flume. As a result, several slices are missing material. Figure 6.22 shows the deposit formed in a three charge experiment (blue, then red, then green) using sequentially larger charges; 400 ml, followed by 600 ml, followed by 800 ml. These incremental charge volume increases were used so as to ensure the final charge was still able to overpass the topographic high of the substrate which results from two prior charges.

The deposit formed by three charges is, as might be expected, similar to that formed by two charges but with an extra contact running over the upper surface. However, this deposit reveals several features which have been less clearly observed (or unobservable) in previous experiments. Figure 6.23 shows the detail of the first edge section in Figure 6.22. This clearly demonstrates a very low angle but laterally extensive tongue of material indicated by the black arrow. This shearing feature gives some indication of the longevity of transport from an eroded substrate even in this rapidly depositing system. Just downstream of the arrowhead there is also an indication that a second tongue is formed from this remobilisation feature, deflecting upwards as the overpassing third charge is deflected by the thicker downstream substrate.

Also clearly demonstrated in this flume are signs of cross-flume sediment transport. Figure 6.24 shows the detail of sections from Figure 6.22 10mm and 20mm from the flume edge. The arrows indicate a shear feature which is developing from the lower (20mm from edge) slice, but propogating into the upper (10mm from edge). This is further evidence for the general flow propogation model proposed in Figure 6.15, with mass transport being encouraged from the central flow channel towards the flume sides.

Similar mass transport patterns are seen in the opposite flume edge sections (Figure 6.25), where several different shear structures propogate across flume. The black arrows show a similar cross-flume transport of shear remobilisation to that seen in Figure 6.24, and clearly demonstrates how several stacked shear features can be generated (i.e. morphology B demonstrated in Figure 6.14). In contrast, however, the yellow arrows show an intriguing cross flume feature which appears to show material movement from the edge towards the centreline - contrary to that predicted by the model in Figure 6.15.

The explanation for the formation of this feature may be that while transport further down the flume may indeed encourage mass transport from the centreline to the edges, at the more proximal extremes of the existing substrate the flow front of the approaching charge is funnelled in the opposite direction. Only when the centreline substrate topography exceeds that of the edge veneers does mass transport switch to that indicated in Figure 6.15. This modification of the model recognises that regardless of whether the flow material at the centre of the flume is advancing ahead of the slower moving edge flow, the edge flow still reacts to topographic obstacles when it reaches them. Therefore, while Figure 6.15 can be seen as representative of the current diversion experienced by some of the centreline flow material, the modified model given in Figure 6.26 is more representative of possible particle motion

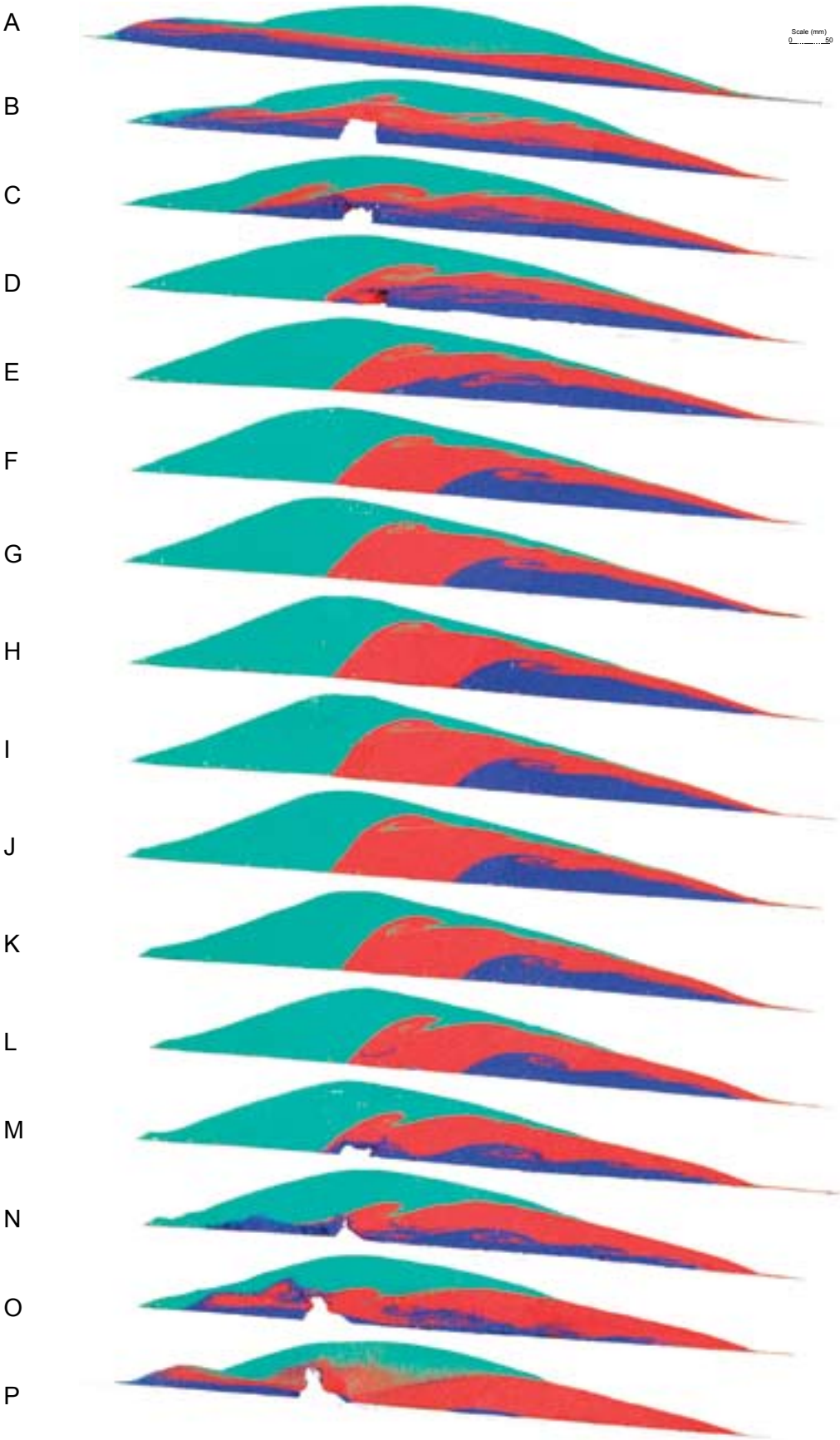

Figure 6.22 Sequence of 10 mm slices through a deposit formed by three monomict charges of 250 micron diameter beads (400 cm^3 blue, then 600 cm^3 red, and finally 800 cm^3 green) into flume C. Rotational reworking is observed at both interfaces. Sections within 30 mm of the flume wall demonstrate interesting cross-flume reworking, as well as well developed secondary (and tertiary) down-slope instabilities.

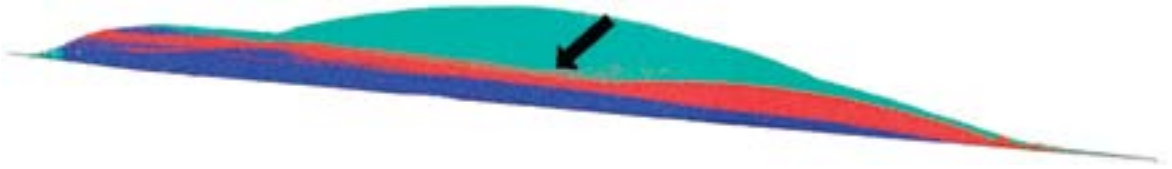

Figure 6.23 Detail of an edge section from Figure 6.18. Arrow indicates a long low angle shear feature.

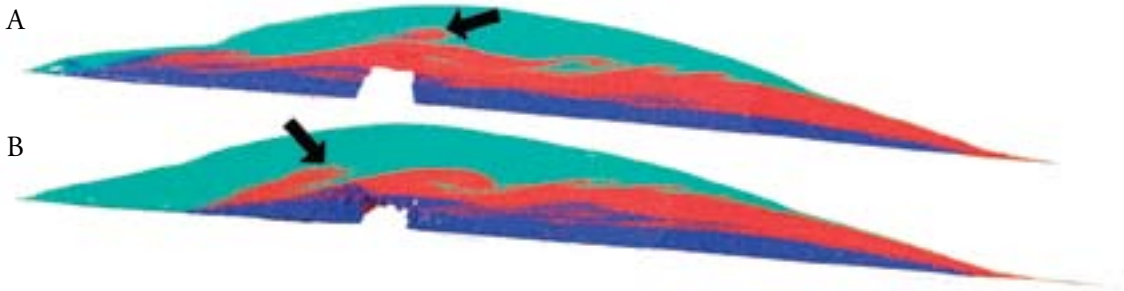

Figure 6.24 Detail from slices 10 mm and 20 mm from the flume edge seen in the experiment represented by Figure 6.18.

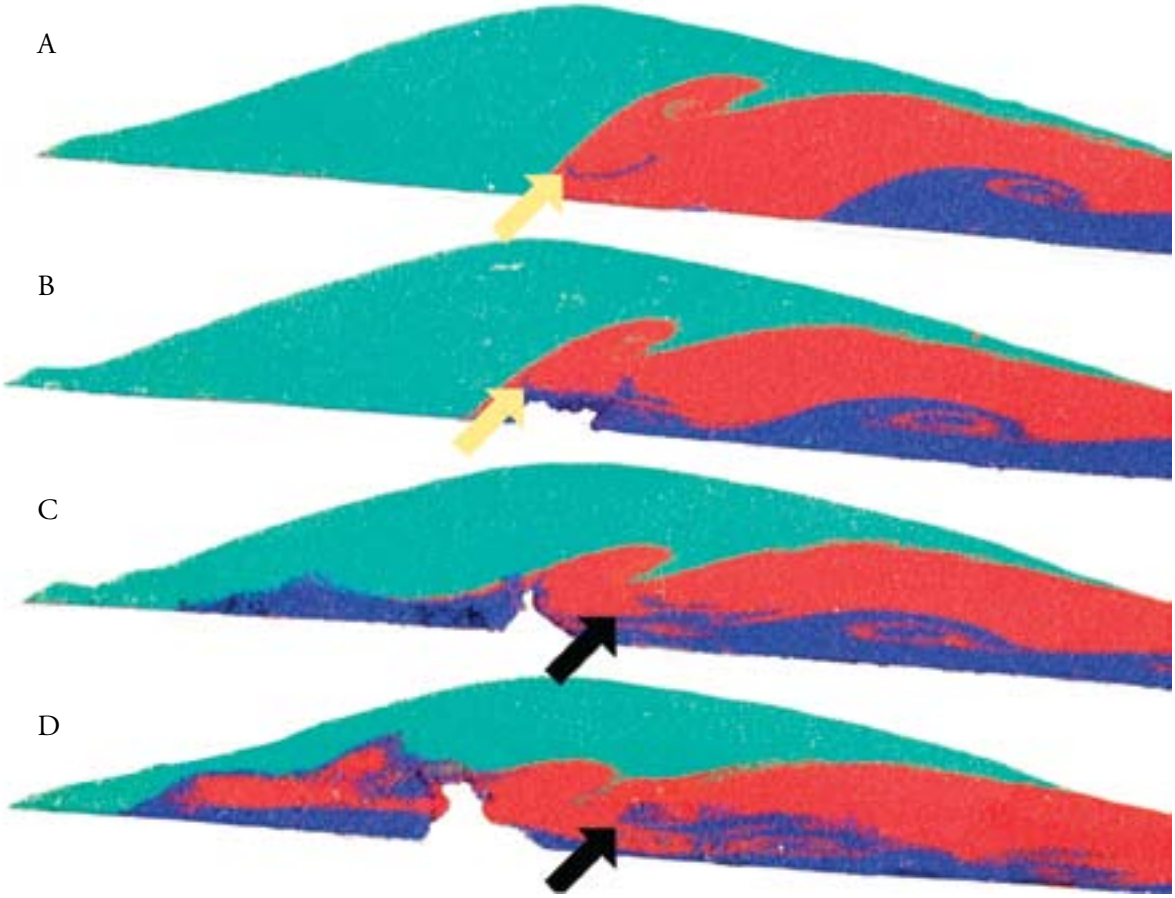

Figure 6.25 10 mm spaced sections representing slice from 40 mm-10 mm from the opposite flume edge of the experiment represented in Figure 6.20.

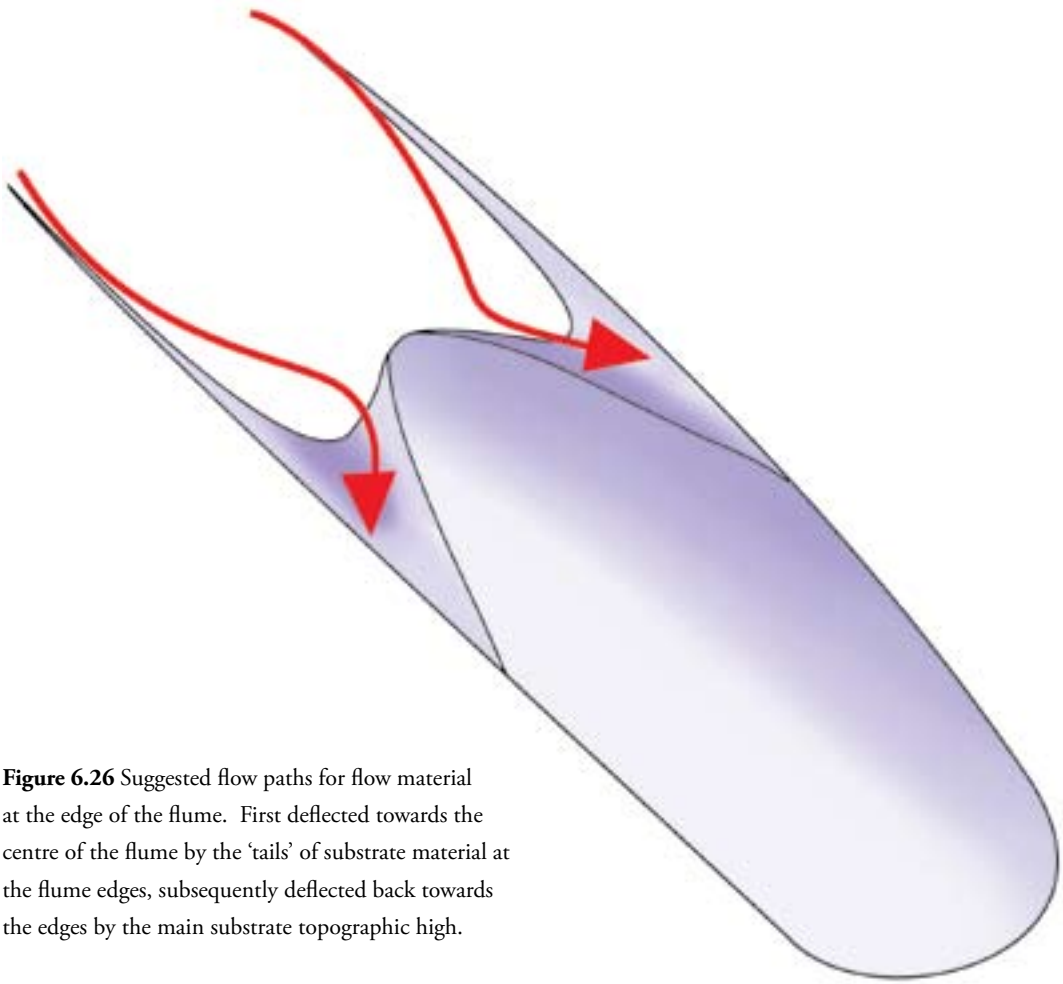

Figure 6.26 Suggested flow paths for flow material at the edge of the flume. First deflected towards the centre of the flume by the 'tails' of substrate material at the flume edges, subsequently deflected back towards the edges by the main substrate topographic high.

from edge flow material, deflected first by the proximal 'tail' of substrate at the flume edges, then by the topography of the main substrate mass.

The final feature well expressed by the deposit in Figure 6.22 is the ability of small scale shear features to form with very small amounts of overpassing flow. Figure 6.27 shows a enlarged section of a centreline slice H of the deposit in Figure 6.22, clearly demonstrating a sequence of shear features growing at each of the flow contacts. These sequences of features appear to be forming by the same process, with similar geometries at both contacts. As the thickness of the over-passing flow reduces, so does the scale of the reworking - although it is notable that the ratio of wavelength to amplitude of these features does not appear to vary considerably. Additionally, even the smaller features appear to show some degree of rotational motion. The most distal shear feature formed at the interface between second (red) and third (green) charges has formed with less than 2mm of overlying material. We do not know if this overlying material aggraded as a single flow pulse or not, but it gives a useful limit for the necessary thickness to form the remobilisation features in this system.

There is, however, a possibility that we can extract some information on the flow pulse thicknesses which might be gained from using polymict charges. Figure 5.9 in the previous chapter demonstrated

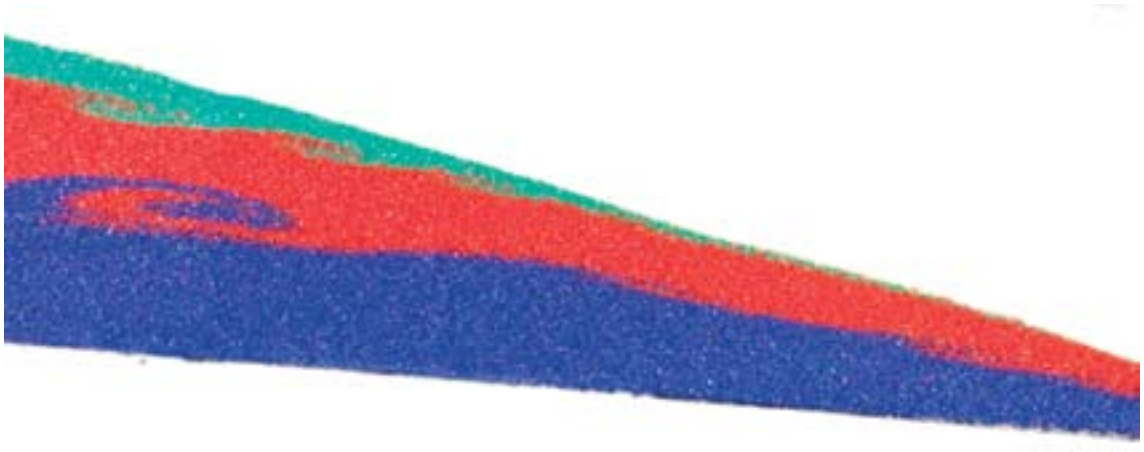

Figure 6.27 detail of sequences of K-H-like growth features along both contacts, from the experiments shown in Figure 6.18.

that fine dense particles concentrate in the lower region of each flow pulse, and appear to highlight the contacts between individual flow pulses which build up a deposit (probably along frontal thrusts). We may therefore run a polymict charge onto a stratigraphy to examine how these internal expressions of a pulsed deposition and instability growth interact.

Figure 6.28 shows a sections from edge to across the centreline of the flume at 10mm intervals, with a stratified horizontal white/blue substrate. The charge is composed of 300 cm^3 of 250 micron silica beads (red), and 200 cm^3 of 250 micron ceramic beads (white). As well as the instability features, the dense ceramic particles again appear to have highlighted the pulse stacks within the deposit. The ceramic beads are concentrated in the centre of the deposit (in line with the sorting mechanisms discussed in Chapter 5), but the broad pattern quite clearly indicates pulses passing over the growing instability. More homogenous mixing of the ceramic beads with the rest of the charge in the proximal part of the deposit perhaps suggests disruption of the laminar regime as the last of the charge arrives at the steepening proximal deposit contact.

The stratification of ceramic particles suggests that the deposits from each pulse range between 5-10mm thicknesses.

6.4 Interpretation

Significant reworking is produced by these small volume flume experiments. While flume B experiments generated shearing features, it is clear that reducing the loading effect in flume C permits the growth of complex and significant instabilities. The mechanism proposed for the reactivation of an otherwise stable granular pack into a dilated granular shear flow is that of conduction of granular temperature through collisional momentum transfer between grains. As grains in the flow travel across a substrate they collide with static grains and impart momentum to them. These travel up into the flow and become entrained. As this granular temperature increase is conducted down through the substrate

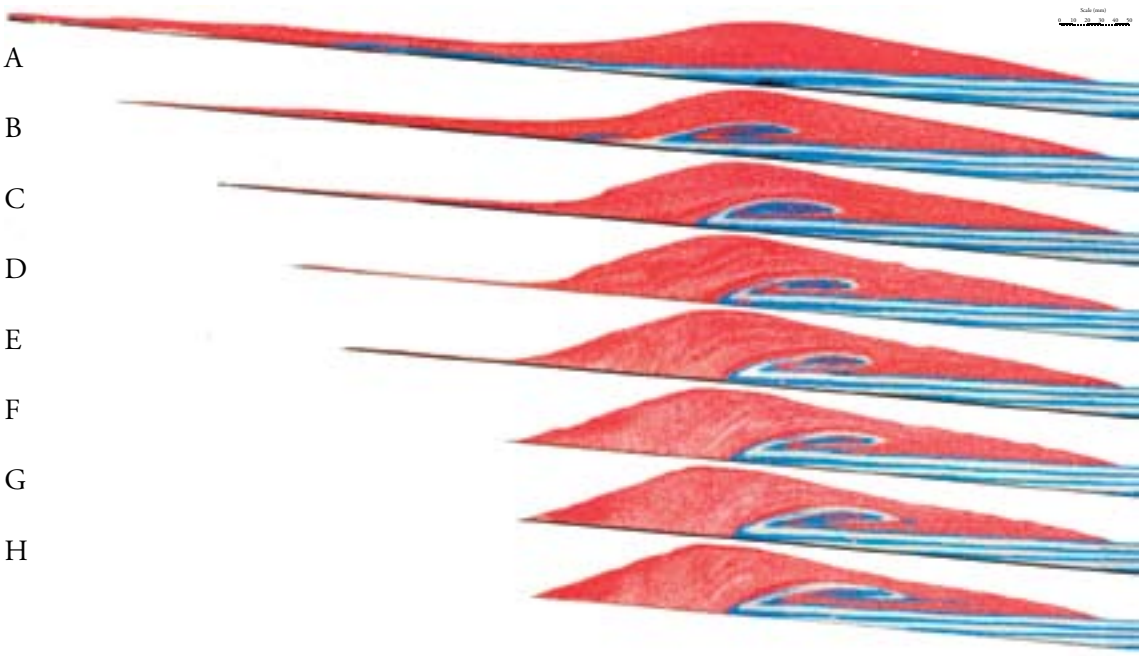

Figure 6.28 Serial sections at 10mm spacing from edge to centre of a 500 cm3 charge, composed of 300 cm^3 of 250 micron silica beads (red), and 200 cm^3 of 250 micron ceramic beads (white) run onto a stratified charge of 250 micron silica beads (blue and white). Ceramic beads within the charge highlight flow pulse bases.

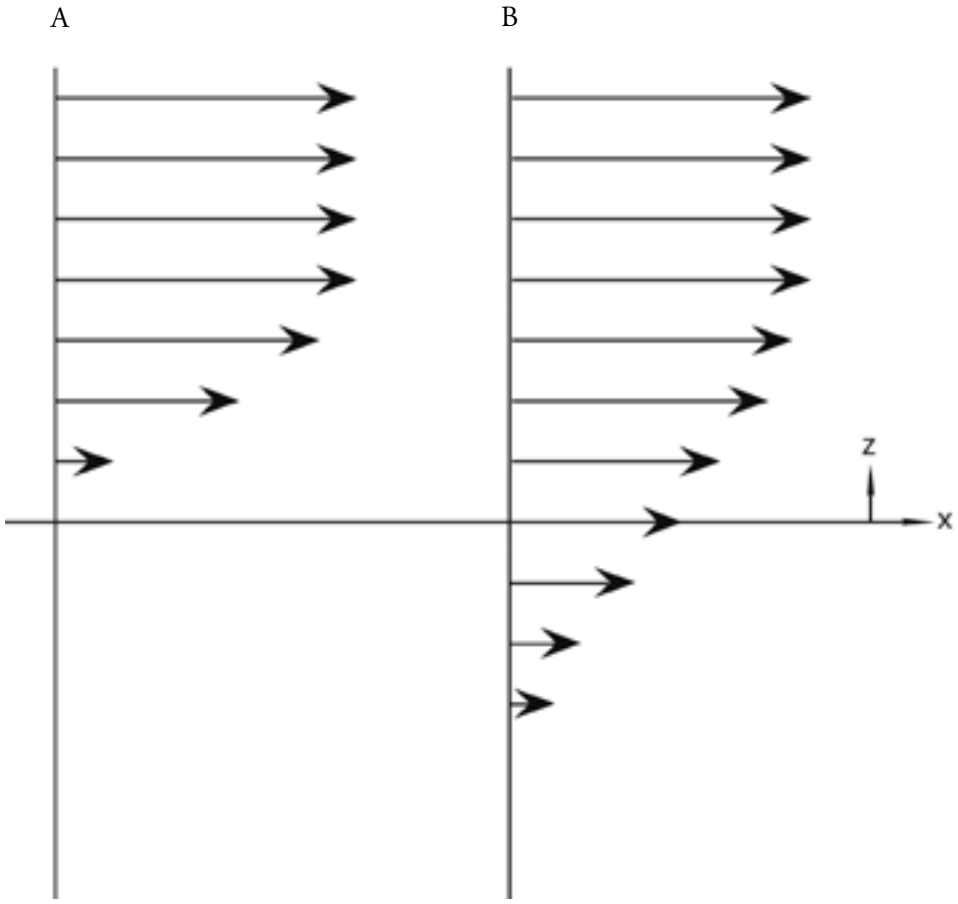

Figure 6.29 Shear profiles of (A) plug flow above a static substrate, and (B) plug flow with remobilised substrate.

a velocity gradient is developed with it. Figure 6.29 illustrates the velocity profile development from a) an active flow above static substrate and b) probable velocity profile through a shearing flow into a substrate remobilised by granular temperature conduction. It should be noted that due to the nature of granular temperature, increased granular temperature is accompanied by increased dilation (and therefore reduction in bulk density. As a result, the velocity profile is paired with a density variation profile, with the over-riding flow having high dilation (low bulk density) in comparison to the slower moving, denser basal zone of the flow, and the stationary, dense static substrate.

The very short period of deposition in these unsteady currents (<0.25 s) suggests that the growth rate of K-H-like instabilities is large. The rapid deposition in the flume allows us to capture an instantaneous representation of the growth of these features, and experiments such as that demonstrated in Figure 6.16 allow us to accelerate instability growth to investigate the geometry and propagation of these instabilities at different points in their growth. In the case of these experiments displacement occurred of up to ~100 mm. Using a flow velocities of 1 - 4 ms^{-1} (see Chapter 4), remobilisation, instability growth and freezing (deposition) occurred in between 0.025 - 0.1 seconds. The growth rate for the instability amplitude can therefore be calculated at sitting between 0.5 - 2 m s^{-1}.

Growth of K-H-like instabilities in granular media has been observed in several different situations (Goldfarb *et al.*, 2002, Caicedo-Carvajal *et al.*, 2006), but not in flume experiments utilising a static loose granular substrate. The predisposition of these experiments to generate K-H-like instabilities suggests that these features are relatively common in thin shearing systems, and have simply not been recognised before - either as a result of material selection / lack of colouring, and/or the ability of sidewall interaction to impair feature development coupled with a scarcity of work investigating the internal structure of flume deposits.

6.5 Conclusions

Thin shearing granular flows are capable of remobilising large quantities of loose substrate material through granular temperature conduction (i.e. momentum transfer between mobile and stationary particles). The velocity and density profiles through the flow and remobilising substrate which develop as a product of this encourage the development of K-H-like instabilities. The propogation of these features through continued flow may displace remobilised substrate significant distances, and redeposition of substrate material is controlled by the depositional regime dominant in the bulk flow. While the highly unsteady and brief flows observed in this flume cause rapid sedimentation and the capture of the growth of these features, steady flow with continued sediment supply may be expected to propagate K-H-like instabilities for significant distances. It is likely that continued growth, rotation and downstream propagation of these features would be represented stratigraphically by a very well mixed region at the scale of the instability amplitude - perhaps, for example, providing an explanation for features such as the mixed ground layer (in the Mt St Helens 1980 stratigraphy identified as A0 by Fisher *et al.*, 1987). This layer is represented by one to five beds of poorly sorted mixtures containing uncharred fragments of organic material and soil schlieren from the ground surface mixed with 0~5% juvenile dacite, with some pre-1980 pumice and ash. Some beds consist of reworked underlying soil or tertiary rocks. Perhaps most intriguingly, there is a location where the interface between the basal

contact consists of finger-like injections, containing a mixture of soil and blast dacite fragments into unconsolidated pumice (Fisher *et al.*, 1987).

It should be highlighted that flows with increasing mass flux (and therefore momentum) may be expected to cause substrate erosion in one place, with redeposition occurring only further downstream where the flow dynamics change such that settling can occur.

The degree and nature of reworking is strongly dependant on sidewall interaction, with flow retardation at sidewalls leading to primarily depositional behaviour in contrast to the erosive capabilities observed in the centre of the flume. The transition between the central and edge regions of the flume is marked by a complex interaction of cross-flume material flow.

The findings that erosion and remobilisation of substrate are so prolific in these flume experiments are in themselves of significance in the consideration of any granular avalanche experiments. In terms of comparison to pyroclastic density current deposition, the dimensional analysis carried out in Chapter 3 suggests that these features should be observable in the field. However, to date there is no published material discussing the occurrence of K-H-like instabilities in ignimbrites or smaller volume PDC or debris flow deposits. This suggests that either (a) the features exist but have not been recognised, (b) they produce a broad mixing zone which is difficult to attribute to K-H-like instabilities, or (c) the dynamics of deposition of natural flows vary from experimental runs in flumes. The following chapter will investigate these possibilities, and the ability of these dense granular flume experiments to provide meaningful analogues to pyroclastic depositional mechanisms.

CHAPTER 7: PDC STRUCTURAL RELATIONSHIPS - FLUME VS FIELD

7.1 Introduction

The flume experiments outlined in the previous three chapters have generated a wide variety of deposits and features as a result of granular initiation, flow and sorting mechanisms, and the way in which they interact with varied particle types, substrate materials, and geometries. This chapter will attempt to assess (1) whether these findings are relevant to the study of PDC, debris avalanches (and other geophysical flows), (2) the occurrence (or not) of similar features and structures in the field, and (3) the potential for development of these experiments to improve and refine our understanding of processes within natural granular currents.

7.2 Relevance to Geophysical Systems

In order to assess the relevance of these experiments to geophysical systems, it is worthwhile considering the range of these systems which contain a granular fluid component. First, it must be re-emphasised that PDC occur on a wide spectrum of scales, from small volume, unsteady dense flows with low mobility, through to sustained steady high-mobility flows with lifetimes in the scale of minutes to hours. Secondly, there are several other geophysical systems which should be considered relevant. Other particle laden flows in nature which may be locally or generally related to the processes and mechanisms discussed in this work include a wider range of unsaturated debris avalanches, including snow and rock avalanches. In addition to these there are a wide variety of flows which have water as the interstitial fluid rather than air, including lahars, marine turbidites and fast-moving fluvial currents. These latter systems are not easily comparable to the flume experiments in this work, due to the significant difference in interstitial fluid properties (e.g. viscosity, density) and therefore will not be discussed.

7.2.1 Depositional system and processes

The depositional system observed in the flume experiments is characterised by a shearing mechanism. The total deposit thickness is built by stacks of over-riding pulses. In the horizontal flume bases of flumes A and B the deposit forms through deceleration, energy dissipation and en-masse freezing of the flow head as the granular temperature drops below the granular fluid threshold. The following flow material then deposits as a series of stacked pulses emplaced along inclined shear planes (Figure 7.1).

This model is in line with that proposed by Schwarzkopf *et al.* (2005), and matches closely the analogue modelling experiments carried out by Shea and van Wyk de Vries (2008). The runouts observed in the flume A and B experiments are very short compared to the height:runout ratios of many geophysical flows. This is likely due to a combination of low pore pressure (resulting in very low fluidisation) and the granular jump generated by the rapid break in slope of these flumes. This means that while the sorting initiation and sorting mechanisms investigated in Chapters 4 and 5 are likely to be relevant, the depositional mechanism cannot be directly compared to that which takes place in

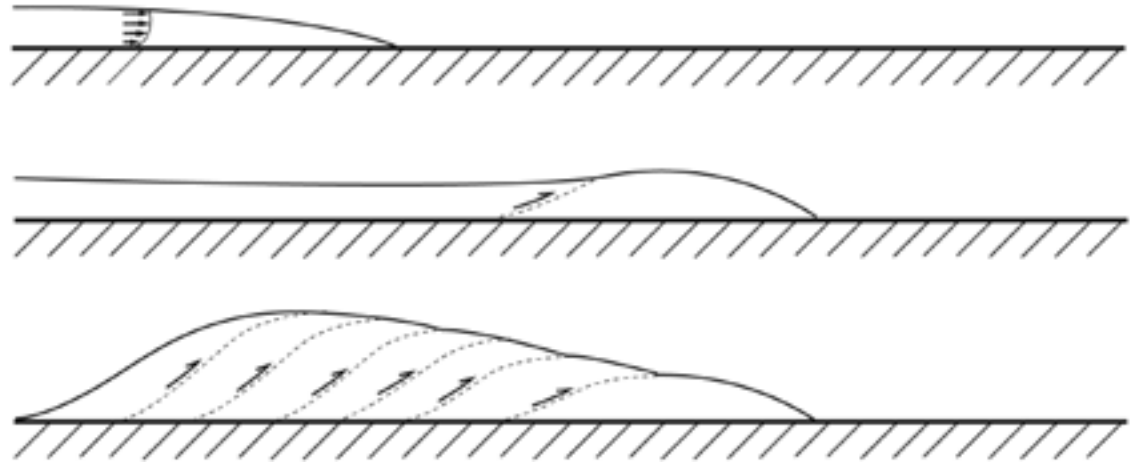

Figure 7.1 Diagram of inferred depositional process and final structure in flumes A and B, showing the presumed velocity profile through the approaching flow and the sequence of aggradation.

long runout debris flows or PDCs. This short runout system is, however very likely to be significant in the investigation of short runout geophysical deposits such as debris avalanches. The work of Shea and van Wyck de Vries (2008) demonstrates that the hummocky surface typified by short runout debris avalanches is a product of stacked over-thrusting flow pulses (Figure 7.2, identified as pressure ridges in Figure 7.3). The work presented in Chapters 4 and 6 indicated that the same processes are occurring in flumes A and B. The scaling of the experiments presented in Chapter 3 was carried out using PDC systems, but the conditions and dimensions of small volume landslides are even more favourable to the experiments, with the reduction of pore pressure being a significant factor.

It is important to note, however, that the resemblance to debris avalanches is not restricted purely

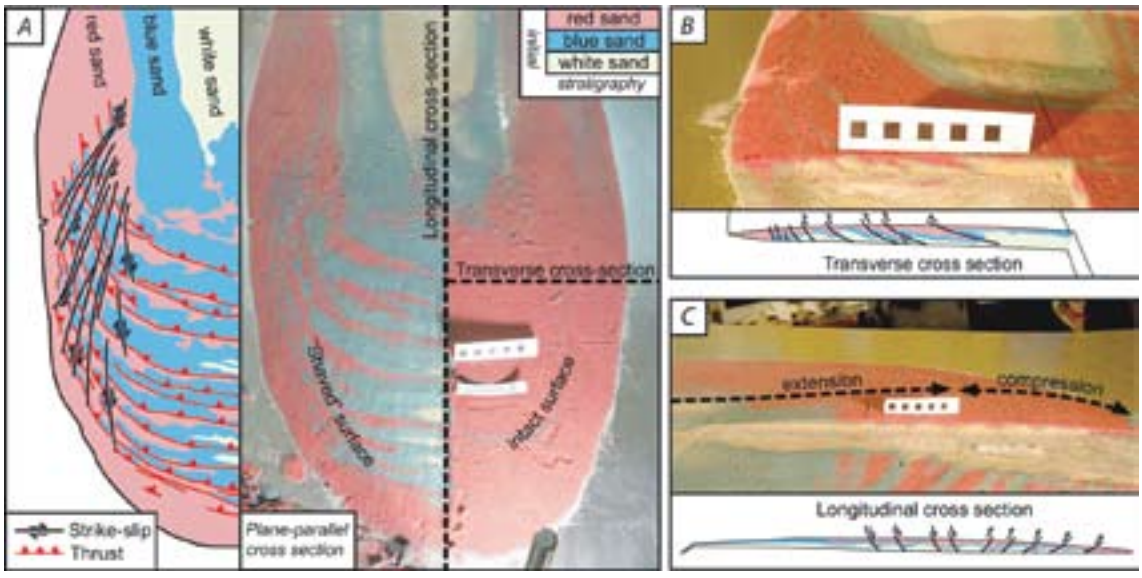

Figure 7.2 Cross sections from some scaled experiments from Shea and van Wyck de Vries, 2008. (A) Types of cross section with base-parallel cross section on left. Note that the lithological repetitions follow thrust-fault orientation, producing a hummocky surface. (B) Transverse and (C) longitudinal cross sections with preserved layering affected by various structures.

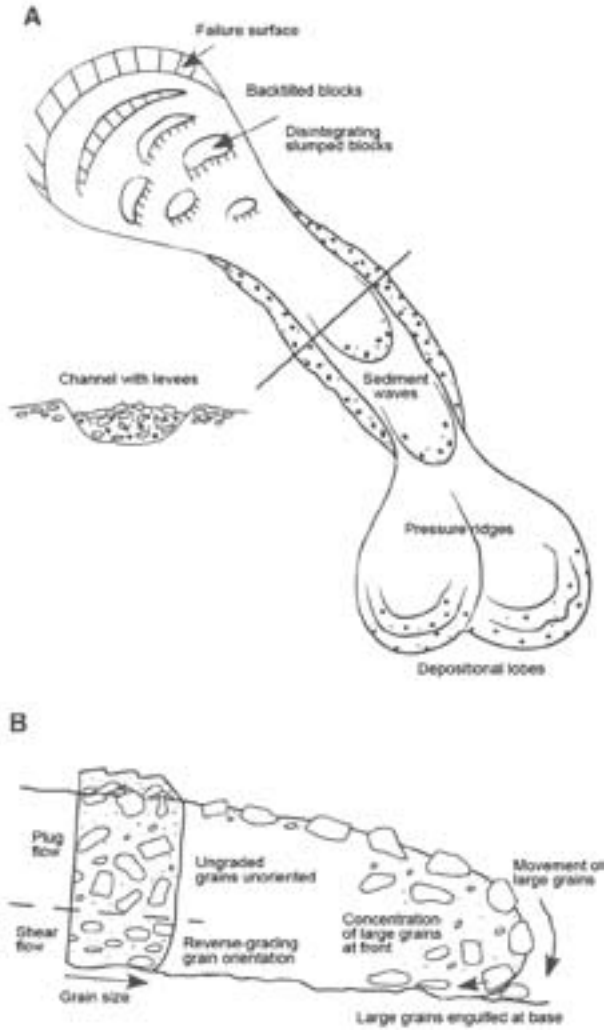

Figure 7.3 Typical debris avalanche morphology, mechanics and deposits. A - plan view showing the geometry of a debris avalanche from the failed surface to the frontal lobes (distorted scale). B – cross-section showing internal structure, main deposits of a debris avalanche and possible sorting mechanisms. (Bridge and Demicco 2008).

to this hummocky terrain. Figure 7.3 illustrates typical debris avalanche features, sorting mechanisms and deposits. The inferred flow mechanism active within the flume experiments (a shearing basal zone below a plug flow, such as that inferred by Schwarzkopf *et al.*, 2005) is directly comparable to that observed in debris avalanches, while the geometrical features typical of debris avalanches each have their analogues in the flume experiments. The head features of back-tilted and slumping blocks are similar to the shearing initiations observed in the flume A experiments (Chapter 4), with the levee formation and size sorting following the same trends. The separate depositional lobes are not observed in these flume experiments, but this is to be expected of highly channelised flume systems with sidewalls.

In addition to small volume debris avalanches, similar scale flows occur from cold small volume PDC initiation. The flows generated by the 1975 Ngauruhoe eruption (outlined in Chapter 3) are typical of this kind of flow, with low fluidisation and hence short runout. The stratigraphies typified by this kind of deposit include lateral levee formation and distal pumice dams (often with hummocky lobate fronts), similar to those seen in Figure 7.3 for non-volcanic debris avalanches.

More problematic is the comparison with larger scale, sustained PDC and long runout highly fluidised landslides. The runout of these systems is associated with more overpassing of material than is achieved in either flume A or B. PDCs in particular are inferred to sediment through progressive aggradation (Branney and Kokelaar 1997), generating a vertical architecture representing temporal variation in the gradually depositing flow rather than vertical variation in a single plug flow pulse (Sparks 1973, 1976). By inclining the runout slope by 5 degrees the depositional system in the flume is modified, permitting far greater overpassing of material (Figure 7.4). This overpassing prolongs the active lifetime of the shearing contacts, and more closely represents the depositional enviromentment

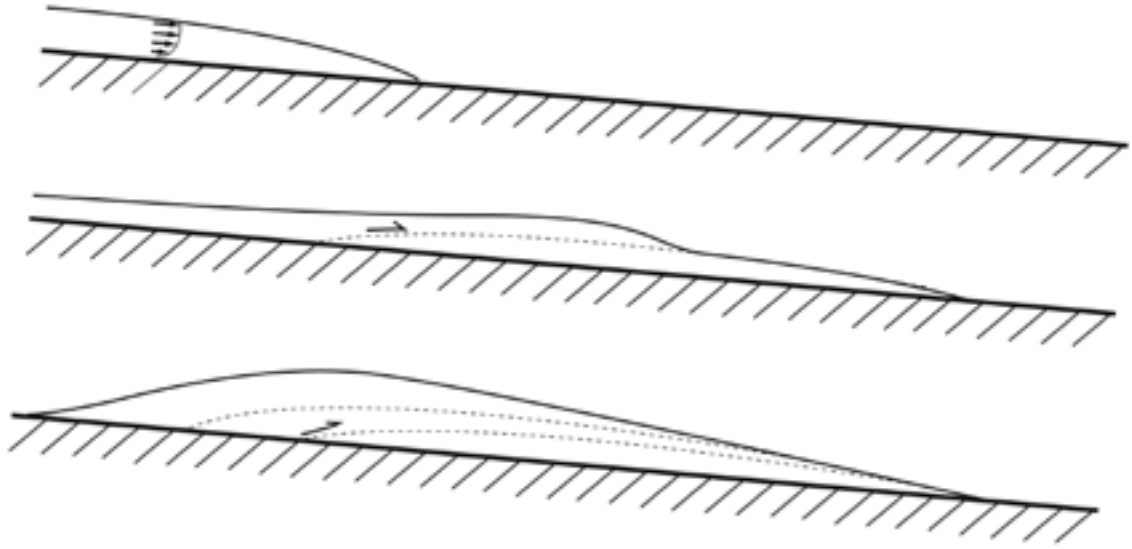

Figure 7.4 Diagram of the inferred depositional process and final structure in flume C, showing the presumed velocity profile through the approaching flow and the sequence of aggradation, based on deposit stratigraphy and observation of deposition.

of geophysical systems. The angles of the shear planes generated in the deposit are greatly reduced. It should be noted that in experiments with multiple charges, later flows interact with steep (angle of repose) proximal-dipping contacts, and the steep shear contacts (Figure 7.1) may again become dominant. This is more significant in the early-forming parts of the deposit, which form before enough proximal deposit can be built up that the topography of the existing substrate can be overpassed.

Even with this modified flume geometry the low mobility of these flows results in very limited aggradational behaviour. Rather, the deposit forms as a sequence of discrete frozen granular plug-like pulses. This re-emphasises the fact that the deposits cannot be considered directly analogous to the deposits formed by a progressively aggraded ignimbrite from a sustained PDC, despite the fact the processes at work are similar. Features preserved in the flume deposits represent snapshots of activity which would be long-lived but spatially transient in sustained currents.

7.2.2 Particulate sorting mechanism

The particulate sorting mechanisms demonstrated in these granular fluids from this study are typical of the mechanisms recognised in any polymict granular system. The general patterns of BNE / RBNE, and proximal/distal/lateral/ventral concentration observed in these flumes are applicable to any channelised granular flow, and therefore have relevance to all of the geophysical systems outlined with a channelised granular fluid dominated current.

In un-channelised systems (e.g. laterally extensive PDC forming a sheet ignimbrite, large scale landslides) the lateral variation formed by particulate sorting might be expected to be supressed, governed instead by local flow dynamics and thalwegs. As a result, levees and distal concentrations of large particles are more likely to be replaced by localised deposition within the aggrading system, as current thalwegs disperse material anisotropically across and along the flow.

The density and particle size scaling makes these experiments particularly useful in investigating the structures which develop in small volume PDC deposits. Landslides and rock or snow avalanches have far less variability in particulate density variation. As a result, the rate of density sorting within these flows might be expected to be significantly reduced. That said, there are still examples of particulate sorting features developing in these more homogenous systems. Figure 7.5 demonstrates 15cm diameter snowballs which have accumulated to form lateral levees at the edge of a snow avalanche (from Jomelli and Bertran 2001).

Figure 7.5 Lateral levees linked to a channel incised through a snow substrate, Champoleon valley, Massif des Ecrins, France. Walking pole for scale, snowballs on the left average 15cm diameter. From Jomelli and Bertran (2001).

As has been dillustrated in Figure 7.3, the sorting effects observed in debris avalanche deposits are very similar to those for small volume PDCs, and produce similar patterns to those seen in the flume experiments. The BNE reverse grading effect is significant, and ultimately responsible for the vertical sorting, and through flow and deposition also lateral and longitudinal sorting. Large particles brought to the upper surface of the flow spall off to form levees. Those at the head of the flow are continuously recycled to form clast-rich terminal deposits, typified by pumice dams in small volume PDCs (see Figure 7.6). This is in line with the work of Felix and Thomas (2004), who demonstrated this particle movement in granular flows, recycling material from the flow head to the edges, and hence forming levees. When combined with the granular sorting mechanisms seen in these flows, large particles become preferentially concentrated at distal and lateral extremes, which agrees with the findings of Vallance and Savage (2000) and Iverson and Vallance (2001).

Highly fluidised long runout PDCs, which have deposition dominated by a granular fluid lower flow boundary zone, are a somewhat more complicated system to consider. The sustained steady flow shown in Figure 7.7 represents a system where the bulk of volume transport occurs in the gas-turbulence dominating the upper flow region. Settling from this basal flow produces a dense basal region of shearing granular fluid. Sedimentation from this granular fluid aggrades a static deposit, implying that any material which is aggraded by this flow must transition through the granular fluid, and hence be subject to the sorting and settling regimes active within this zone.

It is important to note that the contact between the turbulent and granular flow layers (whether diffuse or sharp) is not important solely in terms of settling In addition momentum transfer from

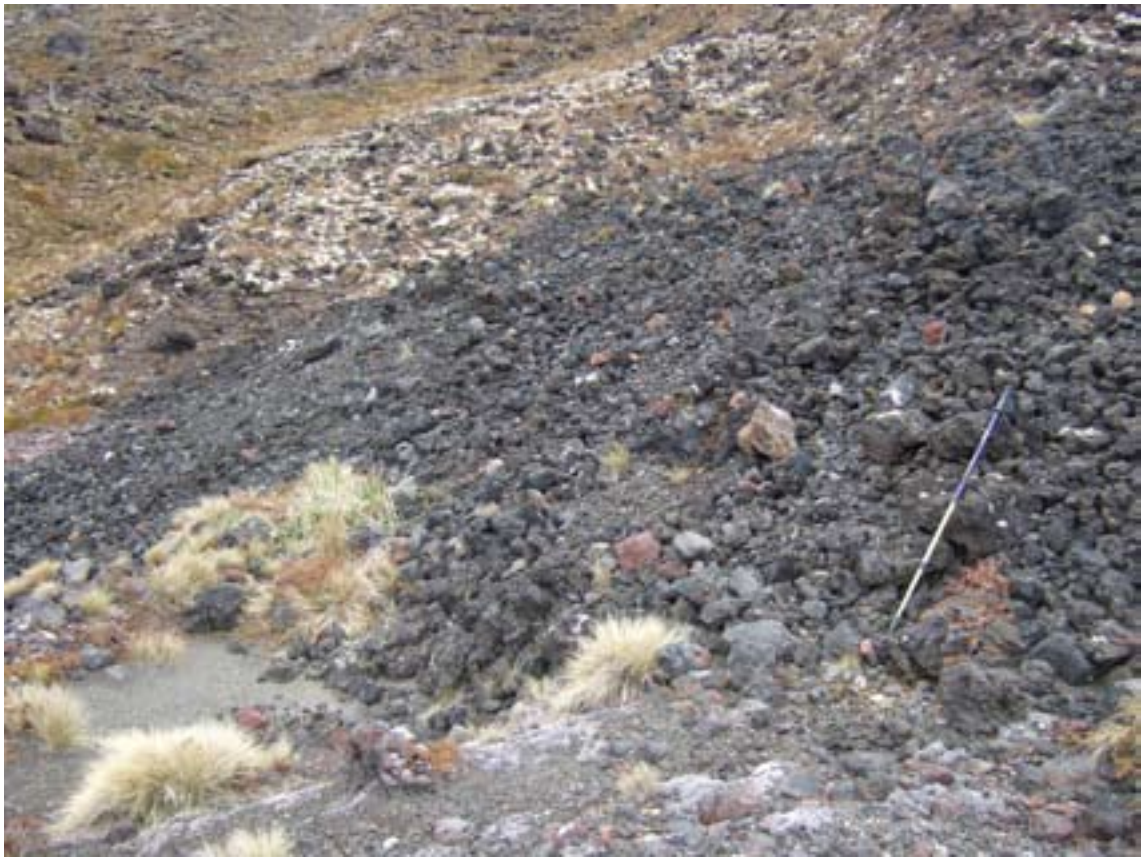

Figure 7.6 Terminal pumice dam on a small volume PDC from an eruption on Ngauruhoe in 1975.

even small particles is able to mobilise large and dense clasts to flow over far greater distances than might otherwise be expected (Dufek *et al.* 2009). The implication of this is that the granular fluid layer is not completely decoupled from the over-riding layer. Energy transfer from the particles moving within the upper turbulent layer (as they interact with the upper surface of the granular layer) is likely to be a significant feature in PDC mobility.

The nature of the contacts between the turbulent gas suspension, the granular fluid, and the substrate is likely to be dynamic, and particularly dependant on the momentum flux of either of the given flow

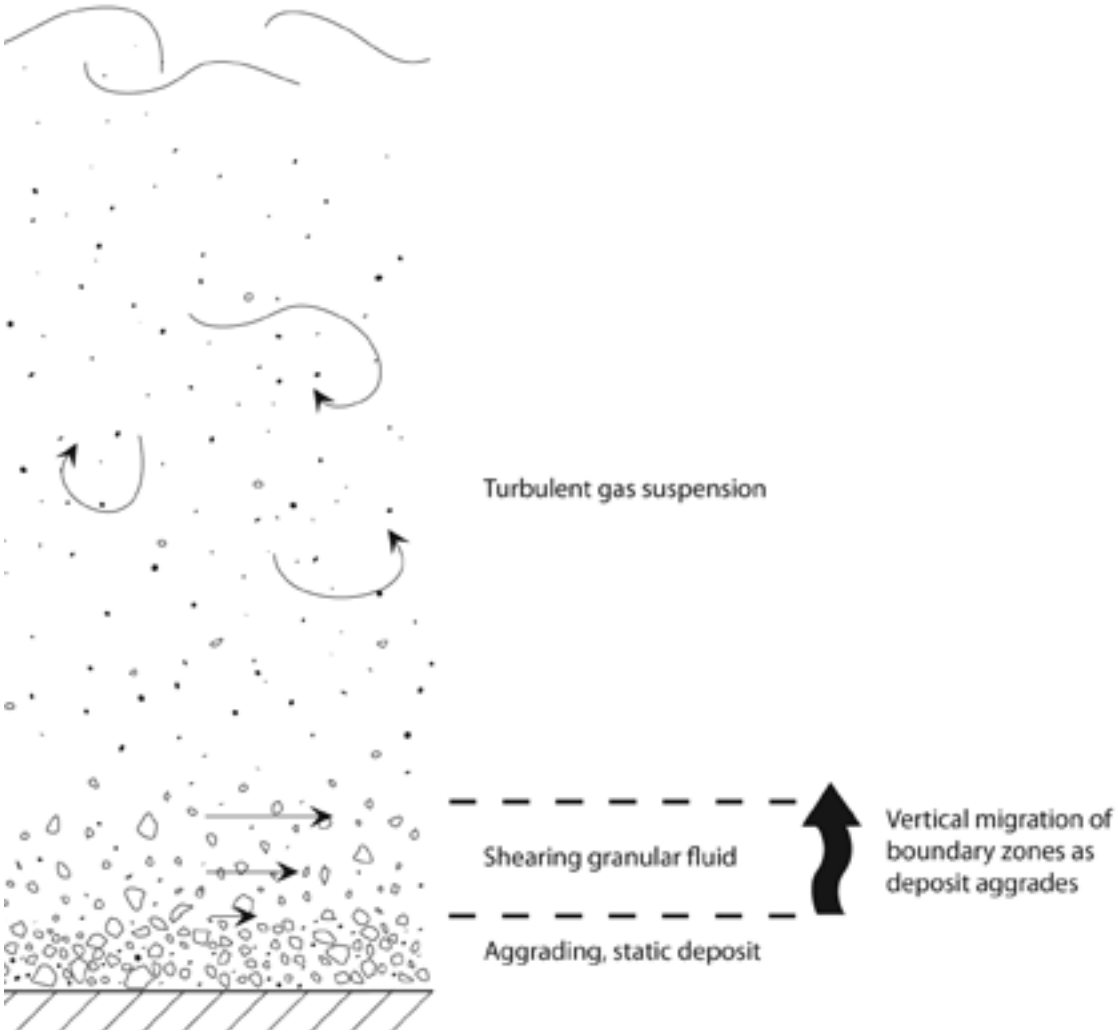

Figure 7.7 Idealised section through a depositing PDC, after Branney and Kokelaar 2002. Nature of boundary zones may be sharp or diffuse

layers. For example, while the idealised section in Figure 7.7 describes a steady flow with a purely depositional regime dominant at both boundaries, it is conceivable (and indeed likely) that if an increase in flow momentum is generated (for example through increased mass flux, or transition onto a steeper slope) the boundary zones will see a propagation of momentum into the lower-energy layers below. The physical result of this would be:

- **Gas suspension - granular fluid interface**. Increased particle interactions will elevate the granular temperature in the lower fluid, expanding and dilating until either a) the dilation reaches a point where effective momentum transfer is hindered, or b) particles transition back from the granular fluid into the turbulent suspension. In the case of a) it might be expected that the increased dilation could act as a buffer, preserving the granular flow regime in the case of short-lived or small momentum fluxes. The result of b) would be top-down thinning of the granular fluid layer, potentially to a thickness of 0. In this extreme case the PDC would develop a profile where sedimentation occurred as direct fallout from the turbulent

suspension (at least until this fall out generated a new granular fluid basal layer).

- **Lower flow boundary zone** between the granular fluid and the substrate. An increase in momentum transfer would, again, increase the granular temperature of the lower layer. This would dilate the substrate allowing the shear profile to penetrate into it, entraining the substrate into the active flow. This would be the proposed mechanism for K-H-like shear generation between a substrate and flow unit. It should be noted, however, that K-H-like instabilities can grow at any velocity shear surface, and therefore are able to form and grow within even an aggrading system. The reason to highlight their formation in this erosive context is that erosive surfaces have much higher visual contrast than the internal structure of single ignimbrite units. Therefore it is K-H-like features developed at these (initially) erosive surfaces which are more likely to be identified in the field.

7.3 K-H-like Instability growth conditions

The prevalence of K-H-like instability structures within the flume experiments raises questions over why fully developed instabilities have not been observed in natural pyroclastic flow deposits. Several possibilities may provide an explanation;

1. The scaling of the flume experiments produces features which are not observed at field scale.

2. The flow mechanics within the flume are different to those within PDCs.

3. The structures do exist but have not been recognised.

4. The structures exist but migrate laterally through a steady current, leaving no recognisable feature other than a well mixed zone in their wake

5. PDC flow boundary zones migrate vertically too rapidly for K-H-like instability growth to occur.

6. Dense shear flows at the base of PDCs are too thin to allow K-H-like instability growth at significant amplitudes.

The scaling calculations performed in Chapter 3 suggest that explanation 1 (scaling) is unlikely, but it is possible that there are processes at work within PDC basal shearing zones which perturb the formation, or have simply not been recognised, and therefore scaled for. Alternatively, it may be that the poorly scaled pore pressure in the flume experiments is significant in their development.

Option 2, that the mechanics in the flume are different to those in PDC is possible, although unlikely. The model of progressive aggradation for PDC deposition is capable of explaining and describing the full range of ignimbrite stratigraphies, and suggests dense grainflow can be dominant at the (depositionally critical) lower flow boundary zone. The one stumbling block to this may be the inferred high pore pressure in high mobility PDCs, which is not present in the unfluidised

experiments.

Possibilities 3 - 6 all imply that K-H-like growth is plausible, but either unrecognised (option 3), leave no lithological record (option 4), or are prevented from growing to significant sizes due to restrictions or variations in the lower flow boundary conditions (options 5 and 6). Whilst the suggestion that the structures exist and have simply not been identified before may seem irrational, there is good reason to consider this option. Importantly, PDC deposits are frequently uniform in colour with often only broad structural heterogeneity such as pumice rafts or lenses. This uniformity has been part of the issue in deciphering the precise flow and deposition mechanism, and in turn could easily mask complicated internal structure.

Assuming that progressive aggradation is the dominant process for ignimbrite-forming PDC deposition, then the steady state currents necessary are very different to those observed in the unsteady flume deposits. The K-H-like structures observed in the flume deposits are preserved precisely because the deposition is nearly instantaneous as the granular fluid deflates and freezes. In a sustained current the lower flow boundary zone can be expected to remain active for much longer timescales. As a result, and "growing" K-H-like instability would continue to travel downstream. This would result in continued mixing of entrained substrate material within active flow material. When this material finally deposits it has travelled potentially great distances, and may be very well mixed. If occurring as a layer within an aggrading unit this may not be significant. However where this has occurred at a boundary between different units there are several important implications which will be considered later in this chapter.

7.3.1 Mathematical Modelling

Working on the assumption that the flume is an accurate analogue of granular flow at the base of PDCs, and therefore whose depositional processes represent a meaningful analogue to PDC deposition, a series of calculations can be carried out in order to assess whether the instabilities still occur and at what scale within a typical PDC.

A caveat must be made before progressing this section. Granular fluid physics are poorly constrained, and with an absence of governing equations the following calculations are derived from a model for K-H growth in standard Newtonian fluids. Whilst this may not correctly predict K-H-like growth conditions in these granular systems, the calculations are able to correctly predict and specify characteristic wavelengths for K-H-like growth in the experiments. However, there are a number of features exhibited in granular materials which are very similar to features observed in fluids. These include Taylor vortices (e.g. Conway *et al.*, 2004), Faraday instabilities (e.g. Garcimartin et al., 2002), and the granular jump (e.g. Boudet et al. 2007). Work by Gray et al., (2003) demonstrated that hydraulic models are able to capture first-order qualitative features of oblique shocks and bores, while later work by Hákonardóttir and Hogg (2005) showed that through systematic measurement of oblique shocks, slightly modified shallow water equations were able to describe the experimental observations. It therefore is not unreasonable to attempt the modelling which follows.

The calculations are based on a relatively simple model assuming static stability (i.e. the denser layer is

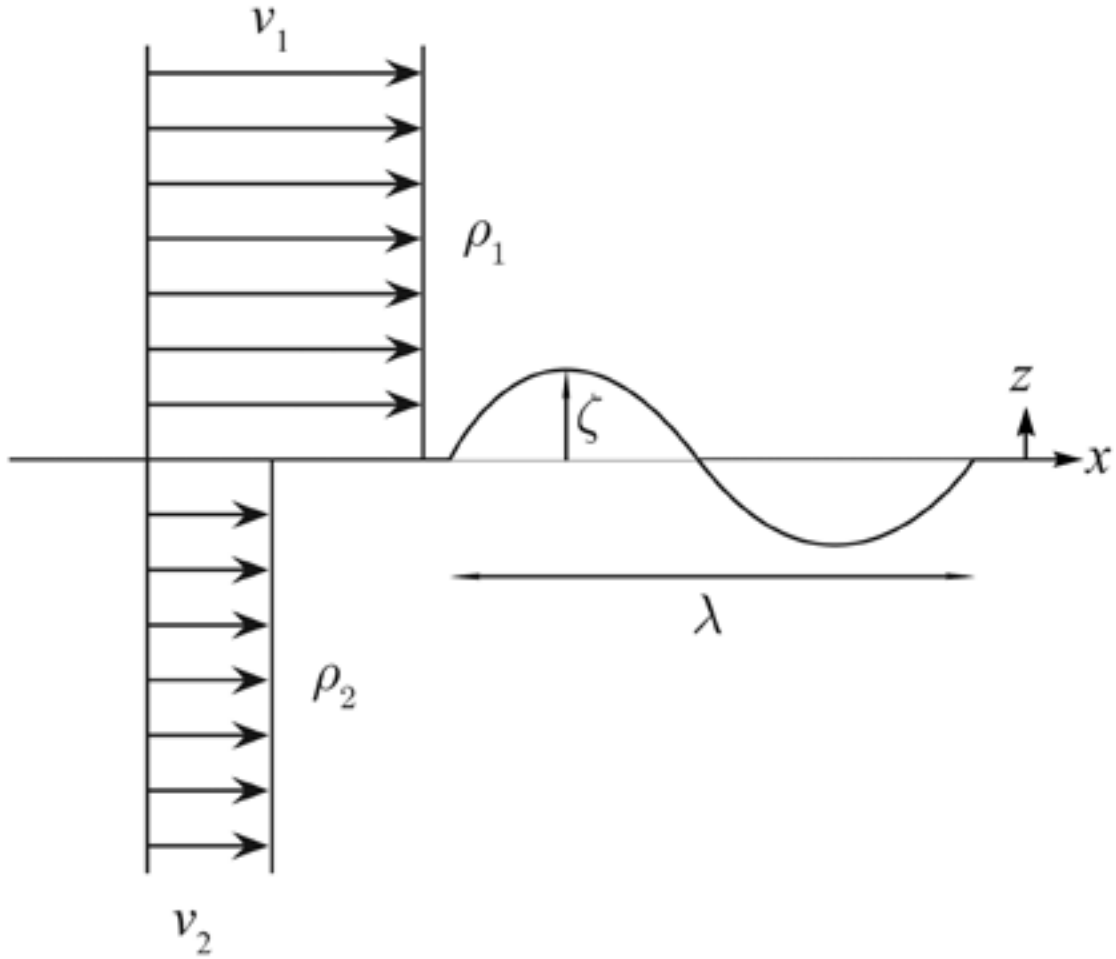

Figure 7.8 Visualisation of the assumed model in subsequent calculations. *v* is velocity, ρ is bulk density, *z* and λ are amplitude and wavelength of the instability respectively. After Kundu and Cohen (2004).

below the less-dense layer), and infinitely thick layers with a sharp shearing contact of zero thickness (Figure 7.8). Whilst the static stability of the flow is reasonable (i.e., granular matter must expand to flow, therefore the over-riding material will have lower bulk density than the underlying deposit) the assumptions on layer and shear transition thickness are clearly not ideal (See Figure 6.29 for more realistic velocity profiles through the flow/substrate system). However, these assumptions allow the generation of relatively simple models which should still describe the behaviour characteristics of the system.

Equations that describe the behaviour of K-H instabilities (Kundu and Cohen, 2004) allow for a solution for the formation of K-H instabilities :

$$I_g = \frac{\rho_2 v_2 + \rho_1 v_1}{\rho_2 + \rho_1} \pm \sqrt{\frac{g}{k}\frac{\rho_2 - \rho_1}{\rho_2 + \rho_1} - \rho_1 \rho_2 \left(\frac{v_1 - v_2}{\rho_2 + \rho_1}\right)^2} \qquad [7.1]$$

where ρ is bulk density in layer 1 or 2, v is velocity in layer 1 or 2, g is acceleration due to gravity (9.81 ms^{-2} at sea level), and k is wavenumber. Instability growth occurs only when I_g is complex.

Equation 7.1 has the visual form:

$$0 < A \pm \sqrt{B} \qquad [7.2]$$

The B term in this equation is itself made up of two separate terms

$$B = \frac{g}{k}\frac{\rho_2 - \rho_1}{\rho_2 + \rho_1} - \rho_1\rho_2\left(\frac{v_1 - v_2}{\rho_2 + \rho_1}\right)^2 \qquad [7.3]$$

With the left hand term describing the restorative force (the tendancy for gravity to stabilise any instability growth), and the right hand term describing the shear force (responsible for development of instability). To satisfy the requirement of a complex I_g, it follows that

$$0 > B \qquad [7.4]$$

This makes physical sense, as we require that the shear force is greater than the restorative force. Therefore B is always negative. Under this condition

$$0 > \frac{g}{k}\frac{\rho_2 - \rho_1}{\rho_2 + \rho_1} - \rho_1\rho_2\left(\frac{v_1 - v_2}{\rho_2 + \rho_1}\right)^2 \qquad [7.5]$$

then it follows that

$$0 > \frac{g}{k}\frac{(\rho_2 - \rho_1)(\rho_2 + \rho_1)}{(\rho_2 + \rho_1)(\rho_2 + \rho_1)} - \rho_1\rho_2\frac{k(v_1 - v_2)^2}{k(\rho_2 + \rho_1)^2} \qquad [7.6]$$

Hence

$$0 > \frac{g}{k}\frac{(\rho_2^2 - \rho_1^2)}{(\rho_2 + \rho_1)^2} - \rho_1\rho_2\frac{k(v_1 - v_2)^2}{k(\rho_2 + \rho_1)^2} \qquad [7.7]$$

which may be simplified such that

$$0 > g(\rho_2^2 - \rho_1^2) - k\rho_1\rho_2(v_1 - v_2)^2 \qquad [7.8]$$

which may be rearranged to show that

$$g\left(\rho_2^2-\rho_1^2\right)<k\rho_1\rho_2\left(v_1-v_2\right)^2 \quad [7.9]$$

This allows us to then analyse the boundary conditions for given situations and determine whether K-H instabilities would be expected to grow or not. Rearranging and substituting various terms into this equation generates a number of useful forms. Firstly, we define the wavenumber, k, in terms of the instability wavelength λ;

$$k=\frac{2\pi}{\lambda} \quad [7.10]$$

This can now be rearranged into equation 7.9

$$\frac{\rho_2^2-\rho_1^2}{\rho_1}<\frac{k\rho_2\left(v_1-v_2\right)^2}{g} \quad [7.11]$$

Values for v_1 can be measured for the flume experiments and field analogues. v_2 is a static layer within these experiments, therefore 0, and the bulk density of the static layer (ρ_2) is known. In this way we can calculate the right-hand side of equation 7.11 and therefore are left with

$$\frac{\rho_2^2-\rho_1^2}{\rho_1}=a \quad [7.12]$$

This simplifies to the quadratic form

$$-\rho_1^2-a\rho_1+\rho_2^2=0 \quad [7.13]$$

Hence we can assess the bulk density (and therefore relative inflation) of the upper layer in flows which demonstrate K-H-like structures.

Rearranging equation 7.11 in terms of velocity flow velocity

$$v_1\geq\sqrt{\frac{g\left(\rho_2^2-\rho_1^2\right)}{k\rho_1\rho_2}} \quad [7.14]$$

This equation can finally be developed to consideration of granular media, substituting the terms for bulk density with terms for particulate concentration, multiplying particle density by phi. We are now able to assess characteristic velocities for given instability wavelengths in a wider range of geophysical situations

$$v_1\geq\sqrt{\frac{g\lambda}{2\pi}\left(\frac{\phi_2}{\phi_1}-\frac{\phi_1}{\phi_2}\right)} \quad [7.15]$$

This equation produces the minimum velocities at which K-H-like instabilities of given wavelength may form, assuming particulate concentrations for each layer of ϕ_1 and ϕ_2. These are plotted in Figure 7.8.

It is worth noting here that as the difference between ϕ_1 and ϕ_2 increases in a system with static stability,

$$\frac{\phi_1}{\phi_2} \rightarrow 0 \qquad [7.16]$$

And therefore as the upper flow becomes more dilute

$$\frac{\phi_2}{\phi_1} - \frac{\phi_1}{\phi_2} \approx \frac{\phi_2}{\phi_1} \qquad [7.17]$$

7.3.2 Results

Data presented in Figure 7.9 confirm the growth of K-H-like in the laboratory scale experiments ($\lambda \approx$ 0.15m, $v_1 \approx 2 ms^{-1}$, $(\phi_2/\phi_1)-(\phi_1/\phi_2) \approx 0.5$, with $\phi_1 \approx 0.45$, derived from 30% expansion from $\phi_1 \approx 0.6$ – a random packed static pile of spheres). The minimum growth condition plot for $(\phi_2/\phi_1)-(\phi_1/\phi_2)$ = 0.5 suggests that these velocities permit instabilities to grow at wavelengths of up to approximately 10m. Velocities more typical of PDCs permit instabilities to grow at wavelengths over 100m. Assuming the model is representative of the physics within PDC, the implications of these results are multiple:

1. Granular flows in PDCs are always unstable to short waves if $v_1 > v_2$.

2. K-H-like instabilities are capable of growing in the typical range of velocities and particulate concentrations seen in natural PDCs. Wavelengths between 0-100m are plausible.

3. Dense flows (low contrast between layers) experience K-H-like growth at lower velocities due to a reduced restorative force.

4. Increasingly long wavelengths become possible with increasing velocity contrast.

It should be re-iterated here that shear flow only occurs in the dense basal region of a PDC. At lower particle concentrations the turbulent regime takes over, and bed forms transition into the hummocky / duneform (cross bedded) styles seen in classic pyroclastic surge deposits. The transition from laminar to turbulent flow can be described using the dimensionless Reynolds number for a flow. The Reynolds number for sediment-fluid mixtures can be defined as:

$$N_R = \frac{\rho_b v d}{\mu} \qquad [7.18]$$

Where ρ_b is bulk density, v is mean flow velocity, d is flow thickness and μ is viscosity. From this it

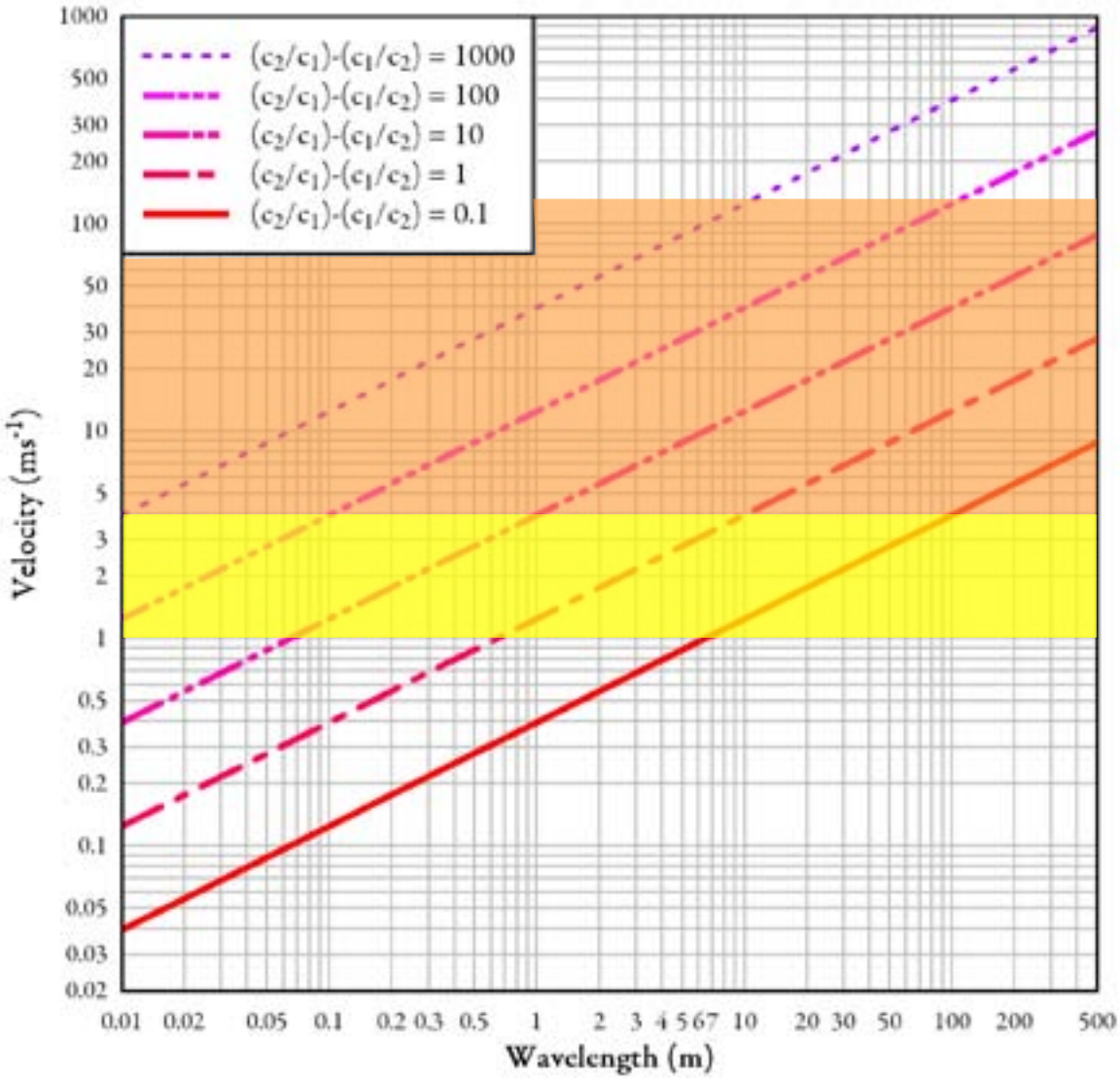

Figure 7.9 Graph demonstrating minimum velocity necessary for K-H-like instability growth at various example particle concentration contrasts across the shear contact. The area above each line represents the region in which K-H-like instabilities are able to grow. The yellow region indicates the velocity field represented by the laboratory flume experiments, and the orange region indicates the approximate velocity field occupied by natural PDCs. Particle concentration contrast in dense granular fluids flowing over a static loose packed substrate is in the order of 1.

can be shown that using realistic dense PDC parameters of ρ_s =2,500 kg m^{-3}, v =10 m s^{-1}, d =1 m , μ = 10^3 Pa s , giving N_R=25. This is well below the threshold for transition between laminar and turbulent flow (N_R =500 - 2000).

7.3.3 Limitations

There are some limitations with this model which need to be considered. Firstly the model assumes a zero-thickness transition between layers. In real shear flows it is more usual to experience a velocity gradient as you pass from one layer into the next (Figure 7.10). With velocity gradients present, we might also expect bulk density differences. Reduced kinetic energy in slower moving regions will

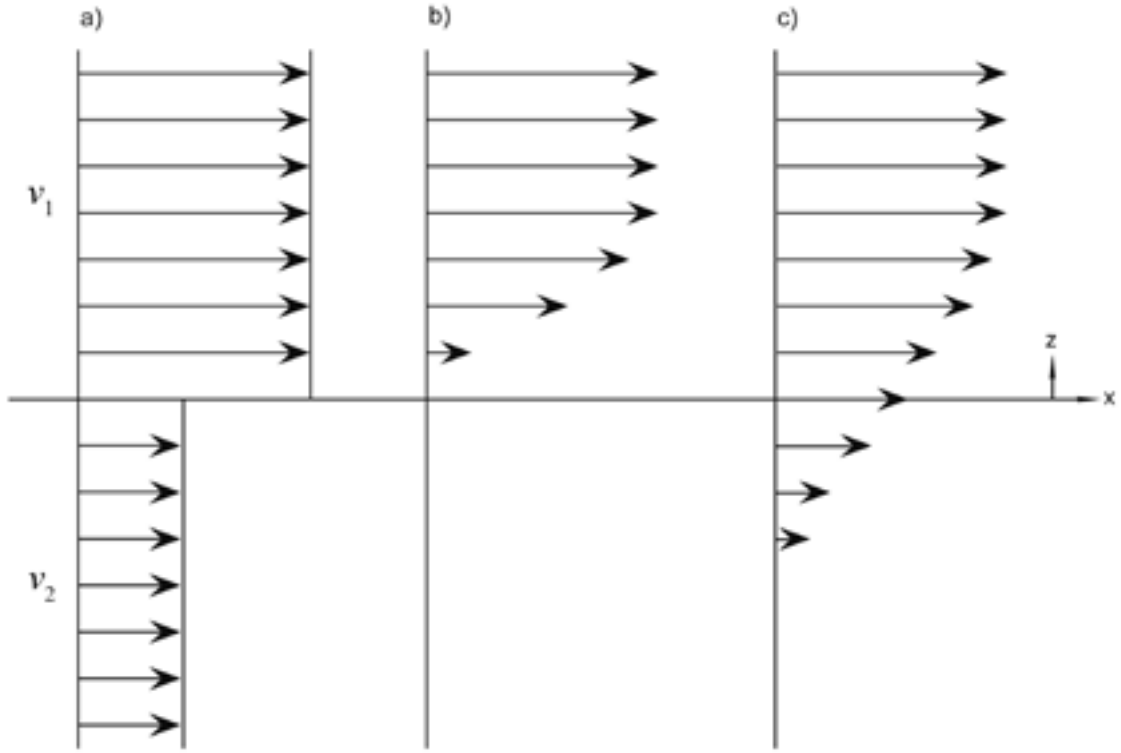

Figure 7.10 Schematic of shear velocity profiles across a contact between two layers. A) the profile assumed in this numerical modelling b) typical velocity profile of a shearing layer over a static bed, c) inferred profile for a remobilisation and entrainment of substrate within the shearing zone.

lead to reductions in granular temperature and therefore localised deflation. Whilst the reduction in velocity will tend to hinder formation of K-H-like instabilities, the reduction in density contrast will coincidentally reduce the restorative force, negating at least some of that effect. Detailed study into the relationship between shear flow velocity profiles and the inflation of granular materials in such an environment would be necessary in order to tease out the precise balance of effects in this situation.

A second limitation to be considered is the models reliance on infinite layer thickness. Both PDCs (assuming progressive aggradation) and the laboratory flume experiments are thin flows with aspect ratios (flow length : flow thickness) in excess of 100:1. As a result there is a possibility that this model will produce K-H-like instabilities in situations where natural PDCs cannot. Typical of this might be the example of 100m scale instabilities in fast moving PDCs. If the dense basal region of the flow is only tens of centimetres thick it is difficult to visualise the formation of K-H-like structures more than tens of centimetres in wavelength.

Finally, the model states only the conditions in which K-H-like instabilities may grow. The actual time it takes to form these structures may be incompatible with the sedimenting conditions within PDC even if the mechanics within the flow are otherwise suitable. If PDC deposits progressively and rapidly aggrade it is easy to visualise how growing K-H-like structures may be buried before developing into visible features.

7.3.4 Conclusions of K-H-like modelling

It must be recognised that no conclusive evidence has been found for the preservation of growing K-H-like instabilities within any single ignimbrite units. Due to the ubiquitous growth conditions at shearing granular fluid/substrate contacts suggested by both the analogue and mathematical modelling conducted in this work we must consider the various explanations.

1. The scaling of the flume experiments produces features which are not observed at field scale.

This has been almost certainly eliminated by the mathematical modelling carried out in this section. The scaling of the experiments, and the modelling both suggest these features should grow in PDC scale systems. The only caveat to this is if the generation of shear instabilities in granular fluids is very significantly different to that in other shearing systems. The fact that Newtonian fluid physics has successfully been applied to granular applications such as the granular jump (e.g. Gray et al., 2003; Hákonardóttir and Hogg , 2005) supports the validity of the relatively simple modelling carried out in this work.

2. The flow mechanics within the flume are different to those within the PDC.

This is unlikely; the settling of material from a turbulent suspension will form a dense basal layer in these flows, resulting in the build up of a granular fluid basal zone. The model explains ignimbrite stratigraphy formation well, and features such as granular fluid particulate sorting within PDCs (e.g. BNE/RBNE) require a granular fluid. However, until such time as conclusive measurements can be made within an active (and depositing) PDC, the absence of a granular fluid cannot be entirely ruled out. Furthermore, the close relation of these experiments to smaller scale short-runout PDC and debris avalanches provides significant opportunity in the future to explore these deposits for similar features.

3. The structures exist but have not been recognised. 4. The structures exist but migrate laterally through a steady current, leaving no recognisable feature other than a well mixed zone in their wake

A far more likely explanation is a combination of options 3 and 4. Steady-state flow in a long runout PDC is likely to generate long-lived shear interfaces at the basal region of the flow. Any growing K-H-like instability will progress along this contact, mixing as it goes. The K-H-like amplitude growth velocities (0.5-2ms^{-1}) and the necessary timescales for ~100mm wavelength instabilities in relatively slow laboratory flume experiments calculated in Chapter 6 (0.025 - 0.1 s) not only imply that the second - minute timescales expected in a steady flow are long enough for this to happen, but also tend to rule out the possible explanation (option 5) of rapid burial by a migrating aggrading lower flow boundary zone; with these growth rates even in a rapidly depositing system at least some form of partially developed K-H-like growth would be expected.

6. Dense shear flows at the base of PDCs are too thin to allow K-H-like instability growth at significant amplitudes.

The final option - that the granular fluid base is too thin to generate significant amplitudes of

instability is difficult to either prove or disprove. Without the observation of PDCs in motion, we are left assessing their deposits to infer the thickness of the transient flow architecture. However, we know that small volume laboratory flume charges generate flows that are a maximum of 20mm thick before contacting the substrate, and that the interaction of these flows with the substrate are able to generate instabilities with an amplitude of up to 30mm. Small volume, single pulse, unsteady PDCs generate terminal pumice dams on the order of 1-2 meters high, and these are a product of granular flow sedimentation. The faster, larger, more sustained currents are unlikely to have granular flow layers of this magnitude; it is likely that the much higher velocity and fluidisation encourages the thinning of this layer considerably. However, even assuming a 20cm thick granular layer we might expect instability amplitudes of up to 30cm. For them to be truly invisible within the deposit, PDCs would require a basal granular flow layer smaller even than that seen in the flume experiments. In a dynamic flow passing over complex terrain, with individual thalwegs of current migrating over time it is difficult to conceive of millimetre scale granular flows maintaining an form of coherence at the velocities observed in PDCs (up to 120ms^{-1}.)

7.5 Shear instabilities in the field

In order to identify K-H-like in the field, then, we must look for:

- Visual contrast in layers where rapid deposition may preserve growth structures
- Well mixed zones of continuous or increasing thickness in the direction of flow

The best target for visual contrast and rapid deposition is the basal contact of ignimbrites. Firstly they have more clear visual contrast than within the bulk of an aggrading unit. Secondly, the base of any PDC unit represents the temporal point in the flow at which momentum transport changes from a high-energy erosional regime, to a lower energy depositional one.

The mixed zones within aggrading ignimbrites are a far more difficult, and less informative target, and were not prioritised in this work.

7.5.1 Tenerife

Tenerife in the Spanish archipelago of the Canary Islands (Figure 7.11) was chosen as the primary field location, due to its outstanding suite of well exposed Pleistocene ignimbrites. It is an ocean island, built on the remnants of three Miocene basaltic shield volcanoes. Subsequent to this, a central stratovolcano (Las Canadas) was emplaced, reaching maximum dimensions of approximately 40km diameter, and 4500m altitude (Carracedo *et al.* 2002). A series of Plinian / Ultra-Plinian eruptions of the Las Canadas edifice occurred between 160-220ka, probably forming the 16 x 9km caldera (although there is some suggestion (e.g. Carracedo, 1994) this may be related to massive flank collapse landslides, represented by the huge Guimar and Orotava valley scars), and depositing the wide-ranging suite of ignimbrites. These are best exposed in the southern Bandas del Sur region of Tenerife (see Figure 7.8), where the desert-like conditions preserve the deposits to an outstanding degree. PDC deposits span a wide range of lithologies from fines rich to fines depleted, lithic charged, pumice

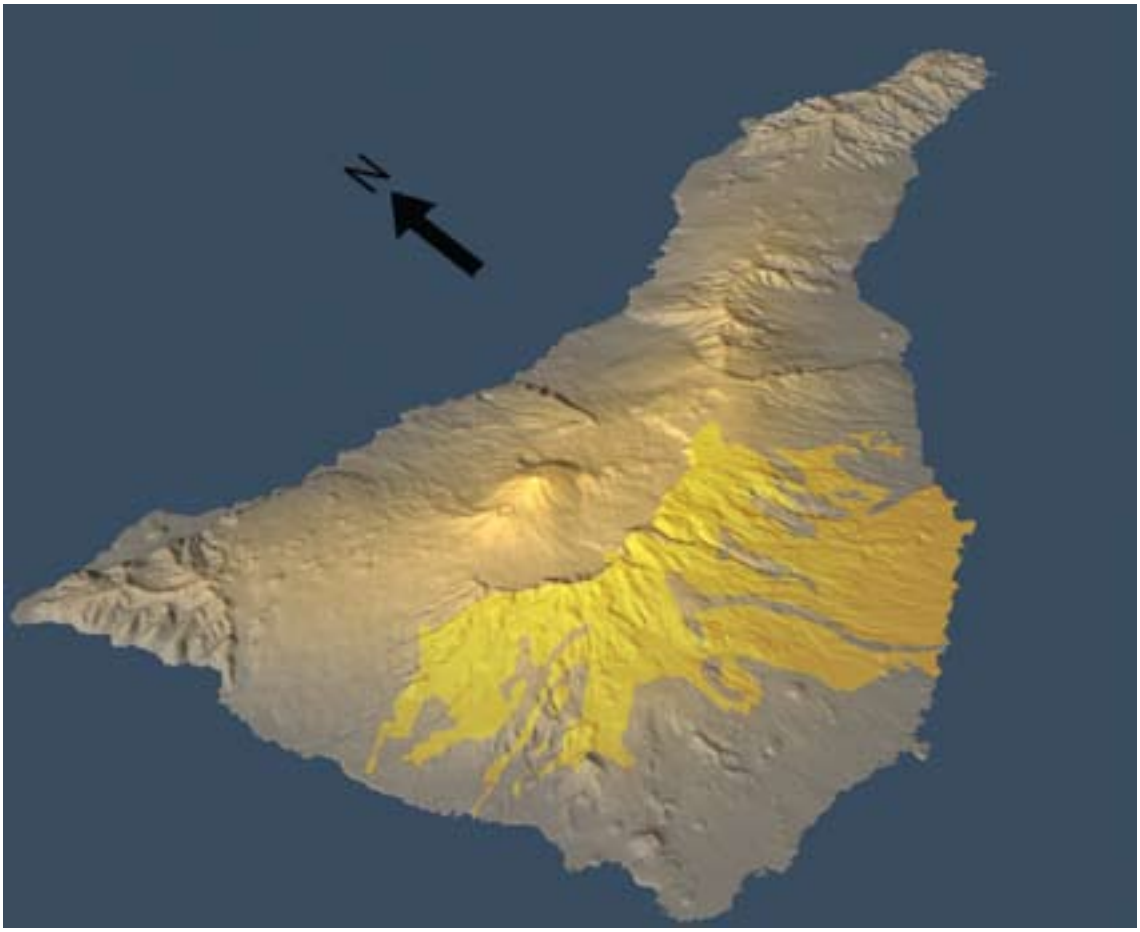

Figure 7.11 Digital elevation model constructed from the Shuttle Radar Topography Mission (SRTM) Version 2, based on 1 arc-second resolution data (see Farr *et al.* 2007 for mission data and processing information). Pico del Teide - 3718m above mean sea level (AMSL) - can be clearly seen sitting within the broad Las Canadas caldera, visible as a prominent curving ridge to the south (locally exceeding 2600m AMSL). Region highlighted in yellows marks the approximate extent of the Canadas Series volcanic rocks in the south of the island (Bandas del Sur formation, outline derived from Gill *et al.* 1994).

charged, and both welded and non-welded units. Channelisation varies considerably, with different PDCs (and individual PDCs longitudinally) having lateral extents varying in orders of magnitude (m - km)

There are very few palaeosols present between the Tenerife ignimbrite units, suggesting either very rapid sequential emplacement, climatic conditions that did not allow palaeosols to develop (unlikely, as palaeosols are locally present), or erosive basal contacts. These contacts are often sharp, and there are numerous examples of channel cuts and fills. Presumably the majority of the PDC deposits (i.e., ignimbrites) propogated offshore, with the Bandas del Sur deposits representing relatively proximal deposits as the flank valleys level out below ~15°.

One of the clearest pieces of evidence for the erosion, remobilisation and redeposition of substrate material by PDCs was found near El Rio, where a 2m thick ignimbrite sits above a thin (20mm) ash fall layer and 1m thick highly pumiceous ignimbrite (Figure 7.12).

Figure 7.12 Fines-rich ignimbrite (red/brown) above a broken ash fall layer and pumice-rich ignimbrite. Flow direction interpreted as approximately towards the reader. Arrows indicate material lifted from the lower fall layer into the upper flow layer, through erosion of the ash fall layer. Location: 28°10'14.24"N 16°29'26.85"W, looking West.

The breaks in the ash fall layer are interpreted as erosive scours due to individual (and most likely migrating) thalwegs in the over-riding flow. The diffuse contact in these areas is derived by entrainment of material from the lower ignimbrite into the basal shearing zone of the active flow. This remobilised material is clearly visible in the upper unit (indicated by arrows), and seems in some places to be lifted as much as 40cm into the flow. The majority is within 10cm (vertically) of the contact. Remobilised material is clearly visible above apparently unbroken in-situ ash layering, suggesting this material has been remobilised from further deposits upstream. Without a perpendicular section it is impossible to assess how far this material may have travelled to gain any insight into the ratio of vertical to longitudinal transport distances.

A similar diffuse contact, showing the remobilisation of substrate into the overpassing flow was observed at a road section 1.3km SW of Arico (Figure 7.13). In this case a fines rich flow unit is overpassing a pumice fall layer. Remobilised pumice clasts are dispersed over a distance of at least 20cm from the contact. Longitudinal travel, again, cannot be measured, but judging from the similarity in appearance between the pumice clasts in-situ within the fall layer, and those remobilised ito the flow, it is unlikely that they have travelled a short distance probably for no more than a few tens of seconds. Angluarity, size and roundness are not appreciably effected, and it might be expected that a collisional grainflow would abraid pumice clasts readily.

Smaller scale features at the basal contact are relatively common in the Las Canadas ignimbrites. Figure 7.14 shows an oblique view of the base of the Poris ignimbrite, with a dashed line highlighting

Figure 7.13 Contact between a pumice fall layer and overpassing fines-rich ignimbrite. Pumice clasts are being remobilised from the fall layer into the flow. Location: 28°10'14N, 16°29'26"W.

the geometry of a shearing feature. This photo also gives a good indication of some of the problems

Figure 7.14 An oblique view of the base of the Poris ignimbrite, with a dashed line highlighting the geometry of a shearing feature.

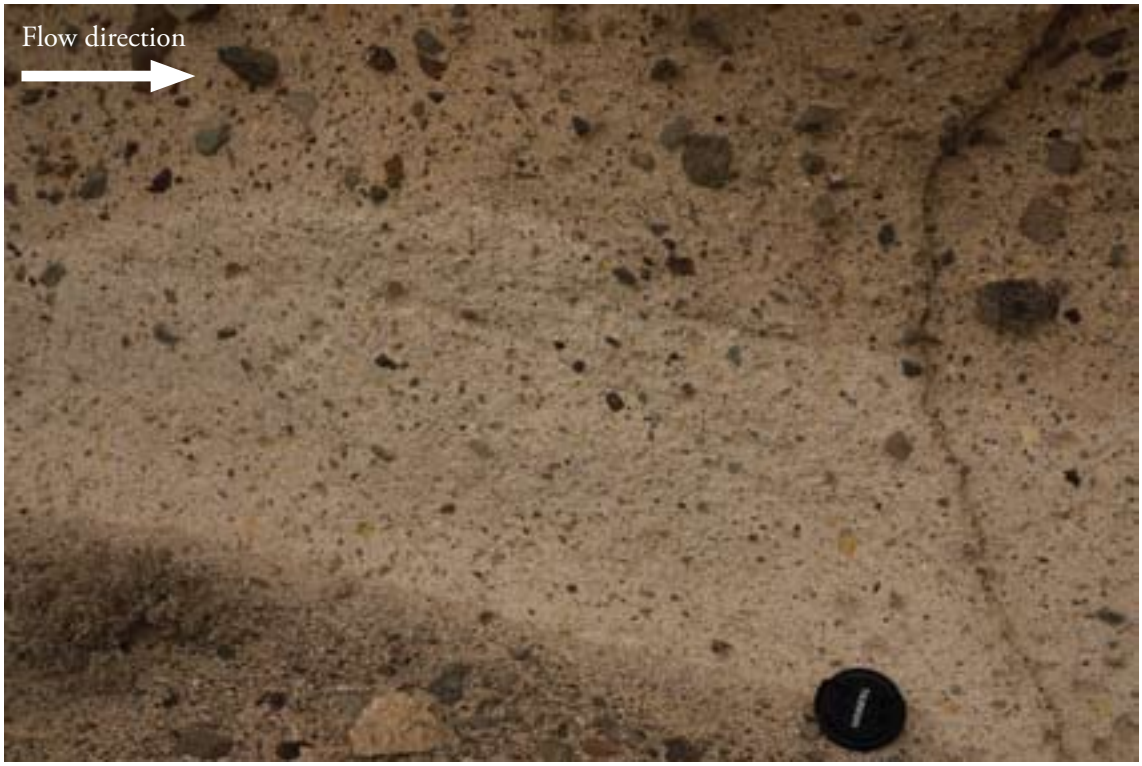

Figure 7.15 Contact between two poorly sorted units. (Lens cap diameter 68mm).

identifying these features due to low contrast between materials.

Figure 7.15 shows a contact between two poorly sorted units (the upper being highly lithic charged), and does not demonstrate the same extent of shear as the previous example, appearing to have a more rounded geometry. Additionally, at the vertical fracture on the right of the image there is a possible second feature forming in the same direction.

The contact between a highly charged flow unit and a reverse graded flow (highlighted by the smeared pale ash-rich horizon) shown in Figure 7.16 (enlarged detail in Figure 7.17) shows convolute interactions

Although most contacts at the base of discrete units have enough of a colour contrast to identify these features, there are cases where contacts within single units can be observed. These contrasts are likely due to one (or a combination) of the following:

1. Break in local deposition during flow (thalweg migration, brief pause in sediment supply, etc.)

2. Change in pyroclast nature (vent widening, change in eruptive style, plume collapse etc.)

3. Erosive contact representing a transition from depositional, to erosive, back to depositional at a point in the channel. Timescale and volume eroded unknown, but sufficient for sediment supply of younger deposit to provide contrast with the older.

Figure 7.16 Basal ignimbrite contact with small uni-directional deformation against a thin preceding ash fall layer (detail in Figure 7.17).

The contact illustrated in Figure 7.18 shows a clear recumbent tongue of material as part of a moderately undulose contact.

Figure 7.17 Detail of contact shown in Figure 7.16. Lens cap diameter 68mm.

Figure 7.18 Contact within an ignimbrite. Lens cap diameter 68mm. Location 28°09'48"N, 12°26'28"W

Figure 7.19 Contact showing a massively bedded ignimbrite above a volcanic ash layer, exhibiting complex recumbent flame structures at the interface. Hammer shaft is 28cm long. Location 6°59'41.30"S , 106°18'26.78"E (Clements pers. comm.. 2010)

Figure 7.20 Detail of a single recumbent flame. The lower downstream part of the flame appears to demonstrate an earlier phase of shear formation, similar to those seen in the laboratory features which often demonstrated multi-stage shearing. Pen 18 cm long. Location 6°59'41.30"S , 106°18'26.78"E (Clements pers. comm.. 2010)

Figure 7.21 Detail of a single recumbent flame demonstrating a secondary shear growth from its downstream tip. Additionally, this tip shows slight deflection as it is lifted over the downstream feature, similar to the deflections observed in the experiments (e.g. Figure 6.21). Location 6°59'41.30"S , 106°18'26.78"E (Clements pers. comm.. 2010)

7.5.2 Tanjung

There are several compelling examples which are indicative of K-H-like growth in the Tanjung formation in the Banten province of West Java, Indonesia - approximately 10km South East of the town of Bayah. These are a sequence of ignimbrite and ash fall layers from an as-yet unidentified source. Flow direction of the upper unit in these photos is from left to right. Figure 7.19 shows a massive, poorly sorted unwelded ignimbrite with normal grading (fine to medium/fine sand grade with rare pebble-sized clasts appearing) running over a planar laminated (in places faintly convolute) volcanic ash, up to 1m thick. The contact between these two units is sharp, but marked by a series of wavelet-form flame structures, all of similar wavelength and amplitude (λ~ 40 cm, z~ 10 cm). Figures 7.20 and 7.21 show the detail of two of these features.

Figure 7.22 shows a scatter plot of the wavelength and amplitude dimensions measured for the instabilities observed in Figure 7.19. The line drawn through these data is calculated using

$$y = C_0 + C_1 x + C_2 x^2 \ldots \qquad [7.23]$$

With coefficients of C_0=-1.1154 and C_1=0.2256. The correlation coefficient for these data is 0.8953. While there is clearly some scatter, it appears that there is at least some correlation between the amplitude and wavelength of these features as might be expected.

7.5.3 Rhum

Further examples of possibly K-H-like derived recumbent flame structures may be present in a pyroclastic succession on the Scottish island of Rhum. The Palaeogene ignimbrites of the Southern Mountain Zone in the Rhum Central Complex were first identified by Holohan *et al.* (2009), having previously been described as subterranean explosion and intrusion breccias or rhyodacite sheets. Figure 7.23 shows a single outcrop from these deposits, with what appear to be small intercalated features, emphasised by erosion, which have similar geometry to what might be expected of an eroded recumbent flame.

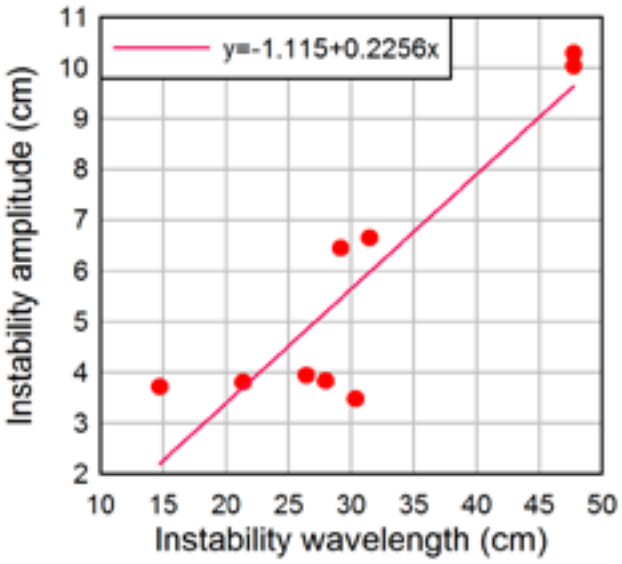

Figure 7.22 Scatter plot of the wavelength and amplitude dimensions measured for the instabilities observed in Figure 7.18

7.6 Discussion

7.6.1 Deposition and sorting

The ability of these flume experiments to model geophysical processes appears to be not only significant, but applicable to numerous different systems, which is in line with the conclusions drawn from the

Figure 7.23 Outcrop and enlargement highlighting a bedform within an ignimbrite unit of the Southern Mountain Zone succession in Rhum, Scotland. Contact demonstrates overturned / intercalated material. Hammer shaft is 25cm long. Location: 56° 57' 30"N 6° 18' 49"W. Reproduced courtesy of E. Holohan.

wide variety of previous granular flume experiments (e.g. Hutter and Koch, 1991; Gray *et al.*, 1998; Denlinger and Iverson, 2001; Choux *et al.*, 2004; Felix and Thomas, 2004). The interrogation of these deposits in three dimensions reveals geometries similar to those observed in small volume pyroclastic deposits, landslides, and debris avalanches. The internal structure of the experiments seems to be in agreement with the inferred flow mechanics for the propagation of all of these above flows, suggesting that not only are the deposits similar, but they are being produced by analogous processes.

When considering larger ignimbrite forming PDCs the situation is a little more complicated. The quasi-steady flow of these events makes directly comparable laboratory modelling challenging. The fluidisation necessary to maintain such flows requires increased pore pressure (e.g. Druitt *et al.* 2007). However the laboratory flumes which generate such conditions require a porous base, and this is problematic when it comes to 3D setting and sectioning and interrogation of internal deposit architecture. Consequently the small volume, unsteady, dense flows generated in the experiments presented herein are unable to reproduce the "runout or overpassing" of substrate observed in large volume PDCs. As a direct result, the deposit architectures preserved in these experiments are not

representative of what might be generated by sustained flows. However, the processes active within the laboratory experiments *are* scaled and representative of the basal granular currents in these larger PDCs. As a result those experiments (that preserve the interaction between subsequent charges) can be considered instantaneous windows on the behaviour of the more steady-state contacts present at the lower flow boundary zone of sustained PDC currents.

The granular sorting mechanisms witnessed in the flumes have been shown to generate

1. Lateral concentrations of large particles
2. Basal, proximal and ventral concentrations of dense particles
3. Distal and surface concentrations of large particles

These three features may be seen as analogous to the typical small-volume PDC features of

1. Levee formation
2. Channelisation of lithics and normal graded lithics in PDCs
3. Terminal pumice dams, and pumice overpassing

Equivalent features are observed in debris avalanches.

In addition, the granular sorting mechanisms in these granular fluids are likely to be significant in controlling what material is deposited from sustained PDCs. The dense granular fluid at the base of these density stratified currents acts as a buffer between direct fallout from the overpassing turbulent regime, and the lower aggrading substrate. Any aggradation happens as a result of settling from the granular fluid. As a result the sorting mechanisms may be expected in sustained basal flow regimes to control what particles are able to sediment at any given time. Buoyant pumice clasts which reach the granular fluid early in the flow may easily travel for some considerable time within the granular fluid before being settled out or overpass to produce pumice clusters. Equally, dense lithic clasts which reach the granular fluid may be expected to deposit very rapidly in the basal region of the flow.

There is a further interesting implication from the flume experiments. Where an unstable PDC deposit retrogressively collapses, a situation is generated where a stratified deposit (with all of the particulate sorting that implies) is remobilised or reworked as a debris avalanche. Assuming there has been some time between the original deposition and the reactivation of this material, it can be assumed that there will be no significant pore-pressure increase that is usually associated with the outgassing of juvenile material. We can now consider what deposit may be formed by such a flow.

1. Experimental work (Chapter 4) confirms that the granular nature of such a debris avalanche will very rapidly re-sort the particulates. The laboratory experiments were able to generate phenomenal sorting in under 1.5 seconds of flow and deposition, and similar sorting rates can be expected in a remobilised

PDC. This tells us that whatever stratigraphies are seen in the final deposit, they will almost certainly be as a result of the remobilisation/reworking and subsequent flow. It is highly unlikely any signature from the original (unstable) deposit might be preserved. It may then be inferred, in line with Torres *et al.* (1996) that secondary PDC deposits are virtually indistinguishable from primary ones.

2. The granular fluid in these experiments produced "stratigraphies" similar to those ascribed to PDC deposition from the collapse of an eruptive column (i.e. primary PDC deposit). This "classic" ignimbrite '2a, 2b' stratigraphy comprises (a) a dense lithic rich basal layer, (b) topped by a massive,

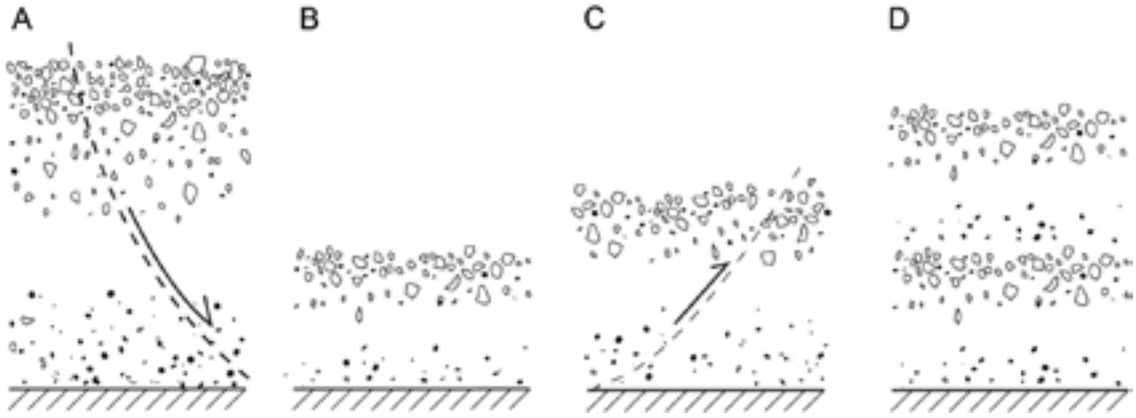

Figure 7.24 Illustrations of products from a retrogressive collapse of ignimbrite material. (A) shows a 'standard' ignimbrite showing inverse graded lithics and normal graded pumices. Dashed line implies a failure slope for retrogressive collapse which 'samples' the original deposit. This remobilised material goes on to form either (B) single pulse, (C) over-thickened deposit formed by compressional shear, or (D) stratified deposit as a result of multople pulses.

reverse graded unit with pumice clasts becoming dominant in the upper horizons. If these discrete pulses of flow in our experiments are able to reproduce typical ignimbrite stratigraphy by reworking, then it follows that where outcrops have been interpreted as primary PDC deposits, there may be reworked ignimbrites. Furthermore, when this is taken alongside the observed ability of debris avalanche deposits to exhibit internal over-thrusting of flow pulses, and that ignimbrite material is generally uniform and difficult to distinguish internal contacts within, there are several possible resultant deposit forms (Figure 7.24)

(A) Illustrates an $mLT_{(nl - ip)}$ (massive lapilli tuff with normal graded lithics and inverse graded pumice) deposit which is reactivating along a shear plane, which is sampling throughout the thicknes of the unit. This retrogressive failure generates a charge which will be may form a variety of stratigraphies.

(B) shows a single pulse deposit which may be expected from this charge. Granular sorting mechanisms in the debris avalanche have reproduced the same grading as originally present. Note that this is a reworked product of a secondary flow, not preserved from the original stratigraphy.

(C) represents the deposit formed by overthrusting (dashed line) typical in debris avalanche deposits.

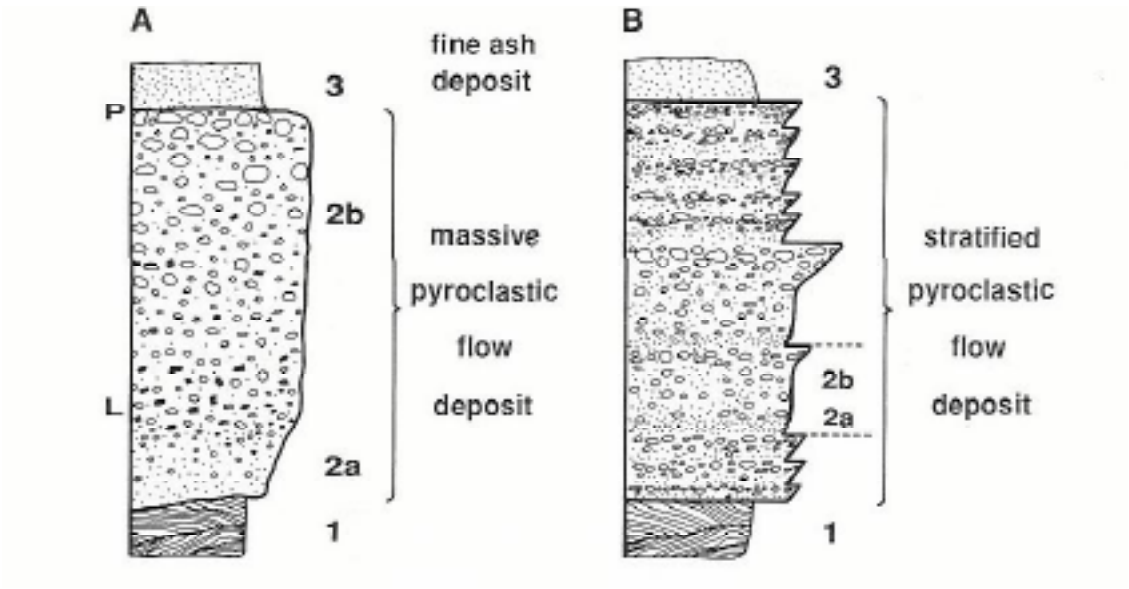

Figure 7.25 Comparative illustrations of massive and stratified PDC deposits. Stratified deposits may contain many repetitions of the mLT(nl, ip) -type lithology more typical of primary ignimbrite. McPhee et al. (1993).

Granular sorting and homogeneity of most ignimbrite material makes recognition of this difficult. Deposit considerably thickened compared to B.

(D) shows the result of two retrogressive failures of the same original deposit forming sequential charges, and resulting in stacked deposits. A single eruptive unit is now represented by two distinct stratigraphic, chemically and compositionally identical units. This form of flow and depositional pattern may even generate stratified PDC deposits (Figure 7.25).

7.6.2 K-H-like Generation

No definitive evidence for K-H-like growth in field ignimbrite deposits has been identified, although a number of quite similar structures are clearly observed at basal contacts. The likelihood is that K-H-like growth in steady-state ignimbrite-forming PDCs results in long-lived instabilities which leave only well mixed regions within the deposit. The basal contacts of these ignimbrites have strong enough visual contrast to more easily observe features, and the proliferation of recumbent flames, many of which seem to share a unidirectional morphology similar to those seen generated in the flume experiments suggests that these are indeed tracers of K-H-like growth. While it is undoubtedly the case that some recumbent flame features in the field are produced by post-depositional loading and subsequent shear, the dry, often clast supported (e.g. Plinian fall) deposits which PDCs travel over are not conducive to such remobilisation. In conjunction with the observations of remobilised pumices being lifted into over-riding flow units (Figures 7.12 and 7.13) we have a mechanism to both re-mobilise and shear substrate in a syn-depositional process.

K-H-like mixing within ignimbrite units has a number of significant implications associated with it. The ability of K-H-like instabilities to produce well mixed zones, and to lift material from underlying substrates into over-riding flows means that care must be taken when collecting data which is reliant

on point sampling included material. The obvious examples of this are temperature proxy data from included charcoals (e.g. Scott *et al.* 2008), and isotopic dating based on remobilised material. Charcoal formed within a hot PDC deposit can be analysed for reflectance, which in turn can be used to infer temperatures of flows. However, charcoal reflectance is sensitive to the time for which it is exposed to temperature, as well as the maximum temperature to which it is exposed (Scott and Glasspool, 2005). Material which is located in one flow could very easily have been incorporated from an older (or, in the case of sampling blow the boundary, younger) unit which may have experienced a very different temperature history. Additionally, with cooling of PDC deposits taking in the region of weeks to months it is plausible that later cool flows may interact with the hot substrate flow, causing mixing and ultimately bulk cooling. This could impact the temperature data for any material in the lower (or, indeed upper) flow.

Furthermore, with broad mixing zones generated it is plausible that contacts between ignimbrite units may be obscured. This in turn will have significant implications for flow volume estimates; any unrecognised unit boundaries will result in multiple units being identified as single units. As a result, overestimation of flow (and hence eruption) volumes is likely. This in turn has implications for the geohazard modelling of flow paths in situations where mixing has confused unit identification. If a model has been made to fit an existing deposit, the reliability is dependant on correct mapping of that deposit. In cases where the deposit has been misinterpreted due to complications such as this, then any modelling based on the error is potentially seriously flawed. This is particularly important with consideration of the fact the K-H-like structures in experiments (and therefore inferred mixing zones within PDCs) most frequently occurred where flows run up onto a slope. The ability of PDC to flow up and over topographic features is a major hazard to communities on the flanks of active volcanoes, and modelling based on misinterpretation in these areas is particularly dangerous.

7.7 Conclusions

The flume experiments reproduce both particulate sorting features and geometries observed in field deposits of large and small volume PDCS and debris avalanches. Lateral and distal concentrations of large particles dues to BNE sorting are ubiquitous, as are ventral proximal concentrations of both large and small dense (ceramic) particles through density sorting (RBNE). The depositional system observed in the flume reproduces the dominant system inferred for debris avalanches, and in turn reproduces surface pressure ridges, while also providing an insight into the mechanism of their formation - i.e. internal thrust pulses as the deposit forms.

Comparison to ignimbrites is more problematic, as the continuous aggradation believed to form them is not directly similar to the depositional system in the flume. However, the sorting mechanisms in the flume are typical of any granular fluid, and therefore represent the same processes that might be expected at the base of a PDC dominated by granular fluids (e.g. the C, E, F and G members in the PDC spectrum described by Figure 1.2).

Formation of K-H-like instabilities in the field cannot, at this point, be proven. However, there are many possible demonstrations of partial instability growth represented by sheared flame structures

at lower contacts. These lower contacts are a key target for observation as there is sufficient colour contrast between the layers for these features to be observed. Structures within ignimbrite units would be masked by homogeneity of material and appearance. K-H-like growth in a sustained current (which does not vertically migrate rapidly) might be expected to result in a mixed zone, not the discrete identifiable structures typified by those formed by the unsteady currents in the flume experiments.

It is apparent that the sorting mechanisms demonstrated are capable of producing complex stratigraphies when multiple charges of material are sequentially deposited. The potential for retrogressive collapse of loose ignimbrite to form pulses of cold debris-flow may easily produce stratigraphies which could be mis-identified as primary PDC deposit. This issue has been recognised in the field by Torres *et al.* (1996) in the study of ignimbrites from the 1991 Pinatubo eruption.

CHAPTER 8: SYNTHESIS

8.1 Summary

A series of innovative analogue experiments have been designed, tested, modified and applied in order to provide baseline data for the investigation of granular flow sorting and deposition as an analogue for PDCs and other geophysical flows. These experiments may also inform future advanced numerical modelling, with the intention of being able to accommodate

- multi-layer flows
- complex terrain
- inter-layer sedimentation
- erosion, remobilisation and deposition of substrate materials
- particulate size and density sorting
- interrogation of internal geometries for validation against field examples

In order to achieve this, the models developed in this work have attempted to tightly constrain key parameters such as particle densities, shape, roundness, size, flume geometries and charge volumes. The main variables investigated were:

- Flume geometry
- Flow velocities
- Initiation features
- Depositional mechanisms
- Particle sorting processes and rates (size, density)
- Sequential charge interactions
- Sidewall friction effects

Simultaneously, these experiments have been used to develop a procedure for the setting, sectioning and 3D interpretation of flume deposits. Modification of approaches used in tectonic sandbox modelling have enabled observation of internal features which have previously not been investigated, most notably the occurrence of shear reworking features (K-H instabilities) in granular flows interacting with static granular substrates.

As well as providing a purely academic baseline suite for future numerical modelling, the experiments provide a useful dataset in the further study of granular fluids, and the ongoing challenges in developing a better understanding of their governing equations. In addition to this, the experiments have been scaled to ensure some degree of geophysical relevance, and have been shown to reproduce geological/natural features typical of rock and snow avalanches, and landslides and small volume PDCs including block and ash flows and proximal ignimbrites. Furthermore, during flow over loose granular substrates, the instantaneous conditions at the shearing contact between the two layers can be considered similar to those experienced at the lower flow boundary zone of large sustained PDCs, and hence the processes active at that boundary may be seen as comparable.

8.1.1 Modelling and reproduction of typical PDC structures

A wide range of experiments have been conducted in this work, and a number of different features have been developed. Granular particulate sorting consistent with the understood processes of Brazil Nut Effect (i.e. BNE) and RBNE (i.e. reverse BNE) generates vertical sorting typified by ignimbrite '2a, 2b' stratigraphy, but also observed in other geophysical flows. In addition, sidewall interaction encourages the lateral expression of these sorting mechanisms, creating features such as levees.

By running multiple charges, or single charges onto loose substrate packs the experiments allow for the investigation of erosive contacts, the formation of shear instabilities (K-H eddies), and the associated formation of what appear to be recumbent flame structures. Shear instability growth therefore provides a syn-depositional mechanism for recumbent flame formation. The growth of full K-H instabilities is likely to result in broad mixing zones within, and at the contacts of ignimbrites. These zones have significant potential to interfere with geological techniques such as isotopic dating and temperature proxy analysis using included clasts, as well as the ability to accurately estimate eruption and flow volumes.

The various sorting and deposition mechanisms observed in these flume experiments, as an analogue for cold dry pyroclastic material suggest that retrogressive failure of an existing ignimbrite deposit can generate secondary ignimbrite architectures which are structurally and chemically indistinguishable from the original deposit. Additionally, stratigraphically complex relationships can be generated by relatively simple flow systems, simply through channelisation, erosion, and re-deposition of material.

8.1.2 Implications for the study of grainflow

The experiments in this work are valuable purely for the insight the grant on the internal mechanisms at work in granular flows, and in the interaction between charges. K-H instabilities have been recognised in granular fluids only relatively recently (Goldfarb *et al.* 2000), and never before at a contact with a static substrate with the associated low granular temperature and dilation. The ubiquitous growth of these features in these flume experiments suggests K-H instabilities are common in these systems, but only identified in these experiments due to the novel colouring, setting and sectioning technique which has been employed.

A more subtle implication of this work is that sidewall interaction is perhaps more significant than is sometimes assumed. While monomict charges appear to be moving relatively isotropically across the flume, addition of polymict charges emphasis a significant lateral component of motion. This is further suggested by the multiple charge experiments, where the depositional and reworking mechanisms at the edges and centreline of the flume were vastly different. However it must be noted that these multi charge experiments are subject to current deflection by substrate topography. Even ignoring these multi-charge experiments, it must be concluded that either a) the sidewall observation of flume experiments cannot be taken as being representative of behaviour anywhere else in the flume or b) polymict charges amplify sidewall effects. If a) is true, then the implications are important for a vast array of work which has assumed sidewall observation is at least partially valid. If b) is true, then there is an intriguing set of experiments to be conducted to quantify and analyse this effect.

8.2 Future work

There are numerous opportunities and directions for future work based on these experiments and field observations, broadly grouped into three categories; developing the laboratory technique, developing the flume experiments, applying the laboratory work to numerical simulation and further field investigation.

8.2.1 Laboratory technique

The technique developed in this work has demonstrated excellent potential for revealing detailed internal structure of granular deposits. A significant restriction experienced in this work was the slice thickness, making high-quality 3D visualisation difficult, and reliant on interpolation over quite large areas. This does not appear to be an issue for the central region of the flume, but the flume edges are strongly effected by sidewall friction, and it is difficult to be sure that interpretations of the charge interactions within 20mm of the flume walls are accurate in three dimensions.

More time experimenting with the setting and sectioning method, as well as experimentation with different packing procedures and materials should allow slice thicknesses to be reduced significantly. Alternatively, rather than the non-destructive method used in these experiments, a destructive method could be applied with all imaging done in the lab. This would allow slice thicknesses to come down to ~1mm.

In order to better visualise the particle motions during initiation, flow and deposition (and hence better observe features such as failure planes, flow pulses, and over-thrusting depositional regions) these flumes are ideally scaled to employ techniques such as Magnetic Resonance Imaging (MRI) to track instantaneous particle positions during flow (e.g. Kleinhans *et al.* 2008). Use of MRI would permit a detailed understanding of deposit accretion, and removes the reliance on sidewall observation. This is important because these experiments have shown this factor to be severely limited by frictional interaction, lateral sorting mechanisms, and current deflection by substrate during flow.

Following on from the use of MRI, and the possibility for finer sequential slicing of set deposits, there is significant room for improvement in the 3D visualisation of these flume deposits. Finer serial

sectioning would allow the employment of imaging techniques developed by the medical imaging community for 3D visualisation of volumes. By treating experimental deposit slices in the same way as serial sections developed from, for example, medical MRI scanners, true 3D visualisation of deposit geometries would be possible. While this was attempted on the current dataset, the serial slice spacing was too great to gain any meaningful information. By reducing slice spacing to ~2mm a significant step forward might be made in interpreting the complex interactions evident at the proximal regions in the multiple charge experiments.

8.2.2 Developing the flume experiments

Time has been the only constraint on the point at which experiments for this work were stopped. There are a wide range of alterations, additions and variables that could be considered in the further development of these experiments, not least due to the wide variety of factors which influence PDC formation, propagation and deposition. In terms of providing further data for the construction of a 4D numerical model able to reproduce internal deposit geometries, the priorities may be summarised as follows.

Pore pressure

In terms of modelling long runout PDC, by far the most significant improvement would be the addition of apparatus to investigate pore pressure effects, and encourage the fluidisation of the charges. By inflating the charge prior to release, then at least some degree of account is made for the constantly exsolving high pore pressure system present in PDC with a high proportion of hot juvenile fragments which in the case of block and ash flows, fragment and release volatiles. One issue with this system is the high porosity of spherical bead packs, resulting in the necessity to reduce the particle sizes used in the experiments. This adds an additional complication of bringing powder physics into play, with vastly enhanced values for particulate cohesion.

Sidewalls

Modification of the flume to remove the sidewalls. We may then be able to investigate the true extent of polymict charges to recreate the sorting and deposits typical of debris flows etc. Most importantly, we could investigate features such as pressure ridges, lobate fronts, and levees. This would be the first stage before developing to more complex flume geometries with pre-formed channels and topographic features for flows to interact with, enabling true scaled analogue modelling of geophysical landforms.

Particle sorting

Use of more varied charge mixtures, with various sizes of each of the pumice and lithic analogue particles would give a greater understanding of the various sorting effects during flow. Other variables such as particle roundness might be investigated, as shape is known to be at least a second order sorting mechanism in granular fluids (e.g. Whiteman and Ridgway, 1988).

Release mechanism

Individual charges are a very simple method of investigating pulses in flow, but a better system would be to implement a variable hopper release which can feed a continuous flow stream into the flume.

The ability to simultaneously change the flow composition would be highly informative and, in conjunction with increased pore pressure fluidisation, allow the experiment to attempt to reproduce ignimbrite stratigraphies in full.

Substrate layering

The technique for laying substrate into the flume prior to a charge is a difficult technique, and a mechanised system for laying even layers would greatly enhance the quality of results looking at reworking of substrate. More complex geometries could be laid, investigating the tendency for topographic features to deflect currents across the flume.

8.2.3 Application to numerical modelling

Ultimately the objective of these analogue experiments was to provide a baseline of data against which numerical model could be gauged. The basis for such a model would likely be a multi-layer depth-averaged flow, able to model a turbulent suspension layer riding above a granular fluid, which itself rides above a loose substrate layer. This is not dissimilar to earlier work Larrieu *et al.* (2006) which looked at a 'raining' mass source supplying a thin flowing layer, and the later work by Doyle *et al.* (2007, 2008) which developed this system, with a basal granular avalanche of constant density being over-ridden and supplied by a sedimenting dilute current.

Sedimentation (and remobilisation) from one layer to another would provide a dynamic system, and by utilising multiple layers the worst of the density stratification problems are eliminated. By allowing material to move between layers in both directions, a far better understanding of how momentum changes in the course of flow impact sedimentation (and erosion). Additionally, by allowing for granular sorting mechanisms to be included, sedimentation can be judged not only by deposit extent and thickness but, vitally, internal geometry. This would result in a sedimentological verification of the model, similar to that possible in other fields, for example turbidity current modelling (e.g. Waltham *et al.* 2008).

8.2.4 Field Investigation

The experiments have clearly demonstrated the ability of granular charges to remobilise granular substrates and to generate K-H instabilities. In the field, observations were focussed on the extensive outcrops of the Bandas del Sur ignimbrite sequences in Tenerife. However, it is apparent that the flume experiments which generated these features are also closely analogous to debris flow deposits. Therefore it would be logical to conduct a field campaign investigating the interaction at the base of debris flow deposits. A particularly promising target might be the distal end of channelised debris flows, where multiple flow pulses often emerge as sequences of depositional lobes (see Figure 7.3).

An intriguing avenue of study would be to assess the extent to which recumbent flames are due to syn-depositional shear processes rather than post-depositional soft sediment deformation, and the occurrence of K-H instabilities in other sedimentary systems. There are numerous subaqueous flows which might be considered capable of generating the shear profiles over soft sediment necessary for K-H instabilities to grow. Modelling of these systems would provide some insight, while field observations may permit a classification of interface features between those which are clearly loading

related (symmetrical, or assymetrical shearing away from the local palaeocurrent direction), clearly shear instability related (assymmetrical, sheared towards the downstream direction, with a rotational component) and those which are not easily categorised into either category (assymetrical, unknown or downstream shear, no rotational component).

8.3 Summary of conclusions

Flume experiments, modelling and field validation demonstrated that:

1. Sidewall friction is significant and even narrow flumes demonstrate significant 3D structure during flow, and hence deposition.

2. Flume designs with sharp breaks in slope trigger rapid transition from non-depositional flow to deposition in a system analogous to a hydraulic jump.

3. Failure of static piles appears to propagate through shear-collapse associated with stress chains in the randomly packed pile, and is therefore not perfectly repeatable. This, however, remains a second-order effect on final geometry.

4. Shears formed during intiation appear to be related to pulses within the flow and therefore influence deposition

5. Increased basal friction amplifies the separation effects on the runout, and therefore amplifies the variations resulting from random packing in the original pile.

6. Drop chute release generates structurally similar deposits to pile collapse, and introduces an extra level of complexity in evaluating the development of stratification in charges.

7. Charge deposition resembles aspects of both plug-like (Sparks, 1976) and aggradational (Branney and Kokelaar, 1992) behaviour, strongly analogous to the transport model proposed by Schwarzkopf *et al.* (2005) for Merapi block-and-ash flows. This is also functionally similar to that inferred for debris flows, including rock and snow avalanches and landslides.

8. The setting and sectioning method is practical, and highly capable of producing meaningful and valuable data on the internal geometry of flume deposits.

9. The repeatability of the flume experiments is excellent, subject to careful set up, and allowing for the flow-pulse variation which is produced by random packing in the collapsing charge pile. These variations due to random packing vary the precise thickness of internal thrust stacks (and their second-order surface expression), but not the first-order final geometry.

10. Granular sorting mechanisms within the flume are in line with those represented in the literature (e.g. Vallance and Savage, 2000; Iverson and Vallance, 2001). However, the behaviour of the current within the flumes has significant impact on the emergence and expression of the sorting phenomenon within the final deposit.

11. 2D Vertical sorting mechanisms such as BNE and RBNE are able to produce typical 3D small-volume PDC, rock and snow avalanche, and landslide features such as levees of large particles, distal concentration of large particles, surface concentration of large particles, and axial proximal concentration of dense particles.

12. Retrogressive failure of an existing ignimbrite deposit can generate secondary ignimbrite architectures/stratigraphies which are structurally and chemically indistinguishable from the primary ignimbrite deposit produced by the collapse of low or high fountains/eruptive columns.

13. Thin shearing granular flows are capable of remobilising large quantities of loose substrate material through granular temperature conduction (i.e. momentum transfer between mobile and stationary particles).

14. The velocity and density profiles through a shearing flow and remobilising substrate which develop as a product of granular temperature conduction encourage the development of K-H-like instabilities.

15. The occurrence of K-H instabilities appears to be ubiquitous in these experiments, and may be expected to be an important and largely unrecognised feature in multi-charge granular systems.

16. The propagation of K-H-like instability features through continued flow may displace remobilised substrate significant distances

17. Steady currents with continued sediment supply may be expected to propagate K-H instabilities for significant distances. It is likely that continued growth, rotation and downstream propagation of these features would be represented stratigraphically by a very well mixed region at the scale of the instability amplitude.

18. Flows with increasing mass (and therefore momentum) flux may be expected to cause substrate erosion in one place, with re-deposition occurring only further downstream where the flow dynamics change such that settling can occur.

19. Mixing caused by K-H-like instabilities may move particles from substrate material into active flow, which subsequently would provide anomalous data for

    a. Temperature proxy data from included charcoals

    b. Dating from included crystals

20. Mixing caused by K-H instabilities may mask unit boundaries, impacting the reliability of eruption, flow and deposit volume estimates, as well as flow propagation extents.

REFERENCES

Anderson, T., and Flett, J.S., 1903, Report on the eruption of the Soufriere of St. Vincent in 1902. *Philosophical Transactions of the Royal Society*, **200**, 353-553.

Bagnold, R.A., 1954, Experiments on a gravity-free dispersion of large solid spheres in a Newtonian fluid under shear. *Proceedings of the Royal Society of London. Series A, Mathematical and Physical Sciences*, **225**, p. 49-63.

Battaglia, M., 1993, On Pyroclastic Flow Emplacement. *Journal of Geophysical Research*, **98**, B12, p. 22,269-22,272

Baxter, G.W., Behringer, R.P., Fagert, T., and Johnson, G.A., 1989, Pattern formation in flowing sand. *Physical Review Letters*, **62**, p. 2825.

Bear, J., 1972, *Dynamics of fluids in porous media*. New York, Dover.

Bernal, J.D., and Mason, J., 1960, Packing of Spheres: Co-ordination of Randomly Packed Spheres: *Nature*, **188**, p. 910-911.

Boudet., J.F., Amarouchene, Y., Bonnier, B., and Kellay, H., 2007, The granular jump. *Journal of Fluid Mechanics*, **572**, p. 413-431

Branney, M.J., and Kokelaar, P., 1992, A reappraisal of ignimbrite emplacement: progressive aggradation and changes from particulate to non-particulate flow during emplacement of high-grade ignimbrite. *Bulletin of Volcanology*, **54**, p. 504-520.

—, 1997, Giant bed from a sustained catastrophic density current flowing over topography; Acatlan ignimbrite, Mexico. *Geology*, **25**, p. 115-118.

—, 2002, *Pyroclastic density currents and the sedimentation of ignimbrites*, Geological Society, London. Memoirs, **27**.

Brey, J.J., Dufty, J.W., Kim, C.S., and Santos, A., 1998, Hydrodynamics for granular flow at low density. *Physical Review E*, **58**, p. 4638.

Bridge, J.S., and Demicco, R.V., 2008, *Earth surface processes, landforms and sediment deposits*. Cambridge, Cambridge University Press, 830 p.

Brown, R.J., Barry, T.L., Branney, M.J., Pringle, M.S., and Bryan, S.E., 2003, The Quaternary pyroclastic succession of southeast Tenerife, Canary Islands: explosive eruptions, related caldera subsidence, and sector collapse. *Geological Magazine*, **140**, p. 265-288.

Bursik, M., Patra, A., Pitman, E.B., Nichita, C., Macias, J.L., Saucedo, R., and Girina, O., 2005,

Advances in studies of dense volcanic granular flows. *Reports on Progress in Physics*, p. 271.

Bursik, M.I., and Woods, A.W., 1996, The dynamics and thermodynamics of large ash flows. *Bulletin of Volcanology*, v. 58, p. 175-193.

Caicedo-Carvajal, C.E., Glasser, B.J., Shonbrot, T., 2006, Granular flow transitions on sinusoidal surfaces. *Journal of Fluid Mechanics*, **556**, p. 253-269

Calder, E.S., Cole, P.D., Dade, W.B., Druitt, T.H., Hoblitt, R.P., Huppert, H.E., Ritchie, L., Sparks, R.S.J., and Young, S.R., 1999, Mobility of Pyroclastic Flows and Surges at the Soufriere Hills Volcano, Montserrat. *Geophysical Research Letters*, **26**, p. 53-540

Campbell, C. S. 1990, Rapid granular flows. *Annual Review of Fluid Mechanics*, **22**, p. 57–92.

Carracedo, J.C., 1994, The Canary Islands: an example of structural control on the growth of large oceanic-island volcanoes. *Journal of Volcanological and Geothermal Research,* **60**, p. 225–241.

Carracedo, J.C., Pérez Torrado, F.J., Ancochea, E., Meco, J., Hernán, F., Cubas, C.R., Casillas, R., Rodrıguez Badiola, E., 2002, Cenozoic Volcanism II: The Canary Islands. In: Gibbons, W., Moreno, T. (Eds.), *The Geology of Spain*. The Geological Society of London, 649pp.

Christenson, B.W., 2000, Geochemistry of fluids associated with the 1995-1996 eruption of Mt. Ruapehu, New Zealand: signatures and processes in the magmatic-hydrothermal system. *Journal of Volcanology and Geothermal Research*, **97**, p. 1-30.

Clarke, A.B., Neri, A., Voight, B., Macedonio, G., and Druitt, T.H., 2002, Computational modelling of the transient dynamics of the August 1997 Vulcanian explosions at Soufriere Hills Volcano, Montserrat: influence of initial conduit conditions on near-vent pyroclastic dispersal. *In:* Druitt, T.H., and Kokelaar, B.P. (eds) *The eruption of Soufrierre Hills Volcano, montserrat, from 1995 to 1999*. Geological Society, London, Memoirs **21**, p. 319-348.

Cole, P.D., Calder, E.S., Sparks, R.S.J., Clarke, A.B., Druitt, T.H., Young, S.R., Herd, R.A., Harford, C.L., and Norton, G.E., 2002, Deposits from dome-collapse and fountain-collapse pyroclastic flows at Soufriere Hills Volcano, Montserrat: *In:* Druitt, T.H., and Kokelaar, B.P. (eds) *The eruption of Soufrierre Hills Volcano, montserrat, from 1995 to 1999*. Geological Society, London, Memoirs **21**, p. 231-262.

Conway, S.L., Shonbrot, T., and Glasser, J., 2004, A Taylor vortex analogy in granular flows. *Nature*, **431**, p. 433

Dade, W.B., and Huppert, H.E., 1996, Emplacement of the Taupo ignimbrite by a dilute turbulent flow. *Nature*, **381**, p. 509-512.

—, 1998, Long-runout rockfalls. *Geology*, **26**, p. 803-806.

Denlinger, R.P., and Iverson, R.M. 2001, Flow of variably fluidized granular masses across three-dimensional terrain 2. Numerical predictions and experimental tests. *Journal of Geophysical Research*, **106** (B1), p. 553-566.

Doyle, E.E., Hogg, A.J., Mader, H.M., and Sparks, R.S.J., 2008, Modeling dense pyroclastic basal flows from collapsing columns. *Geophysical Research Letters*, **35**.

Doyle, E.E., Huppert, H.E., Lube, G., Mader, H.M., and Sparks, R.S.J., 2007, Static and flowing regions in granular collapses down channels: Insights from a sedimenting shallow water model. *Physics of Fluids*, **19**, p. 106601-16.

Doyle, E. E., Sparks, R. S., Mader, H. M., and Hogg, A. J. 2006, A numerical model for the formation and growth of a basal granular avalanche from a hot ash cloud. The first stage in the development of a two layer pyroclastic flow model. *Geophysical Research Abstracts* , **8**, 00046.

Druitt, T., Avard, G., Bruni, G., Lettieri, P., and Maez, F., 2007, Gas retention in fine-grained pyroclastic flow materials at high temperatures. *Bulletin of Volcanology*, **69**, p. 881-901.

Druitt, T.H., 1998, *Pyroclastic density currents.* Geological Society, London, Special Publications, **145**, p. 145-182.

Druitt, T.H., Bruni, G., Lettieri, P., and Yates, J.G., 2004, The fluidization behaviour of ignimbrite at high temperature and with mechanical agitation. *Geophysical Research Letters*, **31**.

Dufek, J., Wexler, J., and Manga, M., 2009, Transport capacity of pyroclastic density currents: Experiments and models of substrate-flow interaction. *Journal of Geophysical Research.*, **114**.

Faqih, A., Chaudhuri, B., Muzzio, F.J., Tomassone, M.S., Alexander, A., and Hammond, S.H., 2006, Flow - induced dilation of cohesive granular materials. *AIChE Journal*, **52**, p. 4124-4132.

Farr, T. G., et al. (2007), The Shuttle Radar Topography Mission. *Reviews of Geophysics*, **45**

Fisher, R.V., 1966, Mechanism of deposition from pyroclastic flows. *American Journal of Science*, v. **264**, p. 350-363.

Fisher, R.V. 1986. Systems of transport and deposition within pyroclastic surges: evidence from Mount St. Helens, Washington. *EOS Transactions of the American Geophysical Union*, **67**, 1246.

Fisher, R.V., Glicken, H.X., and hoblitt, R.P., 1987, May 18, 1980, Mount St Helens deposits in South Coldwater Creek, Washington. *Journal of Geophysical Reserach*, **92**, p. 10267-10283.

Folk, R.L., and Ward, W.C., 1957, Brazos River bar [Texas]; a study in the significance of grain size parameters. *Journal of Sedimentary Research*, v. 27, p. 3-26.

Francis, P.W., and Oppenheimer, C., 1993, *Volcanoes*, Oxford University Press.

Freundt, A. 1999, Formation of high-grade ignimbrites - Part II. A pyroclastic suspension current model with implications also for low-grade ignimbrites. *Bulletin of Volcanology*, **60**, p. 545–576.

Freundt, A. and Schmincke, H.-U. 1986, Emplacement of small-volume pyroclastic flows at Laacher See (East Eifel, Germany). *Bulletin of Volcanology*, **48**, p. 39–59.

Garcimartin, A., Maza, D., Ilquimiche, J. L., and Zuriguel, I., 2002, Convective motion in a vibrated granular layer. *Physical Review E*, **65**, 031303

Gill, R., Thirlwall, M., Marriner, G., Millward, D., Norry, M., Saunders, A. and Mart`i, J. 1994, *Tenerife, Canary Islands. Geologists' Association Guide no. 49*. London: The Geologists' Association, 38 pp.

Goldberg, D.E., 1989, Genetic Algorithms in Search, Optimisation and Machine Learning. Boston, MA, USA: Addison-Wesley Longman Publishing Co., Inc.

Goldfarb, D.J., Glasser, B.J., and Shinbrot, T., 2000, Kelvin-Helmholtz-like shear instabilities in rapid granular flow, *American Physical Society, 53rd Annual Meeting of the Division of Fluid Dynamics*: Washington, DC.

—, 2002, Shear instabilities in granular flows: *Nature*, **415**, p. 302-305.

Goldhirsch, I., and Zanetti, G., 1993, Clustering instability in dissipative gases: *Physical Review Letters*, **70**, p. 1619.

Gray, J.M.N.T., Wieland, M., and Hutter, K., 1999, Gravity-Driven Free Surface Flow of Granular Avalanches over Complex Basal Topography. *Proceedings: Mathematical, Physical and Engineering Sciences*, **455**, p. 1841-1874.

Hagen, G., 1852, Über den Druck und die Bewegung des trockenen Sandes. Berlin Monatsber. Akad. Wiss. , **35**, p. 35-42.

Hales, S., 1727, Vegetable statics (reprinted Oldbourne, London, 1961. Hoskin, M. A. ed.). London: Innys and Woodward.

Hanes, D.M., and Walton, O.R. 2000, Simulations and physical measurements of glass spheres flowing down a bumpy incline. *Powder Technology* , **109**, p. 133-144.

Hayashi, J.N., 1992, A comparison of pyroclastic flow and debris avalanche mobility. *Journal of Geophysical Research*, **97**, p. 9063-9071.

Hoblitt, R. P. 1986, *Observations of eruptions, July 22 and August 7, 1980, at Mount St. Helens, Washington*. US Geological Survey, Professional Paper, **1335**, p. 1–44.

Holohan, E.P., Troll, V.R., Errington, M., Donaldson, C.H., Nicoll, G.R., and Emeleus, C.H., 2009,

The Southern Mountains Zone, Isle of Rum, Scotland: volcanic and sedimentary processes upon an uplifted and subsided magma chamber roof. *Geological Magazine*, **146**, p. 400-418.

Hong, D.C., Quinn, P.V., and Luding, S., 2001, Reverse Brazil Nut Problem: Competition between Percolation and Condensation. *Physical Review Letters*, **86**, p. 3423.

Hou, M., Chen, W., Zhang, T., Lu, K., and Chan, C.K., 2003, Global Nature of Dilute-to-Dense Transition of Granular Flows in a 2D Channel. *Physical Review Letters*, **91**, p. 204301.

Houlsby, G.T., 1979, The work input to a granular material. *Geotechnique* , **29**, 354-358.

Hsu, K.J., 1975, Catastrophic debris streams (sturzstroms) generated by rockfalls. *Geological Society of America bulletin*, **86**, p. 129 - 40.

Iverson, R.M., 1997 The Physics of Debris Flows. *Reviews of Geophysics*, **35**, 3, p.245-296.

Iverson, R.M., and Denlinger, R.P., 2001, Flow of variably fluidised granular masses across three-dimensional terrain 1. Coulomb mixture theory. *Journal of Geophysical Research*, **106** (B1), p. 537-552.

Iverson, R. M. and Vallance, J. W. 2001, New views of granular mass flows. *Geology*, **29**, p. 115–118.

Jaeger, H., Nagel, S., and Behringer, R., 1996, Granular solids, liquids, and gases: *Reviews of Modern Physics*, **68**, p. 1259-1273.

Johnson, G.A., and Olhoeft, G., 1984, *Handbook of physical properties of rocks*, CRC Press, Inc., Boca Raton, Florida.

Jomelli, V. et Bertran, P. 2001, Wet snow avalanche deposits in the French Alps : structure and sedimentology. *Geografiska Annaler*, **83A**, p.15-28.

Kadanoff, L.P., 1999, Built upon sand: Theoretical ideas inspired by granular flows. *Reviews of Modern Physics*, **71**, p. 435.

Kleinhans, M.G., Jeukens, C.R.L.P.N., Bakker, C.J.G., and Frings, R.M., 2008, Magnetic Resonance Imaging of coarse sediment. *Sedimentary Geology*, 208, p. 69-78.

Klinkmüller, M., Rosenau, M., Boutelier, D., Kemnitz, H., and Schreurs, G., 2008, Properties benchmark of granular and viscous analogue materials, *GeoMod2008*: Villa La Pietra, Firenze.

Kudrolli, A., 2004, Size separation in vibrated granular matter: *Reports on Progress in Physics*, **67**, p. 209-247.

Kundu, P.K., and Cohen, I.M., 2004, *Fluid mechanics.* California, Elsevier Academic Press, 759 p.

Kuntz, M. A., Rowley, P. D., MacLeod, N. S., Reynolds, R. L., McBromme, L. A., Kaplan, A. M., *et al.*, 1981, Petrography and particle size distribution of pyroclastic-flow, ash-cloud, and surge deposits. *In:* Lipman, P. W., and Mullineaux, D. R., (eds) *The 1980 Eruptions of Mount St. Helens, Washington*. U.S. Geological Survey Professional Paper , 1250, 525-539.

Larrieu, E., Staron, L., and Hinch, E.J., 2006, Raining into shallow water as a description of the collapse of a column of grains *Journal of Fluid Mechanics*, **554**, p. 259-270.

Legros, F., 2002, The mobility of long-runout landslides. *Engineering Geology*, **63**, p. 301-331.

Levine, A.H., and Kieffer, S.W., 1991, Hydraulics of the August 7, 1980, Pyroclastic flow at Mount St. Helens, Washington. *Geology*, **19**, p. 1121-1124.

Liu, C.-h., 1994, Spatial patterns of sound propagation in sand. *Physical Review B*, **50**, p. 782.

Liu, C.h., Nagel, S.R., Schecter, D.A., Coppersmith, S.N., Majumdar, S., Narayan, O., and Witten, T.A., 1995, Force Fluctuations in Bead Packs. *Science*, **269**, p. 513-515.

Lowe, D. R. 1982, Sediment gravity flows: II. Depositional models with special reference to the deposits of high-density turbidity currents. *Journal of Sedimentary Petrology*, **52**, p. 279–298.

Lube, G., Cronin, S.J., Platz, T., Freundt, A., Procter, J.N., Henderson, C., and Sheridan, M.F., 2007, Flow and deposition of pyroclastic granular flows: A type example from the 1975 Ngauruhoe eruption, New Zealand. *Journal of Volcanology and Geothermal Research*, **161**, p. 165-186.

Lube G., Cronin S.J. and Procter J.N., 2009, Mechanisms behind extreme mobility of volcanic-ice slurry flows - Ruapehu Volcano, New Zealand. *Geology,* **37**, 1, p. 15-18.

Luck, J.M., and Mehta, A., 2004, Dynamics at the angle of repose: jamming, bistability and collapse. *Journal of Statistical Mechanics: Theory and Experiment*, **10**, p. 100-115.

Mair, K., Frye, K.M., and Marone, C., 2002, Influence of grain characteristics on the friction of granular shear zones. *Journal of Geophysical Research*, **107**. p. 2219

Major, J. J. 2000, Gravity-driven consolidation of granular slurries -- Implications for debris-flow deposition and deposit characteristics. *Journal of Sedimentary Research*, **70**, 1, p. 64-83.

McEwen, A.S., and Malin, M.C., 1989, Dynamics of Mount St. Helens' 1980 pyroclastic flows, rockslide-avalanche, lahars, and blast. *Journal of Volcanology and Geothermal Research*, **37**, p. 205-231.

McPhee, J., Doyle, M., and Allen, R., 1993, *Volcanioc textures*, Hobart Centre for Ore Deposit and Exploration Studies, University of Tasmania.

McTaggart, K.C., 1960, The mobility of nuees ardentes. *American Journal of Science*, **258**, p. 369-

382.

Mehta, A., 1994, Granular matter: An interdisciplinary approach. New York: Springer.

Mehta, A., and Barker, G.C., 1994, Disorder, Memory and Avalanches in Sandpiles. *Europhysics Letters*, p. 501.

Mikkelsen, R., Meer van der, D., Weele van der, K. and Lohse, D., 2002, Competitive clustering in a bidisperse granular gas: experiment, molecular dynamics, and flux model. *Physical Review. E*, **70**, 1539-3755

Mobius, M.E., Lauderdale, B.E., Nagel, S.R., and Jaeger, H.M., 2001, Brazil-nut effect: Size separation of granular particles. *Nature*, **414**, p. 270-270.

Murai, I. 1961. A study of the textural characteristics of pyroclastic flow deposits in Japan. *Tokyo University Earthquake Research Institute Bulletin*, **39**, p. 133–248.

Nairn, I.A., and Self, S., 1978, Explosive eruptions and pyroclastic avalanches from Ngauruhoe in February 1975. *Journal of Volcanology and Geothermal Research*, **3**, p. 39-60.

Nakada, S., Shimizu, H., and Ohta, K., 1999, Overview of the 1990-1995 eruption at Unzen Volcano. *Journal of Volcanology and Geothermal Research*, **89**, p. 1-22.

Newhall, C. and Self, S., 1982, The Volcanic Explosivity Index (VEI) An estimate of explosive magnitude for historical volcanism. *Journal of Geophysical Research*, **87**, C2, p. 1231-1238

Ocone, R., and Astarita, G., 1995, Compression and rarefaction waves in granular flow. *Powder Technology*, **82**, p. 231-237.

Ogawa, S., 1978. Multitemperature theory of granular materials. *Proceedings of the US-Japan Seminar on Continuum-Mechanics and Statistical Approaches to the Mechanics of Granular Materials* , p. 208-217.

Ogden, D.E., and Wohletz, K.H., 2009, Vent geometry controls on column structure and collapse *American Geophysical Union Fall Meeting*: San Francisco.

Onoda, G.Y., and Liniger, E.G., 1990, Random loose packings of uniform spheres and the dilatancy onset. *Physical Review Letters*, **64**, p. 2727.

Pouliquen, O., Delour, J., and Savage, S.B., 1997, Fingering in granular flows. *Nature*, **386**, p. 816-817.

Pyle, D.M., 2000, Sizes of volcanic eruptions. *In:* H. Sigurdsson *et al.*, (eds) *Encyclopedia of Volcanology*, Academic Press, p. 263 - 269.

Reynolds, O., 1885, On the dilatancy of media composed of rigid particles in contact. *Philosophical Magazine* Ser. 5 , **20**, p. 496-481.

Rogers, C.A., 1958, The packing of equal spheres. *Proceedings of the London Mathematical Society*, **3-8**, p. 609-620.

Ross, P.-S., and White, J.D.L., 2006, Debris jets in continental phreatomagmatic volcanoes: A field study of their subterranean deposits in the Coombs Hills vent complex, Antarctica. *Journal of Volcanology and Geothermal Research*, **149**, p. 62-84.

Saucedo, R., Macías, J.L., and Bursik, M., 2004, Pyroclastic flow deposits of the 1991 eruption of Volcán de Colima, Mexico. *Bulletin of Volcanology*, **66,** p. 291-306.

Savage, S.B., 1984, The mechanics of rapid granular flows. *Advanced Applied Mechanics*, **24**, p. 289-366.

Savage, S.B., and Hutter, K., 1989, The motion of a finite mass of granular material down a rough incline. *Journal of Fluid Mechanics*, **199**, p. 177-215.

—, 1991, The dynamics of avalanches of granular materials from initiation to runout. Part I. Analysis. *Acta Mechanica*, **86**, p. 201–223.

Schwarzkopf, L.M., Schmincke, H.-U., and Cronin, S.J., 2005, A conceptual model for block-and-ash flow basal avalanche transport and deposition, based on deposit architecture of 1998 and 1994 Merapi flows. *Journal of Volcanology and Geothermal Research*, **139**, p. 117-134.

Scott, A.C., and Glasspool, I.J., 2005, Charcoal reflectance as a proxy for the emplacement temperature of pyroclastic flow deposits. *Geology*, **33**, p. 589-592.

Scott, A.C., Sparks, R.S.J., Bull, I.D., Knicker, H., and Evershed, R.P., 2008, Temperature proxy data and their significance for the understanding of pyroclastic density currents. *Geology*, **36**, p. 143-146.

Scott, G.D., 1960, Packing of Spheres: Packing of Equal Spheres. *Nature*, **188**, p. 908-909.

Shea, T., and van Wyk de Vries, B., 2008, Structural analysis and analogue modeling of the kinematics and dynamics of rockslide avalanches. *Geosphere*, **4**, p. 657-686.

Sheridan, M. F. 1979, Emplacement of pyroclastic flows: a review. In: Chapin, C. E. and Elston, W. E. (eds) Ash-flow Tuffs, *Geological Society of America Special Paper*, **180**, 125–136.

Shinbrot, T., and Muzzio, F.J., 1998, Reverse Buoyancy in Shaken Granular Beds. *Physical Review Letters*, **81**, p. 4365.

Sohn, Y.K., Jeong, J.O., and Son, M., 2005, Long-runout pyroclastic surge on a Cretaceous alluvial

plain, Republic of Korea. *Terra Nova*, **17**, p. 13-24.

Sonin, A. A. 2001, The Physical Basis of Dimensional Analysis. 2nd ed., Department of Mechanical Engineering, MIT.

Spahn, F., Schmidt, J., Petzschmann, O., and Salo, H., 2000, Stability Analysis of a Keplerian Disk of Granular Grains: Influence of Thermal Diffusion. *Icarus*, **145**, p. 657-660.

Sparks, R. S.J., 1976, Grain size variations in ignimbrites and implications for the transport of pyroclastic flows. *Sedimentology* , **23**, 147-188.

Sparks, R.S.J., Barclay, J., Calder, E.S., Herd, R.A., Komorowski, J.C., Luckett, R., Norton, G.E., Ritchie, L.J., Voight, B., and Woods, A.W., 2002, Generation of a debris avalanche and violent pyroclastic density current on 26 December (Boxing Day) 1997 at Soufriere Hills Volcano, Montserrat. *In:* Druitt, T.H., and Kokelaar, B.P. (eds) *The eruption of Soufrierre Hills Volcano, montserrat, from 1995 to 1999*. Geological Society, London, Memoirs **21**, p. 409-434.

Sparks, R.S.J., Self, S., and Walker, G.P.L., 1973, Products of ignimbrite eruptions. *Geology,* **1**, p. 115-118.

Sparks, R.S.J., and Wilson, L., 1976, A model for the formation of ignimbrite by gravitational column collapse. *Journal of the Geological Society*, **132**, p. 441-451.

Sparks, R.S.J., Wilson, L., and Hulme, G., 1978, Theoretical modelling of the generation, movement and emplacement of pyroclastic flows by column collapse. *Journal of Geophysical Research*, **83** (B4), p. 1727-1739.

Torres, R.C., Self, S., Martinez, M. M. L., 1996, Secondary pyroclastic flows from the June 15, 1991, ignimbrite of Mount Pinatubo. *In:* Newhall, C.G., and Punongbayan, R.S, (eds) F*ire and mud: eruptions and lahars of Mount Pinatubo, Phillipines*. University of Washington Press.

Vallance, J.W., and Savage, S.B., 2000, Particle segregation in granular flows down chutes, *In*: Rosato, A., and Blackmore, D., (eds), *Segregation in granular flows (International Union of Theoretical and Applied Mechanics symposium)*. Dordrecht, Netherlands, p. 31-51

Valentine, G. A. and Fisher, R. V. 1986, Origin of layer-1 deposits in ignimbrites. *Geology*, **14**, p. 146–148.

Voight, B., Komorowski, J-C., Norton, G. E., Belousov, A. B., Belousova, M., Boudon, G., Francis, P. W., Franz, W., Heinrich, P., Sparks, R. S. J. and Young, S. R., 2002, The 26 December (Boxing Day) 1997 sector collapse and debris avalanche at Soufriere Hills Volcano, Montserrat. *In:* Druitt, T.H., and Kokelaar, B.P. (eds) *The eruption of Soufrierre Hills Volcano, montserrat, from 1995 to 1999*. Geological Society, London, Memoirs **21**, 363-407

Walker, G. P. L. 1983, Ignimbrite types and ignimbrite problems. *Journal of Volcanology and Geothermal Research*, **17**, 35–88.

Walker, G. P. L., Wilson, C. J. N. and Froggat, P. C. 1980, Fines depleted ignimbrite in New Zealand - the product of a turbulent pyroclastic flow. *Geology*, **8**, p. 245–249.

Waltham, D., Jaffey, N., MacLean, S. & Zampetti, V., 2008, Combined structural reconstruction and stratigraphic modelling of turbidite prospects using 3D seismic data. *Petroleum Geoscience*, **14**, p. 1-9.

Weele, K.v.d., Meer, D.v.d., Versluis, M., and Lohse, D., 2001, Hysteretic clustering in granular gas. *Europhysics Letters*, p. 328.

Whiteman, M., and Ridgway, K., 1988, A comparison between two methods of shape-sorting particles. *Powder Technology*, **56**, p. 83-94.

Wieghardt, K., 1975, Experiments in granular flow. *Annual Review of Fluid Mechanics*, **7**, p. 89-114.

Williams, H. 1957, Glowing avalanche deposits of the Sudbury Basin. *Ontario Department of Mines 65th Annual Report*, p. 57-89.

Wilson, C. J. N. 1980, The role of fluidisation in the emplacement of pyroclastic flows: an experimental approach. *Journal of Volcanology and Geothermal Research*, **8**, p. 231–241.

Wilson, C.J.N., and Walker, G.P.L., 1982, Ignimbrite depositional facies: the anatomy of a pyroclastic flow: *Journal of the Geological Society*, **139**, p. 581-592.

Wilson, L., and Head, J.W. 1981, Morphology and rheology of pyroclastic flows and their deposits, and guidelines for future observations. (P. W. Lipman, and D. R. Mullineaux, Eds.) The 1980 Eruptions of Mount St. Helens, Washington. *U.S. Geological Survey Professional Paper* , **1250**, 513-524.

Wright, J., and Walker, G.P.L., 1981, Eruption, transport and deposition of ignimbrite: A case study from Mexico. *Journal of Volcanology and Geothermal Research*, **9**, p. 20.

Yan, X., Shi, Q., Hou, M., Lu, K., and Chan, C.K., 2003, Effects of Air on the Segregation of Particles in a Shaken Granular Bed. *Physical Review Letters*, **91**, p. 014302.

APPENDIX A - SYMBOLS AND ABBREVIATIONS

List of Symbols

Symbol	*Description*
β	shear rate
γ	strain rate
δ	particle diameter
ε	interstitial fluid volume fraction
ζ	amplitude
θ	angle
θ_b	basal friction angle
θ_r	runout surface angle
κ	permeability
λ	wavelength
μ	viscosity
π	Pi
ρ	density
ρ_b	bulk density
ρ_f	interstitial fluid density
ρ_s	solid particle density
σ	normal stress
τ	shear stress
ϕ	solid volume fraction
ϕ_*	solid volume fraction at maximum packing
ψ	cohesion
φ	internal friction angle
d	flow thickness
g	gravitational aceleration (9.81 ms-2 at sea level)
H	height
I_g	Instability growth condition
k	wavenumber
L	length
l	runout
M	mass
R	roundness
v	velocity
w	flow width
x	horizontal (longitudinal) dimension
y	horizontal (lateral) dimension
z	vertical dimension

Abbreviations

AMSL	Above mean sea level
BAF	Block and ash flow
BNE	Brazil nut effect
K-H	Kelvin Helmholtz
MRI	Magnetic resonance imaging
NB	Bagnold number
NF	Fluidisation number
NP	Pore pressure number
NR	Quasi-Reynolds number
NS	Savage number
PDC	Pyroclastic density current
RBNE	Reverse brazil nut effect
RCP	Random close packing
RLP	Random loose packing
SRTM	Shuttle Radar Topography Mission

APPENDIX B - SCALING DATA

TABLE B.1 DIMENSIONAL ANALYSIS PARAMETERS AND SCALING INTERVALS

	Parameter	Debris flow		PDC		Experiments		Scaling intervals			
		min	max	min	max	min	max	DF small	DF large	PDC small	PDC large
	Runout							0.001	0.00002	0.0003	0.000005
	flow velocity							1	0.033	1	0.008
	fluid density							1		1	
Π_1	Vertical distance travelled	0.00005	1	0.00002	0.667	0.5	0.364	0.04	0.001	0.04	0.0004
Π_2	flow thickness	0.05	0.0003	0.05	0.00005	0.02	0.01	0.004	0.01	0.002	0.2
Π_3	particle density	0.0005	0.004	0.00004	0.008	0.0003	0.001	1		1	
Π_4	particle diameter	2×10^{-6}	0.05	5×10^{-7}	0.007	0.002	0.003	1		1	
Π_5	solid volume fraction	0.5	0.65	0.1	0.65	0.5	0.65	1		1	
Π_6	internal friction angle	25	50	25	50	28	32	1		1	
Π_7	Depositional slope angle	0	30	0	30	0	5	1		1	
Π_8	cohesion	4.4×10^{-6}	0.01	5.5×10^{-5}	1.6	0.0002	0.04	0.1	0.01	0.01	0.0001
Π_9	particle roundness	0.1	0.9	0.1	0.9	0.95	0.95	1.056	9.5	1.056	9.5
Π_{10}	fluid viscosity	9.8×10^{-21}	3.3×10^{-9}	1×10^{-23}	4×10^{-14}	3×10^{-10}	1.5×10^{-8}	1		1	
	gravity	9.81	9.81	9.81	9.81	9.81	9.81	1		1	

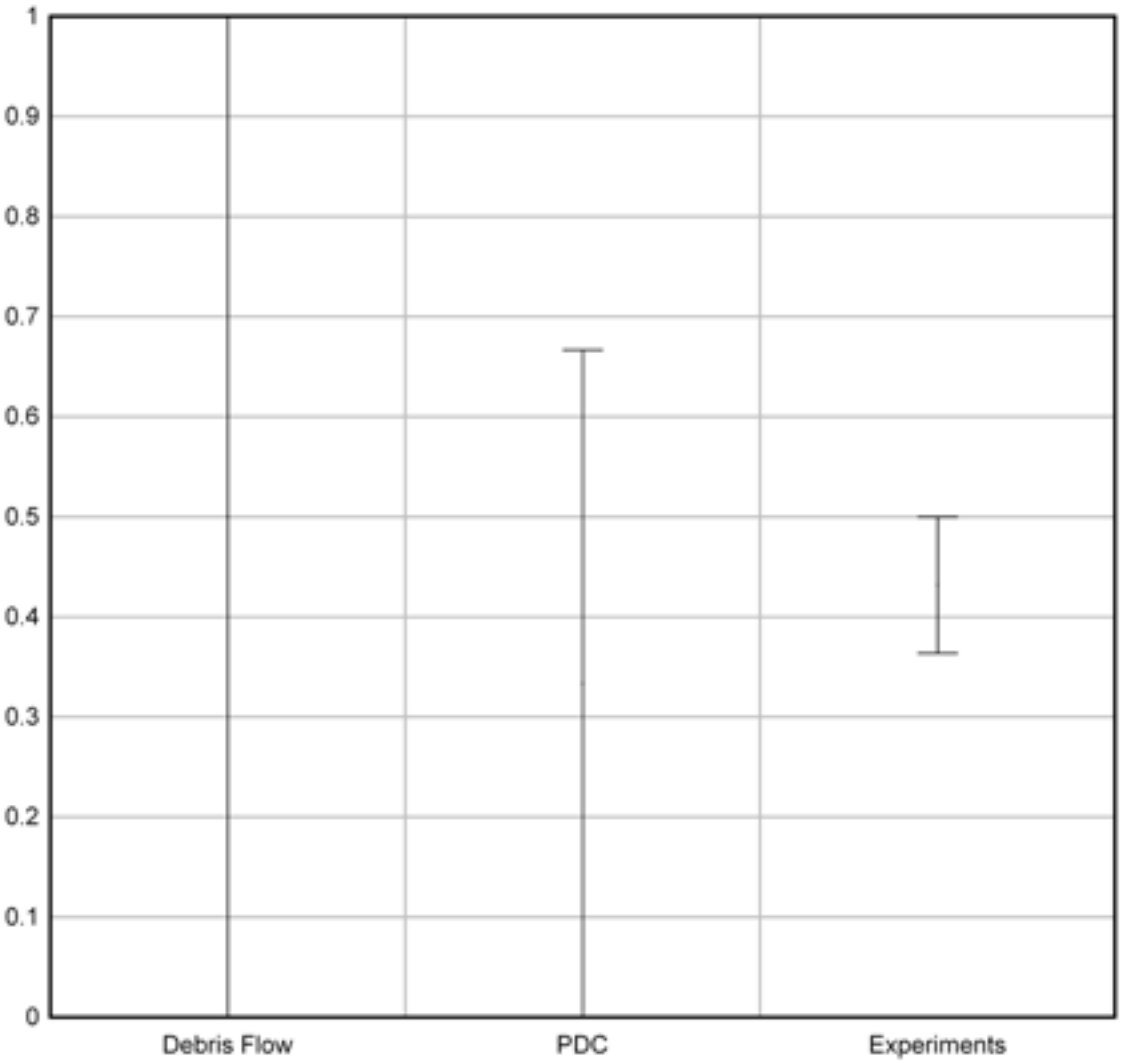

Figure B.1 Dimensionless analysis of Π_1 parameters

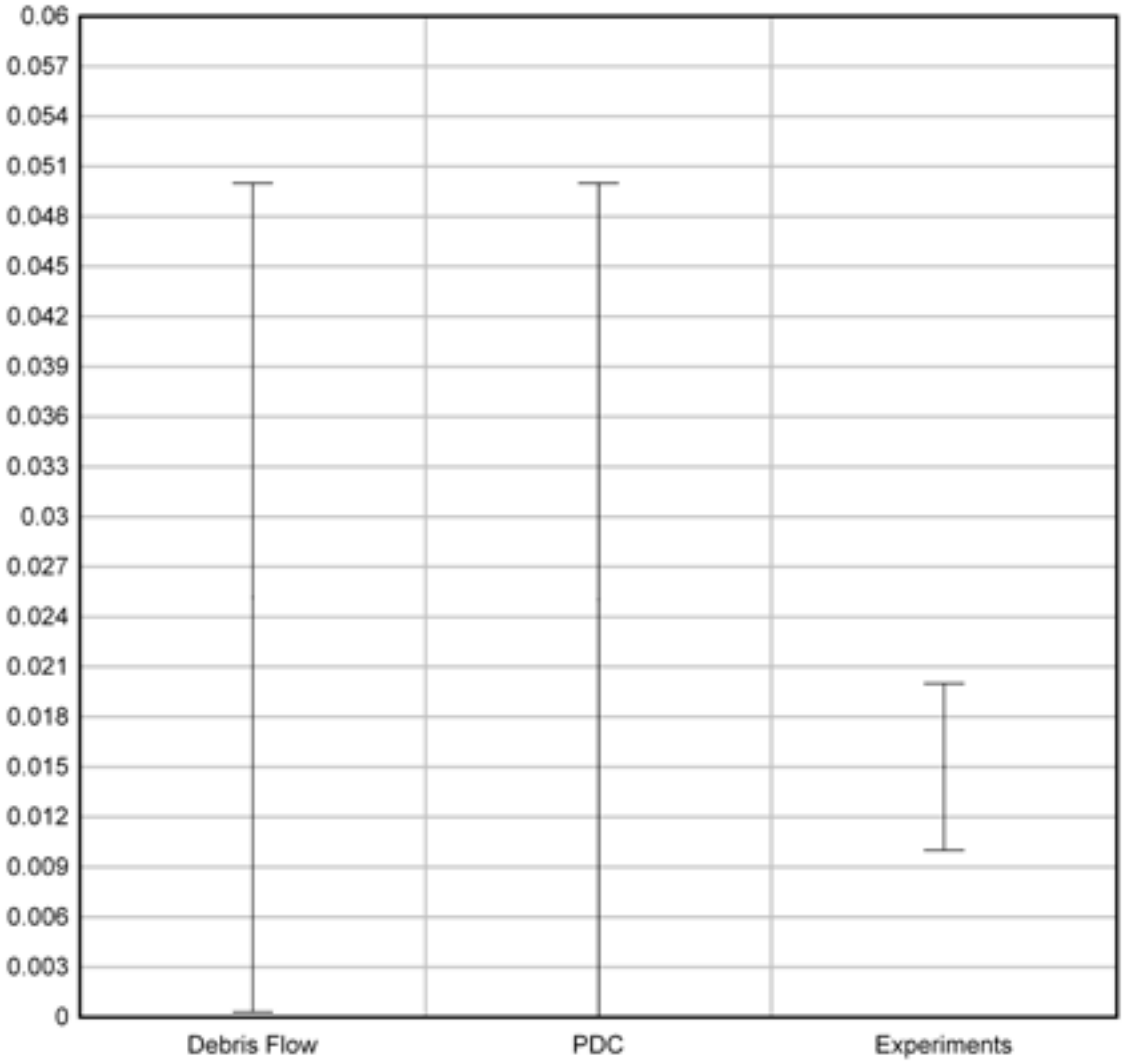

Figure B.2 Dimensionless analysis of Π_2 parameters

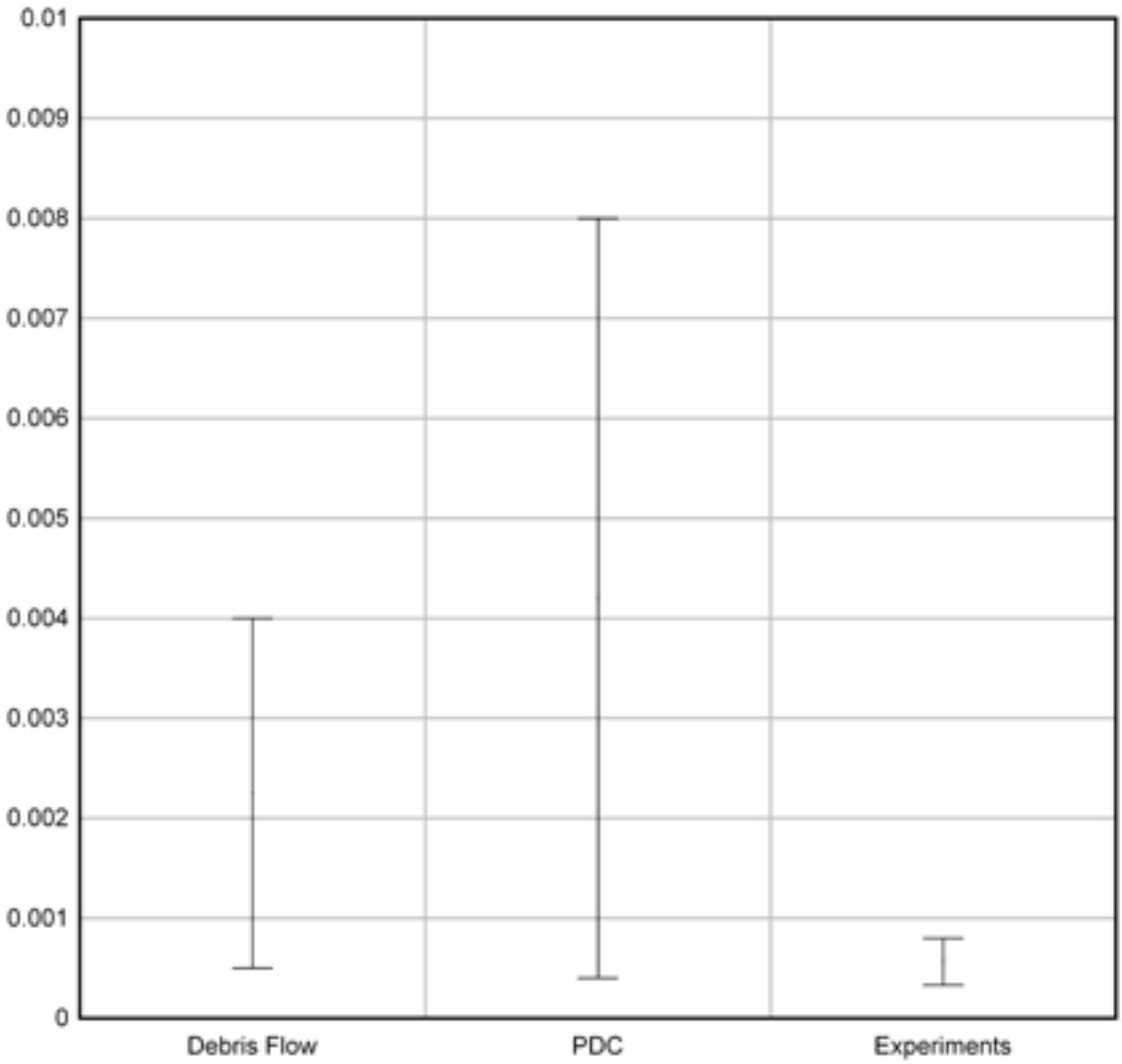

Figure B.3 Dimensionless analysis of Π_3 parameters

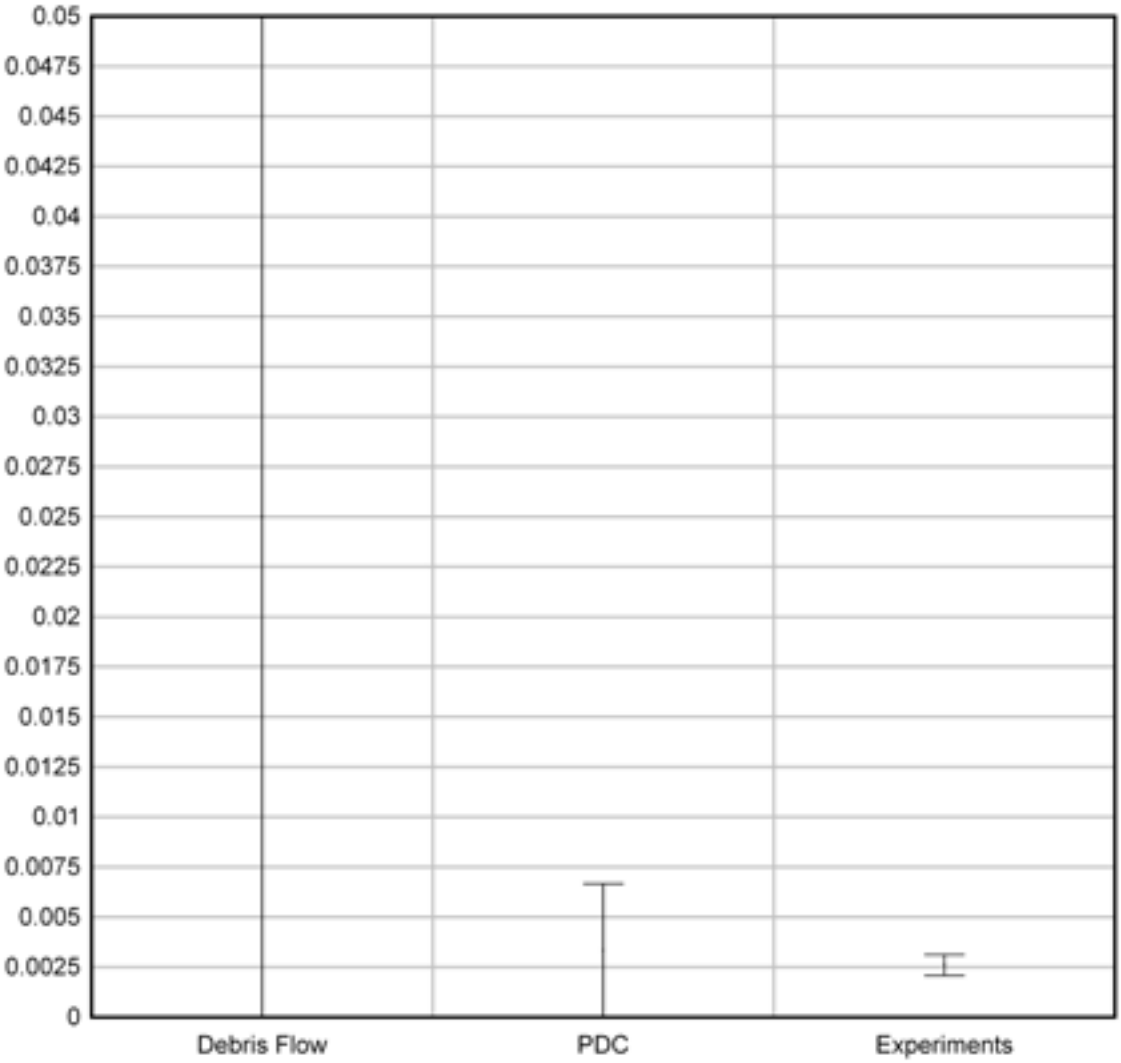

Figure B.4 Dimensionless analysis of Π_4 parameters

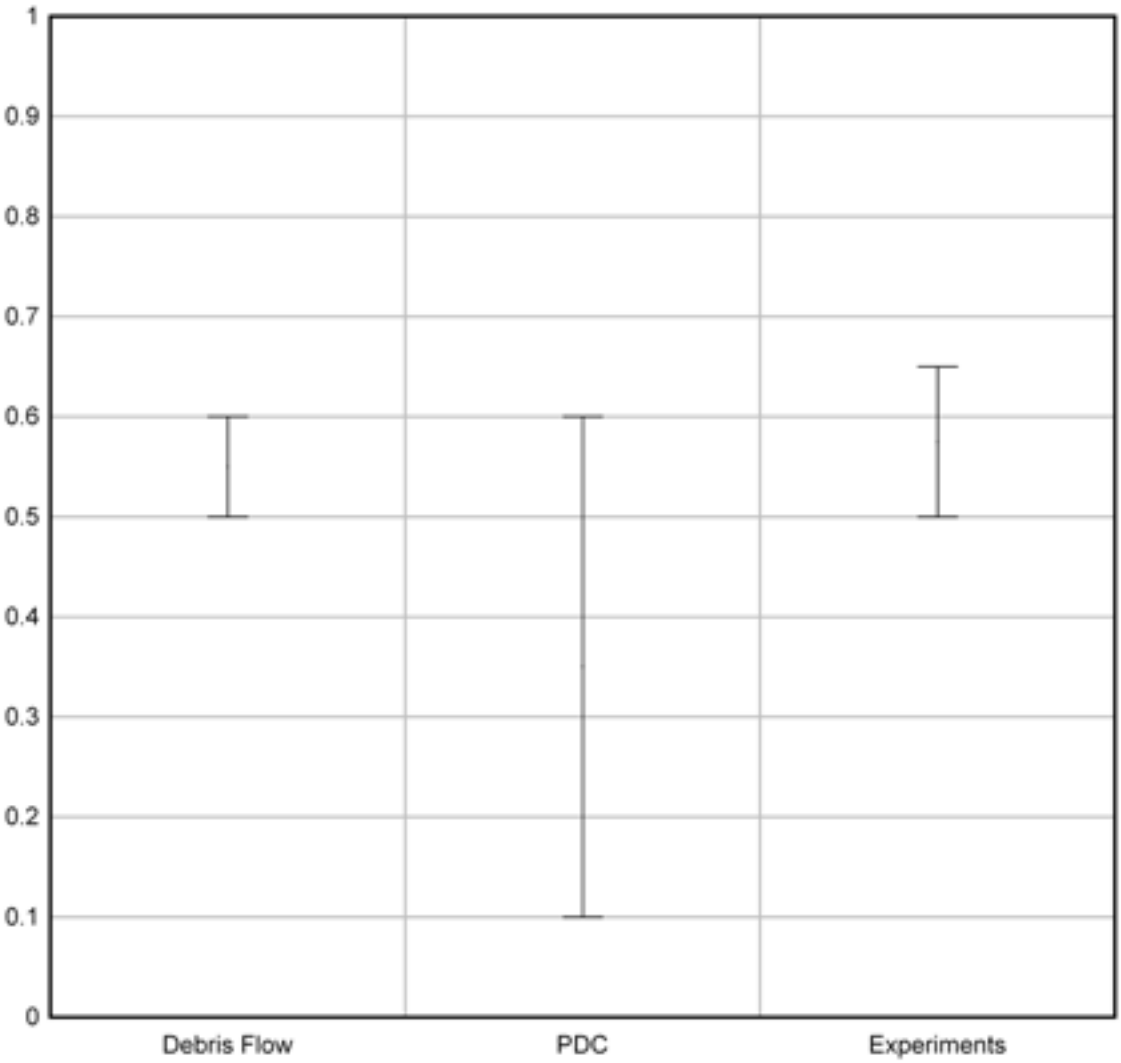

Figure B.5 Dimensionless analysis of Π_5 parameters

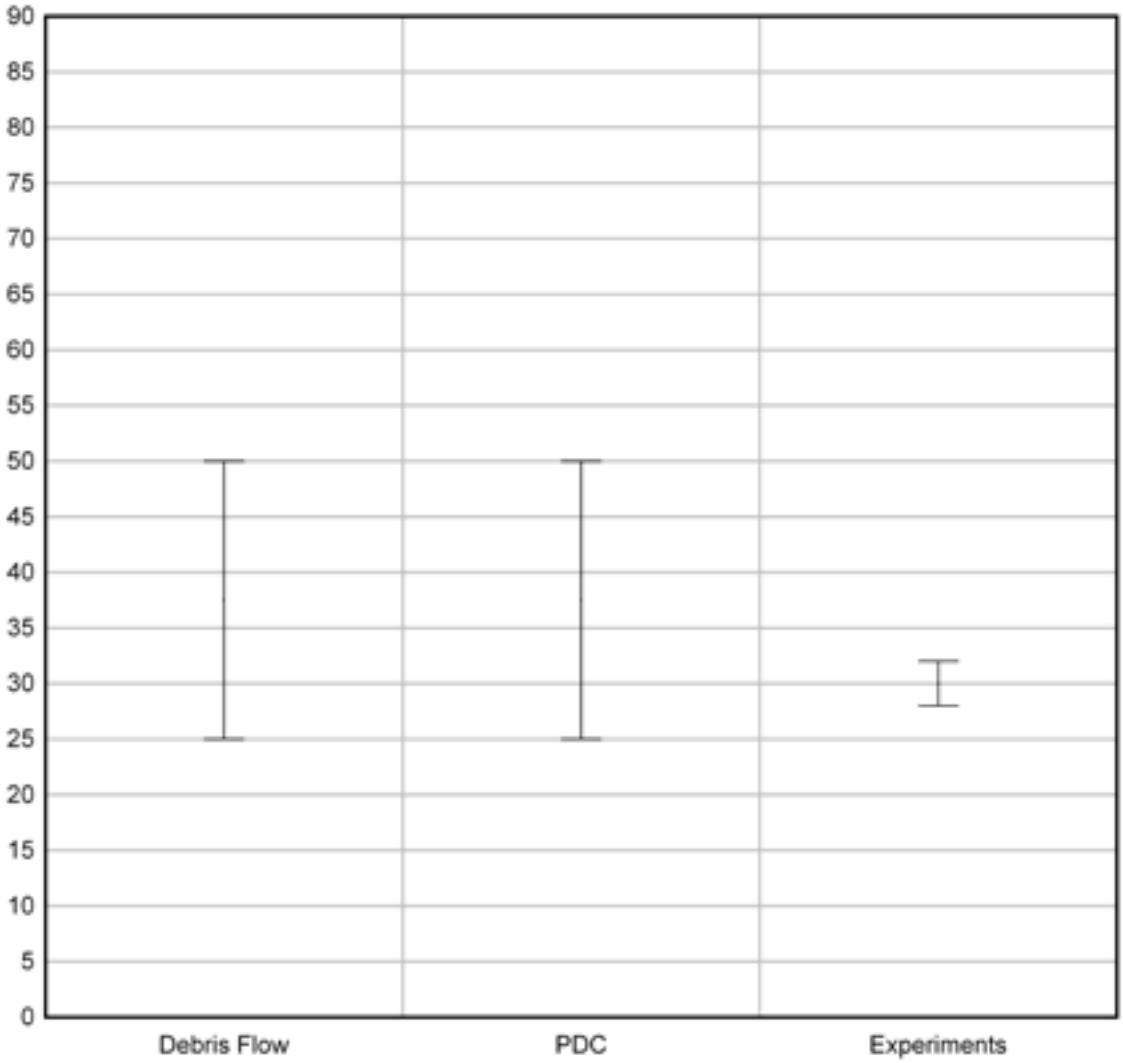

Figure B.6 Dimensionless analysis of Π_6 parameters

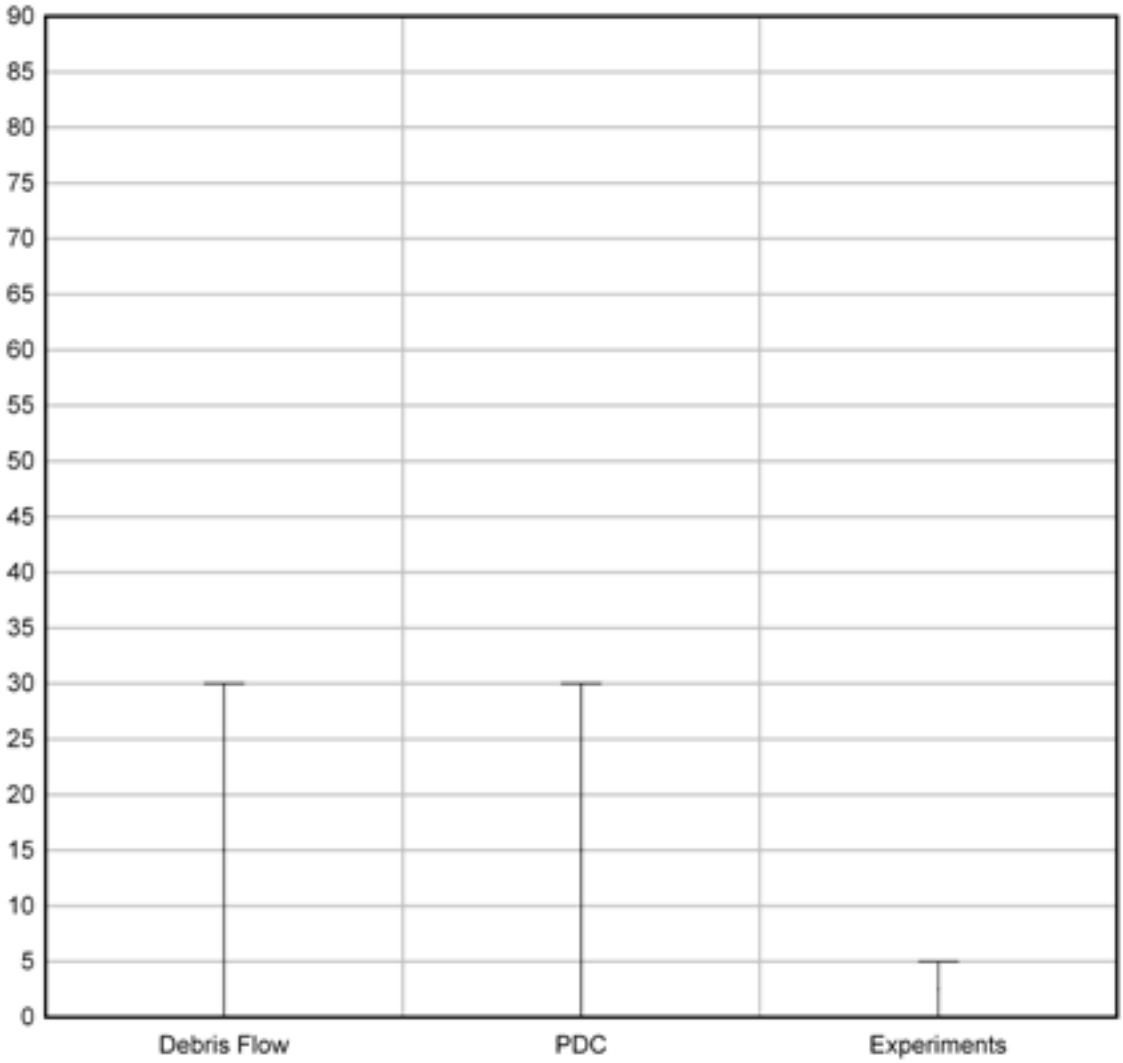

Figure B.7 Dimensionless analysis of Π_7 parameters

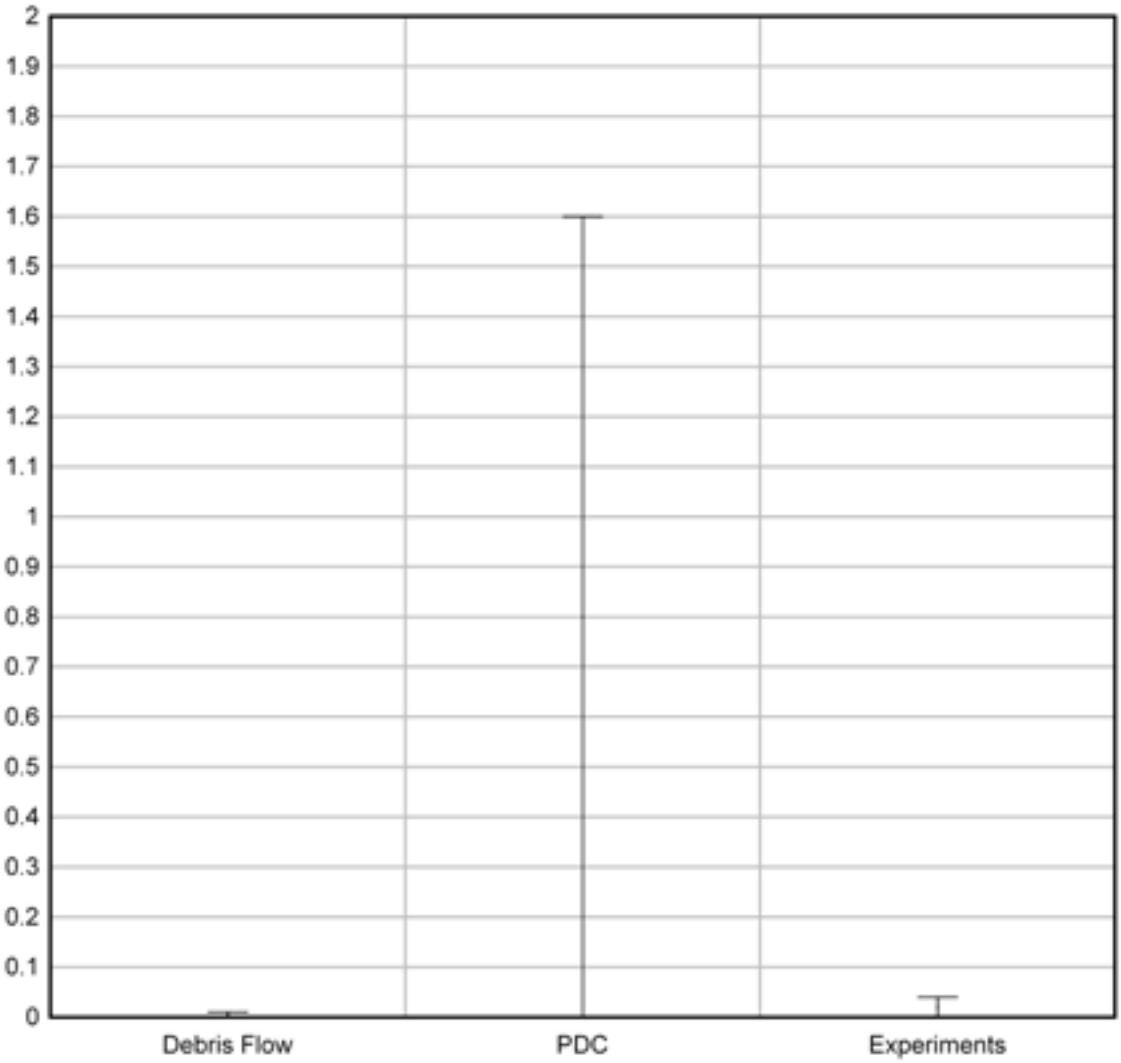

Figure B.8 dimensionless analysis of Π_8 parameters

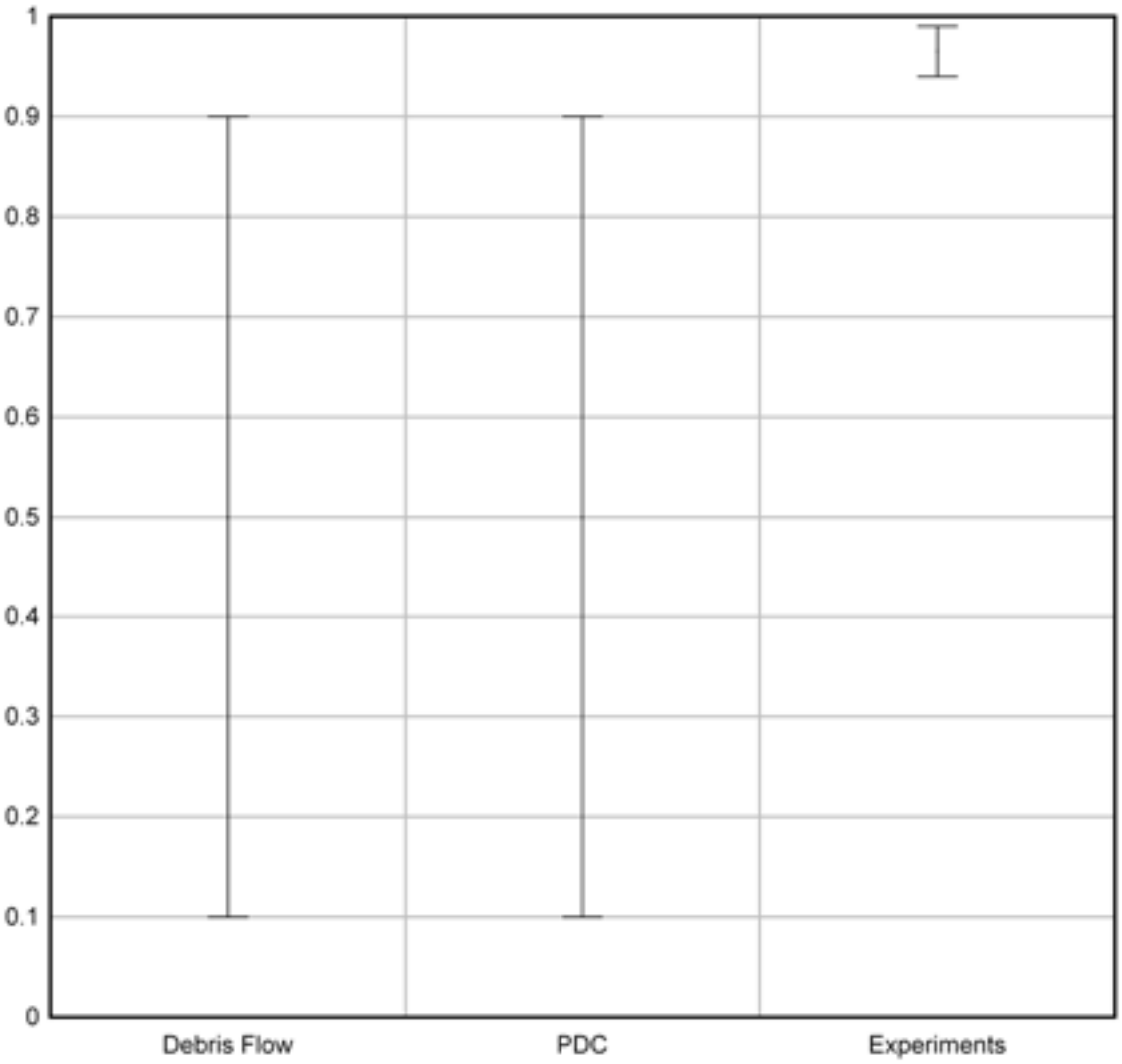

Figure B.9 Dimensionless analysis of Π_9 parameters

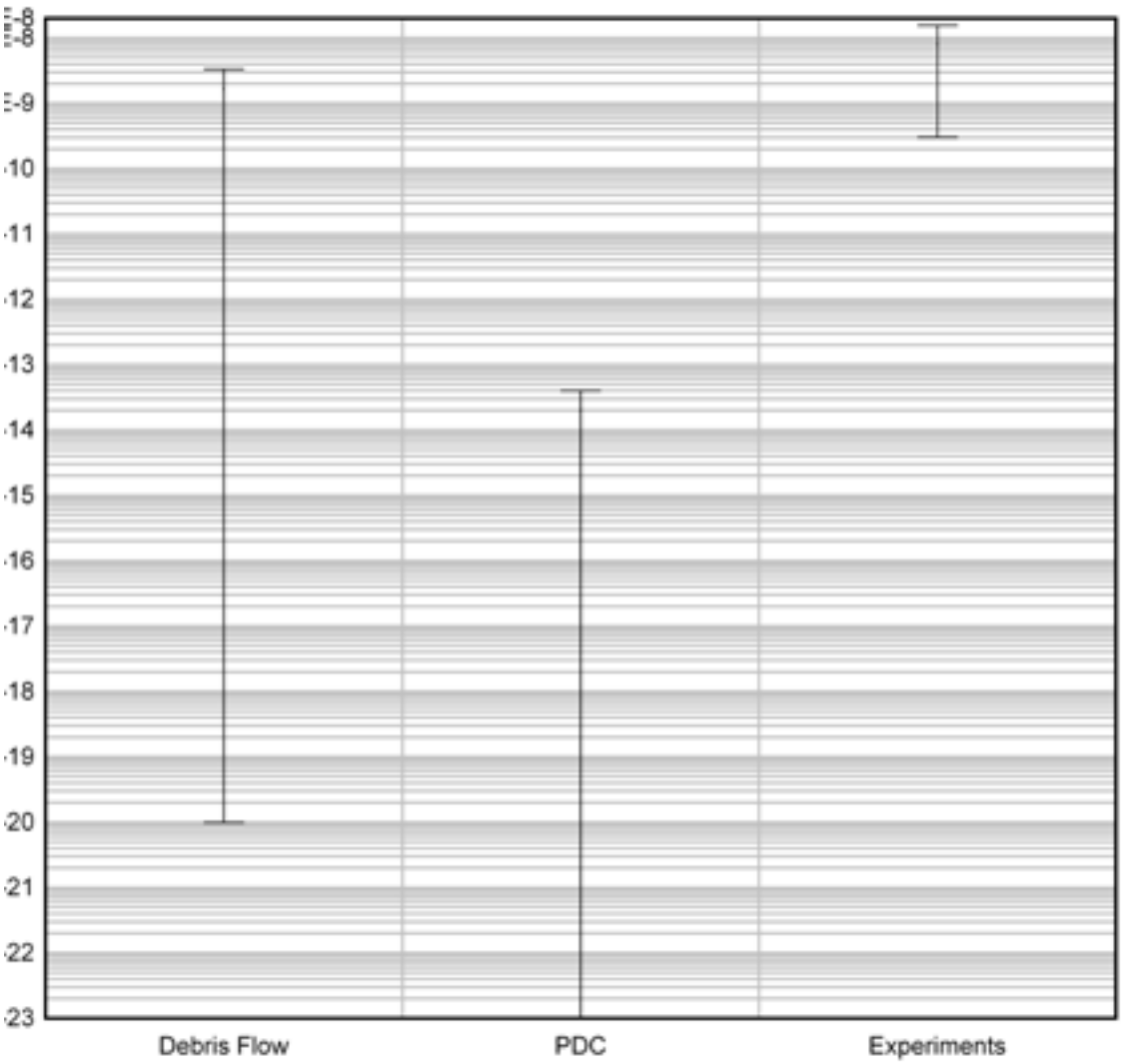

Figure B.10 Dimensionless analysis of Π_{10} parameters.

APPENDIX C - EXPERIMENTAL DATA

TABLE C.1 EXPERIMENTAL MATERIAL PROPERTIES

Material ID	Specific Density (g cm^{-3})	Bulk density (g cm^{-3})	Diameter (mm)	Colour	Material	Finish
ZY 9611	6.00	3.72	1.00-1.20	White	Ceramic	Matt
ZY 96025	6.00	3.85	0.20-0.30	White	Ceramic	Matt
4504/007LS	2.50	1.47	1.00-1.20	Black	Coated glass	Metallic
45015/341LS	2.50	1.50	0.40-0.60	Green	Coated glass	Metallic
45015/021LS	2.50	1.50	0.40-0.60	Orange	Coated glass	Metallic
5216/52LS	2.50	1.51	0.20-0.30	Red	Coated glass	Metallic
5216/288LS	2.50	1.51	0.20-0.30	Blue	Coated glass	Metallic
5216/110LS	2.50	1.51	0.20-0.30	Yellow	Coated glass	Metallic
5216/007-L	2.50	1.51	0.20-0.30	Black	Coated glass	Matt
5216/187-L	2.50	1.51	0.20-0.30	Red	Coated glass	Matt
5216/264-L	2.50	1.51	0.20-0.30	Lilac	Coated glass	Matt
5216/288-L	2.50	1.51	0.20-0.30	Blue	Coated glass	Matt
5216/111-L	2.50	1.51	0.20-0.30	Yellow	Coated glass	Matt
5216/291-L	2.50	1.51	0.20-0.30	Pale grey	Coated glass	Matt
5216/341-L	2.50	1.51	0.20-0.30	Green	Coated glass	Matt

TABLE C.2 VIDEO FOOTAGE RUN LIST

Nº	Base	Tilt (°)	Material	Release type	Charge volume (ml)	Release frame	Front stop frame	FPS	Calculated run time (s)	Runout mm	Field of View
1a	Perspex	0	LA60 Sand	Lock gate	250	1	23	25	0.88	248	wide
1b	Perspex	0	LA60 Sand	Lock gate	250	35		25			slope break in
1c	Perspex	0	LA60 Sand	Lock gate	250			25			slope break in
1d	Perspex	0	LA60 Sand	Lock gate	250			25			slope
1e	Perspex	0	LA60 Sand	Lock gate	250			25		250	runout
1f	Perspex	0	LA60 Sand	Lock gate	250	154	176	25	0.88	245	wide
1g	Perspex	0	LA60 Sand	Lock gate	250	192	214	25	0.88	249	wide
2a	Perspex	0	LA60 Sand	Lock gate	500	231	253	25	0.88	258	wide
3a	Perspex	0	LA60 Sand	Lock gate	250	1	23	25	0.88	243	wide
4a	Perspex	0	LA60 Sand	Lock gate	250	2		25			release
4b	Perspex	0	LA60 Sand	Lock gate	250	19		25			release
4c	Perspex	0	LA60 Sand	Lock gate	250	38		25			release
4d	Perspex	0	LA60 Sand	Lock gate	250	57		25			release
4e	Perspex	0	LA60 Sand	Lock gate	250	74		25			release
5a	Perspex	0	LA60 Sand	Lock gate	250	2	77	85	0.882353	245	wide
5b	Perspex	0	LA60 Sand	Lock gate	250	3	81	85	0.917647	252	wide
5c	Perspex	0	LA60 Sand	Lock gate	250	6	82	85	0.894118	250	wide
5d	Perspex	0	LA60 Sand	Lock gate	500	3	78	85	0.882353	254	wide
5e	Perspex	0	LA60 Sand	Lock gate	500	7	84	85	0.905882	261	wide
5f	Perspex	-5	LA60 Sand	Lock gate	500	4	79	85	0.882353	203	wide
5g	Perspex	-5	LA60 Sand	Lock gate	250	8	87	85	0.929412	211	wide
5h	Perspex	0	LA60 Sand	Lock gate	500	3		85			wide
5i	Sandpaper	-5	LA60 Sand	Lock gate	500	6	83	85	0.905882	24	wide
5j	Sandpaper	0	LA60 Sand	Lock gate	500	2	70	85	0.8	172	wide
5k	Sandpaper	-5	LA60 Sand	Lock gate	500	4		85			wide
5l	Sandpaper	0	LA60 Sand	Lock gate	500	5		85			wide
5m	Sandpaper	-5	LA60 Sand	Lock gate	500	5	80	85	0.882353	22	wide
5n	Sandpaper	5	LA60 Sand	Lock gate	500	9	83	85	0.870588	336	wide
5o	Sandpaper	0	LA60 Sand	Lock gate	250	4	76	85	0.847059	171	wide
6a	Sandpaper	0	LA60 Sand	Drop Chute	250	10	27	25	0.68	220	wide
7a	Sandpaper	0	LA60 Sand	Drop Chute	500	5	72	85	0.788235	225	wide
7b	Sandpaper	0	LA60 Sand	Drop Chute				85			slope
7c	Sandpaper	0	LA60 Sand	Drop Chute				85			slope
7d	Sandpaper	0	LA60 Sand	Drop Chute				85			slope
7e	Sandpaper	0	LA60 Sand	Drop Chute	250	1052	1110	85	0.682353	189	wide
7f	Sandpaper	0	LA60 Sand	Drop Chute	500	1374	1431	85	0.670588	218	wide
7g	Sandpaper	0	LA60 Sand	Drop Chute		1653		85			wide
7h	Sandpaper	0	LA60 Sand	Drop Chute	250	1970	2037	85	0.788235	230	wide
7i	Sandpaper	0	LA60 Sand	Drop Chute	500			85			slope
7j	Sandpaper	0	LA60 Sand + vermiculite	Drop Chute				85			Top
7k	Sandpaper	0	LA60 Sand + vermiculite	Drop Chute	250	2571	2624	85	0.623529	244	wide
8a	Sandpaper		45015/341LS + ZY9611 + 4504/007LS	Lock gate	200	4	18	25	0.56	143	wide

TABLE C.3 REPRODUCABILITY EXPERIMENTS LAB RECORDS - RUN 01

Run Number	01
Charge Size	500ml
Flume ID	B
Release Mechanism	Lock gate

Charge Details				
Charge number	Material	Volume (ml)	Mass (g)	Mix Details
1	5216 11025	500ml	742.39	monomict

Runout Extents		
Distance across flume (mm)	Proximal (mm)*	Distal (mm)*
0	- 111	203
37.5	-91	194
75	- 91	181
112.5	- 87	187
150	- 74	197

Notes
Test run. Flume not level. Thicknesses not measured.

Deposit thickness (mm)												
Distance across flume (mm)	Distance along flume (mm)*											
	-20	-15	-10	-5	0	5	10	15	20	25	30	35
0												
37.5												
75												
112.5												
150												

* Measured from the base of the break in slope

TABLE C.4 REPRODUCABILITY EXPERIMENTS LAB RECORDS - RUN 02

Run Number	02
Charge Size	500ml
Flume ID	B
Release Mechanism	Lock gate

Charge Details				
Charge number	Material	Volume (ml)	Mass (g)	Mix Details
1	5216-288	500	750.17	monomict

Runout Extents		
Distance across flume (mm)	Proximal (mm)*	Distal (mm)*
0	-126	192
37.5	-106	182
75	-106	172
112.5	-100	166
150	-95	163

Notes
Not flat

Deposit thickness (mm)												
Distance across flume (mm)	Distance along flume (mm)*											
	-20	-15	-10	-5	0	5	10	15	20	25	30	35
0			5 .0	15.5	19.0	14.5	7.5	3.0				
37.5			4.0	17.0	25.5	19.5	12.0	4.5				
75			5.0	13.0	25.0	21.0	12.0	2.0				
112.5			0.5	13.0	23.0	20.0	10.5	1.5				
150				9.5	16.0	12.0	5.5	1.0				

* Measured from the base of the break in slope

TABLE C.5 REPRODUCABILITY EXPERIMENTS LAB RECORDS - RUN 03

Run Number	03
Charge Size	500ml
Flume ID	B
Release Mechanism	Lock gate

Charge Details				
Charge number	Material	Volume (ml)	Mass (g)	Mix Details
1	5216-288	500	756.28	monomict

Runout Extents		
Distance across flume (mm)	Proximal (mm)*	Distal (mm)*
0	-111	156
37.5	-94	164
75	-89	154
112.5	-86	148
150	-75	141

Notes
Not flat

Deposit thickness (mm)												
Distance across flume (mm)	Distance along flume (mm)*											
	-20	-15	-10	-5	0	5	10	15	20	25	30	35
0			4.0	13.0	21.5	16.5	9.0	0.5				
37.5				13.5	27.0	22.0	14.5	4.5				
75				11.5	26.5	23.0	14.5	2.5				
112.5				9.5	24.0	22.0	12.0					
150				9.5	17.5	15.0	8.0					

* Measured from the base of the break in slope

TABLE C.6 REPRODUCABILITY EXPERIMENTS LAB RECORDS - RUN 04

Run Number	04
Charge Size	500ml
Flume ID	B
Release Mechanism	Lock gate

Charge Details

Charge number	Material	Volume (ml)	Mass (g)	Mix Details
1	5216-288	500ml	753.07	monomict

Runout Extents

Distance across flume (mm)	Proximal (mm)*	Distal (mm)*
0	-131	184
37.5	-115	176
75	-111	177
112.5	-101	182
150	-95	173

Notes

Not flat

Deposit thickness (mm)

Distance across flume (mm)	Distance along flume (mm)*											
	-20	-15	-10	-5	0	5	10	15	20	25	30	35
0			5.0	17.0	19.0	15.0	4.5	3.0				
37.5			5.0	14.0	25.5	21.0	13.0	5.0				
75			5.0	15.0	23.0	21.0	13.0	2.5				
112.5			0.5	3.5	19.0	18.5	9.5	2.0				
150				11.5	14.5	11.5	5.0	1.5				

* Measured from the base of the break in slope

TABLE C.7 REPRODUCABILITY EXPERIMENTS LAB RECORDS - RUN 05

Run Number	05
Charge Size	500ml
Flume ID	B
Release Mechanism	Lock gate

Charge Details				
Charge number	Material	Volume (ml)	Mass (g)	Mix Details
1	5216-288	500	756.52	monomict

Runout Extents		
Distance across flume (mm)	Proximal (mm)*	Distal (mm)*
0	-111	198
37.5	-95	198
75	-94	171
112.5	-89	166
150	-75	156

Notes
Not flat

Deposit thickness (mm)												
Distance across flume (mm)	Distance along flume (mm)*											
	-20	-15	-10	-5	0	5	10	15	20	25	30	35
0			0.5	16.0	22.0	17.0	10.0	4.0				
37.5				17.0	27.5	22.0	13.5	7.0				
75				13.5	25.0	20.5	13.0	5.5				
112.5				12.5	22.0	18.5	11.0	2.0				
150				9.0	14.5	12.5	6.0	0.5				

* Measured from the base of the break in slope

TABLE C.8 REPRODUCABILITY EXPERIMENTS LAB RECORDS - RUN 06

Run Number	06
Charge Size	500ml
Flume ID	B
Release Mechanism	Lock gate

Charge Details				
Charge number	Material	Volume (ml)	Mass (g)	Mix Details
1	5216-288	500	754.20	monomict

Runout Extents		
Distance across flume (mm)	Proximal (mm)*	Distal (mm)*
0	-98.5	157
37.5	-92	162
75	-91	160
112.5	-93	161.5
150	-98	153

Notes

Deposit thickness (mm)												
Distance across flume (mm)	Distance along flume (mm)*											
	-20	-15	-10	-5	0	5	10	15	20	25	30	35
0				11.0	18.5	16.0	10.5	1.5				
37.5				14.5	24.0	22.0	14.0	6.5				
75				11.5	25.0	23.0	16.0	6.0				
112.5				11.0	24.0	21.0	14.0	5.5				
150				11.0	19.0	15.0	8.5	1.0				

* Measured from the base of the break in slope

TABLE C.9 REPRODUCABILITY EXPERIMENTS LAB RECORDS - RUN 07

Run Number	07
Charge Size	500ml
Flume ID	B
Release Mechanism	Lock gate

Charge Details

Charge number	Material	Volume (ml)	Mass (g)	Mix Details
1	5216-288	500	755.34	monomict

Runout Extents

Distance across flume (mm)	Proximal (mm)*	Distal (mm)*
0	-91.5	205
37.5	-86	206
75	-85	197
112.5	-88	204
150	-92	204

Notes

Deposit thickness (mm)

Distance across flume (mm)	Distance along flume (mm)*											
	-20	-15	-10	-5	0	5	10	15	20	25	30	35
0				10.0	17.0	13.5	9.0	4.0	0.5			
37.5				10.5	23.0	21.0	13.0	8.0	0.5			
75				11.0	23.5	23.0	13.0	8.0				
112.5				13.0	23.0	21.0	12.5	7.5	0.5			
150				11.0	18.0	14.0	8.5	4.0	0.5			

* Measured from the base of the break in slope

TABLE C.10 REPRODUCABILITY EXPERIMENTS LAB RECORDS - RUN 08

Run Number	08
Charge Size	500ml
Flume ID	B
Release Mechanism	Lock gate

Charge Details				
Charge number	Material	Volume (ml)	Mass (g)	Mix Details
1	5216-288	500	753.86	monomict

Runout Extents		
Distance across flume (mm)	Proximal (mm)*	Distal (mm)*
0	-92	161
37.5	-86	167
75	-83	167
112.5	-86	167.5
150	-88	160

Notes

Deposit thickness (mm)												
Distance across flume (mm)	Distance along flume (mm)*											
	-20	-15	-10	-5	0	5	10	15	20	25	30	35
0				10.0	17.0	15.0	10.5	1.5				
37.5				11.0	23.5	22.0	13.5	7.0				
75				10.0	23.5	22.0	15.0	6.5				
112.5				10.0	22.5	21.5	14.0	5.0				
150				10.0	17.0	16.0	10.5	2.0				

* Measured from the base of the break in slope

TABLE C.11 REPRODUCABILITY EXPERIMENTS LAB RECORDS - RUN 09

Run Number	09
Charge Size	500ml
Flume ID	B
Release Mechanism	Lock gate

Charge Details

Charge number	Material	Volume (ml)	Mass (g)	Mix Details
1	5216-288	500	755.28	monomict

Runout Extents

Distance across flume (mm)	Proximal (mm)*	Distal (mm)*
0	-96.5	173.5
37.5	-89	177
75	-89	169
112.5	-91.5	173.5
150	-97.5	171

Notes

Deposit thickness (mm)

Distance across flume (mm)	Distance along flume (mm)*											
	-20	-15	-10	-5	0	5	10	15	20	25	30	35
0				12.0	17.5	14.0	9.5	3.0				
37.5				13.5	24.0	20.5	12.5	6.0				
75				11.5	24.0	20.5	13.0	5.5				
112.5				12.5	23.5	20.0	12.5	5.5				
150				11.5	18.0	13.5	8.5	2.5				

* Measured from the base of the break in slope

TABLE C.12 REPRODUCABILITY EXPERIMENTS LAB RECORDS - RUN 10

Run Number	10
Charge Size	500ml
Flume ID	B
Release Mechanism	Lock gate

Charge Details

Charge number	Material	Volume (ml)	Mass (g)	Mix Details
1	5216-288	500	757.44	monomict

Runout Extents

Distance across flume (mm)	Proximal (mm)*	Distal (mm)*
0	-100	184
37.5	-94	184
75	-94	179
112.5	-95	178
150	-98.5	171

Notes

Deposit thickness (mm)

Distance across flume (mm)	Distance along flume (mm)*											
	-20	-15	-10	-5	0	5	10	15	20	25	30	35
0			0.0	11.0	17.5	14.0	8.5	3.0				
37.5				13.0	23.0	20.5	12.0	5.5				
75				11.5	23.0	20.5	12.5	6.5				
112.5				12.5	22.5	20.5	13.0	5.5				
150				11.0	12.5	13.5	8.5	2.5				

* Measured from the base of the break in slope

TABLE C.13 REPRODUCABILITY EXPERIMENTS LAB RECORDS - RUN 11

Run Number	11
Charge Size	500ml
Flume ID	B
Release Mechanism	Lock gate

Charge Details				
Charge number	Material	Volume (ml)	Mass (g)	Mix Details
1	5216-288	500	755.02	monomict

Runout Extents		
Distance across flume (mm)	Proximal (mm)*	Distal (mm)*
0	-93	190
37.5	-87	192
75	-86	180
112.5	-87	187
150	-87	179

Notes

Deposit thickness (mm)												
Distance across flume (mm)	Distance along flume (mm)*											
	-20	-15	-10	-5	0	5	10	15	20	25	30	35
0				10.0	18.0	13.5	10.5	4.5				
37.5				11.5	24.0	22.0	13.5	8.5				
75				11.0	24.5	22.0	15.5	7.0				
112.5				12.5	23.0	21.0	12.5	6.5				
150				10.0	16.5	13.5	9.5	3.0				

* Measured from the base of the break in slope

TABLE C.14 REPRODUCABILITY EXPERIMENTS LAB RECORDS - RUN 12

Run Number	12
Charge Size	500ml
Flume ID	B
Release Mechanism	Lock gate

Charge Details

Charge number	Material	Volume (ml)	Mass (g)	Mix Details
1	5216-288	500	754.85	monomict

Runout Extents

Distance across flume (mm)	Proximal (mm)*	Distal (mm)*
0	-95	179
37.5	-89.5	181
75	-87.5	169
112.5	89	175
150	92	175

Notes

Deposit thickness (mm)

Distance across flume (mm)	Distance along flume (mm)*											
	-20	-15	-10	-5	0	5	10	15	20	25	30	35
0				13.0	19.5	14.0	9.0	2.5				
37.5				13.0	23.5	21.5	13.0	6.0				
75				11.0	23.5	21.0	13.0	6.0				
112.5				12.0	23.0	21.0	12.5	5.0				
150				11.0	18.0	13.0	8.5	2.5				

* Measured from the base of the break in slope

TABLE C.15 REPRODUCABILITY EXPERIMENTS LAB RECORDS - RUN 13

Run Number	13
Charge Size	500ml
Flume ID	B
Release Mechanism	Lock gate

Charge Details

Charge number	Material	Volume (ml)	Mass (g)	Mix Details
1	5216-288	500	754.85	monomict

Runout Extents

Distance across flume (mm)	Proximal (mm)*	Distal (mm)*
0	-91	159
37.5	-84	165
75	-83	162
112.5	-84	167
150	-89	166

Notes

Deposit thickness (mm)

Distance across flume (mm)	Distance along flume (mm)*											
	-20	-15	-10	-5	0	5	10	15	20	25	30	35
0				11.0	18.0	15.0	10.0	1.5				
37.5				11.0	24.5	21.0	14.0	5.5				
75				10.0	24.0	24.0	14.5	6.5				
112.5				11.0	24.0	22.0	14.0	5.0				
150				11.0	18.0	16.5	9.0	2.0				

* Measured from the base of the break in slope

TABLE C.16 REPRODUCABILITY EXPERIMENTS LAB RECORDS - RUN 14

Run Number	14
Charge Size	500ml
Flume ID	B
Release Mechanism	Lock gate

Charge Details				
Charge number	Material	Volume (ml)	Mass (g)	Mix Details
1	5216-288	500	754.85	monomict

Runout Extents		
Distance across flume (mm)	Proximal (mm)*	Distal (mm)*
0	-90	174
37.5	-85	177
75	-85	167
112.5	-86	179
150	-89	169

Notes

Deposit thickness (mm)												
Distance across flume (mm)	Distance along flume (mm)*											
	-20	-15	-10	-5	0	5	10	15	20	25	30	35
0				10.0	17.5	14.0	8.5	2.5				
37.5				11.5	23.5	21.5	12.5	6.5				
75				11.0	24.0	22.0	12.5	6.5				
112.5				11.5	22.5	21.5	12.5	5.5				
150				10.0	17.5	14.5	8.5	2.5				

* Measured from the base of the break in slope

TABLE C.17 REPRODUCABILITY EXPERIMENTS LAB RECORDS - RUN 15

Run Number	15
Charge Size	500ml
Flume ID	B
Release Mechanism	Lock gate

Charge Details				
Charge number	Material	Volume (ml)	Mass (g)	Mix Details
1	5216-288	500	754.85	monomict

Runout Extents		
Distance across flume (mm)	Proximal (mm)*	Distal (mm)*
0	-88	194
37.5	-83	198
75	-82	190
112.5	-83	197
150	-88	192

Notes

Deposit thickness (mm)												
Distance across flume (mm)	Distance along flume (mm)*											
	-20	-15	-10	-5	0	5	10	15	20	25	30	35
0				10.0	17.0	15.0	9.0	4.5				
37.5				10.5	23.5	22.0	14.5	6.5				
75				10.0	24.0	22.5	14.0	7.0				
112.5				11.0	23.5	21.5	14.0	6.5				
150				10.0	16.5	15.0	9.5	4.5				

* Measured from the base of the break in slope

TABLE C.18 REPRODUCABILITY EXPERIMENTS LAB RECORDS - RUN 16

Run Number	16
Charge Size	500ml
Flume ID	B
Release Mechanism	Lock gate

Charge Details				
Charge number	Material	Volume (ml)	Mass (g)	Mix Details
1	4501-341	500	750.12	monomict

Runout Extents		
Distance across flume (mm)	Proximal (mm)*	Distal (mm)*
0	-75	212
37.5	-68	209
75	-64	198
112.5	-65	197
150	-68	203

Notes

Deposit thickness (mm)												
Distance across flume (mm)	Distance along flume (mm)*											
	-20	-15	-10	-5	0	5	10	15	20	25	30	35
0				10.0	17.0	14.5	9.0	5.0	1.0			
37.5				10.0	22.0	21.0	13.0	8.0	1.0			
75				7.5	21.0	21.0	15.0	8.0				
112.5				9.5	22.0	21.0	13.0	7.0				
150				9.0	16.0	15.0	9.5	3.5	0.5			

* Measured from the base of the break in slope

TABLE C.19 REPRODUCABILITY EXPERIMENTS LAB RECORDS - RUN 17

Run Number	17
Charge Size	500ml
Flume ID	B
Release Mechanism	Lock gate

Charge Details

Charge number	Material	Volume (ml)	Mass (g)	Mix Details
1	4501-341	500	750.12	monomict

Runout Extents

Distance across flume (mm)	Proximal (mm)*	Distal (mm)*
0	-70	214
37.5	-66	214
75	-65	204
112.5	-66	212
150	-68	214

Notes

Deposit thickness (mm)

Distance across flume (mm)	Distance along flume (mm)*											
	-20	-15	-10	-5	0	5	10	15	20	25	30	35
0				8.0	15.5	14.0	9.5	4.0	1.0			
37.5				8.5	21.0	21.0	12.5	8.0	1.0			
75				8.0	20.0	21.0	15.5	9.0	0.5			
112.5				8.5	21.0	21.0	13.0	7.5	1.0			
150				7.5	16.0	14.0	9.5	4.0	1.0			

* Measured from the base of the break in slope

TABLE C.20 REPRODUCABILITY EXPERIMENTS LAB RECORDS - RUN 18

Run Number	18
Charge Size	500ml
Flume ID	B
Release Mechanism	Lock gate

Charge Details

Charge number	Material	Volume (ml)	Mass (g)	Mix Details
1	4501-341	500	750.12	monomict

Runout Extents

Distance across flume (mm)	Proximal (mm)*	Distal (mm)*
0	-68	217
37.5	-62	215
75	-63	204
112.5	-64	214
150	-67	218

Notes

Deposit thickness (mm)

Distance across flume (mm)	Distance along flume (mm)*											
	-20	-15	-10	-5	0	5	10	15	20	25	30	35
0				8.5	15.5	13.5	9.5	3.0	1.0			
37.5				7.5	21.0	21.0	14.5	8.0	1.0			
75				7.0	20.0	21.0	14.5	8.0	0.5			
112.5				7.0	21.0	21.0	13.5	8.0	1.0			
150				7.0	15.0	14.0	9.5	3.5	1.0			

* Measured from the base of the break in slope

TABLE C.21 REPRODUCABILITY EXPERIMENTS LAB RECORDS - RUN 19

Run Number	19
Charge Size	500ml
Flume ID	B
Release Mechanism	Lock gate

Charge Details

Charge number	Material	Volume (ml)	Mass (g)	Mix Details
1	4501-341	500	750.12	monomict

Runout Extents

Distance across flume (mm)	Proximal (mm)*	Distal (mm)*
0	-67	220
37.5	-60	216
75	-59	203
112.5	-61	208
150	-64	208

Notes

Deposit thickness (mm)

Distance across flume (mm)	Distance along flume (mm)*											
	-20	-15	-10	-5	0	5	10	15	20	25	30	35
0				6.0	14.5	14.5	9.5	4.0	1.0			
37.5				6.0	21.0	21.0	14.0	8.5	1.5			
75				5.0	20.5	22.0	15.5	9.0	0.5			
112.5				6.0	21.0	21.0	14.5	8.0	1.0			
150				6.5	14.5	14.5	9.5	5.0	1.0			

* Measured from the base of the break in slope

TABLE C.22 REPRODUCABILITY EXPERIMENTS LAB RECORDS - RUN 20

Run Number	20
Charge Size	500ml
Flume ID	B
Release Mechanism	Lock gate

Charge Details

Charge number	Material	Volume (ml)	Mass (g)	Mix Details
1	4501-341	500	750.12	monomict

Runout Extents

Distance across flume (mm)	Proximal (mm)*	Distal (mm)*
0	-64	214
37.5	-60	212
75	-59	203
112.5	-60	211
150	-64	212

Notes

Deposit thickness (mm)

Distance across flume (mm)	Distance along flume (mm)*											
	-20	-15	-10	-5	0	5	10	15	20	25	30	35
0				7.0	14.5	14.0	9.0	4.5	1.0			
37.5				7.5	20.0	21.5	14.5	8.0	1.0			
75				7.0	20.0	22.0	15.0	8.5	0.5			
112.5				8.0	20.5	21.5	14.0	8.0	1.0			
150				7.0	15.0	15.0	10.0	4.5	1.0			

* Measured from the base of the break in slope

TABLE C.23 REPRODUCABILITY EXPERIMENTS LAB RECORDS - RUN 21

Run Number	21
Charge Size	500ml
Flume ID	B
Release Mechanism	Lock gate

Charge Details

Charge number	Material	Volume (ml)	Mass (g)	Mix Details
1	4501-341	500	750.12	monomict

Runout Extents

Distance across flume (mm)	Proximal (mm)*	Distal (mm)*
0	-65	217
37.5	-61	217
75	-59	207
112.5	-61	213
150	-64	218

Notes

Deposit thickness (mm)

Distance across flume (mm)	Distance along flume (mm)*											
	-20	-15	-10	-5	0	5	10	15	20	25	30	35
0				6.5	15.0	13.0	10.5	4.5	1.0			
37.5				7.0	21.0	21.0	15.0	8.0	1.0			
75				6.5	20.0	21.5	15.5	9.0	0.5			
112.5				7.0	20.5	21.0	15.0	7.0	1.0			
150				6.5	15.0	14.0	10.5	4.5	1.0			

* Measured from the base of the break in slope

TABLE C.24 REPRODUCABILITY EXPERIMENTS LAB RECORDS - RUN 22

Run Number	22
Charge Size	500ml
Flume ID	B
Release Mechanism	Lock gate

Charge Details				
Charge number	Material	Volume (ml)	Mass (g)	Mix Details
1	4501-341	500	750.12	monomict

Runout Extents		
Distance across flume (mm)	Proximal (mm)*	Distal (mm)*
0	-64	219
37.5	-61	213
75	-57	206
112.5	-61	210
150	-62	215

Notes

Deposit thickness (mm)												
Distance across flume (mm)	Distance along flume (mm)*											
	-20	-15	-10	-5	0	5	10	15	20	25	30	35
0				7.0	15.0	14.5	10.0	4.0	1.0			
37.5				6.0	21.0	21.0	15.0	8.0	1.0			
75				6.0	20.0	21.5	16.0	9.0	0.5			
112.5				7.0	21.0	21.0	15.0	8.0	1.0			
150				6.0	15.0	14.5	10.0	4.5	1.0			

* Measured from the base of the break in slope

TABLE C.25 REPRODUCABILITY EXPERIMENTS LAB RECORDS - RUN 23

Run Number	23
Charge Size	500ml
Flume ID	B
Release Mechanism	Lock gate

Charge Details				
Charge number	Material	Volume (ml)	Mass (g)	Mix Details
1	4501-341	500	750.12	monomict

Runout Extents		
Distance across flume (mm)	Proximal (mm)*	Distal (mm)*
0	-62	220
37.5	-57	222
75	-55	204
112.5	-57	198
150	-59	201

Notes

Deposit thickness (mm)												
Distance across flume (mm)	Distance along flume (mm)*											
	-20	-15	-10	-5	0	5	10	15	20	25	30	35
0				6.0	15.5	14.0	11.0	5.0	1.5			
37.5				6.0	20.2	21.0	15.5	9.0	2.0			
75				6.0	19.5	22.0	16.0	9.5	1.0			
112.5				6.5	20.0	21.0	15.0	9.5				
150				6.0	15.0	15.0	11.0	5.0	1.0			

* Measured from the base of the break in slope

TABLE C.26 REPRODUCABILITY EXPERIMENTS LAB RECORDS - RUN 24

Run Number	24
Charge Size	500ml
Flume ID	B
Release Mechanism	Lock gate

Charge Details

Charge number	Material	Volume (ml)	Mass (g)	Mix Details
1	4501-341	500	750.12	monomict

Runout Extents

Distance across flume (mm)	Proximal (mm)*	Distal (mm)*
0	-58	226
37.5	-55	224
75	-55	216
112.5	-56	222
150	-61	226

Notes

Deposit thickness (mm)

Distance across flume (mm)	Distance along flume (mm)*											
	-20	-15	-10	-5	0	5	10	15	20	25	30	35
0				5.5	13.0	13.5	10.0	4.0	1.0			
37.5				4.0	19.5	21.0	15.5	8.5	2.0			
75				4.0	19.0	22.0	15.5	9.5	1.5			
112.5				4.0	21.0	21.5	15.0	9.0	2.5			
150				6.0	15.0	14.5	10.5	5.0	1.5			

* Measured from the base of the break in slope

TABLE C.27 REPRODUCABILITY EXPERIMENTS LAB RECORDS - RUN 25

Run Number	25
Charge Size	500ml
Flume ID	B
Release Mechanism	Lock gate

Charge Details				
Charge number	Material	Volume (ml)	Mass (g)	Mix Details
1	4501-341	500	750.12	monomict

Runout Extents		
Distance across flume (mm)	Proximal (mm)*	Distal (mm)*
0	-62	223
37.5	-59	221
75	-56	213
112.5	-58	219
150	-62	223

Notes

Deposit thickness (mm)												
Distance across flume (mm)	Distance along flume (mm)*											
	-20	-15	-10	-5	0	5	10	15	20	25	30	35
0				7.0	14.0	13.5	9.5	5.0	1.5			
37.5				5.5	19.5	21.0	15.5	8.5	2.0			
75				6.0	19.0	21.5	16.0	9.5	1.0			
112.5				6.0	20.0	21.0	15.5	8.5	2.0			
150				7.0	14.5	15.0	10.0	5.5	1.5			

* Measured from the base of the break in slope

TABLE C.28 REPRODUCABILITY EXPERIMENTS LAB RECORDS - RUN 26

Run Number	26
Charge Size	500ml
Flume ID	B
Release Mechanism	Lock gate

Charge Details				
Charge number	Material	Volume (ml)	Mass (g)	Mix Details
1	4505-007	500	735.15	monomict

Runout Extents		
Distance across flume (mm)	Proximal (mm)*	Distal (mm)*
0	-32	263
37.5	-31	260
75	-28	256
112.5	-32	266
150	-34	272

Notes

Deposit thickness (mm)												
Distance across flume (mm)	Distance along flume (mm)*											
	-20	-15	-10	-5	0	5	10	15	20	25	30	35
0					12.5	14.0	9.5	7.0	3.0	1.0		
37.5					15.0	19.0	16.0	12.0	6.5	1.5		
75					14.5	21.0	19.0	13.5	7.0	1.5		
112.5					16.0	20.0	170	12.5	6.0	2.0		
150					13.0	15.0	12.0	8.0	4.0	2.0		

* Measured from the base of the break in slope

TABLE C.29 REPRODUCABILITY EXPERIMENTS LAB RECORDS - RUN 27

Run Number	27
Charge Size	500ml
Flume ID	B
Release Mechanism	Lock gate

Charge Details				
Charge number	Material	Volume (ml)	Mass (g)	Mix Details
1	4505-007	500	735.15	monomict

Runout Extents		
Distance across flume (mm)	Proximal (mm)*	Distal (mm)*
0	-34	265
37.5	-28	272
75	-24	259
112.5	-27	272
150	-36	264

Notes

Deposit thickness (mm)												
Distance across flume (mm)	Distance along flume (mm)*											
	-20	-15	-10	-5	0	5	10	15	20	25	30	35
0					8.5	14.5	11.5	7.5	4.5	1.0		
37.5					15.0	19.5	17.0	12.0	7.0	2.0		
75					13.5	21.0	18.0	13.5	8.0	2.0		
112.5					14.0	20.0	17.0	12.5	7.0	2.0		
150					8.5	14.5	12.0	8.0	4.5	1.0		

* Measured from the base of the break in slope

TABLE C.30 REPRODUCABILITY EXPERIMENTS LAB RECORDS - RUN 28

Run Number	28
Charge Size	500ml
Flume ID	B
Release Mechanism	Lock gate

Charge Details				
Charge number	Material	Volume (ml)	Mass (g)	Mix Details
1	4505-007	500	735.15	monomict

Runout Extents		
Distance across flume (mm)	Proximal (mm)*	Distal (mm)*
0	-33	270
37.5	-28	277
75	-25	265
112.5	-28	274
150	-30	268

Notes

Deposit thickness (mm)												
Distance across flume (mm)	Distance along flume (mm)*											
	-20	-15	-10	-5	0	5	10	15	20	25	30	35
0					13.0	14.5	11.5	8.5	4.0	1.5		
37.5					15.0	20.0	17.5	12.0	7.5	2.0		
75					14.0	21.0	19.0	13.5	8.0	2.0		
112.5					15.0	20.0	17.0	12.0	7.5	2.0		
150					12.5	14.5	12.0	8.0	4.5	1.0		

* Measured from the base of the break in slope

TABLE C.31 REPRODUCABILITY EXPERIMENTS LAB RECORDS - RUN 29

Run Number	29
Charge Size	500ml
Flume ID	B
Release Mechanism	Lock gate

Charge Details				
Charge number	Material	Volume (ml)	Mass (g)	Mix Details
1	4505-007	500	735.15	monomict

Runout Extents		
Distance across flume (mm)	Proximal (mm)*	Distal (mm)*
0	-32	278
37.5	-29	271
75	-22	265
112.5	-25	270
150	-28	265

Notes

Deposit thickness (mm)												
Distance across flume (mm)	Distance along flume (mm)*											
	-20	-15	-10	-5	0	5	10	15	20	25	30	35
0					14.0	15.0	12.0	8.0	4.5	2.0		
37.5					15.0	19.5	17.0	13.0	7.5	2.0		
75					13.5	21.5	19.0	14.5	8.0	1.0		
112.5					15.0	19.5	17.0	12.0	6.5	2.0		
150					12.0	15.0	12.0	7.5	4.5	1.0		

* Measured from the base of the break in slope

TABLE C.32 REPRODUCABILITY EXPERIMENTS LAB RECORDS - RUN 30

Run Number	30
Charge Size	500ml
Flume ID	B
Release Mechanism	Lock gate

Charge Details

Charge number	Material	Volume (ml)	Mass (g)	Mix Details
1	4505-007	500	735.15	monomict

Runout Extents

Distance across flume (mm)	Proximal (mm)*	Distal (mm)*
0	-32	278
37.5	-29	284
75	-25	262
112.5	-27	277
150	-30	282

Notes

Deposit thickness (mm)

Distance across flume (mm)	Distance along flume (mm)*											
	-20	-15	-10	-5	0	5	10	15	20	25	30	35
0					12.5	14.0	11.5	8.0	3.5	1.0		
37.5					15.0	19.5	16.0	12.5	8.0	2.0		
75					14.5	21.0	18.0	13.5	8.5	2.0		
112.5					15.0	20.0	16.0	13.0	8.0	2.0		
150					13.0	15.0	11.5	7.5	3.5	1.0		

* Measured from the base of the break in slope

TABLE C.33 REPRODUCABILITY EXPERIMENTS LAB RECORDS - RUN 31

Run Number	31
Charge Size	500ml
Flume ID	B
Release Mechanism	Lock gate

Charge Details				
Charge number	Material	Volume (ml)	Mass (g)	Mix Details
1	4505-007	500	735.15	monomict

Runout Extents		
Distance across flume (mm)	Proximal (mm)*	Distal (mm)*
0	-33	263
37.5	-30	270
75	-25	265
112.5	-28	273
150	-30	265

Notes

Deposit thickness (mm)												
Distance across flume (mm)	Distance along flume (mm)*											
	-20	-15	-10	-5	0	5	10	15	20	25	30	35
0					13.0	15.0	12.0	8.0	3.5	1.0		
37.5					15.0	19.5	19.5	12.0	6.0	2.0		
75					12.0	21.0	21.0	13.0	8.0	2.0		
112.5					15.0	20.0	20.0	11.0	6.0	2.0		
150					13.0	15.0	15.0	8.0	4.0	1.0		

* Measured from the base of the break in slope

TABLE C.34 REPRODUCABILITY EXPERIMENTS LAB RECORDS - RUN 32

Run Number	32
Charge Size	500ml
Flume ID	B
Release Mechanism	Lock gate

Charge Details				
Charge number	Material	Volume (ml)	Mass (g)	Mix Details
1	4505-007	500	735.15	monomict

Runout Extents		
Distance across flume (mm)	Proximal (mm)*	Distal (mm)*
0	-32	277
37.5	-27	280
75	-23	267
112.5	-25	274
150	-29	272

Notes

Deposit thickness (mm)												
Distance across flume (mm)	Distance along flume (mm)*											
	-20	-15	-10	-5	0	5	10	15	20	25	30	35
0					12.0	15.0	12.0	7.5	3.0	2.5		
37.5					14.0	20.0	17.5	12.0	7.0	2.0		
75					11.0	21.0	19.0	13.0	8.0	2.0		
112.5					14.0	19.5	16.5	11.5	6.5	2.0		
150					12.0	14.5	13.0	8.0	4.0	2.0		

* Measured from the base of the break in slope

TABLE C.35 REPRODUCABILITY EXPERIMENTS LAB RECORDS - RUN 33

Run Number	33
Charge Size	500ml
Flume ID	B
Release Mechanism	Lock gate

Charge Details				
Charge number	Material	Volume (ml)	Mass (g)	Mix Details
1	4505-007	500	735.15	monomict

Runout Extents		
Distance across flume (mm)	Proximal (mm)*	Distal (mm)*
0	-32	273
37.5	-28	276
75	-25	273
112.5	-25	273
150	-27	270

Notes

Deposit thickness (mm)												
Distance across flume (mm)	Distance along flume (mm)*											
	-20	-15	-10	-5	0	5	10	15	20	25	30	35
0					13.0	14.5	12.0	8.0	4.0	2.0		
37.5					14.5	19.5	16.5	11.5	7.0	2.5		
75					13.0	21.0	18.5	13.5	8.5	2.5		
112.5					14.0	20.0	17.0	12.0	7.0	2.0		
150					17.5	15.0	12.0	8.0	4.0	1.5		

* Measured from the base of the break in slope

TABLE C.36 REPRODUCABILITY EXPERIMENTS LAB RECORDS - RUN 34

Run Number	34
Charge Size	500ml
Flume ID	B
Release Mechanism	Lock gate

Charge Details

Charge number	Material	Volume (ml)	Mass (g)	Mix Details
1	4505-007	500	735.15	monomict

Runout Extents

Distance across flume (mm)	Proximal (mm)*	Distal (mm)*
0	-34	264
37.5	-28	282
75	-23	265
112.5	-25	274
150	-28	276

Notes

Deposit thickness (mm)

Distance across flume (mm)	Distance along flume (mm)*											
	-20	-15	-10	-5	0	5	10	15	20	25	30	35
0					13.0	15.0	11.5	8.0	4.0	1.5		
37.5					15.0	20.0	16.5	12.0	7.0	2.0		
75					11.5	21.0	19.5	14.0	7.5	2.0		
112.5					14.0	20.0	17.0	11.5	6.5	2.0		
150					11.5	14.5	12.0	8.0	4.0	1.0		

* Measured from the base of the break in slope

TABLE C.37 REPRODUCABILITY EXPERIMENTS LAB RECORDS - RUN 35

Run Number	35
Charge Size	500ml
Flume ID	B
Release Mechanism	Lock gate

Charge Details

Charge number	Material	Volume (ml)	Mass (g)	Mix Details
1	4505-007	500	735.15	monomict

Runout Extents

Distance across flume (mm)	Proximal (mm)*	Distal (mm)*
0	-31	259
37.5	-25	282
75	-22	268
112.5	-24	273
150	-26	273

Notes

Deposit thickness (mm)

Distance across flume (mm)	Distance along flume (mm)*											
	-20	-15	-10	-5	0	5	10	15	20	25	30	35
0					12.0	14.0	12.5	8.0	4.5	1.5		
37.5					14.5	19.5	17.5	12.0	7.0	2.5		
75					8.0	21.0	18.5	14.0	9.0	2.5		
112.5					13.5	19.5	17.5	12.5	7.0	2.0		
150					12.0	14.0	12.5	9.0	4.5	1.0		

* Measured from the base of the break in slope

TABLE C.38 REPRODUCABILITY EXPERIMENTS LAB RECORDS - RUN 36

Run Number	36
Charge Size	500ml
Flume ID	B
Release Mechanism	Lock gate

Charge Details

Charge number	Material	Volume (ml)	Mass (g)	Mix Details
1	ZY 96025	500	1926.09	monomict

Runout Extents

Distance across flume (mm)	Proximal (mm)*	Distal (mm)*
0	-46	255
37.5	-42	250
75	-39	229
112.5	-41	227
150	-44	235

Notes

Deposit thickness (mm)

Distance across flume (mm)	Distance along flume (mm)*											
	-20	-15	-10	-5	0	5	10	15	20	25	30	35
0					11.0	14.0	12.5	8.5	3.5	0.5		
37.5					18.0	21.0	15.5	12.0	7.0	0.0		
75					15.5	22.0	17.0	12.5	7.0			
112.5					16.5	21.5	16.0	11.5	6.0			
150					11.0	15.0	13.0	9.0	1.0			

* Measured from the base of the break in slope

TABLE C.39 REPRODUCABILITY EXPERIMENTS LAB RECORDS - RUN 37

Run Number	37
Charge Size	500ml
Flume ID	B
Release Mechanism	Lock gate

Charge Details

Charge number	Material	Volume (ml)	Mass (g)	Mix Details
1	ZY 96025	500	1926.09	monomict

Runout Extents

Distance across flume (mm)	Proximal (mm)*	Distal (mm)*
0	-44	235
37.5	-41	246
75	-39	228
112.5	-41	227
150	-45	230

Notes

Deposit thickness (mm)

Distance across flume (mm)	Distance along flume (mm)*											
	-20	-15	-10	-5	0	5	10	15	20	25	30	35
0					10.0	14.5	13.0	9.0	3.0			
37.5					17.0	21.5	16.0	11.5	7.0			
75					15.0	22.0	16.5	12.5	7.0			
112.5					17.0	22.0	16.0	11.5	7.0			
150					11.0	15.0	13.0	9.0	3.0			

* Measured from the base of the break in slope

TABLE C.40 REPRODUCABILITY EXPERIMENTS LAB RECORDS - RUN 38

Run Number	38
Charge Size	500ml
Flume ID	B
Release Mechanism	Lock gate

Charge Details

Charge number	Material	Volume (ml)	Mass (g)	Mix Details
1	ZY 96025	500	1926.09	monomict

Runout Extents

Distance across flume (mm)	Proximal (mm)*	Distal (mm)*
0	-45	232
37.5	-42	241
75	-39	233
112.5	-42	245
150	-45	247

Notes

Deposit thickness (mm)

Distance across flume (mm)	Distance along flume (mm)*											
	-20	-15	-10	-5	0	5	10	15	20	25	30	35
0					11.0	15.0	13.0	8.5	3.0			
37.5					16.0	21.5	17.0	11.5	6.0			
75					15.0	22.0	17.0	12.0	7.0			
112.5					16.0	21.5	16.5	11.5	5.5			
150					10.5	15.0	13.0	9.0	3.0			

* Measured from the base of the break in slope

TABLE C.41 REPRODUCABILITY EXPERIMENTS LAB RECORDS - RUN 39

Run Number	39
Charge Size	500ml
Flume ID	B
Release Mechanism	Lock gate

Charge Details				
Charge number	Material	Volume (ml)	Mass (g)	Mix Details
1	ZY 96025	500	1926.09	monomict

Runout Extents		
Distance across flume (mm)	Proximal (mm)*	Distal (mm)*
0	-44	222
37.5	-40	230
75	-39	222
112.5	-40	222
150	-44	223

Notes

Deposit thickness (mm)												
Distance across flume (mm)	Distance along flume (mm)*											
	-20	-15	-10	-5	0	5	10	15	20	25	30	35
0					10.5	15.0	13.0	8.0	2.5			
37.5					16.5	22.0	17.0	12.5	6.0			
75					14.0	22.5	17.5	12.0	6.0			
112.5					15.5	22.0	17.0	12.0	6.0			
150					10.5	16.0	3.5	8.5	2.5			

* Measured from the base of the break in slope

TABLE C.42 REPRODUCABILITY EXPERIMENTS LAB RECORDS - RUN 40

Run Number	40
Charge Size	500ml
Flume ID	B
Release Mechanism	Lock gate

Charge Details

Charge number	Material	Volume (ml)	Mass (g)	Mix Details
1	ZY 96025	500	1926.09	monomict

Runout Extents

Distance across flume (mm)	Proximal (mm)*	Distal (mm)*
0	-42	241
37.5	-38	245
75	-36	233
112.5	-38	234
150	-42	230

Notes

Deposit thickness (mm)

Distance across flume (mm)	Distance along flume (mm)*											
	-20	-15	-10	-5	0	5	10	15	20	25	30	35
0					10.0	14.5	12.5	8.0	3.5			
37.5					15.0	21.0	16.5	12.0	7.0			
75					13.0	22.0	17.0	8.0	7.5			
112.5					15.0	21.0	16.5	12.0	6.5			
150					10.0	15.0	13.0	8.0	3.5			

* Measured from the base of the break in slope

TABLE C.43 REPRODUCABILITY EXPERIMENTS LAB RECORDS - RUN 41

Run Number	41
Charge Size	500ml
Flume ID	B
Release Mechanism	Lock gate

Charge Details				
Charge number	Material	Volume (ml)	Mass (g)	Mix Details
1	ZY 96025	500	1926.09	monomict

Runout Extents		
Distance across flume (mm)	Proximal (mm)*	Distal (mm)*
0	-42	259
37.5	-39	255
75	-35	242
112.5	-38	243
150	-42	249

Notes

Deposit thickness (mm)												
Distance across flume (mm)	Distance along flume (mm)*											
	-20	-15	-10	-5	0	5	10	15	20	25	30	35
0					10.0	14.0	12.5	9.0	3.5	0.5		
37.5					15.0	21.0	15.5	12.5	6.5	0.5		
75					12.5	21.5	16.0	13.0	6.5			
112.5					14.5	21.0	16.0	12.0	6.5			
150					10.0	14.5	12.5	9.0	3.5			

* Measured from the base of the break in slope

TABLE C.44 REPRODUCABILITY EXPERIMENTS LAB RECORDS - RUN 42

Run Number	42
Charge Size	500ml
Flume ID	B
Release Mechanism	Lock gate

Charge Details				
Charge number	Material	Volume (ml)	Mass (g)	Mix Details
1	ZY 96025	500	1926.09	monomict

Runout Extents		
Distance across flume (mm)	Proximal (mm)*	Distal (mm)*
0	-38	222
37.5	-35	235
75	-32	232
112.5	-34	232
150	-38	230

Notes

Deposit thickness (mm)												
Distance across flume (mm)	Distance along flume (mm)*											
	-20	-15	-10	-5	0	5	10	15	20	25	30	35
0					10.0	14.5	13.0	9.0	3.5			
37.5					13.0	21.5	17.5	12.5	6.5			
75					11.0	22.0	18.0	13.0	7.0			
112.5					13.0	21.5	17.5	12.5	6.0			
150					10.0	15.0	14.0	9.0	3.5			

* Measured from the base of the break in slope

TABLE C.45 REPRODUCABILITY EXPERIMENTS LAB RECORDS - RUN 43

Run Number	43
Charge Size	500ml
Flume ID	B
Release Mechanism	Lock gate

Charge Details				
Charge number	Material	Volume (ml)	Mass (g)	Mix Details
1	ZY 96025	500	1926.09	monomict

Runout Extents		
Distance across flume (mm)	Proximal (mm)*	Distal (mm)*
0	-41	230
37.5	-38	236
75	-36	233
112.5	-37	228
150	-40	221

Notes

Deposit thickness (mm)												
Distance across flume (mm)	Distance along flume (mm)*											
	-20	-15	-10	-5	0	5	10	15	20	25	30	35
0					10.0	14.5	12.5	8.0	3.5			
37.5					13.0	21.5	17.0	12.0	6.0			
75					12.0	22.0	17.0	12.5	6.5			
112.5					13.0	21.5	17.5	12.0	6.0			
150					10.0	14.5	12.5	8.0	3.5			

* Measured from the base of the break in slope

TABLE C.46 REPRODUCABILITY EXPERIMENTS LAB RECORDS - RUN 44

Run Number	44
Charge Size	500ml
Flume ID	B
Release Mechanism	Lock gate

Charge Details				
Charge number	Material	Volume (ml)	Mass (g)	Mix Details
1	ZY 96025	500	1926.09	monomict

Runout Extents		
Distance across flume (mm)	Proximal (mm)*	Distal (mm)*
0	-39	246
37.5	-36	245
75	-34	243
112.5	-35	247
150	-38	250

Notes

Deposit thickness (mm)												
Distance across flume (mm)	Distance along flume (mm)*											
	-20	-15	-10	-5	0	5	10	15	20	25	30	35
0					9.5	15.0	13.5	10.0	3.5			
37.5					13.0	21.0	17.0	12.5	7.0			
75					10.5	21.0	17.0	13.0	8.0			
112.5					12.0	21.0	16.5	12.5	7.0			
150					10.0	15.0	14.0	10.0	3.5			

* Measured from the base of the break in slope

TABLE C.47 REPRODUCABILITY EXPERIMENTS LAB RECORDS - RUN 45

Run Number	45
Charge Size	500ml
Flume ID	B
Release Mechanism	Lock gate

Charge Details

Charge number	Material	Volume (ml)	Mass (g)	Mix Details
1	ZY 96025	500	1926.09	monomict

Runout Extents

Distance across flume (mm)	Proximal (mm)*	Distal (mm)*
0	-39	250
37.5	-36	253
75	-34	250
112.5	-35	247
150	-39	251

Notes

Deposit thickness (mm)

Distance across flume (mm)	Distance along flume (mm)*											
	-20	-15	-10	-5	0	5	10	15	20	25	30	35
0					9.5	14.0	13.5	9.0	3.5	0.0		
37.5					13.0	21.0	17.0	12.5	6.5	0.0		
75					11.0	21.5	17.5	13.0	7.0	0.0		
112.5					13.0	21.0	17.5	12.5	6.5			
150					10.0	14.0	14.0	9.5	3.0	0.0		

* Measured from the base of the break in slope

TABLE C.48 REPRODUCABILITY EXPERIMENTS LAB RECORDS - RUN 46

Run Number	46
Charge Size	500ml
Flume ID	B
Release Mechanism	Lock gate

Charge Details				
Charge number	Material	Volume (ml)	Mass (g)	Mix Details
1	96025 ZY	100	385.24	monomict

Runout Extents		
Distance across flume (mm)	Proximal (mm)*	Distal (mm)*
0	-12	131
37.5	-2	132
75	1	137
112.5	-	132
150	-10	129

Notes

Deposit thickness (mm)												
Distance across flume (mm)	Distance along flume (mm)*											
	-20	-15	-10	-5	0	5	10	15	20	25	30	35
0					3.0	4.0	3.5					
37.5					0.5	8.5	5.0					
75						8.5	5.0					
112.5					0.0	8.5	5.0					
150					3.0	4.0	3.5					

* Measured from the base of the break in slope

TABLE C.49 REPRODUCABILITY EXPERIMENTS LAB RECORDS - RUN 47

Run Number	47
Charge Size	500ml
Flume ID	B
Release Mechanism	Lock gate

Charge Details				
Charge number	Material	Volume (ml)	Mass (g)	Mix Details
1	96025 ZY	100	385.24	monomict

Runout Extents		
Distance across flume (mm)	Proximal (mm)*	Distal (mm)*
0	-9	136
37.5	4	140
75	6	150
112.5	3	146
150	-6	148

Notes

Deposit thickness (mm)												
Distance across flume (mm)	Distance along flume (mm)*											
	-20	-15	-10	-5	0	5	10	15	20	25	30	35
0					3.0	4.0	3.5					
37.5						8.5	5.5					
75						9.0	6.0					
112.5						8.5	6.0					
150					3.0	4.0	3.5					

* Measured from the base of the break in slope

TABLE C.50 REPRODUCABILITY EXPERIMENTS LAB RECORDS - RUN 48

Run Number	48
Charge Size	500ml
Flume ID	B
Release Mechanism	Lock gate

Charge Details				
Charge number	Material	Volume (ml)	Mass (g)	Mix Details
1	96025 ZY	200	770.31	monomict

Runout Extents		
Distance across flume (mm)	Proximal (mm)*	Distal (mm)*
0	-10	123
37.5	0	132
75	2	133
112.5	0	128
150	-9	126

Notes

Deposit thickness (mm)												
Distance across flume (mm)	Distance along flume (mm)*											
	-20	-15	-10	-5	0	5	10	15	20	25	30	35
0					3.0	4.0	3.5					
37.5					0.0	8.5	5.0					
75						9.0	5.0					
112.5					0.0	8.5	5.0					
150					3.0	4.0	3.5					

* Measured from the base of the break in slope

TABLE C.51 REPRODUCABILITY EXPERIMENTS LAB RECORDS - RUN 49

Run Number	49
Charge Size	500ml
Flume ID	B
Release Mechanism	Lock gate

Charge Details

Charge number	Material	Volume (ml)	Mass (g)	Mix Details
1	ZY 96025	100	382.04	monomict
2	ZY 96025	100	382.03	monomict

Runout Extents

Distance across flume (mm)	Proximal (mm)*	Distal (mm)*
0	-43	142
37.5	-41	142
75	-40	148
112.5	-41	140
150	-42	135

Notes

Deposit thickness (mm)

Distance across flume (mm)	Distance along flume (mm)*											
	-20	-15	-10	-5	0	5	10	15	20	25	30	35
0						12.0	5.0	5.0				
37.5						13.0	8.5	6.0				
75						11.5	8.0	5.5				
112.5						13.0	8.5	5.5				
150						12.0	5.0	4.0				

* Measured from the base of the break in slope

TABLE C.52 REPRODUCABILITY EXPERIMENTS LAB RECORDS - RUN 50

Run Number	50
Charge Size	500ml
Flume ID	B
Release Mechanism	Lock gate

Charge Details

Charge number	Material	Volume (ml)	Mass (g)	Mix Details
1	96025 ZY	200	770.31	monomict

Runout Extents

Distance across flume (mm)	Proximal (mm)*	Distal (mm)*
0	-20	173
37.5	-15	175
75	-9	177
112.5	-14	172
150	-17	120

Notes

Deposit thickness (mm)

Distance across flume (mm)	Distance along flume (mm)*											
	-20	-15	-10	-5	0	5	10	15	20	25	30	35
0					4.5	6.5	7.0	2.0				
37.5					3.5	13.0	9.5	5.0				
75					3.0	12.5	9.5	4.0				
112.5					4.0	13.0	9.0	3.0				
150					4.5	7.0	7.0	1.0				

* Measured from the base of the break in slope

TABLE C.53 REPRODUCABILITY EXPERIMENTS LAB RECORDS - RUN 51

Run Number	51
Charge Size	500ml
Flume ID	B
Release Mechanism	Lock gate

Charge Details

Charge number	Material	Volume (ml)	Mass (g)	Mix Details
1	96025 ZY	200	770.31	monomict

Runout Extents

Distance across flume (mm)	Proximal (mm)*	Distal (mm)*
0	-17	181
37.5	-11	182
75	-4	182
112.5	-11	175
150	-15	174

Notes

Deposit thickness (mm)

Distance across flume (mm)	Distance along flume (mm)*											
	-20	-15	-10	-5	0	5	10	15	20	25	30	35
0					4.5	6.5	6.5	2.0				
37.5					4.0	13.0	9.5	4.5				
75					1.5	12.0	9.5	3.5				
112.5					3.5	13.0	9.5	3.5				
150					4.5	7.0	7.0	1.5				

* Measured from the base of the break in slope

TABLE C.54 REPRODUCABILITY EXPERIMENTS LAB RECORDS - RUN 52

Run Number	52
Charge Size	500ml
Flume ID	B
Release Mechanism	Lock gate

Charge Details

Charge number	Material	Volume (ml)	Mass (g)	Mix Details
1	96025 ZY	200	770.31	monomict

Runout Extents

Distance across flume (mm)	Proximal (mm)*	Distal (mm)*
0	-15	178
37.5	-9	183
75	-4	188
112.5	-9	174
150	-14	177

Notes

Deposit thickness (mm)

Distance across flume (mm)	Distance along flume (mm)*											
	-20	-15	-10	-5	0	5	10	15	20	25	30	35
0					4.5	6.0	7.0	2.0				
37.5					4.0	13.0	9.5	4.5				
75					3.0	12.5	9.0	4.0				
112.5					3.5	13.0	9.5	3.0				
150					4.5	7.0	7.0	2.0				

* Measured from the base of the break in slope

TABLE C.55 REPRODUCABILITY EXPERIMENTS LAB RECORDS - RUN 53

Run Number	53
Charge Size	500ml
Flume ID	B
Release Mechanism	Lock gate

Charge Details

Charge number	Material	Volume (ml)	Mass (g)	Mix Details
1	96025 ZY	300	1155.57	monomict

Runout Extents

Distance across flume (mm)	Proximal (mm)*	Distal (mm)*
0	-51	175
37.5	-49	177
75	-49	181
112.5	-50	180
150	-51	179

Notes

Deposit thickness (mm)

Distance across flume (mm)	Distance along flume (mm)*											
	-20	-15	-10	-5	0	5	10	15	20	25	30	35
0				1.0	14.0	7.0	7.0	2.0				
37.5					16.0	12.0	9.5	4.5				
75					15.5	11.5	8.5	4.5				
112.5					16.5	12.5	9.5	4.5				
150				2.0	14.0	7.0	7.0	2.0				

* Measured from the base of the break in slope

TABLE C.56 REPRODUCABILITY EXPERIMENTS LAB RECORDS - RUN 54

Run Number	54
Charge Size	500ml
Flume ID	B
Release Mechanism	Lock gate

Charge Details				
Charge number	Material	Volume (ml)	Mass (g)	Mix Details
1	96025 ZY	300	1155.57	monomict

Runout Extents		
Distance across flume (mm)	Proximal (mm)*	Distal (mm)*
0	-24	212
37.5	-21	215
75	-17	209
112.5	-21	200
150	-23	209

Notes

Deposit thickness (mm)												
Distance across flume (mm)	Distance along flume (mm)*											
	-20	-15	-10	-5	0	5	10	15	20	25	30	35
0				6.0	9.0	9.0	5.0	0.5				
37.5				6.0	16.0	12.0	8.5	0.5				
75				5.0	15.0	12.0	8.0	0.5				
112.5				6.0	16.0	12.0	8.5	0.5				
150				6.0	9.5	9.0	5.0	0.5				

* Measured from the base of the break in slope

TABLE C.57 REPRODUCABILITY EXPERIMENTS LAB RECORDS - RUN 55

Run Number	55
Charge Size	500ml
Flume ID	B
Release Mechanism	Lock gate

Charge Details

Charge number	Material	Volume (ml)	Mass (g)	Mix Details
1	96025 ZY	300	1155.57	monomict

Runout Extents

Distance across flume (mm)	Proximal (mm)*	Distal (mm)*
0	-23	200
37.5	-21	210
75	-16	214
112.5	-21	205
150	-23	206

Notes

Deposit thickness (mm)

Distance across flume (mm)	Distance along flume (mm)*											
	-20	-15	-10	-5	0	5	10	15	20	25	30	35
0				6.5	9.5	9.5	5.0	0.5				
37.5				6.0	16.0	12.0	8.0	0.5				
75				5.0	15.5	12.0	8.0	0.5				
112.5				6.0	16.0	12.0	8.0	0.5				
150				6.5	9.5	9.0	5.0	0.5				

* Measured from the base of the break in slope

TABLE C.58 REPRODUCABILITY EXPERIMENTS LAB RECORDS - RUN 56

Run Number	56
Charge Size	500ml
Flume ID	B
Release Mechanism	Lock gate

Charge Details

Charge number	Material	Volume (ml)	Mass (g)	Mix Details
1	96025 ZY	300	1155.57	monomict

Runout Extents

Distance across flume (mm)	Proximal (mm)*	Distal (mm)*
0	-24	215
37.5	-21	216
75	-16	207
112.5	-21	205
150	-24	214

Notes

Deposit thickness (mm)

Distance across flume (mm)	Distance along flume (mm)*											
	-20	-15	-10	-5	0	5	10	15	20	25	30	35
0				6.5	9.0	9.5	5.0	0.5				
37.5				6.0	16.0	12.0	7.5	0.5				
75				5.5	16.0	11.5	8.0	0.5				
112.5				6.0	16.0	12.0	7.5	0.5				
150				6.5	9.0	9.0	5.0	0.5				

* Measured from the base of the break in slope

TABLE C.59 REPRODUCABILITY EXPERIMENTS LAB RECORDS - RUN 57

Run Number	57
Charge Size	500ml
Flume ID	B
Release Mechanism	Lock gate

Charge Details

Charge number	Material	Volume (ml)	Mass (g)	Mix Details
1	96025 ZY	300	1155.57	monomict

Runout Extents

Distance across flume (mm)	Proximal (mm)*	Distal (mm)*
0	-60	134
37.5	-57	135
75	-54	139
112.5	-56	136
150	-60	132

Notes

Deposit thickness (mm)

Distance across flume (mm)	Distance along flume (mm)*											
	-20	-15	-10	-5	0	5	10	15	20	25	30	35
0				7.0	19.5	11.0	4.0					
37.5				6.0	20.0	12.0	5.5					
75				7.0	19.0	11.5	4.5					
112.5				6.0	20.5	11.0	5.5					
150				7.0	20.0	11.0	3.5					

* Measured from the base of the break in slope

TABLE C.60 REPRODUCABILITY EXPERIMENTS LAB RECORDS - RUN 58

Run Number	58
Charge Size	500ml
Flume ID	B
Release Mechanism	Lock gate

Charge Details

Charge number	Material	Volume (ml)	Mass (g)	Mix Details
1	96025 ZY	400	1540.87	monomict

Runout Extents

Distance across flume (mm)	Proximal (mm)*	Distal (mm)*
0	-65	172
37.5	-63	180
75	-62	182
112.5	-63	178
150	-66	181

Notes

Deposit thickness (mm)

Distance across flume (mm)	Distance along flume (mm)*											
	-20	-15	-10	-5	0	5	10	15	20	25	30	35
0				8.5	20.0	10.5	7.0	1.5				
37.5				8.5	23.0	13.0	8.5	4.5				
75				9.0	22.0	12.5	8.5	5.0				
112.5				9.0	23.0	13.0	8.5	4.5				
150				8.5	20.0	10.5	7.0	1.5				

* Measured from the base of the break in slope

TABLE C.61 REPRODUCABILITY EXPERIMENTS LAB RECORDS - RUN 59

Run Number	59
Charge Size	500ml
Flume ID	B
Release Mechanism	Lock gate

Charge Details

Charge number	Material	Volume (ml)	Mass (g)	Mix Details
1	96025 ZY	400	1540.87	monomict

Runout Extents

Distance across flume (mm)	Proximal (mm)*	Distal (mm)*
0	-26	233
37.5	-23	237
75	-20	237
112.5	-23	245
150	-25	243

Notes

Deposit thickness (mm)

Distance across flume (mm)	Distance along flume (mm)*											
	-20	-15	-10	-5	0	5	10	15	20	25	30	35
0					8.0	12.0	12.5	8.0	1.5			
37.5					8.0	20.0	16.0	11.0	5.0			
75					6.0	19.0	16.0	11.0	6.0			
112.5					8.0	19.5	16.0	11.0	5.0			
150					8.0	12.0	13.0	8.0	1.5			

* Measured from the base of the break in slope

TABLE C.62 REPRODUCABILITY EXPERIMENTS LAB RECORDS - RUN 60

Run Number	60
Charge Size	500ml
Flume ID	B
Release Mechanism	Lock gate

Charge Details				
Charge number	Material	Volume (ml)	Mass (g)	Mix Details
1	96025 ZY	400	1540.87	monomict

Runout Extents		
Distance across flume (mm)	Proximal (mm)*	Distal (mm)*
0	-29	231
37.5	-25	240
75	-22	238
112.5	-25	232
150	-29	237

Notes

Deposit thickness (mm)												
Distance across flume (mm)	Distance along flume (mm)*											
	-20	-15	-10	-5	0	5	10	15	20	25	30	35
0				8.0	12.0	12.5	7.5	1.5				
37.5				9.5	19.0	15.0	11.0	3.5				
75				6.5	19.0	15.0	11.5	4.0				
112.5				9.0	19.5	16.0	11.0	3.5				
150				8.0	12.0	12.5	7.5	1.5				

* Measured from the base of the break in slope

TABLE C.63 REPRODUCABILITY EXPERIMENTS LAB RECORDS - RUN 61

Run Number	61
Charge Size	500ml
Flume ID	B
Release Mechanism	Lock gate

Charge Details				
Charge number	Material	Volume (ml)	Mass (g)	Mix Details
1	96025 ZY	400	1540.87	monomict

Runout Extents		
Distance across flume (mm)	Proximal (mm)*	Distal (mm)*
0	-28	250
37.5	-26	251
75	-23	243
112.5	-26	246
150	-28	253

Notes

Deposit thickness (mm)												
Distance across flume (mm)	Distance along flume (mm)*											
	-20	-15	-10	-5	0	5	10	15	20	25	30	35
0					7.5	12.0	11.5	7.5	2.0	0		
37.5					9.0	19.0	15.0	10.0	5.0	0		
75					7.0	18.5	15.0	11.0	5.0			
112.5					9.0	19.5	15.5	10.5	5.0			
150					7.0	12.0	12.0	8.0	2.0	0		

* Measured from the base of the break in slope

TABLE C.64 REPRODUCABILITY EXPERIMENTS LAB RECORDS - RUN 62

Run Number	62
Charge Size	500ml
Flume ID	B
Release Mechanism	Lock gate

Charge Details

Charge number	Material	Volume (ml)	Mass (g)	Mix Details
1	5216-288	100	151.04	monomict

Runout Extents

Distance across flume (mm)	Proximal (mm)*	Distal (mm)*
0	-41	89
37.5	-37	94
75	-34	93
112.5	-36	94
150	-41	88

Notes

Deposit thickness (mm)

Distance across flume (mm)	Distance along flume (mm)*											
	-20	-15	-10	-5	0	5	10	15	20	25	30	35
0					5.0	4.0						
37.5					7.0	7.5						
75					7.5	8.0						
112.5					7.0	7.0						
150					5.0	4.0						

* Measured from the base of the break in slope

TABLE C.65 REPRODUCABILITY EXPERIMENTS LAB RECORDS - RUN 63

Run Number	63
Charge Size	500ml
Flume ID	B
Release Mechanism	Lock gate

Charge Details

Charge number	Material	Volume (ml)	Mass (g)	Mix Details
1	5216-288	100	151.04	monomict

Runout Extents

Distance across flume (mm)	Proximal (mm)*	Distal (mm)*
0	-37	82
37.5	-34	95
75	-31	99
112.5	-34	98
150	-37	95

Notes

Deposit thickness (mm)

Distance across flume (mm)	Distance along flume (mm)*											
	-20	-15	-10	-5	0	5	10	15	20	25	30	35
0					4.5	4.0						
37.5					7.5	7.0						
75					7.0	8.0						
112.5					7.5	7.0						
150					4.5	4.0						

* Measured from the base of the break in slope

TABLE C.66 REPRODUCABILITY EXPERIMENTS LAB RECORDS - RUN 64

Run Number	64
Charge Size	500ml
Flume ID	B
Release Mechanism	Lock gate

Charge Details				
Charge number	Material	Volume (ml)	Mass (g)	Mix Details
1	5216-288	100	151.04	monomict

Runout Extents		
Distance across flume (mm)	Proximal (mm)*	Distal (mm)*
0	-38	84
37.5	-34	96
75	-32	93
112.5	-34	94
150	-40	86

Notes

Deposit thickness (mm)												
Distance across flume (mm)	Distance along flume (mm)*											
	-20	-15	-10	-5	0	5	10	15	20	25	30	35
0					4.5	4.0						
37.5					7.5	7.0						
75					7.0	7.0						
112.5					7.0	7.0						
150					5.0	4.0						

* Measured from the base of the break in slope

TABLE C.67 REPRODUCABILITY EXPERIMENTS LAB RECORDS - RUN 65

Run Number	65
Charge Size	500ml
Flume ID	B
Release Mechanism	Lock gate

Charge Details

Charge number	Material	Volume (ml)	Mass (g)	Mix Details
1	5216-288	100	151.04	monomict

Runout Extents

Distance across flume (mm)	Proximal (mm)*	Distal (mm)*
0	-35	93
37.5	-30	100
75	-27	103
112.5	-30	102
150	-34	94

Notes

Deposit thickness (mm)

Distance across flume (mm)	Distance along flume (mm)*											
	-20	-15	-10	-5	0	5	10	15	20	25	30	35
0					5.0	4.0						
37.5					6.5	7.0						
75					6.5	7.0						
112.5					6.5	7.0						
150					5.0	4.0						

* Measured from the base of the break in slope

TABLE C.68 REPRODUCABILITY EXPERIMENTS LAB RECORDS - RUN 66

Run Number	66
Charge Size	500ml
Flume ID	B
Release Mechanism	Lock gate

Charge Details

Charge number	Material	Volume (ml)	Mass (g)	Mix Details
1	5216-288	100	151.04	monomict

Runout Extents

Distance across flume (mm)	Proximal (mm)*	Distal (mm)*
0	-34	90
37.5	-30	102
75	-30	103
112.5	-32	101
150	-36	92

Notes

Deposit thickness (mm)

Distance across flume (mm)	Distance along flume (mm)*											
	-20	-15	-10	-5	0	5	10	15	20	25	30	35
0					4.5	4.0						
37.5					6.5	7.0						
75					7.0	7.0						
112.5					7.0	8.0						
150					5.0	5.0						

* Measured from the base of the break in slope

TABLE C.69 REPRODUCABILITY EXPERIMENTS LAB RECORDS - RUN 67

Run Number	67
Charge Size	500ml
Flume ID	B
Release Mechanism	Lock gate

Charge Details				
Charge number	Material	Volume (ml)	Mass (g)	Mix Details
1	5216-288	100	151.04	monomict

Runout Extents		
Distance across flume (mm)	Proximal (mm)*	Distal (mm)*
0	-36	90
37.5	-33	97
75	-32	101
112.5	-34	97
150	-38	95

Notes

Deposit thickness (mm)												
Distance across flume (mm)	Distance along flume (mm)*											
	-20	-15	-10	-5	0	5	10	15	20	25	30	35
0					5.0	4.0						
37.5					7.5	6.5						
75					7.0	6.5						
112.5					7.0	7.0						
150					5.0	4.0						

* Measured from the base of the break in slope

TABLE C.70 REPRODUCABILITY EXPERIMENTS LAB RECORDS - RUN 68

Run Number	68
Charge Size	500ml
Flume ID	B
Release Mechanism	Lock gate

Charge Details

Charge number	Material	Volume (ml)	Mass (g)	Mix Details
1	5216-288	100	301.93	monomict

Runout Extents

Distance across flume (mm)	Proximal (mm)*	Distal (mm)*
0	-79	100
37.5	-75	103
75	-74	111
112.5	-75	104
150	-79	97

Notes

Deposit thickness (mm)

Distance across flume (mm)	Distance along flume (mm)*											
	-20	-15	-10	-5	0	5	10	15	20	25	30	35
0				9.0	10.0	4.0	0					
37.5				9.0	12.0	7.0	0					
75				10.0	12.0	7.0	0					
112.5				9.5	12.0	7.0	0					
150				9.0	10.0	4.5	0					

* Measured from the base of the break in slope

TABLE C.71 REPRODUCABILITY EXPERIMENTS LAB RECORDS - RUN 69

Run Number	69
Charge Size	500ml
Flume ID	B
Release Mechanism	Lock gate

Charge Details

Charge number	Material	Volume (ml)	Mass (g)	Mix Details
1	5216-288	100	301.93	monomict

Runout Extents

Distance across flume (mm)	Proximal (mm)*	Distal (mm)*
0	-50	123
37.5	-45	122
75	-45	129
112.5	-47	124
150	-52	129

Notes

Deposit thickness (mm)

Distance across flume (mm)	Distance along flume (mm)*											
	-20	-15	-10	-5	0	5	10	15	20	25	30	35
0				0.0	7.5	7.0	2.5					
37.5					11.0	12.0	4.0					
75					11.0	12.0	4.0					
112.5					11.5	12.0	5.0					
150				2.5	8.0	7.5	3.0					

* Measured from the base of the break in slope

TABLE C.72 REPRODUCABILITY EXPERIMENTS LAB RECORDS - RUN 70

Run Number	70
Charge Size	500ml
Flume ID	B
Release Mechanism	Lock gate

Charge Details				
Charge number	Material	Volume (ml)	Mass (g)	Mix Details
1	5216-288	100	301.93	monomict

Runout Extents		
Distance across flume (mm)	Proximal (mm)*	Distal (mm)*
0	-53	125
37.5	-46	130
75	-45	132
112.5	-47	128
150	-53	124

Notes

Deposit thickness (mm)												
Distance across flume (mm)	Distance along flume (mm)*											
	-20	-15	-10	-5	0	5	10	15	20	25	30	35
0				2.5	8.0	7.5	2.0					
37.5					12.0	13.0	3.5					
75					11.5	12.0	3.0					
112.5					12.0	13.0	3.5					
150				3.0	8.0	7.5	2.0					

* Measured from the base of the break in slope

TABLE C.73 REPRODUCABILITY EXPERIMENTS LAB RECORDS - RUN 71

Run Number	71
Charge Size	500ml
Flume ID	B
Release Mechanism	Lock gate

Charge Details				
Charge number	Material	Volume (ml)	Mass (g)	Mix Details
1	5216-288	100	301.93	monomict

Runout Extents		
Distance across flume (mm)	Proximal (mm)*	Distal (mm)*
0	-50	129
37.5	-45	126
75	-44	130
112.5	-47	127
150	-52	126

Notes

Deposit thickness (mm)												
Distance across flume (mm)	Distance along flume (mm)*											
	-20	-15	-10	-5	0	5	10	15	20	25	30	35
0				0.0	7.0	6.5	3.0					
37.5					12.0	12.0	4.5					
75					11.0	11.5	4.0					
112.5					12.0	12.0	4.5					
150				3.0	7.5	6.5	3.0					

* Measured from the base of the break in slope

TABLE C.74 REPRODUCABILITY EXPERIMENTS LAB RECORDS - RUN 72

Run Number	72
Charge Size	500ml
Flume ID	B
Release Mechanism	Lock gate

Charge Details

Charge number	Material	Volume (ml)	Mass (g)	Mix Details
1	5216-288	100	453.12	monomict

Runout Extents

Distance across flume (mm)	Proximal (mm)*	Distal (mm)*
0	-84	129
37.5	-82	140
75	-82	138
112.5	-82	135
150	-86	134

Notes

Deposit thickness (mm)

Distance across flume (mm)	Distance along flume (mm)*											
	-20	-15	-10	-5	0	5	10	15	20	25	30	35
0				10.0	11.0	8.0	2.5					
37.5				10.0	12.0	12.0	4.0					
75				10.0	11.0	11.5	4.5					
112.5				10.0	12.0	12.0	4.0					
150				10.0	11.0	8.5	2.5					

* Measured from the base of the break in slope

TABLE C.75 REPRODUCABILITY EXPERIMENTS LAB RECORDS - RUN 73

Run Number	73
Charge Size	500ml
Flume ID	B
Release Mechanism	Lock gate

Charge Details

Charge number	Material	Volume (ml)	Mass (g)	Mix Details
1	5216-288	100	453.12	monomict

Runout Extents

Distance across flume (mm)	Proximal (mm)*	Distal (mm)*
0	-98	103
37.5	-94	107
75	-94	107
112.5	-94	110
150	-98	102

Notes

Deposit thickness (mm)

Distance across flume (mm)	Distance along flume (mm)*											
	-20	-15	-10	-5	0	5	10	15	20	25	30	35
0				12.5	17.0	3.5	0.5					
37.5				14.5	20.0	6.0	0.5					
75				13.5	19.5	5.0	0.5					
112.5				15.0	20.0	6.0	0.5					
150				12.5	17.0	3.5	0.5					

* Measured from the base of the break in slope

TABLE C.76 REPRODUCABILITY EXPERIMENTS LAB RECORDS - RUN 74

Run Number	74
Charge Size	500ml
Flume ID	B
Release Mechanism	Lock gate

Charge Details

Charge number	Material	Volume (ml)	Mass (g)	Mix Details
1	5216-288	100	453.12	monomict

Runout Extents

Distance across flume (mm)	Proximal (mm)*	Distal (mm)*
0	-64	168
37.5	-56	160
75	52	163
112.5	-52	167
150	-54	158

Notes

Deposit thickness (mm)

Distance across flume (mm)	Distance along flume (mm)*											
	-20	-15	-10	-5	0	5	10	15	20	25	30	35
0				6.0	12.0	10.5	5.5	1.0				
37.5				5.0	15.5	16.0	8.5	1.0				
75				5.0	14.5	14.5	8.0	1.0				
112.5				4.5	15.0	16.0	8.0	1.0				
150				3.0	10.0	9.5	4.0	0.5				

* Measured from the base of the break in slope

TABLE C.77 REPRODUCABILITY EXPERIMENTS LAB RECORDS - RUN 75

Run Number	75
Charge Size	500ml
Flume ID	B
Release Mechanism	Lock gate

Charge Details				
Charge number	Material	Volume (ml)	Mass (g)	Mix Details
1	5216-288	100	453.12	monomict

Runout Extents		
Distance across flume (mm)	Proximal (mm)*	Distal (mm)*
0	-60	150
37.5	-55	144
75	-55	144
112.5	-56	143
150	-61	148

Notes

Deposit thickness (mm)												
Distance across flume (mm)	Distance along flume (mm)*											
	-20	-15	-10	-5	0	5	10	15	20	25	30	35
0				4.0	10.5	10.0	5.0	0.0				
37.5				4.0	15.5	15.5	9.0					
75				3.5	15.0	15.0	8.5					
112.5				4.0	15.5	15.5	9.0					
150				5.0	10.5	10.0	5.0					

* Measured from the base of the break in slope

TABLE C.78 REPRODUCABILITY EXPERIMENTS LAB RECORDS - RUN 76

Run Number	76
Charge Size	500ml
Flume ID	B
Release Mechanism	Lock gate

Charge Details				
Charge number	Material	Volume (ml)	Mass (g)	Mix Details
1	5216-288	100	453.12	monomict

Runout Extents		
Distance across flume (mm)	Proximal (mm)*	Distal (mm)*
0	-60	168
37.5	-56	157
75	-55	162
112.5	-56	155
150	-61	155

Notes

Deposit thickness (mm)												
Distance across flume (mm)	Distance along flume (mm)*											
	-20	-15	-10	-5	0	5	10	15	20	25	30	35
0				6.0	11.5	10.0	5.5	0.5				
37.5				4.0	15.0	15.0	8.0	0.5				
75				4.5	15.0	15.0	8.0	0.5				
112.5				4.0	15.0	15.0	8.0	0.5				
150				5.0	11.0	10.0	5.5	0.5				

* Measured from the base of the break in slope

TABLE C.79 REPRODUCABILITY EXPERIMENTS LAB RECORDS - RUN 77

Run Number	77
Charge Size	500ml
Flume ID	B
Release Mechanism	Lock gate

Charge Details				
Charge number	Material	Volume (ml)	Mass (g)	Mix Details
1	5216-288	100	604.09	monomict

Runout Extents		
Distance across flume (mm)	Proximal (mm)*	Distal (mm)*
0	-105	129
37.5	-101	124
75	-101	131
112.5	-100	130
150	-105	131

Notes

Deposit thickness (mm)												
Distance across flume (mm)	Distance along flume (mm)*											
	-20	-15	-10	-5	0	5	10	15	20	25	30	35
0			3.0	15.5	19.0	7.0	2.0					
37.5			2.0	17.5	22.0	11.5	3.5					
75			2.0	16.0	22.0	11.0	3.0					
112.5			0.0	17.5	22.0	12.0	4.0					
150			3.0	15.0	19.0	7.0	2.0					

* Measured from the base of the break in slope

TABLE C.80 REPRODUCABILITY EXPERIMENTS LAB RECORDS - RUN 78

Run Number	78
Charge Size	500ml
Flume ID	B
Release Mechanism	Lock gate

Charge Details

Charge number	Material	Volume (ml)	Mass (g)	Mix Details
1	5216-288	100	604.09	monomict

Runout Extents

Distance across flume (mm)	Proximal (mm)*	Distal (mm)*
0	-73	179
37.5	-66	175
75	-66	180
112.5	-67	178
150	-73	186

Notes

Deposit thickness (mm)

Distance across flume (mm)	Distance along flume (mm)*											
	-20	-15	-10	-5	0	5	10	15	20	25	30	35
0				7.0	15.0	13.0	6.5	2.0				
37.5				7.0	18.0	17.0	10.0	3.0				
75				6.0	18.0	17.0	10.0	2.0				
112.5				7.0	18.0	17.0	10.0	3.0				
150				7.0	15.5	13.0	6.5	2.0				

* Measured from the base of the break in slope

TABLE C.81 REPRODUCABILITY EXPERIMENTS LAB RECORDS - RUN 79

Run Number	79
Charge Size	500ml
Flume ID	B
Release Mechanism	Lock gate

Charge Details				
Charge number	Material	Volume (ml)	Mass (g)	Mix Details
1	5216-288	100	604.09	monomict

Runout Extents		
Distance across flume (mm)	Proximal (mm)*	Distal (mm)*
0	-73	172
37.5	-67	173
75	-76	183
112.5	-67	176
150	-73	179

Notes

Deposit thickness (mm)												
Distance across flume (mm)	Distance along flume (mm)*											
	-20	-15	-10	-5	0	5	10	15	20	25	30	35
0				8.0	14.0	12.0	6.5	2.0				
37.5				8.0	19.5	18.5	10.0	3.5				
75				6.0	18.5	18.0	11.0	2.0				
112.5				8.0	19.5	18.0	10.0	3.5				
150				8.0	14.0	12.0	6.5	2.0				

* Measured from the base of the break in slope

TABLE C.82 REPRODUCABILITY EXPERIMENTS LAB RECORDS - RUN 80

Run Number	80
Charge Size	500ml
Flume ID	B
Release Mechanism	Lock gate

Charge Details				
Charge number	Material	Volume (ml)	Mass (g)	Mix Details
1	5216-288	100	604.09	monomict

Runout Extents		
Distance across flume (mm)	Proximal (mm)*	Distal (mm)*
0	-73	171
37.5	-67	172
75	-66	177
112.5	-67	182
150	-73	186

Notes

Deposit thickness (mm)												
Distance across flume (mm)	Distance along flume (mm)*											
	-20	-15	-10	-5	0	5	10	15	20	25	30	35
0				7.0	14.5	12.0	7.0	2.0				
37.5				7.5	19.0	18.0	11.0	3.5				
75				7.0	18.0	18.0	11.5	4.0				
112.5				7.5	19.0	18.0	11.0	3.5				
150				7.0	14.0	12.0	7.0	1.0				

* Measured from the base of the break in slope

APPENDIX D - NGAURUHOE SAMPLE ANALYSIS

TABLE D.1 NGAURUHOE SAMPLE DENSITY ANALYSIS

Mass	Volume	Mass	
102.40	81	PRNg6-01	1.264197531
93.26	63	PRNg6-01	1.48031746
45.24	45	PRNg6-01	1.005333333
32.94	32	PRNg6-01	1.029375
28.94	28	PRNg6-01	1.033571429
16.10	24	PRNg6-01	0.670833333
280.43	193	PRNg6-01	1.453005181
139.00	92	PRNg6-01	1.510869565
94.23	102	PRNg6-01	0.923823529
287.33	117	PRNg6-01	2.455811966
15.27	6	PRNg6-01	2.545
115.00	80	PRNg6-01	1.4375
365.00	175	PRNg6-06	2.085714286
615.00	248	PRNg6-06	2.47983871
112.17	95	PRNg6-06	1.180736842
50.08	34	PRNg6-06	1.472941176
27.63	19	PRNg6-06	1.454210526
4.81	4	PRNg6-06	1.2025
4.76	3.5	PRNg6-06	1.36
5.80	3	PRNg6-06	1.933333333
3.23	2.5	PRNg6-06	1.292
130.00	88	PRNg6-06	1.477272727
50.00	68	PRNg6-06	0.735294118
120.00	150	PRNg6-06	0.8
325.00	160	PRNg6-06	2.03125
95.00	96	PRNg6-06	0.989583333
56.00	55	PRNg6-06	1.018181818
220.00	126	PRNg6-06	1.746031746
136.23	112	PRNg6-05	1.216339286
101.47	72	PRNg6-05	1.409305556
61.37	40	PRNg6-05	1.53425
69.65	42	PRNg6-05	1.658333333
22.07	30	PRNg6-05	0.735666667
18.09	20	PRNg6-05	0.9045
17.94	20	PRNg6-05	0.897
47.15	46	PRNg6-05	1.025
9.86	13	PRNg6-05	0.758461538
9.20	12	PRNg6-05	0.766666667
10.50	11	PRNg6-05	0.954545455
14.65	18	PRNg6-05	0.813888889
8.27	14	PRNg6-05	0.590714286
52.52	48	PRNg6-05	1.094166667
453.00	208	PRNg6-06	2.177884615

PRNg6-01 PRNg6-03L

Phonolite density: 2.56g/cm3

Vesicularity		Mass	Volume
0	2.56	620	242.1875
20	2.048	500	244.140625
40	1.536	375	244.140625
60	1.024	250	244.140625
80	0.512	125	244.140625

PRNg6-01 Bin	PRNg6-05 Frequency	PRNg6-06 Frequency	Frequency
0.1	0	0	0
0.2	0	0	0
0.3	0	0	0
0.4	0	0	0
0.5	0	0	0
0.6	0	1	0
0.7	1	0	0
0.8	0	3	2
0.9	0	2	0
1	1	2	1
1.1	3	2	1
1.2	0	0	1
1.3	0	1	2
1.4	0	0	1
1.5	3	1	3
1.6	1	1	0
	1.7	0	1
1.8	0	0	1
1.9	0	0	0
2	0	0	1
2.1	0	0	2
2.2	0	1	0
2.3	0	0	0
2.4	0	0	0
2.5	1	0	1
2.6	1	0	0
2.7	0	0	0
2.8	0	0	0
2.9	0	0	0
3	0	0	0
>3	0	0	0

TABLE D.2 GRAINSIZE ANALYSIS OF SAMPLE PRNg6-02

	SIEVING ERROR:	0.1%					ANALYST and DATE:	Pete Rowley, 7/16/2008	
	SAMPLE IDENTITY:	PRNg6-02							
	SAMPLE TYPE:	Unimodal, Poorly Sorted					TEXTURAL GROUP:	Sand	
	SEDIMENT NAME:	Poorly Sorted Fine Sand							
		µm						GRAIN SIZE DISTRIBUTION	
MODE 1:	267.5	1.984			GRAVEL:	0.0%		COARSE SAND:	13.0%
MODE 2:					SAND:	90.8%		MEDIUM SAND:	20.1%
MODE 3:					MUD:	9.2%		FINE SAND:	24.3%
D_{10}:	65.24	-0.474						V FINE SAND:	18.4%
MEDIAN or D_{50}:	236.9	2.078			V COARSE GRAVEL:	0.0%		V COARSE SILT:	1.5%
D_{90}:	1388.7	3.938			COARSE GRAVEL:	0.0%		COARSE SILT:	1.5%
(D_{90} / D_{10}):	21.29	-8.312			MEDIUM GRAVEL:	0.0%		MEDIUM SILT:	1.5%
(D_{90} - D_{10}):	1323.5	4.412			FINE GRAVEL:	0.0%		FINE SILT:	1.5%
(D_{75} / D_{25}):	4.957	3.852			V FINE GRAVEL:	0.0%		V FINE SILT:	1.5%
(D_{75} - D_{25}):	455.4	2.309			V COARSE SAND:	14.9%		CLAY:	1.5%

	METHOD OF MOMENTS			FOLK and WARD METHOD		
	Arithmetic	Geometric	Logarithmic	Geometric	Logarithmic	Description
	µm	µm		µm		
MEAN:	398.0	157.3	2.219	266.5	1.908	Medium Sand
SORTING:	440.3	5.563	1.962	3.702	1.888	Poorly Sorted
SKEWNESS:	1.430	-1.345	0.969	0.021	-0.021	Symmetrical
KURTOSIS:	3.612	4.601	3.767	1.203	1.203	Leptokurtic

TABLE D.3 GRAINSIZE ANALYSIS OF SAMPLE PRNg6-03

	SIEVING ERROR:	-36.5%	SAMPLE STATISTICS				
	SAMPLE IDENTITY:	PRNg6-04				ANALYST and DATE:	Pete Rowley, 7/16/2008
	SAMPLE TYPE:	Unimodal, Poorly Sorted				TEXTURAL GROUP:	Sand
	SEDIMENT NAME:	Poorly Sorted Very Coarse Sand					

	µm				GRAIN SIZE DISTRIBUTION	
MODE 1:	267.5	1.984	GRAVEL:	0.0%	COARSE SAND:	20.2%
MODE 2:			SAND:	97.1%	MEDIUM SAND:	24.2%
MODE 3:			MUD:	2.9%	FINE SAND:	19.2%
D_{10}:	115.2	-0.901			V FINE SAND:	8.3%
MEDIAN or D_{50}:	437.0	1.194	V COARSE GRAVEL:	0.0%	V COARSE SILT:	0.5%
D_{90}:	1867.0	3.118	COARSE GRAVEL:	0.0%	COARSE SILT:	0.5%
(D_{90} / D_{10}):	16.21	-3.462	MEDIUM GRAVEL:	0.0%	MEDIUM SILT:	0.5%
(D_{90} - D_{10}):	1751.8	4.019	FINE GRAVEL:	0.0%	FINE SILT:	0.5%
(D_{75} / D_{25}):	4.688	-181.429	V FINE GRAVEL:	0.0%	V FINE SILT:	0.5%
(D_{75} - D_{25}):	793.4	2.229	V COARSE SAND:	25.2%	CLAY:	0.5%

	METHOD OF MOMENTS			FOLK and WARD METHOD		
	Arithmetic µm	Geometric µm	Logarithmic	Geometric µm	Logarithmic	Description
MEAN :	552.1	221.7	1.344	465.6	1.103	Medium Sand
SORTING:	494.8	6.851	1.536	2.731	1.449	Poorly Sorted
SKEWNESS:	0.777	-1.814	1.389	-0.038	0.038	Symmetrical
KURTOSIS:	2.032	5.587	6.002	0.787	0.787	Platykurtic

TABLE D.4 GRAINSIZE ANALYSIS OF SAMPLE PRNg6-04

SIEVING ERROR:	10.6%		SAMPLE STATISTICS				
SAMPLE IDENTITY:	PRNg6-04					ANALYST and DATE:	Pete Rowley, 7/16/2008
SAMPLE TYPE:	Unimodal, Poorly Sorted					TEXTURAL GROUP:	Sand
SEDIMENT NAME:	Poorly Sorted Very Coarse Sand						

	µm				GRAIN SIZE DISTRIBUTION	
MODE 1:	267.5	1.984	GRAVEL:	0.0%	COARSE SAND:	19.5%
MODE 2:			SAND:	97.9%	MEDIUM SAND:	23.6%
MODE 3:			MUD:	2.1%	FINE SAND:	21.9%
D_{10}:	115.9	-0.814			V FINE SAND:	9.2%
MEDIAN or D_{50}:	403.6	1.309	V COARSE GRAVEL:	0.0%	V COARSE SILT:	0.4%
D_{90}:	1758.3	3.109	COARSE GRAVEL:	0.0%	COARSE SILT:	0.4%
(D_{90} / D_{10}):	15.17	-3.819	MEDIUM GRAVEL:	0.0%	MEDIUM SILT:	0.4%
(D_{90} - D_{10}):	1642.4	3.923	FINE GRAVEL:	0.0%	FINE SILT:	0.4%
(D_{75} / D_{25}):	4.772	31.74	V FINE GRAVEL:	0.0%	V FINE SILT:	0.4%
(D_{75} - D_{25}):	751.3	2.254	V COARSE SAND:	23.8%	CLAY:	0.4%

	METHOD OF MOMENTS			FOLK and WARD METHOD		
	Arithmetic µm	Geometric µm	Logarithmic	Geometric µm	Logarithmic	Description
MEAN :	549.7	239.3	1.380	434.9	1.201	Medium Sand
SORTING:	494.6	5.956	1.472	2.738	1.453	Poorly Sorted
SKEWNESS:	0.803	-1.950	1.122	0.025	-0.025	Symmetrical
KURTOSIS:	2.039	6.558	5.366	0.780	0.780	Platykurtic